# Study of $CeO_2$ synthesis from liquid precursors in a RF-inductively coupled plasma reactor

Ian Castillo

Department of Chemical Engineering

McGill University, Montreal

June 2007

A thesis submitted to McGill University in partial fulfillment of the requirements of the degree of Doctor of Philosophy

*Your file Votre référence*
*ISBN: 978-0-494-38566-1*
*Our file Notre référence*
*ISBN: 978-0-494-38566-1*

"... a mi esposa Heather ..."

"... a mis padres Alfredo y Patricia ..."

"... a mi hermana Io ..."

*"Try not to become a man of success but rather to become a man of value"*
Albert Einstein

*"Begin at the beginning and go on till you come to the end: then stop"*
Lewis Carroll,
Alice's Adventures in Wonderland. Said by the King to the White Rabbit

## Abstract

A new reactor and a novel in-situ sampling technique were developed for the study of the synthesis of $CeO_2$ powders produced from dissolved cerium nitrate salts. The reactor minimized particle recirculation and provided a highly symmetric and undisturbed plasma flow suitable for the analysis of the phenomena affecting the formation of $CeO_2$ powders. The sampling probe provided in-situ sampling of in-flight $CeO_2$ particles and allowed continuous sampling without cross contamination. The sampled particles were collected using a wet collection system composed of a mist atomizer acting as a scrubber and a custom-made spray chamber. The entire collection system is portable and it was tested in the particle range of 20 nm to 100 μm. This information provided a picture of how $CeO_2$ particles were formed. A numerical simulation of different plasma operating parameters using Fluent was presented. A comprehensive droplet-to-particle formation mechanism was deduced based on calorimetry, thermodynamics of $CeO_2$ formation, numerical simulations and collected particles. The effect of adding water soluble fuels (alanine and glycine) to the original cerium nitrate solutions was investigated. Fuel addition decreased the temperature of $CeO_2$ formation by acting as a local heat source as a result of fuel auto-ignition. The addition of fuel caused "particle size discrimination", and a single mode particle size distribution centered between 50-140 nm was achieved along the centerline of the reactor.

Also, heat and mass transfer effects were numerically investigated in evaporating solution droplets (20-40 μm in diameter) containing dissolved hexahydrated cerium nitrate in a stationary rf Ar-$O_2$ thermal plasma. This model was developed to study the evaporation of a solution droplet surrounded by a porous crust in a stagnant rf Ar-$O_2$ thermal plasma under reduced pressure. It considered a three phase system: a liquid core of dissolved $Ce(NO_3)_3.6H_2O$ in water, a dry porous crust of homogeneously precipitated spherical crystals of equal size, and an Ar-$O_2$ plasma under reduced pressure. The impact of different plasma operating parameters on the temperature and dissolved solid content profiles in the droplet was studied, i.e. surrounding plasma temperature, initial salt content and droplet size, plasma gas composition, and system pressure. Temperature and composition dependant thermophysical properties were used. The model was solved in a

moving boundary frame using an ALE approach and considering Stefan flow. It provided the necessary information to understand the droplet to particle transformation steps in regions where in-flight probing was unfeasible, i.e. torch zone.

## Résumé

Un nouveau réacteur et une technique innovatrice d'échantillonnage in situ furent développés pour étudier la synthèse de poudres de $CeO_2$ produites à partir de sels de nitrate de cérium dissous. Le réacteur minimise la recirculation des particules et fournit un plasma non perturbé et grandement symétrique approprié pour l'analyse des phénomènes affectant la formation de poudres de $CeO_2$. De plus, une sonde permet un échantillonnage in situ et en vol des particules de $CeO_2$ et ce, en continu et sans contamination croisée.

Les particules ainsi captées sont recueillies grâce à un système de collecte par voie humide qui est composé d'un atomiseur de brume (mist atomizer) qui joue le rôle d'un récureur (scrubber) et d'une chambre d'atomisation (spray chamber) maison. Le système d'échantillonnage est mobile et fut testé sur des particules ayant des tailles de 20 nm à 100 μm. C'est grâce à l'analyse des particules ainsi recueillies que nous sommes en mesure de comprendre comment les particules de $CeO_2$ sont formées. Nous présentons aussi une simulation numérique, effectuée avec le logiciel Fluent, qui utilise les différents paramètres d'expérimentation. Le mécanisme détaillé de la formation des particules à partir de gouttelettes fut déduit grâce à des études calorimétriques, à une étude thermodynamique de la formation du $CeO_2$, à des simulations numériques et à l'analyse des particules recueillies. Nous avons aussi étudié l'effet d'un ajout de combustibles hydrosolubles (l'alanine et la glycine) à la solution originale de nitrate de cérium. Cette addition de combustibles diminue la température de formation du $CeO_2$ en agissant comme une source locale de chaleur résultant de l'auto-ignition du combustible. Aussi, le combustible cause une « ségrégation des particules » selon leur taille. En effet, une distribution monomodale de la taille des particules, centrée entre 40 et 140 nm, fut obtenue le long de l'axe central du réacteur.

De plus, les effets des transferts de masse et de chaleur furent numériquement étudiés lors de l'évaporation, dans un plasma thermique radiofréquence (RF) stationnaire d'Ar et d'$O_2$, de gouttelettes (20-40 μm de diamètre) d'une solution contenant du nitrate de

cérium hexahydraté dissous. Ce modèle fut développé pour étudier l'évaporation de gouttelettes entourées d'une enveloppe poreuse dans un plasma thermique RF stagnant d'Ar et d'$O_2$ sous pression réduite. Le modèle considère un système à trois phases : 1) le cœur liquide de $Ce(NO_3)_3*6H_2O$ dissous dans l'eau, 2) une enveloppe poreuse sèche constituée de cristaux sphériques de taille uniforme précipités de manière homogène et 3) un plasma d'Ar et d'$O_2$ opéré à pression réduite. L'impact des différents paramètres d'opération du plasma sur la température et la concentration de sels dissous à l'intérieur des gouttelettes fut étudié, i.e. la température du plasma entourant les gouttelettes, le contenu initial en sel des gouttelettes et leurs tailles, la composition du gaz formant le plasma et la pression dans le réacteur. Les propriétés thermo-physiques qui dépendent de la température et de la concentration furent utilisées. Le modèle fut résolu avec une frontière mobile en utilisant une approche ALE et en considérant un flux de Stefan (Stefan flow). Le modèle fournit les informations nécessaires pour comprendre les étapes de la transformation d'une gouttelette en particules dans les régions où l'échantillonnage en vol était impossible i.e. près de la torche.

## Acknowledgments

I would like to express my most sincere gratitude to Professor Richard Munz for his moral support, edifying discussions and thoughtful guidance, without which this thesis would never have been written.

I would like to thank Professor François Gitzhofer and all other members of the CRTP Sherbrooke for their advice and for lending me the DPV-2000.

Many thanks to the non-academic staff that help me carrying out my research activities: Mr. Walter Greenland for building the reactor that I used, Mr. Frank Caporuscio, Mr. Luciano Cusmich, Mr. Gerald Lepkyj, Mr. Alain Gagnon and Mr. Ranjan Roy for their technical support, Ms. Monique Riendeau for the X-ray diffraction training, and Ms. Helen Campbell for the SEM training.

I thank the present members of the CRTP McGill with special mention to L. N. Rao, Frederic Marion, and Ramona Turcu, for their company, advice and support. Special thanks to Frederic and Emilie Marion for their help in the Abstract translation. Also, I would like to thank Marie Desroches, Gaurav Gupta and Gino de Luca for their help in numerous stages of my work.

Finally, I wish to acknowledge the financial support provided by the Natural Science and Engineering Research Council of Canada (NSERC), Fonds de Recherche sur la Nature et Technologies (FQRNT), Eugene Lamonthe Scholarship and McGill internal fee waivers and funding.

# Table of contents

## List of figures

## List of tables

# Chapter 1 Introduction

## 1.1 Problem definition and project scope

In 1999, researchers at the CRTP (Centre de Recherche en Technolgie des Plasmas) began a project to investigate the combinatorial chemistry production of the different solid oxide fuel cell (SOFC) components (cathode, anode, electrolyte and internal reformer) using thermal plasma technology (Canadian Foundation for Innovation CFI, 1999). The project also encompassed the diagnosis and evaluation of the individual cell components and of the overall cell performance. Ultimately, the project's aim was an automated, quick and reliable in-line manufacturing of SOFCs for industrial applications. Thermal plasma technology was proposed as a novel alternative to manufacture each cell component due to the short time required to produce the components in a plasma environment.

This interdisciplinary project was subdivided based on the different cell components, i.e. cathode, anode, electrolyte and internal reformer. The current thesis is concerned with the electrolyte. It was demonstrated in previous work [*Castillo*, 2005] that doped $CeO_2$ based electrolyte powders suitable for cell testing could be produced. These powders are the starting material for the production of electrolyte layers by other plasma treatments, by conventional sintering methods or by direct plasma spraying of the particles to form electrolyte layers.

From our previous work it was concluded that the success of the overall thermal plasma synthesis of SOFCs materials greatly depended on the understanding of the droplet-to-particle formation mechanisms. These mechanisms determine particle size which is a key parameter to direct plasma spraying of materials for SOFCs layers. Therefore, a detailed experimental and numerical understanding of particle formation in thermal plasma synthesis from liquid precursors was needed and this is the primary focus of the thesis.

## 1.2 Thesis objectives

To establish a comprehensive experimental and conceptual knowledge of the phenomena affecting synthesis of oxide particles from liquid feedstock in a RF-inductive coupled plasma. Specifically, the following objectives were formulated

1 Develop a reactor capable of experimentally studying the local spatial evolution of synthesized particles under different plasma operating conditions in real time.
2 Develop a quick and continuous sampling technique that allows the study of numerous operating conditions by sampling particles in-flight.
3 Determine particle size, velocity and temperature at different spatial locations in real time
4 Develop a numerical model to explain the atomized droplet-to-oxide particle transformation and the factors affecting this transformation

## 1.3 Thesis outline

This thesis is divided into 10 chapters and appendices and is a manuscript-based thesis. The first part of the thesis covers the experimental work with some modeling support (Chapters 4 and 5) and the second part (Chapter 6 and 7) describes the modeling work. Each journal article constitutes a chapter. **The experimental and modeling work complement each other. However, the experimental work concentrates primarily on analyzing the transformation of droplet-to-particle cerium oxide downstream of the reactor inlet; whereas the modeling work focuses on analyzing the transformation steps between the atomizing probe and the reactor inlet.**

The experimental work is presented first because it shows the experimental setup used and better situates the reader in the general context of this project. Due to the nature of a manuscript-based thesis, care has been taken to minimize repetition and facilitate a fluent reading. At the beginning of each chapter a brief chapter introduction (before the

"Abstract") is given before the manuscript is presented. Each chapter will have its pertaining literature review, introduction and references related to the subject discussed.

In addition to the literature review presented in each chapter, a concise literature review (Chapter 3) has been added to introduce the reader to thermal plasmas, solid oxide fuel cells, in-flight sampling, synthesis of ceramic particles in rf-thermal plasmas, and evaporation of solution droplets before the body of the thesis. Reading this chapter allows a clearer understanding of the project and fills the unavoidable gaps left by the compressed writing style necessary in manuscripts. Further, the **integrity of the articles has been preserved as much as possible and they are presented in full in their respective chapters**. The thesis requirements established by McGill University mandate that a separate literature review chapter (Chapter 3) must be included, even in the case of manuscript-based theses. Therefore, some overlap between the contents of Chapter 3 and the individual article introductions in Chapters 4, 5, 6 and 7 should be expected.

The references contained in each manuscript are listed in numerical format at the end of each chapter and any other references used in this thesis are listed in brackets and alphabetically cited at the end of the thesis under "References". Finally, the experimental techniques and methodologies used in this work are described in each chapter as needed. The only technique that is described separately is the particle size characterization technique based on laser diffraction that was developed and published by the author of this thesis (Chapter 8) and was essential to provide primary particle size distributions.

**Chapter 1: Introduction**

This chapter includes a thesis introduction, a definition of the scope of the thesis and a statement of objectives. The thesis outline is described

**Chapter 2: Contributions of authors**

A description of the work carried out by the authors of the manuscripts is stated.

**Chapter 3: Literature review**

The literature review is divided into three major parts. First, solid oxide fuel cells (SOFC) are described, i.e. components, cell operation and nature and composition of electrolyte materials. Second, the different plasma systems used to produce SOFCs components and other attempts made to analyze particles in flight in thermal plasma reactors are described. Third, models dealing with evaporation of solution droplets at high temperatures are described.

**Chapter 4: Experimental results. Part 1**

The reactor and sampling system design are discussed. The results obtained from calorimetry, thermodynamic simulations and modeling of the reactor flow are presented. Also, a detailed particle formation mechanism starting from liquid droplets and ending with solid powders is described. The characterization of the different $CeO_2$ based powders synthesized is described, i.e. X-ray diffraction, SEM, and particle size distribution.

**Chapter 5: Experimental results. Part 2**

An in-depth analysis of the size distribution of the synthesized powders is presented in this chapter. CCD images of the synthesized particles are shown and used to determine particle speeds. The effects of adding alanine and glycine to the liquid precursors are studied.

**Chapter 6: Numerical results. Part 1**

The model developed to study droplet explosion is described. The first part of the model considered the evaporation of a solution droplet immersed in thermal plasma gas and simultaneously solved the heat, mass and momentum equations with moving boundary conditions. This part of the model applies until the point of crust formation.

**Chapter 7: Numerical results. Part 2**

The second part of the model is presented here. The model encompassed the transient evaporation of solution droplets surrounded by a porous crust immersed in plasma gas.

The heat, mass and momentum equations in those 3 different domains were solved with moving boundary conditions. A simple model was also developed to determine the point of crust rupture.

**Chapter 8: Particle size characterization of $CeO_2$ and $CeO_2$ doped powders using laser diffraction**

The technique developed to characterize $CeO_2$ and $CeO_2$ doped powders using laser diffraction is presented. The drawbacks and range of operation are discussed.

**Chapter 9: Conclusions and original contributions**

This chapter summarizes the major contributions enumerated in this study and states the original contributions of this thesis.

**Chapter 10: Future work and recommendations.**

Finally, the recommendations for future research endeavors are discussed

## Chapter 2 Contributions of authors

This chapter describes the author's contributions to the manuscripts that are incorporated in the thesis. The first 2 manuscripts are experimental work, manuscript 3 and 4 are numerical simulations and manuscript 5 describes the technique developed to accurate measure primary particle size distributions for $CeO_2$ particles (an essential component of this work). I wrote the first draft of all papers and contributed to modifications as the work evolved.

1 **Castillo, I** and Munz, R. J. New in-situ sampling and analysis of the production of $CeO_2$ powders from liquid precursors using a novel wet collection system in a rf inductively coupled thermal plasma reactor. Part 1: Reactor design and sampling probe. *Plasma Chemistry and Plasma Processing* (submitted) (Chapter 4)

I carried out all the experimental, analytical and modeling work shown in this article. I am also the first author of the article.

2 **Castillo, I** and Munz, R. J. New in-situ sampling and analysis of the production of $CeO_2$ powders from liquid precursors using a novel wet collection system in a rf inductively coupled thermal plasma reactor. Part 2: Analysis of $CeO_2$ powders, fuel addition and image analysis. *Plasma Chemistry and Plasma Processing* (submitted) (Chapter 5)

I carried out all the experimental, analytical and modeling work shown in this article. I am also the first author of the article.

3 **Castillo, I** and Munz, R. J. Transient heat, mass and momentum transfer of an evaporating stationary droplet containing dissolved cerium nitrate in a rf thermal argon-oxygen plasma under reduced pressure. *International Journal of Heat and Mass Transfer*, **50**(1-2), 240-256 (2007) (Chapter 6)

I developed the mathematical model described in this work, conducted the numerical simulations and analyzed the results. I am the first author of the article

4 **Castillo, I** and Munz, R. J. Transient modeling of heat, mass, momentum transfer of an evaporating cerium nitrate solution droplet with a surrounding shell in a rf thermal argon-oxygen plasma under reduced pressure. *International Journal of Heat and Mass Transfer*, (in print) (Chapter 7)

I developed the mathematical model described in this work, conducted the numerical simulations and analyzed the results. I am the first author of the article

5 Desroches, M. J. **Castillo, I** and Munz, R. J. Determination of Particle Size Distribution by Laser Diffraction of Doped-$CeO_2$ Powder Suspensions: Effect of Suspension Stability and Sonication *Particle Syst. and Particle charact.*, **22**(5), 310-319 (2006) (Chapter 8)

I developed the technique to analyze the $CeO_2$ powders using laser diffraction. I guided and assisted the summer student (Desroches, M. J.) with the experimental part of the work. I wrote the article based on her summer report. I am the second author of the article.

# Chapter 3 Literature review

## 3.1 Solid oxide fuel cells

Despite their modern high-tech allure, fuel cells have been known for more than 160 years. The solid oxide fuel cell was first conceived following the discovery of solid oxide electrolytes in 1899 by Nerst. He reported that the conductivity of pure metal oxides rose only very slowly with temperature and remained relatively low, whereas mixtures of metal oxides can possess dramatically higher conductivities. Many mixed oxides which exhibit high conductivity at elevated temperatures were quickly identified, including the particularly favorable composition of 85% zirconium oxide and 15% yttrium oxide patented by Nerst in 1899. In 1905 Haber filed the first patent on fuel cells with a solid electrolyte, using glass and porcelain as the electrolyte material, and platinum and gold as the electrode materials. Despite a very significant search by Baur and other researchers for suitable materials for SOFC operation, the development of SOFC was hindered until the 1960s. In the early 1960s a rapidly increasing number of patents were filed associated with SOFC technology. Advances in preparation and production methods through the 1970s led to the development of considerably thinner electrolytes, which significantly increased cell performance [*Ormerod, 2002*]. In the last two decades, a major effort has been devoted to develop commercial SOFCs in research centers and industrial power generation facilities.

### *3.1.1 Types of fuel cells and environmental impact*

Fuel cells are generally classified by the chemical characteristics of the electrolyte used as the ionic conductor in the cell, as summarized in Table 3.I. The first five types are characterized by their low to medium temperature of operation (50 to 210 °C), their relatively low electrical generation efficiencies (40 to 50 % when operated on readily available fuels such as methanol and hydrocarbons, 50 % when pure hydrogen fuel is used). The latter three types are characterized by their high temperature of operation (600 to 1000 °C), their ability to utilize methane directly in the fuel cell and their higher

efficiencies (45 to 60 % for common fuels such as natural gas or methanol and 70 % with heat recovery) [*Stambouli, 2002*].

**Table 3. I Technical characteristics of selected fuel cells [Stambouli, 2002]**

Technical characteristics of different fuel cells

| Types of fuel cell | Electrolyte | Operating T | Fuel | Oxidant | Efficiency |
|---|---|---|---|---|---|
| Alkaline (AFC) | potassium hydroxide (KOH) | 50–200°C | pure hydrogen, or hydrazine | $O_2$/Air | 50–55% |
| Direct methanol (DMFC) | polymer | 60–200°C | liquid methanol | $O_2$/Air | 40–55% |
| Phosphoric acid (PAFC) | phosphoric acid | 160–210°C | hydrogen from hydrocarbons and alcohol | $O_2$/Air | 40–50% |
| Sulfuric acid (SAFC) | sulfuric acid | 80–90°C | alcohol or impure hydrogen | $O_2$/Air | 40–50% |
| Proton-exchange membrane (PEMFC) | polymer, proton exchange membrane | 50–80°C | less pure hydrogen from hydrocarbons or methanol | $O_2$/Air | 40–50% |
| Molten carbonate(MCFC) | molten salt such as nitrate, sulphate, carbonates... | 630–650°C | hydrogen, carbon monoxide, natural gas, propane, marine diesel | $CO_2/O_2$/Air | 50–60% |
| Solid oxide (SOFC) | ceramic as stabilised zirconia and doped perovskite | 600–1000°C | natural gas or propane | $O_2$/Air | 45–60% |
| Protonic ceramic (PCFC) | thin membrane of barium cerium oxide | 600–700°C | hydrocarbons | $O_2$/Air | 45–60% |

Among these cells, SOFCs are the most promising alternative because they have a wide range of operation and can run on natural gas. SOFCs are also resistant to carbon monoxide, which is electrochemically oxidized to $CO_2$ at the anode. In contrast, PEM fuel cells are highly susceptible to poisoning by CO, and thus require complex and expensive external processing of hydrocarbon feeds to convert all the CO to $CO_2$ [*Ormerod, 2003*]. Additionally, SOFCs are liquid free which eliminates potential problems such as corrosion and loss of electrolyte.

The environmental impact of SOFC implementation depends upon the source of fuel used. If pure hydrogen is used, fuel cells have virtually no emissions except water and heat. However, hydrogen is rarely used due to problems with storage and transportation. The most common fuel, especially for stationary applications, is natural gas, which is cheap, abundant and readily available. Hydrogen must be extracted from natural gas through a series of reforming reactions and it is during this stage that most of the pollutant emissions associated with SOFCs operation are generated.

Compared to other fuel cells or power generation units, SOFC have a much lower fuel consumption to produce a given amount of electricity, even if they run on natural gas, as a result of their higher energy efficiency. Also, emissions of $NO_x$, $SO_x$ and particulates are very low which greatly decreases the formation of acid rain and the emission of smog-causing pollutants [*Stambouli, 2002*]

### *3.1.2 Operation, configuration and applications*

A fuel cell consist of two electrodes (the anode and the cathode) separated by an electrolyte (Fig. 3.1). Fuel (e.g. hydrogen or natural gas) is fed to the anode where it is oxidized and electrons are released to the external circuit. The electron flow (from the anode to the cathode) through the external circuit produces direct-current electricity. The electrolyte conducts ions between the two electrodes. SOFCs are connected in electrical series to build voltage and a series of cells is referred to as a stack. Stacks are connected through components called bipolar separators or interconnects, which have the dual function of distributing the fuel and air to the anode and cathode respectively, as well as of providing the electrical contact between adjacent cells (*Minh, 1993*).

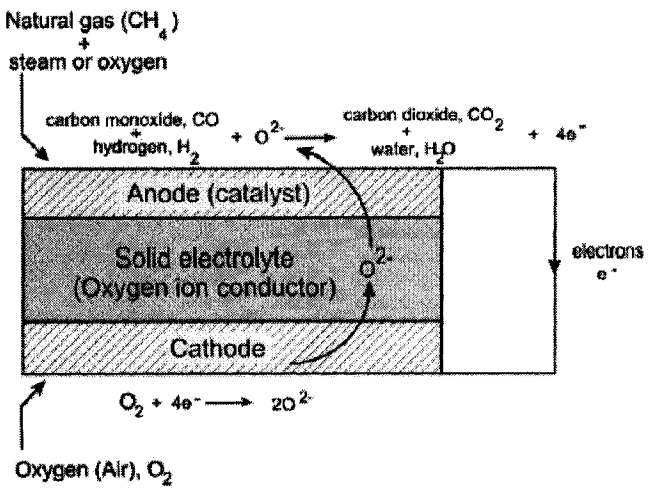


**Fig. 3. 1 Schematic diagram showing the operating principles of a SOFC running on natural gas [*Ormerod, 2003*]**

The potential applications of fuel cells in society are ever increasing and range from very small-scale ones requiring only a few Watts to a large-scale distributed power generation

of hundreds of MW. SOFCs are especially suited for highly-populated urban areas where localized pollution is a major issue as a result of their better utilization of fossil and renewable fuels, such as biomass and landfill gas. Further, SOFCs can provide both the power and hot water from a single system to individual households, larger residential units and business and industrial facilities. This offers a greater efficiency than the current situation where electricity is distributed from a small number of centralized power stations, while heating is supplied by decentralized boiler units. In the short term, SOFCs can cope with the developing market where there is a real need for high quality, uninterrupted power supply. Such applications include information technology companies, airports and hospitals [*Ormerod, 2003*].

### *3.1.3 Components. Electrolyte*

Solid oxide fuel cells have 3 basic components, electrolyte, anode and cathode. This thesis is focused on the electrolyte and it is beyond the scope of this thesis to do a complete literature review on the other two components.

Stabilized zirconia ($ZrO_2$), especially yttria-stabilized zirconia (YSZ), is the most common electrolyte in SOFCs because it possesses an adequate level of oxygen-ion conductivity and exhibits desirable stability in both oxidizing and reducing atmospheres. It is also unreactive towards other components used in the SOFC. Despite all the advantages of YSZ as electrolyte material, its main drawback is that the cell needs to be operated at temperatures in the range of 700 to 1,000 °C. At these cell temperatures, the cost of the materials used in an SOFC is still high since high temperature alloys and expensive ceramics have to be used. By dropping the operating temperature to below 800 °C, the use of inexpensive materials such as stainless steel for manifold, piping, heat exchangers, blowers, etc., can be achieved and the system is less prone to thermal degradation. For example, the use of stainless steel interconnects would bring the cost of this component down to around 7 $/kW-1 [*Baron, 2004*]. Nonetheless, intermediate temperatures are not ideal for all applications. For SOFC-combined cycle and hybrid systems the system efficiency is higher when operated at high temperatures (850-1000 °C). However, it was recognized in the 1990s that if smaller units were to be built, it

would be advantageous to reduce the operating temperature to 600-800 °C, or even lower, to reduce cost and improve start-up times. In summary, the advantages of reducing the operating temperature are: 1) Faster start-up and operating response. Developers are aiming at a start-up time of less than 10 minutes for some applications. 2) A wider and cheaper range of materials can be used to construct the device. 3) Increased material durability. 4) Increased product robustness. 5) Reduced overall cost [*Baron, 2004*].

Reducing the operating temperature of an SOFC can result in a decrease in the fuel cell power density because of the decrease of the electrolyte ionic conductivity and of the catalytic activity of the electrode. To overcome this, one can either reduce the thickness of the electrolyte or use alternative electrolyte and electrode materials that will retain a satisfactory performance at these intermediate temperatures. The mechanical strength of the electrolyte determines its minimum thickness. Steele estimated 15 μm as the minimum thickness for supported electrolytes (Figure 3.2). At this thickness, the conductivity for the $Ce_{0.9}Gd_{0.1}O_{1.95}$ at 500 °C is comparable to that of YSZ $(ZrO_2)_{0.9}(Y_2O_3)_{0.1}$ at 700 °C as shown in Figure 3.2 [*Steele, 2001*]. Although the electrolyte $Bi_2V_{0.9}Cu_{0.1}O_{5.35}$ exhibits higher conductivities at lower temperatures, it is not stable in the reducing environment imposed by the fuel in the anode compartment of a fuel cell.

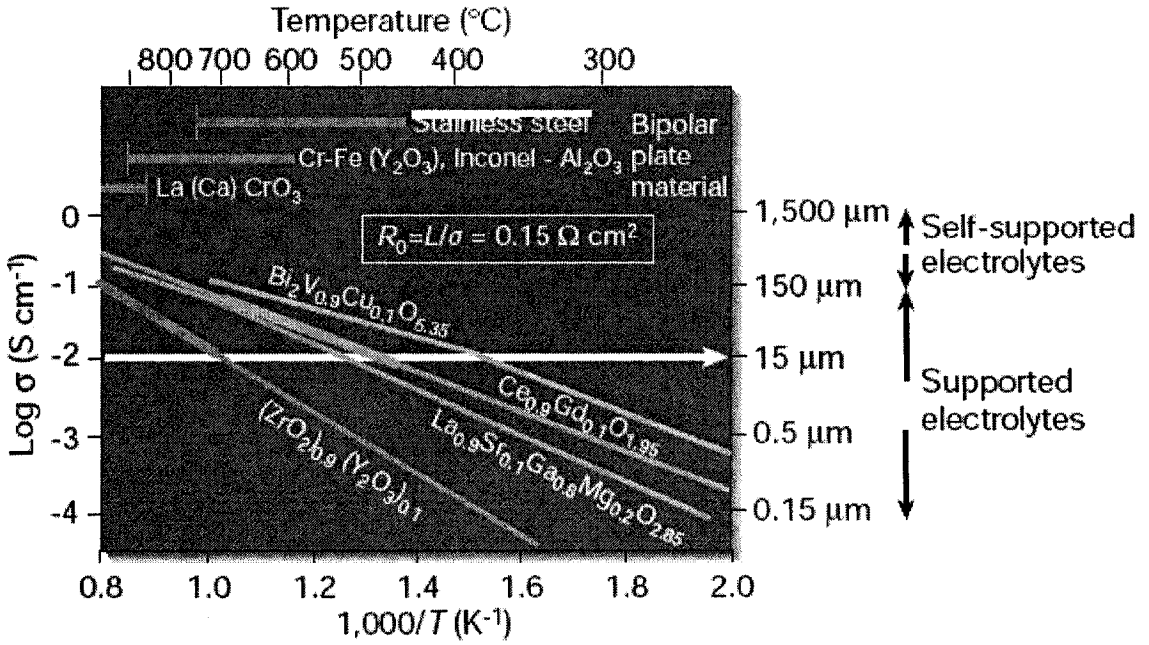


**Fig. 3. 2 Specific conductivity over reciprocal temperature for selected solid oxide electrolytes.**

In that past few years, doped $CeO_2$ has attracted a significant amount of attention and it is regarded as the most suitable replacement for YSZ as electrolyte material. For an up-to-date and comprehensive review of the performance of doped $CeO_2$ as electrolyte material, see Yano [*Yano, 2007*] and Rambabu [*Rambabu, 2006*]. It was demonstrated in our previous work [*Castillo, 2005*] that $CeO_2$ based electrolyte powders of suitable dopant amounts for cell testing could be achieved using rf thermal plasma synthesis from liquid precursors.

## 3.2 In-flight sampling of thermal plasma synthesized particles

### *3.2.1 Thermal plasmas*

Thermal plasma technology has evolved over the past decade into an advanced interdisciplinary science. Its principal applications are in materials processing, including extractive metallurgy, melting and refining or metals and alloys, plasma chemical synthesis, plasma chemical vapor deposition, plasma and arc spraying, plasma waste destruction, and plasma synthesis of advanced ceramics. Plasma synthesis of fine

particles down to the nanometer size range is one of the recent plasma applications, and it is still in its early stage of development [*Boulos, 1992*].

The high energy-density combined with the high temperature of thermal plasmas leads to high reactivity and to material heating and quenching rates in the order of $10^5$-$10^7$ K/s. Moreover, the fact that the energy is generated through electrical coupling into the plasma and not through a combustion process also provides the additional means for the independent control of the chemistry of the reaction mixtures and its specific energy level. These are unique and important features of thermal plasma processing which allow the rapid synthesis of materials with unique and enhanced properties at high temperatures [*Boulos, 1991*].

### *3.2.2 RF (radio frequency) inductively coupled discharges*

An RF-inductively coupled discharge, among the different ways to generate plasmas, was used in this project. In RF-induction plasma torches, energy coupling to the plasma is accomplished through the electromagnetic field of the induction coil. The plasma gas does not come into contact with electrodes, thus eliminating possible sources of contamination and allowing for the operation of such plasma torches with a wide range of gases, including inert, reducing, oxidizing and other corrosive atmospheres. Pure argon or its mixture with other gases is still the usual choice as the plasma gas largely because of its ease of ionization. The excitation frequency is typically between 200 kHz and 20 MHz. Laboratory units run at power levels of the order of 30-50 kW. In addition, induction plasmas are characterized by their large volume, low velocity and high energy density, and by their ability to offer injected particles a relatively long in-flight heating time of the order of 10 to 35 ms (compared to 0.5 to 1.0 ms in the DC plasma spraying units) [*Boulos, 1992*]. The relatively low radial thermal and velocity gradients in the plasma core (in comparison to the steep axial gradients) ensure a relative homogeneous treatment of a high reactant throughput injected in the central region of the plasma [*Bouyer, 2001*].

The plasma torch is composed, as shown in Fig. 3.3, of a water cooled confinement tube, typically, 35 to 70 mm in internal diameter and 150 to 200 mm long, for plasma torches with a nominal power rating in the range of 30 to 150 kW, respectively.

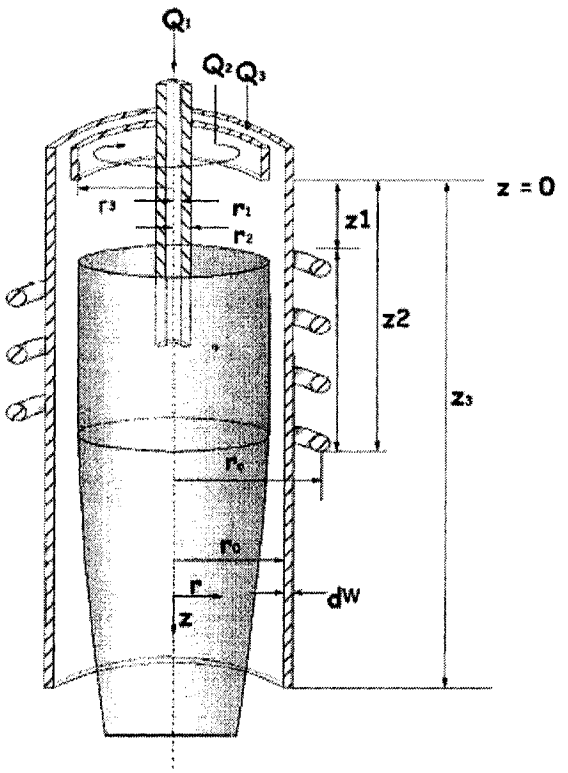


**Fig. 3. 3 Schematic diagram of the induction plasma torch (Tekna PL-35 torch) (*Merkhouf et al, 2000*)**

The confinement tube is surrounded by a three to five turn induction coil connected to the RF power supply. The coil is water-cooled with a rigid configuration to maintain a constant impedance matching to the power supply and to ensure optimum energy transfer. The upstream part of the torch is the gas distributor head, which is responsible for the introduction of the different gases. Three different gas streams are introduced into the torch. The sheath gas ($Q_3$) serves to protect the wall of the plasma confinement tube from the high temperature of the discharge and sometimes to favor the oxidation or reduction of the chemical species injected into the plasma (using either oxygen or hydrogen). The central gas ($Q_2$), which has a swirl velocity component, serves to stabilize the plasma. The powder or atomizing gas ($Q_1$) serves as a carrier for the axial injection of the powder or as an atomizing gas. A water-cooled stainless steel probe, which penetrates through the torch head, is used to introduce the powder, suspension or solution axially into the center

of the discharge. Due to the complexity of the flow pattern in the discharge region, the position of the tip of the powder injection probe is of critical importance. If located above the first turn of the coil, it could result in the excessive deposition of the powder on the wall of the plasma confinement tube in the case of powder injection. In the case of suspension or solutions injection, it could result as possible recirculation and/or backflow of the atomized droplets. A low probe position will result in excessive cooling of the plasma and a reduction of the particle residence time in the discharge. This will give rise to a reduction of the ability of the plasma to completely melt the particles in-flight. A more detailed and technical description of the plasma system is provided in chapter 4, in which the experimental apparatus is described

### *3.2.3 Thermal plasma synthesis of $CeO_2$ electrolytes and other cell components*

The real disadvantage in the production of SOFC components using conventional methods is the great number of steps involved, and thus the overall process becomes expensive, time consuming and prone to contamination. This has promoted the investigation of alternative processes. The aim of these processes is to allow the synthesis and deposition of SOFC components starting from suitable precursors (mostly liquid due to their ease of injection and facility to control their composition) in one step. These alternatives are chemical vapor deposition (CVD), electrochemical vapor deposition (EVD), and aerosol assisted metal-organic CVD (MOCVD) [*Song*, 2003]. Both radio frequency and direct current thermal plasmas have been successfully applied to synthesize oxides and deposit ceramic coatings. The first attempts to produce SOFC components using thermal plasmas emerged as a consequence of this success. In recent years, it has been demonstrated that both RF-inductively coupled and DC thermal plasma could be implemented to prepare SOFC components.

The use of thermal plasma to fabricate SOFCs was demonstrated in a pioneering work [*Gitzhofer, 2000*] with 4 different thermal plasma techniques. In all cases, the cells obtained showed comparable performances (i.e. similar open voltage values) to cells produced by conventional ceramic methods. The main advantage of the thermal treatment was the ability to achieve much higher deposition rates. Liquid solutions/suspensions

obtained from dissolved chlorides, nitrates, hydroxides, oxalates and organic salts have all been employed in the production of oxide materials for SOFCs components, i.e. fine $Ce_{0.8}La_{0.1}Y_{0.1}O_x$ particles [*Bonneau, 2001*] YSZ and $MoSi_2$ [*Gutierrez, 2001*] and perovskite powders [*Schiller, 1999*], and Ni/YSZ anode layers [*Lemoine, 2003*]. Nitrates are the preferred salts because they are relatively inexpensive and water soluble, which greatly reduces the time to prepare solutions.

In all the above cases, the synthesis route involved the use of RF-inductively coupled thermal plasma. New production methods such as thermal plasma chemical vapor deposition (TPCVD) and suspension plasma spraying (SPS) involve the use of liquid precursors as well. Several liquid precursors have been employed in the production of SOFC components. Solutions are favored over suspensions for better homogeneity and a more accurate control of the composition of the dissolved solid materials. RF-induction plasmas are particularly suited for particle synthesis due to their large volume, low velocity and high energy density, and their ability to offer axially injected particles a relatively long in-flight time (10 to 35 ms compared to 0.5 to 1 ms in DC plasma units) [*Boulos*, 1992] Further, the relatively low thermal and velocity gradients in the plasma core (in comparison to the steep axial gradients) ensure an homogeneous treatment of the material injected in the central region of the plasma [*Bouyer*, 2001]

Previous work using a rf thermal plasma reactor for the synthesis of doped-$CeO_2$ particles [*Castillo*, 2005] showed that the stoichiometry of the doped oxide could be controlled. The thermal plasma route provided a rapid and effective way to produce the oxides but multimodal particle size distributions were observed. Multimodal particle size distributions were also encountered in similar rf reactor systems in the production of doped-$CeO_2$ [*Lu Jia*, 2005] and alumina [*Goortani*, 2006]. These studies identified reactor recirculation eddies as the main cause for multimodal size distributions due to different particle residence times. Despite the effectiveness of the synthesis of ceramic materials in rf thermal plasma reactors, the mechanisms involved in droplet-to-particle formation have not been well understood; partly because of the lack of in-situ and in-flight sampling. Therefore, there is a need for an in-flight particle sampling device

capable of withdrawing representative samples in-situ at different reactor locations at various plasma operating conditions.

### *3.2.3 In-flight particle collection under thermal plasma conditions*

Measuring particle sizes in-flight at reduced pressures and at elevated temperatures is encountered in aerosol synthesis reactors, semiconductor equipment, etc. There are several techniques used to carry out these analyses as summarized in the work of Hafiz *et al.* [*Wang, 2005*] namely laser light scattering [*Boufendi, 1999*], sampling from the exhaust of turbomolecular pumps [*Forsyth, 2002*] mobility analysis at low pressure [*Seol, 2000*] and particle beam mass spectrometry [*Nijhawan, 2003*] These techniques all have limitations and drawbacks. Laser light scattering is not intrusive but it is not trivial to deconvolute the different signals associated with particle size, shape, concentration and refractive index. Sampling at the exhaust of pumps carries the risk of biasing size distribution as a result of particle coagulation and deposition as the aerosol travels through the pump. Mobility analysis at low pressure is limited by the size distribution that can be analyzed as well as the quantity of sample. Finally, PBMS (a system designed at University of Minnesota) is restricted in the particle size range between 5-500 nm. Hafiz attempted to overcome the drawbacks by developing a sampling scheme combining an air ejector with a scanning mobility particle sizer [*Wang, 2005*]. This scheme operated in the range of 5-100 nm. The main drawback of this scheme was the analyzed sample is lost and that it required a large flow of dilution gas. This system is also most efficient when a narrow particle distribution is expected.

There is very limited literature studying droplet-to-particle formation mechanisms for oxides from liquid precursors in rf thermal plasma reactors. Most of the work has been done in DC plasma torches [*Fazilleau, 2006* and *Delbos, 2006*] where particle diagnostics and imaging are easier as the plasma discharge is atmospheric and no reactor is involved. We have done recent numerical simulation studies describing these mechanisms in rf thermal plasma reactors. The details of these models are presented in this thesis. It was concluded that the atomized droplets developed a crust as a result of solvent evaporation. This crust bursts due to pressure build-up of the trapped solvent within this crust giving

rise to an array of various particle sizes responsible for multimodal distributions. But first a review of the available literature regarding evaporation of solution droplets is presented below.

## 3.3 Evaporation of solution droplets immersed in high temperature gases

### *3.3.1 Solution plasma synthesis of ceramics*

The manufacturing of ceramic powders from liquid precursors using radio frequency (rf) thermal plasmas has been developed in the past 10 years [*Bouyer, 1997; Müller, 2002; Bouyer, 2001; Delbos, 2003 and Lau, 1988*]. This technique consists of the evaporation and calcination of atomized solution or suspension droplets injected axially to the plasma core. In this paper only the case of solution droplets was investigated. Most of these processes are operated under reduced pressure and the droplets usually contain a non-volatile salt (nitrates, acetates, chlorides, etc) dissolved in water or any other suitable solvent. The hot plasma environment provides the driving force for evaporation and calcination of the salt, resulting in the production of high-purity oxide particles. Thus, oxygen-rich plasmas are often employed. The use of liquid precursors encompasses applications such as production of ceramic materials for SOFC (solid oxide fuel cells) (perovskites, $Y_2O_3$, $CeO_2$, NiO, etc) [*Gitzhofer, 2000*] and thermal barrier coatings ($ZrO_2$) [*Fauchais, 2003*].

One of the main advantages of rf thermal plasma over other processing techniques is the ability to achieve a uniform chemical composition in the synthesized particles in a clean electrode-free environment. It has been shown that the stoichiometry of these powders can be controlled accurately even when doped oxide particles are synthesized [*Castillo, 2005*]. However, the resulting particles varied greatly in size from few nanometers to micron size, suggesting that more than one droplet-to-particle conversion mechanism was possible. Few attempts have been conducted to understand this large size variation by sampling particles in-flight [*Lu Jia, 2005*], largely due to the high plasma temperatures and the inaccessibility of sampling in the plasma core. Therefore, studying the droplet-to-

particle conversion in rf thermal plasmas through numerical simulation seems to be a logical alternative.

### *3.3.2 Evaporating solution droplets*

Evaporating droplets were first studied experimentally and theoretically by Charlesworth and Marshall [*Charlesworth, 1960*]. They suspended droplets containing various dissolved salts in a hot-air stream and pointed out that mass diffusion in the droplet played a key role in determining the onset of salt precipitation. The work of Schlünder [*Schlünder, 1964*] and Gardner [*Gardner, 1965*] demonstrated that the product of the drop radius times its rate of change over time remained constant for most of the evaporation process. More recently, Xiong and Kodas [*Xiong, 1993*] investigated the spray pyrolysis of sodium chloride solution drops in air. In this comprehensive study small micron size droplets [1-10 μm] were examined. It was reported that the point of solute nucleation was relatively independent of processing parameters, except solution concentration and initial droplet size. Their findings were based on the evaporation of droplets in air at atmospheric pressure. The change in droplet diameter was not rigorously calculated from the solution of the heat and mass transfer between the drop and the surrounding media. A more formal treatment of the solution of the mass and heat transport equations of these phenomena was conducted by Javanthi *et al* [*Javanthi, 1993*]. It was found that droplet shrinkage and solute diffusion were the rate limiting processes, because their characteristic time constants were larger than those of heat conduction inside and outside the droplet and vapor diffusion outside the droplet. However, bulk flow as a result of solvent evaporation was neglected in this study. A rigorous approach of droplet evaporation was reported by Elperin [*Elperin, 1995*] for the case of slurry droplets, but it was assumed that the evaporation stage resembled that of a pure component droplet. Therefore, there is a need for a rigorous treatment of evaporating solutions droplets when heat-mass-momentum transfers are considered. Also the rate of shrinkage of droplets over time must be taken into account.

### *3.3.3 Modeling of evaporating droplets in thermal plasma*

Droplets are injected into the plasma core by means of a liquid blast atomizer that provides a log-normal droplet size distribution centered around 20-30 μm in diameter.

This process is similar to the well known spray pyrolysis technique [*Yu, 1997*], but the operating temperatures are higher, the droplets are often in the low micro size range (< 50 μm) and the reactor chamber is operated under vacuum. As a result, the thermal plasma treatment is a more "rapid" version of spray pyrolysis, since the conditions for solvent evaporation are enhanced. Previous theoretical and experimental studies in spray pyrolysis of non-volatile solute droplets have suggested the development of a thin crust surrounding the evaporating droplet. The crust is formed because the non-volatile salt precipitates out of solution, primarily at the droplet surface [Figure 3.4]. A fast evaporation rate removes solvent from the droplet surface more quickly than it can be replenished by mass diffusion, resulting in the formation of a crust [*Charlesworth, 1960*]. Having a crust around an evaporating liquid core retards the rate at which inner solvent escapes from the droplet [*Elperin, 1995*], because the solvent must travel through a solid phase. This effect leads to an increase of the solvent vapor pressure that causes fracturing and/or bursting of the crust. As a consequence, after calcination takes place, solid particles of different sizes are formed. A recent study by Ozturk [*Ozturk, 2004*] has shown that solid and hollow particles of $ZrO_2$ can be produced using thermal plasmas from zirconium acetate depending on the plasma operating conditions. Ozturk's findings provide evidence that a comprehensive model explaining droplet-to-particle conversion is needed.

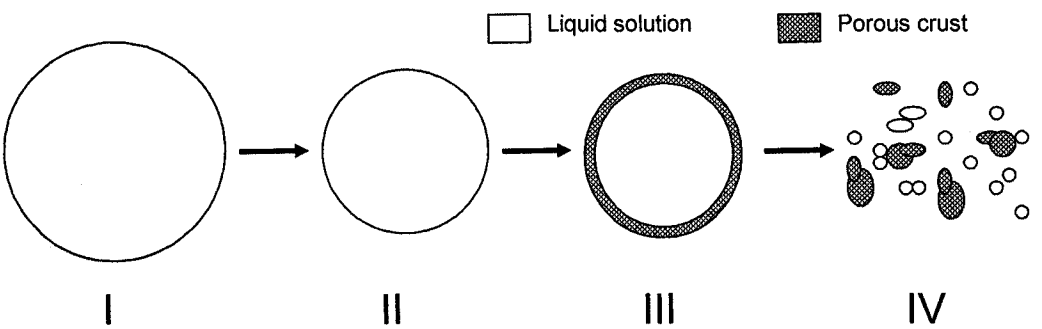


**Fig. 3. 4 Mechanism of droplet to particle conversion considering crust shattering**

Even though pressure build-up inside the crust as a result of solvent evaporation is widely accepted as the main cause of crust bursting, few papers discuss this issue in detail [*Elperin, 1995* and *Byun, 1999*]. The shattering of the crust is often related to the degree of superheating of the solution inside the crust and whether the liquid has reached its

boiling point. This type of analysis provides little insight of the actual "forces" that prevent the crust from bursting. Therefore, an analysis of these forces acting at the receding crust/droplet interface will give a more realistic picture of when the crust will burst due to pressure build up.

Three different phases co-exist at the droplet/crust interface, i.e. a liquid solution wetting a solid crust and a gaseous evaporating solvent. The solution forms liquid bridges in the form of menisci that connect the newly precipitated solid particles along this interface. The forces present in these bridges are surface tension and a negative capillary pressure as a result of the solid particle curvatures. These two forces are commonly combined and termed capillary forces. The detailed description of meniscus properties and the capillary force for pendular liquid rings has been extensively investigated [*Cho, 1989; Orr, 1975 and Willett, 2000*]. However, the connection of these forces to the problem of evaporating solution droplets with a surrounding crust has not been made to the authors' knowledge. Also, as a result of the small droplet size (20-30 μm in diameter), the precipitated particles forming the crust are likely to be in the nanometer range (i.e. the size of single precipitated crystals). Hence, the flow of evaporating solvent through porous media lies within the transient flow regime ($0.1 < Kn < 10$), between a continuum flow and a free molecular flow. This effect was considered in this work and it was adapted from the work of Tang [*Tang, 2005*]

# Chapter 4 New in-situ sampling and analysis of the production of $CeO_2$ powders from liquid precursors using a novel wet collection system in a rf inductively coupled thermal plasma reactor. Part 1: Reactor system and sampling probe

In this chapter the first part of the experimental results are presented. The reactor system, sampling probe and wet collection system are described. **Section 4.3.7 refers to different droplet-to-particle transformation stages. Stage I and II were elucidated based on the numerical results obtained in Chapter 6 and 7 and belong to the zone between the atomizing probe and the inlet of the reactor. Stage III corresponds to the work presented in Chapter 4 and 5 and belongs to the zone downstream of the reactor inlet.** The reason of presenting the experimental results first is to better situate the reader in the general context of the experiment and the overall analysis.

## Abstract

A new reactor and a novel in-situ sampling technique were developed for the study of the synthesis of $CeO_2$ powders produced from dissolved cerium nitrate salts. The conical reactor minimized particle recirculation and provided a highly symmetrical and undisturbed plasma flow suitable for the analysis of the phenomena affecting the formation of $CeO_2$ powders. Both a calorimetric study of the reactor and a thermodynamic analysis of $CeO_2$ formation were conducted at typical plasma operating conditions. The sampling probe is described and near-isokinetic sampling was achieved. The sampled particles were collected using a miniature wet collection system composed of a mist atomizer acting as a scrubber and a custom-made spray chamber. The entire collection system is portable and it was tested in the particle size range of 10 nm to 100 μm. A numerical simulation of the velocity and temperature fields of the plasma gas in the reactor at different plasma operating conditions was done using Fluent. A comprehensive droplet-to-particle formation mechanism was deduced based on

calorimetry, thermodynamics of $CeO_2$ formation, numerical simulations and collected particles. No traces of other oxidation states other than $CeO_2$ were found.


## Keywords

Radio-frequency inductively coupled plasma, $CeO_2$ particles, sampling probe, iso-kinetic sampling, solution plasma synthesis of particles, particle size distribution, calorimetry


## 4.1 Introduction

Doped $CeO_2$ has attracted much attention for use in solid oxide fuel cell electrolytes in recent years mainly due to its higher ionic conductivity than YSZ at lower temperatures and its inertness towards the cathode and anode materials[1]. Specifically, the $CeO_2$-$Sm0_{1.5}$ and $CeO_2$-$GdO_{1.5}$ mixtures are superior ionic conductors at intermediate temperatures (~600-800 °C) than zirconia based mixtures[2]. The potential of $CeO_2$-based materials for SOFC (solid oxide fuel cells) electrolytes has been extensively investigated by Steele[3]. The results indicated that $CeO_2$ based electrolytes at ~ 600°C have comparable performances to commercial zirconia based electrolytes at ~ 850°C.

The use of thermal plasma to synthesize oxide particles was developed in the early 90s by Zhu *et al.*[4], to obtain fine powders of $YBa_2Cu_3O_7$ from nitrate solutions. It was also reported that the plasma chemical treatment of salts and their aqueous solutions was a promising alternative to synthesize rare-earth oxides [5]. The use of thermal plasma to fabricate SOFCs was demonstrated in a pioneering work[6] with 4 different thermal plasma techniques. In all cases, the cells obtained showed comparable performances (i.e. similar open voltage values) to cells produced by conventional ceramic methods. The main advantage of the thermal treatment was the ability to achieve much higher deposition rates. Liquid solutions/suspensions obtained from dissolved chlorides, nitrates, hydroxides, oxalates and organic salts have all been employed in the production of oxide materials for SOFCs components, i.e. fine $Ce_{0.8}La_{0.1}Y_{0.1}O_x$ particles[7] YSZ and $MoSi_2$[8] and perovskite powders[9], and Ni/YSZ anode layers[10]. Nitrates are the preferred salts because they are relatively inexpensive and water soluble, which greatly reduces the time to prepare solutions.

In all the above cases, the synthesis route involved the use of RF-inductively coupled thermal plasma. New production methods such as thermal plasma chemical vapor deposition (TPCVD) and suspension plasma spraying (SPS) involve the use of liquid precursors as well. Several liquid precursors have been employed in the production of SOFC components. Solutions are favored over suspensions for better homogeneity and a more accurate control of the composition of the dissolved solid materials. RF-induction plasmas are particularly suited for particle synthesis due to their large volume, low velocity and high energy density, and their ability to offer axially injected particles a relatively long in-flight time (10 to 35 ms compared to 0.5 to 1 ms in DC plasma units)[11] to ensure an homogeneous treatment of the material injected in the central region of the plasma[12].

Previous work using a rf thermal plasma reactor for the synthesis of doped-$CeO_2$ particles[13] showed that the stoichiometry of the doped oxide could be controlled. The thermal plasma route provided a rapid and effective way to produce the oxides but multimodal particle size distributions were observed. Multimodal particle size distributions were also encountered in similar rf reactor systems in the production of doped-$CeO_2$[14] and alumina[15]. These studies identified reactor recirculation eddies as the main cause for multimodal size distributions due to different particle residence times. Despite the effectiveness of the synthesis of ceramic materials in rf thermal plasma reactors, the mechanisms involved in droplet-to-particle formation have not been well understood; partly because of the lack of in-situ and in-flight sampling. Therefore, there is a need for an in-flight particle sampling device capable of withdrawing representative samples in-situ at different reactor locations at various plasma operating conditions. This is what our work has achieved.

Measuring particle sizes in-flight at reduced pressures and at elevated temperatures is encountered in aerosol synthesis reactors, semiconductor equipment, etc. Several techniques are used to carry out these analyses as summarized in the work of Hafiz *et al.*[16] namely laser light scattering[17], sampling from the exhaust of turbomolecular pumps[18-19], mobility analysis at low pressure [20] and particle beam mass

spectrometry[21]. These techniques all have limitations and drawbacks. Laser light scattering is not intrusive but it is not trivial to deconvolute the different signals associated with particle size, shape, concentration and refractive index. Sampling at the exhaust of pumps carries the risk of biasing size distribution as a result of particle coagulation and deposition as the aerosol travels through the pump. Mobility analysis at low pressure is limited by the size distribution that can be analyzed as well as the quantity of sample. Finally, PBMS (a system developed at the University of Minnesota) is restricted in the particle size range between 5-500 nm. Hafiz attempted to overcome the drawbacks by developing a sampling scheme combining an air ejector with a scanning mobility particle sizer[16]. This scheme operated in the range of 5-100 nm. The main drawback of this scheme was that the analyzed sample is lost and that it required a large flow of dilution gas. This system is also most efficient when a narrow particle distribution is expected.

There is very limited literature studying droplet-to-particle formation mechanisms for oxides from liquid precursors in rf thermal plasma reactors. Most of the work has been done in DC plasma torches[22-23] where particle diagnostics and imaging are easier as the plasma discharge is atmospheric and no reactor is involved. We have recently carried out numerical simulation studies describing these mechanisms in rf thermal plasma reactors. The details of these models are presented elsewhere [24-25]. It was concluded that the atomized droplets developed a crust as a result of solvent evaporation. This crust bursts due to pressure build-up of the trapped solvent within this crust giving rise to an array of various particle sizes responsible for multimodal distributions.

The purpose of our work was to experimentally study the production of $CeO_2$ powders from liquid precursors in order to validate and complement the droplet-to-particle formation mechanisms described earlier. This was done in two parts. In part 1 of this paper, a new reactor design that minimized particle recirculation and promoted a highly symmetrical gas flow is presented. A new sampling probe was developed to collect particles in-flight and the particles were collected using a miniature wet collection system. The sampling probe was capable of collecting particles ranging from 30 nm to

100 μm. A numerical simulation of the velocity and temperature fields of the plasma gas in the reactor at different plasma operating conditions was done using Fluent. A comprehensive droplet-to-particle formation mechanism was deduced based on calorimetry, thermodynamics of $CeO_2$ formation, numerical simulations and collected particles. In Chapter 5, the effects of varying the plasma plate power and plasma gas flow rate as well as the effect of fuel addition to the liquid precursors on both droplet-to-particle formation mechanisms and particle size were studied.

## 4.2 Experimental methodology

### *4.2.1 Experimental setup: Plasma unit*

The complete experimental setup consists of an induction plasma torch (PL-50 Tekna Inc.), a 60 kW radio frequency power supply (Lepel generator with an oscillator frequency 3-5 MHz) (not shown), a truncated conical stainless steel water-cooled reactor (50 cm in length, 5 cm ID at the top of the cone and a 7° angle of expansion) and a water-cooled cylindrical stainless steel heat exchanger. The reactor was operated under vacuum (roughly 1/3 atm). The atomizing probe is a Tekna Inc. SA-792 x 0.8/1.0 mm. internal diameter x 260 mm long. The tip of the atomizing probe was located just below the uppermost induction coil of the torch. The solutions were injected by a peristaltic pump. The sampling probe collected particles at a distance Z downstream of the torch nozzle exit. The probe was designed to move in the radial and axial directions. Two view ports are located perpendicular to the centerline of the reactor and as close as possible to the exit of the torch. The centers of the view ports are located at Z=4.12 cm and Z=9.12 cm respectively. The experimental setup of the plasma unit is shown schematically in Fig. 4.1.

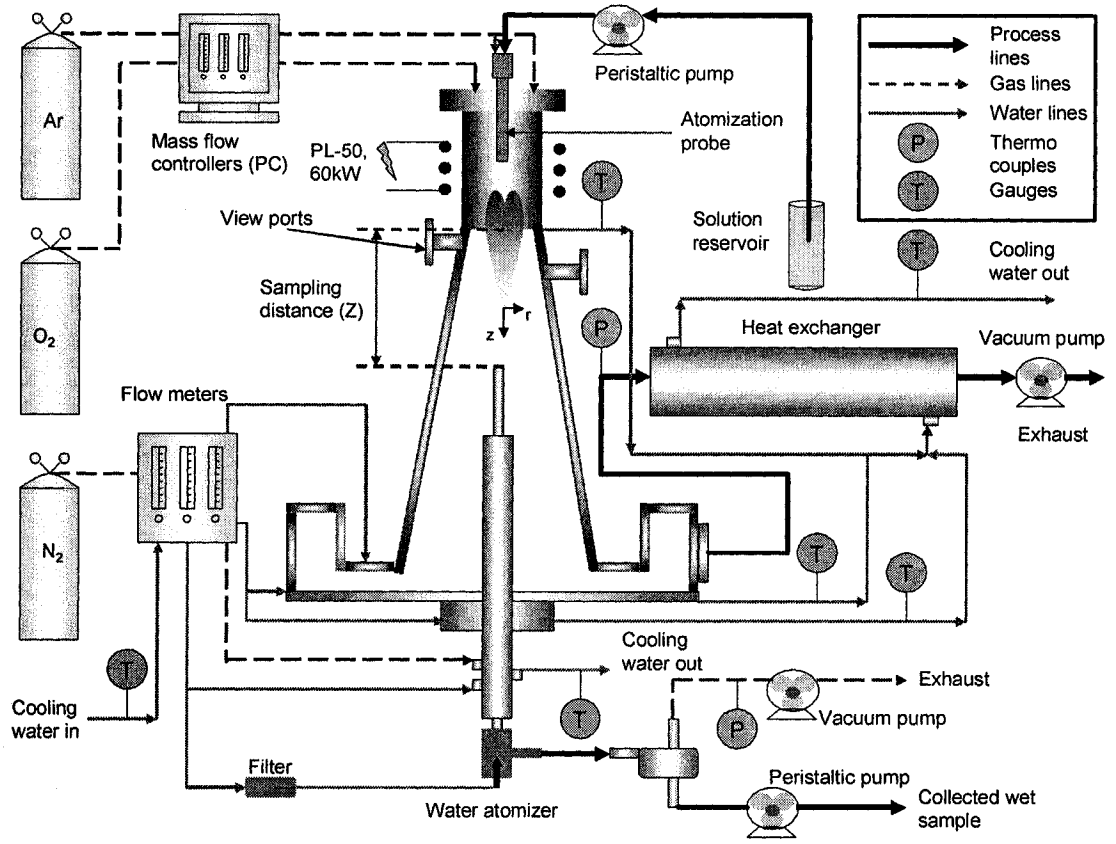


**Fig. 4. 1 Schematic representation of the plasma unit**

Three different gases were used: argon was the atomizing and the central gas, oxygen was the sheath gas and nitrogen was used as quench gas for the probe. Mass flow controllers were used for the torch gases and a calibrated flowmeter was employed for the $N_2$ gas. Cooling water entered the reactor shell counter current to the gas flow at 2 different reactor locations. The sampling probe and the reactor bottom plate were also water cooled. The water temperature at all water inlets and outlets in the experimental setup was measured using T-type thermocouples.

### *4.2.2 Experimental setup: Sampling probe*

The sampling probe consists of 2 parts: the body of the probe and an inner concentric tube inside the probe. The body is a water-cooled stainless steel tube with an increase in external diameter 10-cm away from the tapered probe tip. The tip of the probe has a 120° inner angle and a 2-mm orifice. The inner tube is ¼-in pipe size (ID=0.302-in or 0.767 cm) and is centered in the probe by 4-welded baffles evenly spaced that also allowed the

pass of quench gas. The length of the probe is 60-cm (Fig 4.2 shows a schematic drawing of the probe tip)

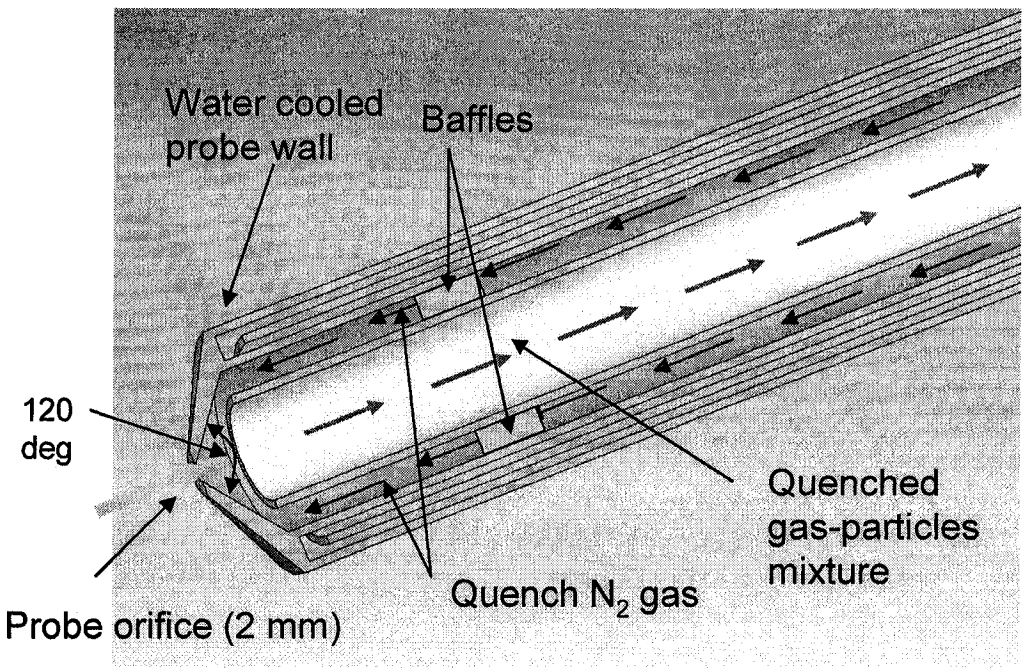


**Fig. 4. 2 Schematic representation of the sampling probe**

The probe is designed such that the quench gas immediately cools and dilutes the incoming sampled gas containing particles. This is done to prevent particle nucleation and growth along the probe before the particles are analyzed. The residence time of particles traveling from the tip of the sampling probe to the moment that they come into contact with the wet collection system is about 35 ms. Particle accumulation was negligible inside the probe as only a very small amount of particles (1-2 mg) were observed when cleaning it. The particle collection time was typically of the order of 4-5 minutes and the amount of particles sampled was about 1-2 g.

### *4.2.3 Experimental setup: Wet collection system*

This system consists of 2 components: a counter-current commercial no-drip misting spray nozzle (McMaster-Carr flat full cone and spray angle of 70°, operated at 40 psig) and a customized cyclonic chamber (SPC®). The spray mist from the nozzle directly contacts the incoming mixture of gas plus particles acting as a scrubber, i.e. the particles are captured by water droplets from the nozzle. This "wet" mist is then cyclonically

separated into a less wet gas and a slurry containing the sampled particles. The slurry is continuously pumped out of the chamber by a peristaltic pump (Fig. 4.3).

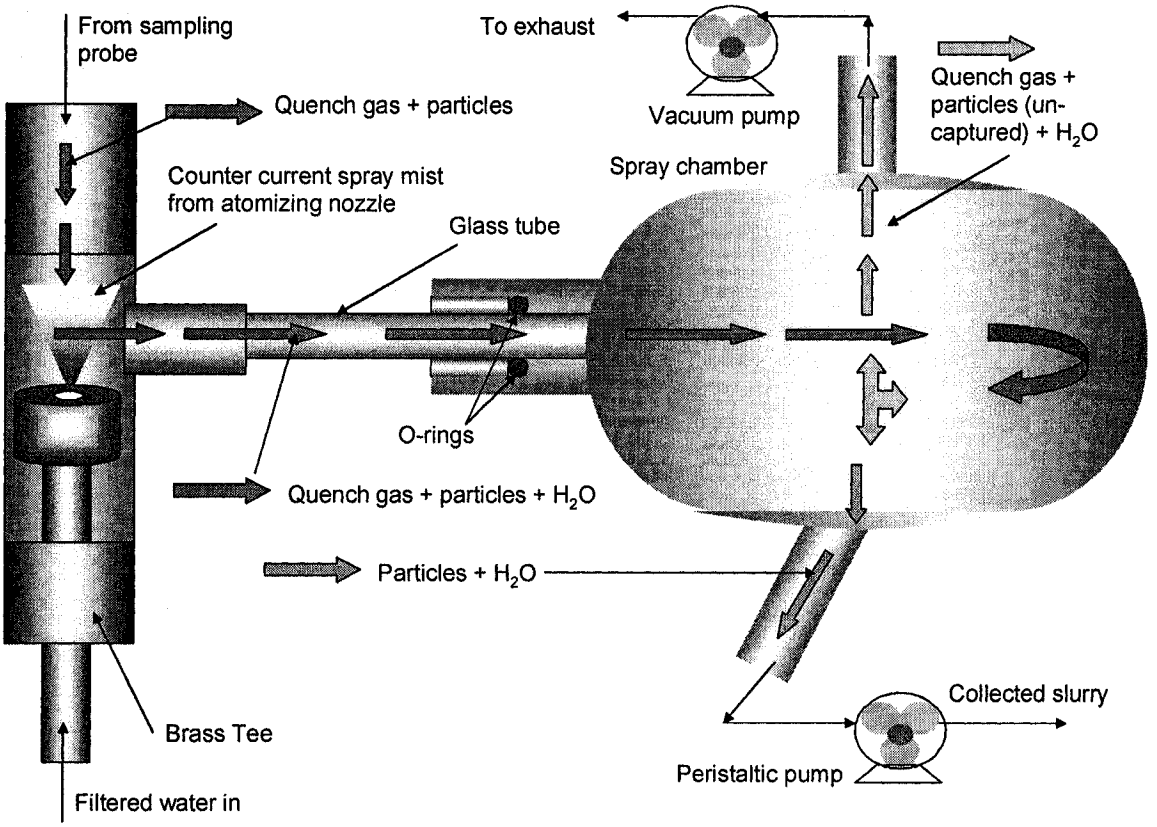


**Fig. 4. 3 Schematic representation of the wet collection system**

The cyclonic chamber does not have 100% efficiency and some of the sampled particles are lost in the vacuum line. The reason of the gas loss is the relative large volume of the wet mist compared to the size of the cyclonic chamber and the lack of an inner central exhaust to provide a physical obstruction to gas flow. Despite this, particles larger than 1 μm were captured efficiently in the slurry as proven by laser diffraction measurements. Sampling tobacco smoke confirmed that the collected slurry in the cyclonic chamber also contained representative amounts of particles in the range of 30 nm to 1 μm as proven by laser diffraction and SMPS measurements.

### *4.2.4 Characterization techniques*

The measurements of solid particle size were carried out using the Mastesizer 2000 (Malvern Instruments) with the Hydro 2000 S as the liquid injector. The minimum diameter detection limit was 20 nm. Each sample was dispersed in distilled water and subjected to 10 minutes of ultrasound to promote particle de-agglomeration. A dispersant agent was used to help stabilize the de-agglomerated suspension and the analysis was done at pH=10. The dispersant agent used was 50% active content 2-phosphonobutane-1,2,4-tricarboxylic acid (PBTCA) supplied by Jiangsu Jianghai (China) and the concentration of the dispersant in the suspension was 0.04% by volume. The pH was adjusted with sodium hydroxide 5N solution (Fisher SS256B). Further details of this technique are explained elsewhere[26].

The X-Ray diffraction analysis was done using a PHILIPS PW1710 powder X-ray diffraction system equipped with a copper X-ray source operated at 800 W. The Philips PC APD and Philips PC Identify software were used.

Finally, the synthesized $CeO_2$ powders were analyzed using a Hitachi 4700 Field Emission Scanning Electron Microscope (FE-SEM) in ultrahigh resolution mode. Each sample was mounted on a silicon wafer carbon taped to an SEM aluminum stub. Each sample was dispersed in ethanol and sonicated for 5 min before deposition on the wafer.

A Scanning Mobility Particle Sizer (SMPS) Model 3934 with a Electrostatic classifier (Model 3071A) and a Ultrafine condensation particle counter (Model 3025A) were used to obtain particle sizes that could be compared to those obtained using the wet collection system. The SMPS device was connected directly to the sampling probe and the vacuum was created using a venturi vacuum pump (JS150M operated at 80 psig). The venturi was operated at a flow rate of 125 slpm (T=25 °C, 1 atm) of ultra pure air. The SMPS functions at pressures close to atmospheric and provides a near real-time particle size distribution of aerosol mixtures. This instrument measures particle with a size range of 10 nm to 1000 nm[27].

### *4.2.5 Experimental conditions*

The experimental conditions are shown in Table I. The liquid flow rate of the atomized solution was kept constant at 6.0 ml/min. The atomized probe was ¾ of a turn open. The sampling probe quench gas flow rate and the reactor pressure were kept constant at 14 slpm of $N_2$ and 0.33 atm.

**Table 4. I Summary of experimental conditions**

| | | Gas flow rates [slpm, T=25 °C, P=1 atm] | | | Sampling position [cm] | | |
|---|---|---|---|---|---|---|---|
| No | Plate power [kW] | Central (Ar) | Sheath ($O_2$) | Atomizing (Ar) | Z=20 | Z=30 | Z=40 |
| 1 | 45 | 20 | 100 | 5 | | Y | Y |
| **2** | **35** | **20** | **100** | **5** | **Y** | **Y** | **Y** |
| 3 | 25 | 20 | 100 | 5 | | | Y |
| 4 | 35 | 15 | 80 | 5 | | Y | Y |
| 5 | 25 | 15 | 80 | 5 | | | Y |

Base case condition in bold

### *4.2.6 Numerical simulations*

The numerical simulations were carried out using the parameters described in Table II and the computational domain is schematically shown in Fig 4.4. The wall boundary conditions were experimentally determined: the conical wall temperature was 308 K and the temperature of the bottom plate was 305 K. The inlet gas temperature was assumed to have a semi-parabolic profile (n=3.3) (closer to flat than to parabolic (n=2)), i.e.

$T_{inlet} = T_{wall} + (T_{max} - T_{wall}) * \left[1 - \left(r/R\right)^n\right]$ where r=inlet radius and R=0.025 m. The mean inlet gas temperatures were obtained from the calorimetric measurements.

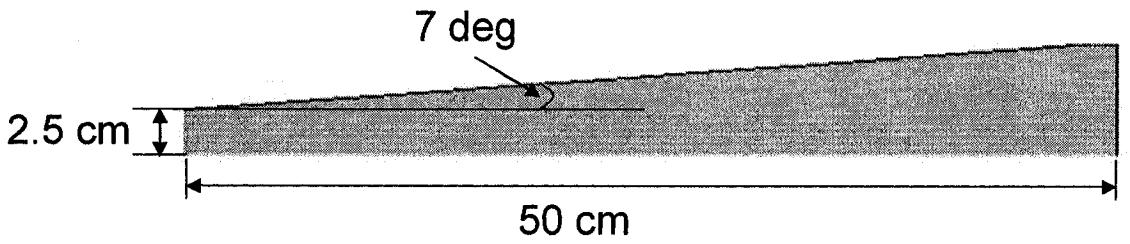


**Fig. 4. 4 Schematic representation of the reactor's computational domain**

Further, the mean inlet reactor temperatures were corrected to account for the heat losses due to water vaporization from the atomized liquid injection. Having liquid injection resulted in approximately a 500 K decrease of the estimated mean inlet temperature. With this temperature information and knowing the temperature profiles, the maximum inlet temperatures were computed. The inlet gas velocity was directly computed from the known inlet gas mass flow rate and the inlet temperature profile. The plasma flow was considered fully mixed and fully developed. The simulation was solved using FLUENT 6.1 and had approximately 12,500 elements. The reactor was considered to be at steady state.

**Table 4. II Numerical simulation parameters**

| No | Plate power [kW] | Mean inlet gas temperature [K] | Pressure [kPa] | Inlet gas flow [kg/s] | Central (Ar) [slpm] | Sheath ($O_2$) [slpm] | Atomizing (Ar) [slpm] |
|---|---|---|---|---|---|---|---|
| 1 | 45 | 4,350 | 0.33 | $2.86e^{-3}$ | 20 | 100 | 5 |
| 2 | 35 | 3,350 | 0.33 | $2.86e^{-3}$ | 20 | 100 | 5 |
| 3 | 25 | 2,350 | 0.33 | $2.86e^{-3}$ | 20 | 100 | 5 |
| 4 | 35 | 4,200 | 0.33 | $2.29e^{-3}$ | 15 | 80 | 5 |
| 5 | 25 | 3,500 | 0.33 | $2.29e^{-3}$ | 15 | 80 | 5 |

## 4.3 Results and discussion

This section describes the reactor design, calorimetric studies, the wet collection system and the conditions needed to obtain iso-kinetic sampling. Then a $CeO_2$ thermodynamic analysis is presented, followed by the numerical simulation of the temperature and

velocity profiles of the reactor. A description of the comprehensive droplet-to-particle formation mechanism is discussed. The paper concludes by comparing the particle size distribution of the collected samples from the reactor to that of samples collected using the in-situ sampling probe. The analysis of the effect of different plasma operating parameters on $CeO_2$ formation will be discussed in the second part of this work.

### *4.3.1 Reactor design*

The reactor was designed to study droplet-to-particle formation mechanisms as well as to sample particles in flight. To this end it is critical to minimize factors that could bias both particle residence time and particle size, such as recirculation eddies and sudden quenching of the plasma gas. Providing a gradual gas expansion from the torch to the reactor minimized both recirculation eddies and sudden quenching of the gas. This gradual expansion was achieved by building a conical reactor with a 7° half angle of expansion in the cone (14° in total). Further, in similar rf thermal plasma systems, the plasma gas exits the reactor through a single opening often located at one side of the reactor which causes flow asymmetry. In our reactor, there is a 4 mm gap between the conical section of the reactor and the bottom plate along the plate circumference. This gap is maintained by 6 pins welded on the reactor walls. The $\Delta P$ across this small gap is higher than the $\Delta P$ in the annular manifold which leads to a single exhaust (see Fig. 4.5a). As a result, the plasma gas is forced to exit radially in a uniform manner. This provides a highly symmetric flow pattern in the reactor chamber. A schematic drawing of the reactor is shown in Figure 4.5a and the reactor streamlines are plotted in Fig 4.5b based on the results of a FLUENT simulation of the base case operating conditions.

The uniformity of the deposition of the synthesized particles on the bottom reactor plate is shown in Figure 4.6. The deposition of the synthesized particles was used as an indication of gas flow uniformity. If the gas flow was not uniform, denser particle deposition regions would be observed.

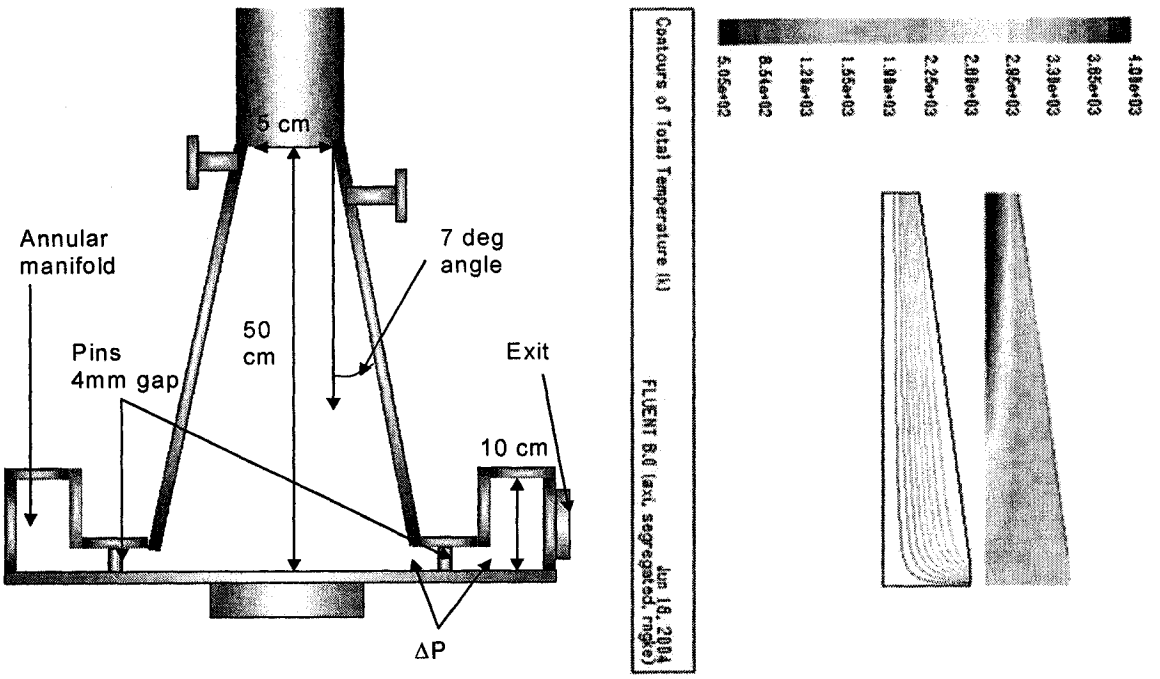


**Fig. 4. 5 a) Schematic of the reactor (not to scale), b) Reactor streamlines and temperature profile for a typical reactor operating condition (Table 4.I # 2 @ P=35kW, $C_{(Ar)}/S_{(O2)}/A_{(Ar)}$=20/100/5 slpm)**

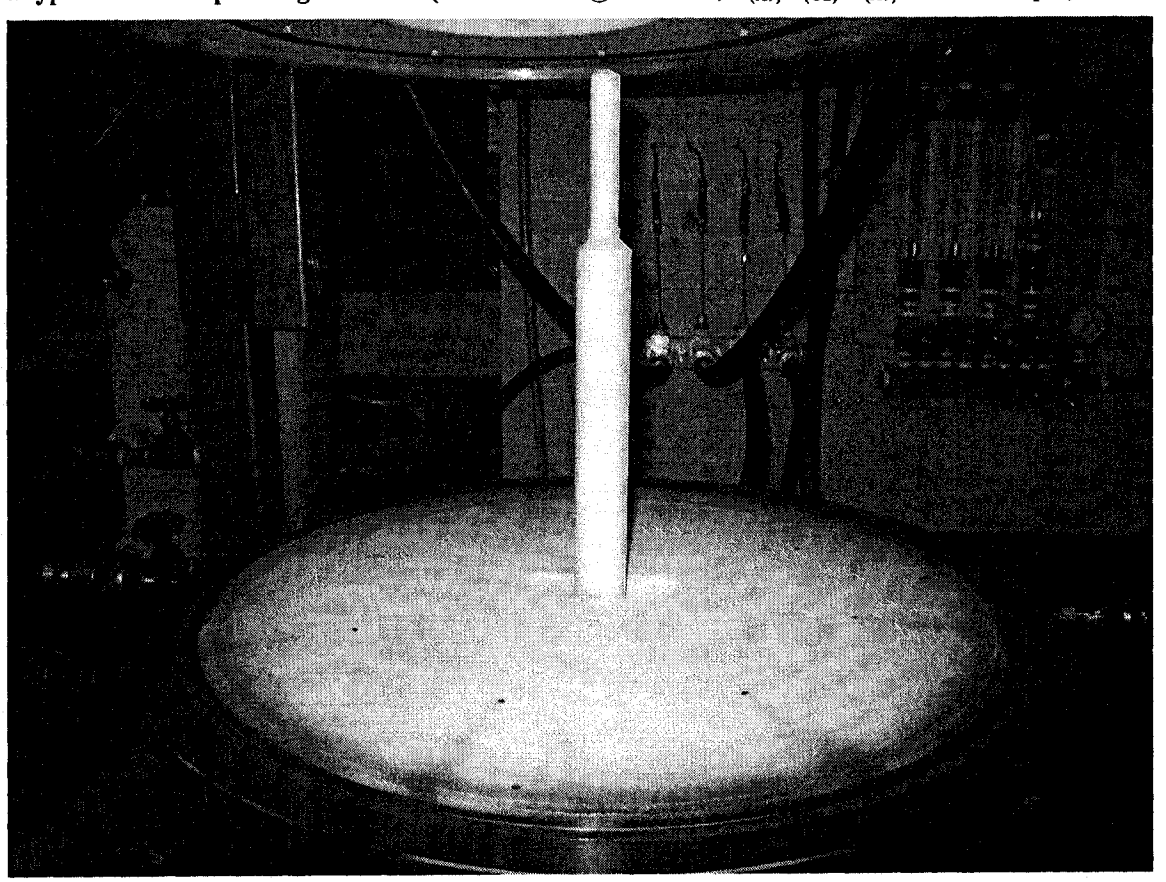

**Fig. 4. 6 Deposition of the synthesized $CeO_2$ on the reactor bottom plate and sampling probe**

### *4.3.2 Calorimetry*

A calorimetric analysis in the reactor system was done for three reasons: 1) To determine the mean plasma gas temperature at the inlet of the reactor (i.e. exit of the torch) so that the numerical simulations of the reactor can provide accurate estimations of the temperature and velocity profiles of the plasma gas. With those profiles, an initial guess of the quench gas required in the sampling probe to ensure near-isokinetic conditions can be obtained. 2) To provide a correlation of the heat load versus Z-location of the probe so that similar probes can be designed in comparable plasma systems. 3) To determine the time scale to reach steady state.

There are 2 routes to calculate the mean plasma gas inlet reactor/exit of torch temperature. The first route takes into account the effective plate power and the heat losses at the torch walls and atomizing probe. The effective plate power is defined as the nominal plate power (i.e. P=V*I) minus the heat losses in the generator (typically 10-11kW). With this method, the mean plasma gas temperature at the exit of the torch can be calculated. The second route, takes into consideration heat losses of the plasma gas in the reactor/heat exchanger system and thus, the mean plasma gas temperature at the inlet of the reactor can be calculated.

Route 1

$$Q_{\text{gas exit torch}} = Q_{\text{effective plate power}} - Q_{\text{torch walls}} - Q_{\text{atomizing probe}} - Q_{\text{gas in}} \quad (1)$$

Route 2

$$Q_{\text{gas in reactor}} = Q_{\text{reactor walls}} + Q_{\text{bottom plate}} + Q_{\text{exchanger}} + Q_{\text{sampling probe}} + Q_{\text{gas out}} \quad (2)$$

Where

$$Q_{\text{gas exit torch}} = \text{mass flow rate of gas x mean heat capacity x } (T_{\text{gas exit torch}} - 300) \quad (3)$$

$$Q_{\text{gas in reactor}} = \text{mass flow rate of gas x mean heat capacity x } (T_{\text{gas in reactor}} - 300) \quad (4)$$

$$Q_{\text{gas out}} = \text{mass flow rate of gas x mean heat capacity x } (T_{\text{gas out reactor}} - 300) \quad (5)$$

And $Q_{\text{effective plate power}} + Q_{\text{torch walls}} + Q_{\text{atomizing probe}} + Q_{\text{reactor walls}} + Q_{\text{bottom plate}} + Q_{\text{exchanger}} + Q_{\text{sampling probe}} + Q_{\text{gas out}}$ are measured calorimetrically and $T_{\text{gas exit torch}} \sim T_{\text{gas inlet reactor}}$.

Route 1 was used to estimate the mean plasma gas inlet reactor temperature because there were fewer terms to compute. The mean inlet reactor/torch exit temperatures are shown in Table 4.II (3rd column) as function of nominal plate powers (2nd column). Due to both $\Delta T$ and flow rate fluctuations, the calorimetry analysis using route 1 or 2 will not yield the same exact result, but the difference in estimated temperatures was within 8% error.

In the interest of showing the heat distribution history in the system, a typical calorimetric study for a 25 kW plate power is shown in Figure 4.7a and 4.7b without solution injection. Figure 4.7a and 4.7b illustrates the heat loads for route 1 and route 2, respectively. It is important to note that $Q_{gas}$ in (route 1) and $Q_{exchanger}$ and $Q_{gas\ out}$ (route 2) are negligible due to minimal $\Delta T$ and hence are not shown. Walls 1 and 2 referred to the left and right side of the conical reactor and the bottom plate refers to the plate covering the base of the cone. In the case of 25 kW plate power, approximately 7.8 kW are dissipated on the 2 reactor walls, bottom plate, sampling probe and heat exchanger (Figure 4.7b). A similar result is obtained by subtracting the torch and atomizing probe heat loads from the effective plate power (Figure 4.7a). It takes approximately 100 s to achieve steady state and there is a 10% difference in the heat loads of the reactor walls due to their different surface areas. The view ports which are not water cooled are located on the right side (side 2) which decreases the heat transfer area to the right side of the wall.

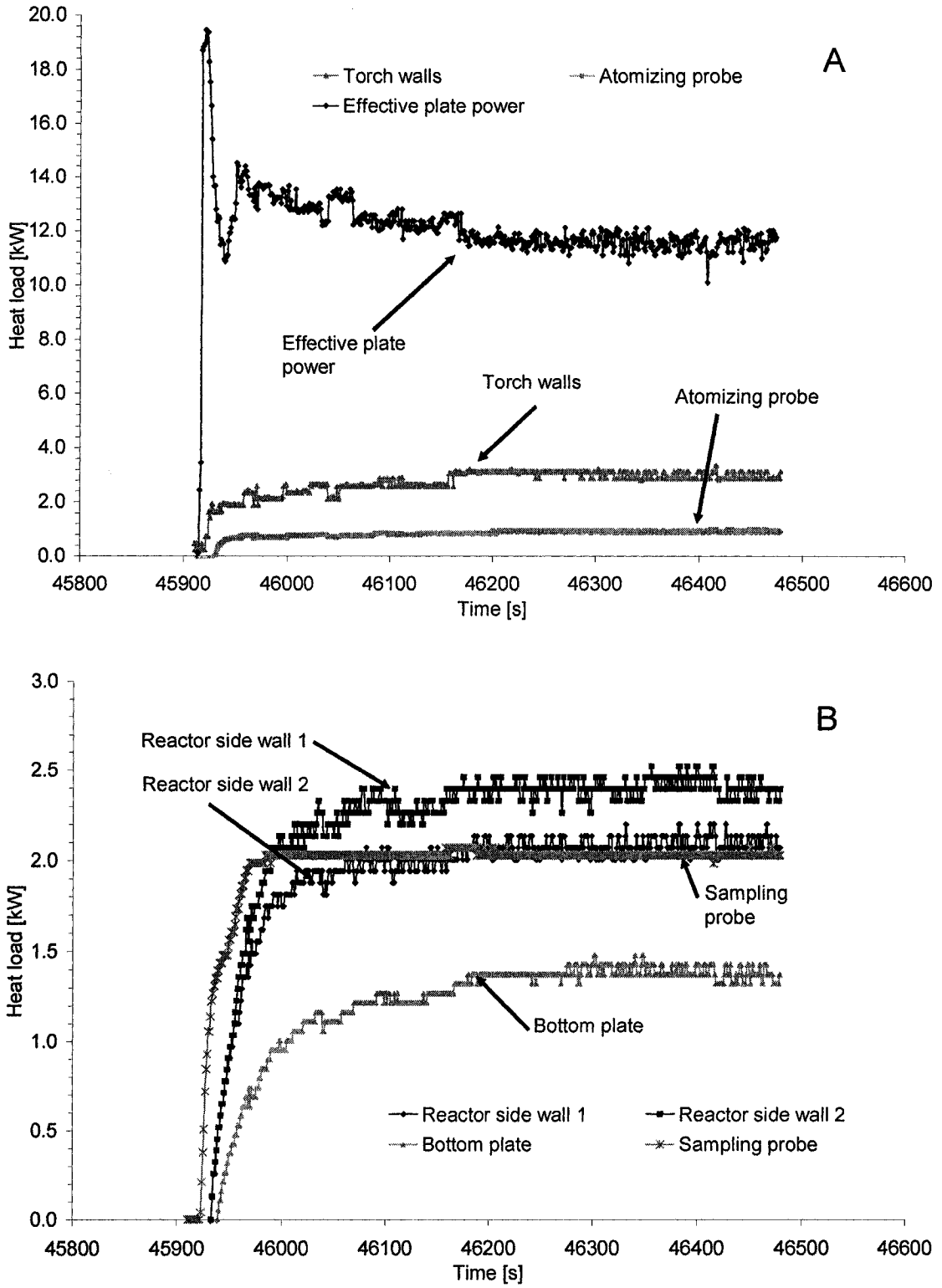


**Fig. 4. 7 Heat load in different system zones @ P=25 kW, P=3 psi, CG/SG/AG=20 slpm Ar/100 slpm O2/No gas, Z=15 cm**

The heat load of the water in the sampling probe was measured at various probe centerline locations (along Z axis) (Fig. 4.8) while keeping the plate power constant (i.e. 25 kW).

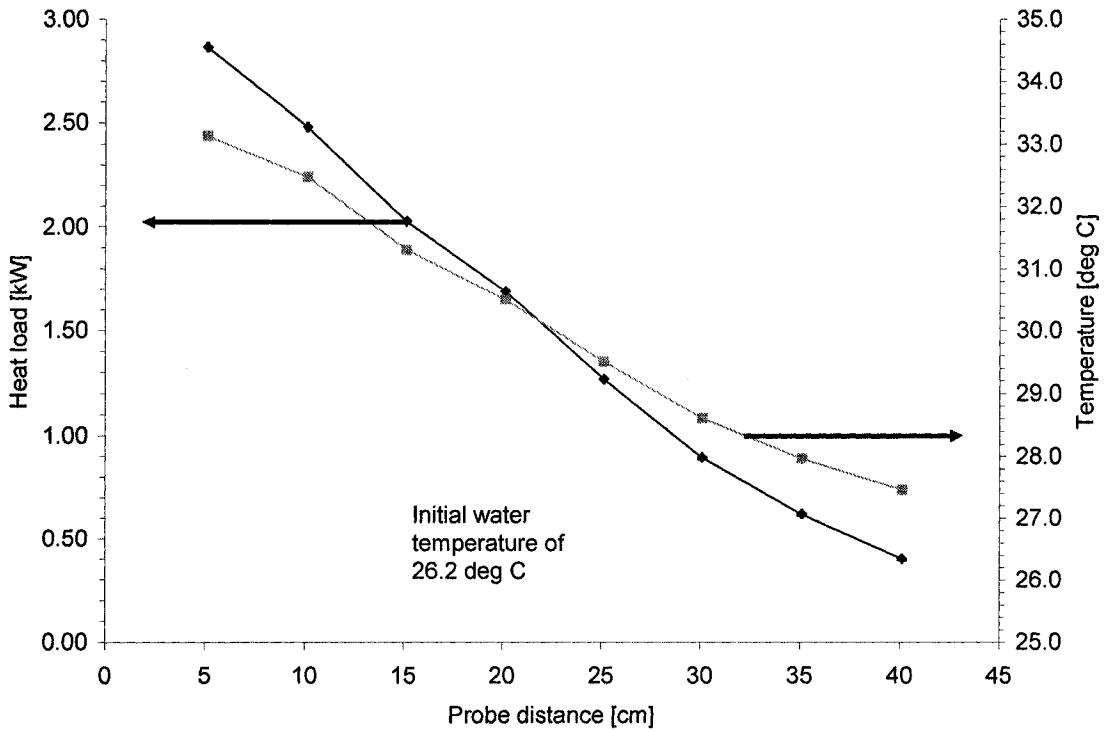


**Fig. 4. 8 Heat load along the center line of the reactor @ P=25 kW, P=3 psi, CG/SG/AG=20 slpm Ar/100 slpm O2/No gas, Z= movable**

The probe reaches steady state faster than any other section of the reactor and approximately halve of the heat load of the upper cone of the reactor is dissipated at the probe when located 15 cm away from the torch exit. It is important to note that the heat load of the sampling probe is an average of the entire probe body and not only of the probe tip. Therefore, the $\Delta T$, surface area and heat transfer coefficient between the plasma gas and the water cooled probe vary with probe location. The closer the probe to the exit of the torch nozzle, the higher the heat load, because the $\Delta T$, surface area and heat transfer coefficient all increase.

### *4.3.3 Understanding the wet collection system*

A wet collection system was preferred over other particle collection devices because particle agglomeration can be minimized by post treatments. These include sonication, surfactant addition and pH adjustment in-situ. As a result, the immediate analysis of the primary particle size of the particles suspended in the slurry is possible. The wet collection also permits a broad range of particle size sampling from 30 nm to 100 μm.

Another advantage of a wet collection system is that multiple samples can be acquired without the need of shutting down the plasma and without any cross contamination. The suspension of particles sampled from the probe was collected in Erlenmeyer flasks and become transparent once the collection is finished (no more particles present). Therefore, a visual analysis shows when the inside of the probe does not contain any appreciable amount of particles from previous collections. Figure 4.9 demonstrates the difference between two Erlenmeyer flaks during the collection (A) and when the collection is finished (B).

**Fig. 4. 9 Erlenmeyer flasks showing the collected particles (A) and no-particles present (B)**

The minimum size of particles that can be captured using the wet collection was investigated with cigarette tobacco smoke. The results are shown in Figure 4.10 in which cumulative particle size distribution of wet collected samples is compared to that

collected using the SMPS (Scanning Mobility Particle Sizer). These two instruments have different methods of operation and thus the size comparison is only done for the purpose of determining whether the wet collection can sample particles in the low nanometer range. Two replicates of the same experiment were done for each method.

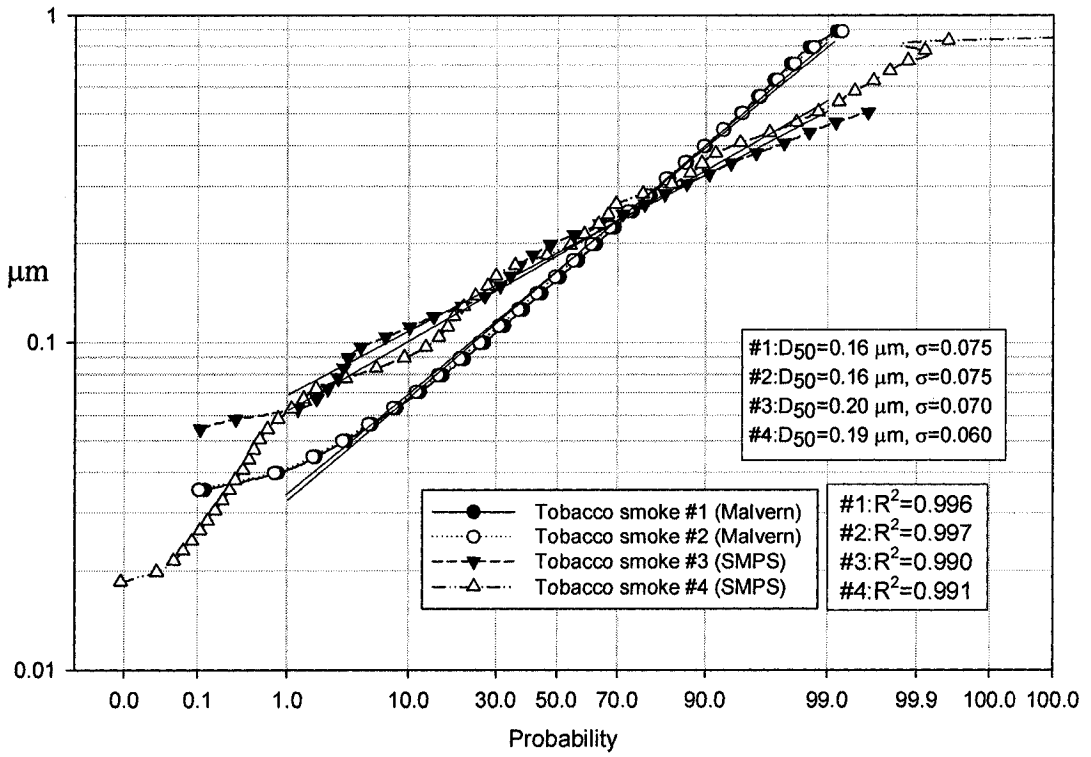


**Fig. 4. 10 Particle size distribution of cigarette smoke using both the wet collection system and the SMPS**

The cumulative graph in Figure 4.10 shows the results. The tails of the four distributions were truncated so that the line fitting was done over the linear range between the probability points of 1 to 99%. The experiments with wet collection and SMPS collection showed reproducible results because the fitted lines superimposed, a better reproducibility was obtained with the wet collection. The standard deviations were calculated by taking the ratio of the median size (size value at 50% probability, $D_{50}$) and the size at 15.78% probability of the fitted lines.

The median values ($D_{50}$) were compared to the values in the literature. Tobacco smoke has been reported to have values ranging from 0.01 to 4 μm[28], which agrees with our

results. The wet collection does not show particles smaller than 30 nm in diameter. This is because these particles approach the lower detection limit of the Malvern instrument (20 nm) and also because of the ineffectiveness of the cyclonic chamber to capture such small particles. Fortunately, for the $CeO_2$ experiments conducted in this work, this particle size range represents less than 0.9% in volume of the total particles present. The bulk of the $CeO_2$ particles produced are in the 0.1-0.2 μm range. The SMPS has an upper detection range of 1 μm and therefore it cannot be used to validate the wet system for particles larger than 1 μm in diameter. However, particles in this range are more likely to be captured in the cyclonic chamber as its efficiency increases with increasing particle size. As expected, the SMPS has a higher sensitivity for particles lower than 50 nm.

The $D_{50}$ values for the wet collection (Malvern) are 0.16 μm in both cases and are lower than the $D_{50}$ values from the SMPS (i.e. $D_{50}$=0.2 and 0.19 μm). The $D_{50}$ of the wet collection should be biased towards larger particles, because it cannot capture all the smaller particles (<30 nm) but that does not appear to be the case. The reason for this discrepancy is because, in the interest of directly comparing the two methods in one graph (Figure 4.10), the tail of the wet distribution for particles larger than 1 μm was truncated. The wet results needed to be renormalized and thus it appeared as if this method is more effective to capture smaller particles. Whereas in the raw distribution (not shown), the $D_{50}$ values for the wet collection are slightly higher than for the SMPS collection, $D_{50}$=22 to $D_{50}$=20 respectively.

### *4.3.4 Near-isokinetic sampling*

Isokinetic sampling is achieved when the sampling probe is aligned parallel to the free gas stream and the gas velocity entering the probe is equal to the free gas stream velocity. This is schematically shown in Figure 4.11.

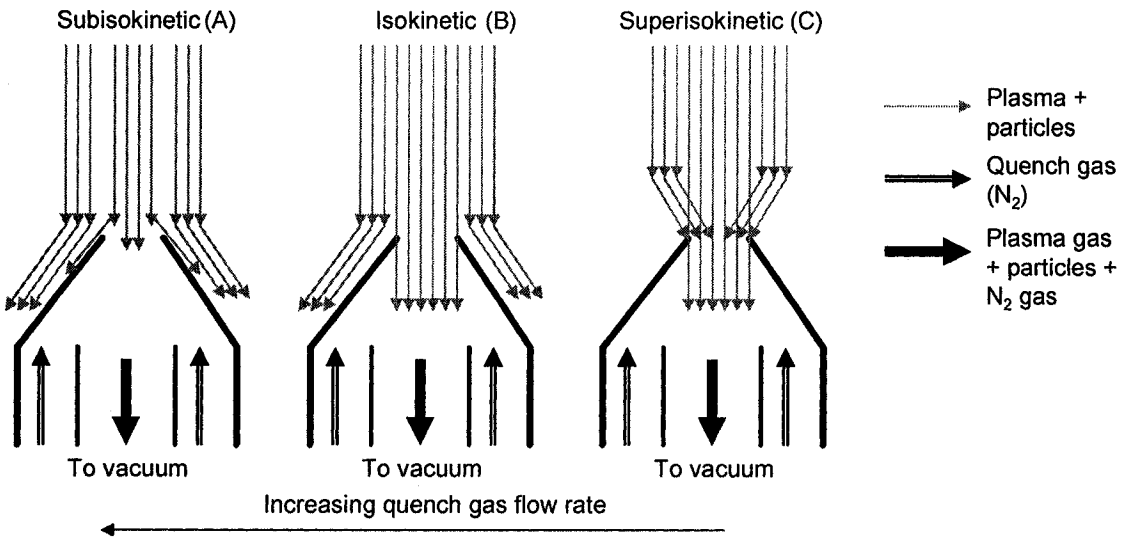


**Fig. 4. 11 Schematic of possible sampling conditions**

There are three possible scenarios all of which were experimentally observed. Case A happened when the flow rate of the quench gas exceeded the amount of gas flow that could be withdrawn by the vacuum pump. Thus little to no particle collection was observed. Case C happened when there was insufficient quench gas. As a result, the probe withdraws gas from adjacent gas streams (in this scenario the probe "over samples"). Experimentally, it was found that a quench gas flow rate of 14 slpm gave near isokinetic sampling since adding more quench gas shifts the probe operation to condition A depicted in Figure 4.11. The total gas flow rate, i.e. the quench gas + the plasma gas + particles, was measured using a gilibrator (Gilian $^{TM}$) and found to be approximately 20 slpm. Therefore, 6 slpm of plasma gas were sampled.

### *4.3.5 Thermodynamic calculation of the formation of $CeO_2$*

An equilibrium free energy calculation was performed using the thermodynamic software FactSage$^{TM}$ 5.4[29] to predict the most thermodynamically favored form of cerium oxide. This analysis was also used to determine whether gaseous ceramic species could be expected. The thermodynamics analysis is shown in Fig. 4.12a and Fig. 4.12b for two representative experimental conditions, entry #2 and #4 in Table 4.I, respectively. All the entry numbers of Table 4.I correspond to the same number on Table 4.II. Also, it is important to note that the temperatures shown in Table 4.II (3$^{rd}$ column) are the mean

inlet temperatures as calculated from calorimetry. Consequently, the temperatures along the centerline region of the reactor are higher than the mean temperature whereas temperatures in regions closer to the reactor walls are lower. The temperature ranges shown Figure 4.12a and 4.12b were arbitrarily input to the thermodynamic software and are meant to be used as a comparison to suggest which species are formed at given temperatures. FactSage produces an equilibrium curve based solely on free energy minimization of a closed isothermal system (no flow).

The results shown in Figures 4.12a and 4.12b indicate that $CeO_{2(s)}$ is the preferred oxidation state of cerium at temperatures lower than 2,400 K and that a liquid and a gas phase can co-exist at temperatures ranging from 2,700 to 3,200 K. All but one case (entry #3) had mean temperatures in the range where liquid and gas cerium oxides are expected and even mean temperatures exceeding 4,000 K were estimated for 2 experimental conditions (entry #1 and #4). The amount of gas present in the system did not have a significant effect on the temperatures at which different phases are formed. This is illustrated by the close resemblance of Fig. 4.12a (Table 4.I #2) and 4.12b (Table 4.I #4) where the amount of gas was varied from 20/100 to 15/80 slpm, Ar central/O2 sheath respectively.

It is likely that even in the lowest mean temperature estimated (i.e. 2,350 K for entry #3) liquid and gaseous cerium oxide can be formed. This is because the plasma gas mixture exits the torch region where higher temperatures than the mean exit temperatures would be expected.

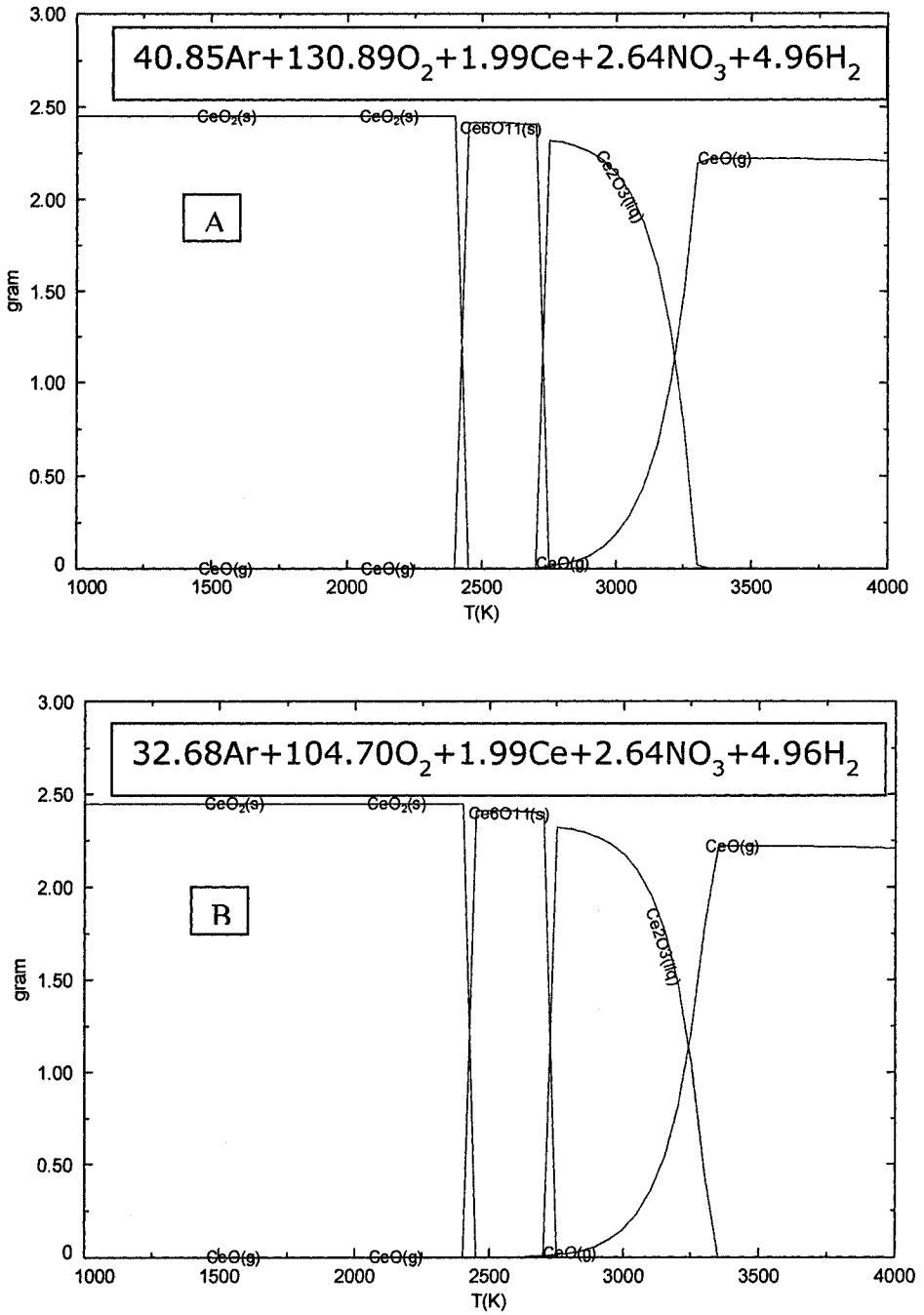


**Fig. 4. 12 Thermodynamic analysis of the formation of $CeO_2$ based on free energy minimization using FactSage 5.4 ™. A) Table 4.I #2 @ P=35kW, $C_{(Ar)}/S_{(O2)}/A_{(Ar)}$=20/100/5 slpm and B) Table 4.I #5 @ P=35kW, $C_{(Ar)}/S_{(O2)}/A_{(Ar)}$=15/80/5 slpm**

### *4.3.6 Numerical simulation of the temperature and velocity fields in the reactor*

The mean gas temperatures at the exit of the torch nozzle estimated from calorimetric analyses were used as inlet conditions for the numerical simulation of the temperature and velocity profiles of plasma gas in the reactor. The mean inlet temperatures are typically 250-300 K lower than the maximum inlet temperature. The experimental conditions described in Table 4.I can be regrouped into 5 different cases shown in Table 4.II (*1-to-1 correspondance*, i.e. #1 Table 4.I corresponds to #1 Table 4.II). The temperature and velocity profiles of cases 1 to 3 are shown in Figure 4.13a and 4.13b respectively. The profiles for cases 4 and 5 were compared to the base case (entry #2 in Table 4.II) and are plotted in Fig. 4.14a and 4.14b. The axial distances at which sampling of the plasma gas was done are indicated with straight vertical lines (Z=20, 30 and 40 cm). **The following analysis was conducted based on centerline temperature and velocity values unless indicated otherwise.**

Figures 4.13a and 4.13b illustrate the effect of increasing plate power on the temperature and velocity of the plasma gas. Figure 13a shows that gas temperatures at the inlet of the reactor range from 2,200 K to 4,000 K with increasing plate power from 25 kW to 45 kW. The plasma gas is cooled as it travels in the reactor. Figure 4.13b shows that the maximum gas velocities are achieved at the centerline reactor inlet (24 m/s for 25kW and 44 m/s for 45 kW) and that gas velocity also increases with increasing plate power.

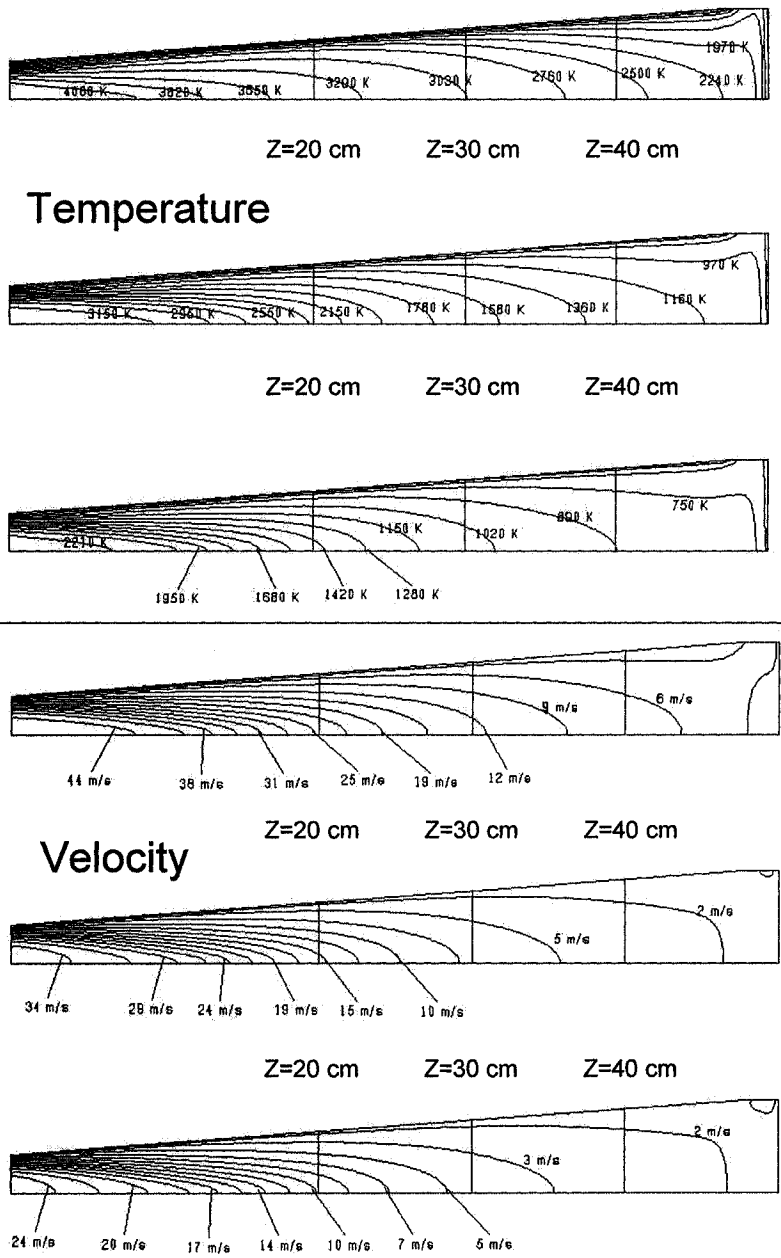


Case 1. P=45kW
C/S/A=20/100/5 slpm Ar/$O_2$/Ar

Case 2. P=35kW
C/S/A=20/100/5 slpm Ar/$O_2$/Ar

Case 3. P=25kW
C/S/A=20/100/5 slpm Ar/$O_2$/Ar

Case 1. P=45kW
C/S/A=20/100/5 slpm Ar/$O_2$/Ar

Case 2. P=35kW
C/S/A=20/100/5 slpm Ar/$O_2$/Ar

Case 3. P=25kW
C/S/A=20/100/5 slpm Ar/$O_2$/Ar

**Fig. 4. 13 Temperature and velocity profiles of cases 1 to 3 Table 4.II @ 1) P=45 kW, 2) P=35 kW and 3) P=25 kW, $C_{(Ar)}/S_{(O2)}/A_{(Ar)}$=20/100/5 slpm, P=0.33 kPa**

The temperature of the plasma gas at the reactor inlet increased by about 40% per every 10 kW plate power increase, i.e. 4% per kW. At the first sampled location downstream of the reactor inlet (Z=20 cm), the % increase/kW of the gas temperature is higher (~5%/kW) than at the inlet conditions. This rate of temperature increase, augments at the other 2 downstream reactor locations 6%/kW at Z=30 cm and 7%/kW at Z=40 cm. In the

case of the plasma gas velocity, the velocities at the inlet of the reactor also increased by 4%/kW. The increase was 5, 6 and 7%/kW at the sampled locations Z=20, 30 and 40 cm respectively. This indicates that temperature and velocity values are equally sensitive to an increase in plate power at the same reactor locations but the effect of increasing plate power is greater downstream of the reactor inlet. Further, the water cooled walls of the reactor reduced the plasma gas temperature by ~37% (45 kW case) from the reactor inlet to Z=40 cm (centerline); whereas, the gas temperature is reduced by 60 % at Z=40 cm for the case of 25 kW plate power.

Figures 4.14a and 4.14b show the velocity and temperature profile of 2 different conditions (case 4 and 5) and compares them to the base case profiles (case 2). In case 4, the central and sheath plasma gas flow were decreased by 20% while keeping the plate power constant at 35kW. The temperature and velocity of the plasma gas at the reactor inlet increased by ~25% and ~30% respectively from the base case. Downstream of the reactor, at Z=20, 30 and 40 cm the % temperature increases to 53%, 89% and 215% respectively, whereas at the same locations the % increases of velocity are 66%, 50% and 50% respectively. This indicates that decreasing the gas flow rate has a strong effect on gas temperature but a lesser effect on gas velocity. In case 5, the central and sheath plasma gas flow were decreased by 20% and the plate power was also decreased from 35 kW to 25 kW in order to compare the effect of changing the in-flight residence time of the produced $CeO_2$ particles while keeping the mean plasma temperature history constant.

The temperature and velocity values decreased by about 50% at the inlet conditions and also at all other Z-locations 20, 30 and 40 cm as a result of the combined changed of gas flow and plate power (at the centerline).

The temperatures predicted by the numerical model are sufficiently high to have liquid and gaseous $CeO_2$ as predicted by the thermodynamic simulation. Solid $CeO_2$ is formed as the gas cools and particle sintering is expected to occur at ~1,600 K (2/3 of the melting temperature of $CeO_2$).

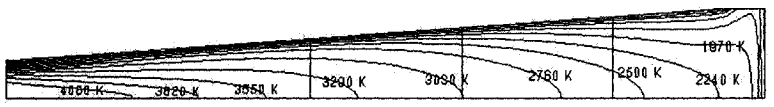


Case 4. P=35kW
C/S/A=15/80/5 slpm $Ar/O_2/Ar$

Z=20 cm Z=30 cm Z=40 cm

Temperature


Case 2. P=35kW
C/S/A=20/100/5 slpm $Ar/O_2/Ar$

Z=20 cm Z=30 cm Z=40 cm

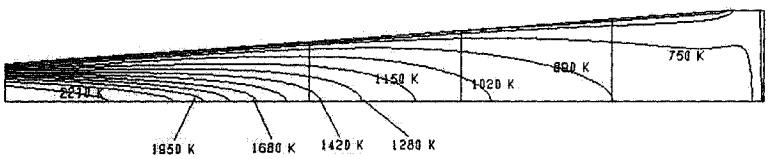


Case 5. P=25kW
C/S/A=15/80/5 slpm $Ar/O_2/Ar$

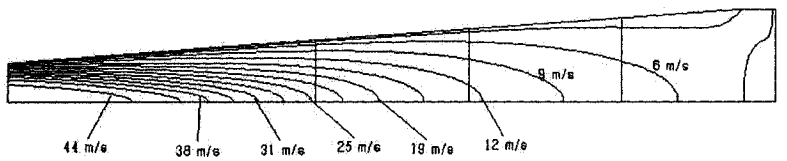


Case 4. P=35kW
C/S/A=15/80/5 slpm $Ar/O_2/Ar$

Z=20 cm Z=30 cm Z=40 cm

Velocity

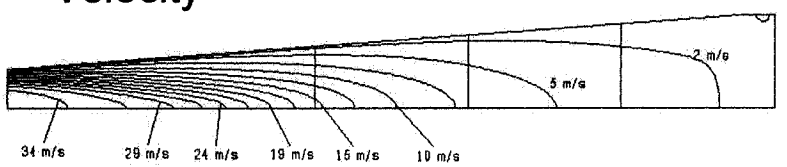


Case 2. P=35kW
C/S/A=20/100/5 slpm $Ar/O_2/Ar$

Z=20 cm Z=30 cm Z=40 cm

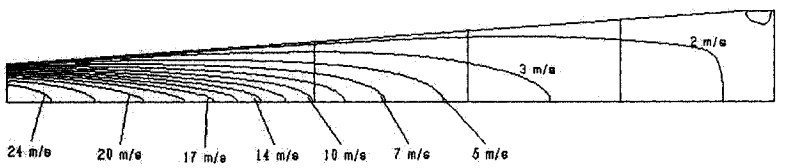


Case 5. P=25kW
C/S/A=15/80/5 slpm $Ar/O_2/Ar$

**Fig. 4. 14 Temperature and velocity profiles of cases 2, 4 and 5 Table 4.II @ 2) P=35 kW $C_{(Ar)}/S_{(O2)}/A_{(Ar)}$=20/100/5 slpm, 4) P=35 kW $C_{(Ar)}/S_{(O2)}/A_{(Ar)}$=15/80/5 slpm and 5) P=25 $C_{(Ar)}/S_{(O2)}/A_{(Ar)}$=15/80/5 slpm, all at P=0.33 kPa**

### *4.3.7 Comprehensive droplet-to-particle mechanism*

The mechanism discussed below and summarized in Figure 4.15 is proposed to account for the formation of different sizes of $CeO_2$ particles from starting atomized droplets of ~30 μm in diameter.

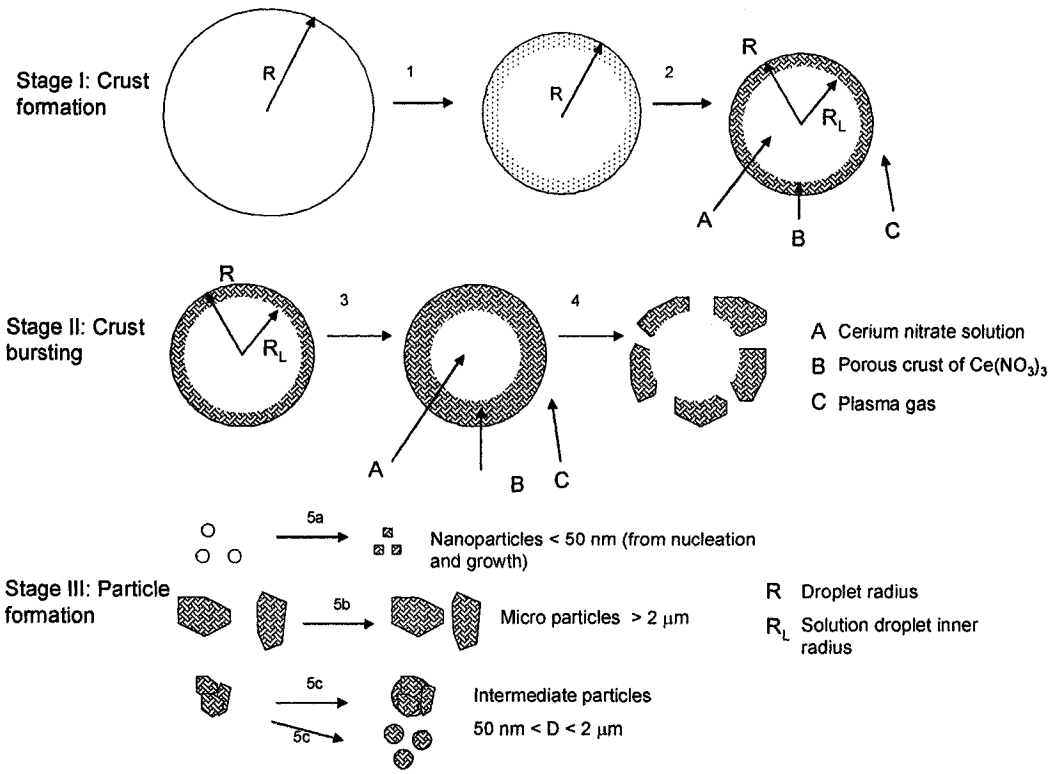


**Fig. 4. 15 Comprehensive droplet-to-particle formation mechanisms for $CeO_2$ under rf thermal plasma conditions**

Previous numerical simulation work (Chapter 6 and 7) demonstrated that a crust is formed in plasma operating conditions similar to those used in this work[24-25] as described in the literature review. In our previous work we explained that the primary reason for crust bursting is the pressure buildup at the solution/crust interface. The crust is formed because of the much slower rate of mass transfer compared to heat transfer in the evaporating solution droplet.

After crust bursting the system is composed of much smaller liquid droplets (< 50 nm) and both small (50 nm < D < 2 μm) and large (> 2 μm) shattered crust fragments.

Experimentally, three different classes of particles have been identified (5a, 5b and 5c shown in Figure 4.15). The most likely causes for the formation of these particles are the following: 5a) The liquid core of the shattered droplet creates much smaller droplets (<50 nm) of the initial cerium nitrate solution (too small to reform a crust) as well as shattered solid crust fragments of similar size. These will both undergo calcination of the nitrate salt and most likely evaporate to form a mixture of $CeO(g)/CeO_2(g)$. When the plasma temperature decreases, $CeO_2$ nanoparticles are formed as a result of nucleation and growth (< 50 nm). 5b) Shattered fragments in the 50 nm < D < 2 μm range are directly calcined and melt into spheres. These spheres may coalesce or sinter to form larger particles depending on the particle temperature and residence time. 5c) Large porous crust fragments calcine to form $CeO_2$ particles which may remain porous and retain essentially the same size (> 2 μm).

Nanoparticles are most easily collected by thermophoresis and turbulent diffusion onto the reactor walls and on the outer wall of the sampling probe. They also tend to follow the flow lines. Micron size and intermediate particles are most likely caught by inertial impaction and turbulent diffusion depending on their size.

### *4.3.8 Comparison of particle size distribution of samples collected using the sampling probe*

The sampling probe developed in this work aimed at providing a representative sample of particles formed at various reactor locations for a given set of plasma operating conditions. To test this claim, the size distributions of the wet collected particles (probe at Z=40 cm) and of particles collected on the bottom plate of the reactor were compared. The hypothesis was that if the sampling was done in close proximity to where particles were collected, both size distributions should be similar (Figure 4.16).

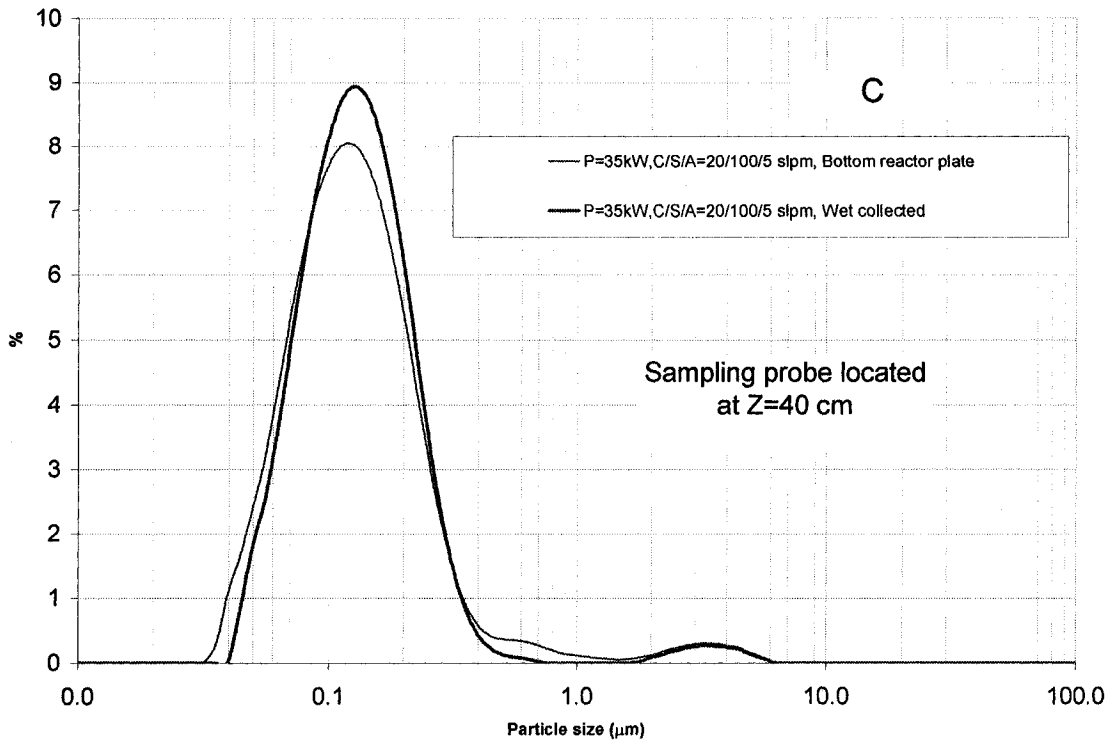


**Fig. 4. 16 Particle size distribution of $CeO_2$ collected samples P=35 kW $C_{(Ar)}/S_{(O2)}/A_{(Ar)}$=20/100/5 slpm, P=1/3 atm, Sampling probe Z=40 cm**

The size distributions shown in Figure 4.16 are similar with slightly more smaller particles present in the wet collected sample. Since smaller particles are harder to capture, it would be expected that less fine particles would be present in the material at the bottom of the reactor than would be captured in the sampling probe. Despite this, the size distribution agreement between samples is sufficient to validate that our sampling method provides representative sampling. Further, SEM micrographs were taken comparing these 2 cases (Figure 4.17a and 4.17b). These images are very similar and confirm what was observed in the laser diffraction analysis, i.e. that representative sampling can be achieved.

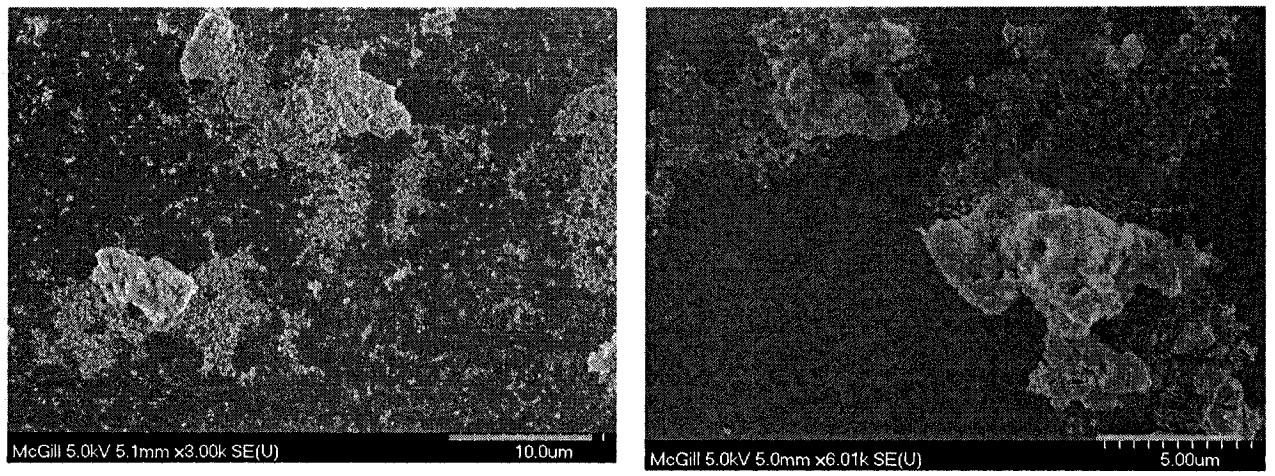


A B

**Fig. 4. 17 SEM micrographs of CeO2 collected from a) bottom plate, b) sampling probe @ P=35kW, $C_{(Ar)}/S_{(O2)}/A_{(Ar)}$=20/100/5 slpm, P=1/3 atm**

The combination of the plasma operating parameters and the different particle collection mechanisms are responsible for determining the $CeO_2$ particle size distribution at a given reactor location. The various particle sizes proposed in the aforementioned mechanisms are subjected to different collection mechanisms and thus appear at different reactor locations. This will be subject of study in the second part of this work

### *4.3.9 Oxidation state of cerium oxide particles*

Figure 4.18 shows X-ray diffraction spectra for samples taken at different reactor locations. They indicate that fully oxidized cerium oxide ($CeO_2$) was produced and it was present everywhere in the reactor in its fluorite structure. Also, the oxidation state of $Ce_2O_3$ was not present in the collected samples, suggesting a complete oxidation of the cerium. The X-ray pattern from the sampling probe was obtained from the synthesized particles deposited on the outside walls of the water cooled probe. This X-ray pattern has broader peaks which is indicative of smaller crystallite size particles.

Finally, for $CeO_2$ nanoparticles the fluorite structure is the preferred crystalline configuration as proven by X-ray (Figure 4.18). This is further shown in Figure 4.18 where a typical fluorite structure (A) was compared to an SEM image of a sample collected on the bottom plate (B).

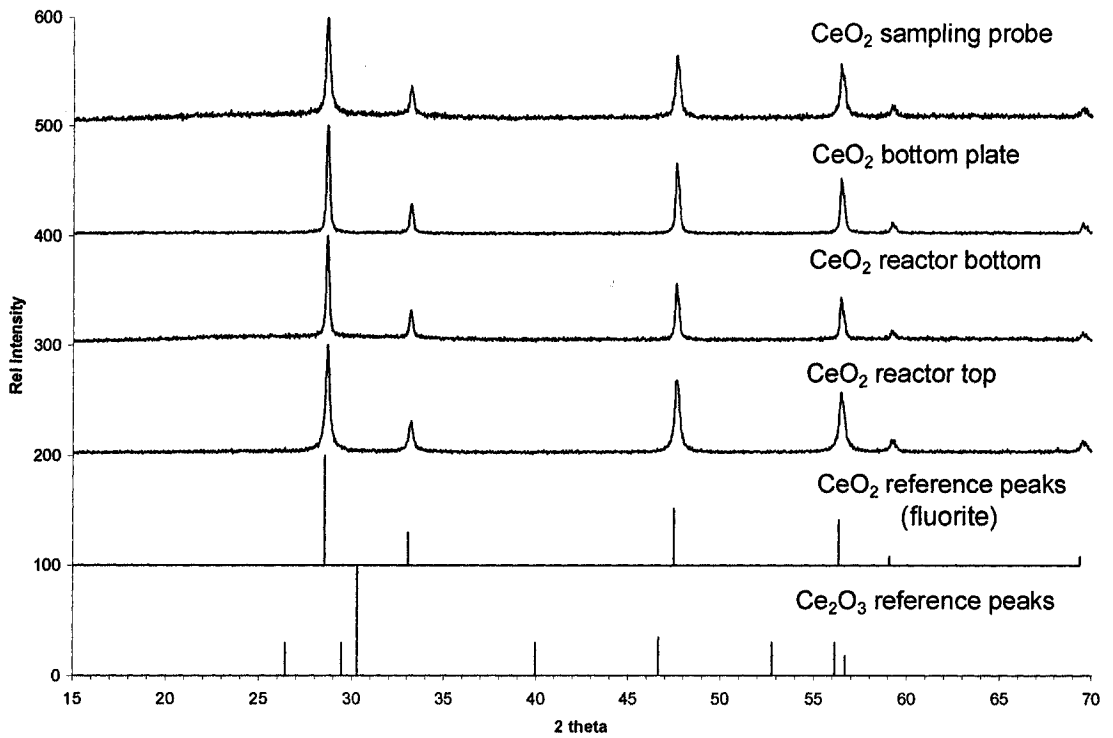


**Fig. 4. 18 X-ray diffraction pattern of $CeO_2$ samples at different reactor locations**

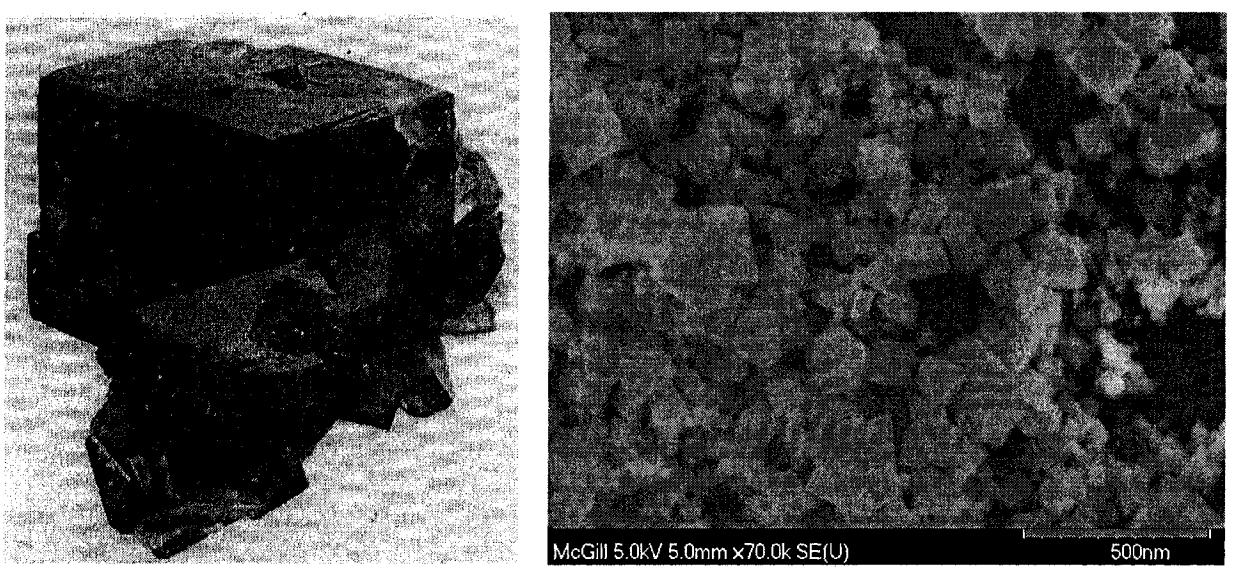


A B

**Fig. 4. 19 a) Typical fluorite structure, b) SEM micrograph of $CeO_2$ collected on the reactor bottom plate P=35kW, $C_{(Ar)}/S_{(O2)}/A_{(Ar)}$=20/100/5 slpm, P=1/3 atm**

## 4.4 Conclusions

A new reactor and a novel in-situ sampling technique were developed for the study of the synthesis of $CeO_2$ powders produced from dissolved cerium nitrate salts. The new conical reactor minimized particle recirculation and provided a highly symmetrical and undisturbed plasma flow suitable for the analysis of the phenomena affecting the formation of $CeO_2$ powders. The in-situ sampling consisted of a water cooled probe operated at near-isokinetic conditions and connected to a miniature wet collection system. The sampling probe used $N_2$ gas to quench and to dilute the sampled plasma gas with particles. The collection system is composed of a mist atomizer acting as a scrubber and a custom-made spray chamber. The entire collection system is portable and it worked in the 30 nm to 100 μm particle size range. A wet collection system was preferred over other particle collection devices because particle agglomeration can be minimized by post treatments. These include sonication, surfactant addition and pH adjustment in-situ. The other advantage of a wet collection system is that multiple samples can be acquired without the need of shutting down the plasma and without any cross contamination.

Both a calorimetric study of the reactor and a thermodynamic analysis of $CeO_2$ formation were conducted in the nominal plate power range of 25 to 45 kW. The calorimetric studies allowed the calculation of the mean inlet reactor temperature which was used as a boundary condition for the numerical simulation of the velocity and temperature profiles of the reactor system at different plate powers and gas flows. Further, a thermodynamic simulation demonstrated that $CeO_{2(s)}$ is the preferred oxidation state of cerium at temperatures lower than 2,400 K and that a liquid and a gas phase can co-exist at temperatures ranging from 2,700 to 3,200 K. Numerical simulations showed that plasma gas temperature and velocity increased with increasing plate power along the reactor centerline. The effect of increasing plate power was more pronounced at downstream reactor locations. Decreasing gas flow rates also increased gas temperature and velocity for the same Z-centerline locations in the reactor. The calculated temperature fields in this study shown centerline reactor temperatures above 2,500 K for all but one of the cases thus suggesting that $CeO_{(g)}/CeO_2$ gas was formed.

Finally, a comprehensive droplet-to-particle formation mechanism was proposed based on numerical simulation of the temperature and velocity fields in the reactor, preliminary in-flight sampling, thermodynamics, calorimetry and former numerical simulations of the particle formation. From this, three main particles sizes were indentified: nanoparticles (<50 nm), intermediate particles of 50 nm to 2 μm and micron particles larger than 2 μm. Also, the cerium oxide synthesized was fully oxidized to $CeO_2$(fluorite) and no $Ce_2O_3$ was present in the reactor.

## 4.5 Acknowledgments

The authors thank the financial support by the Natural Sciences and Engineering Research Council of Canada and the Ministry of Education of the Province of Quebec through its FQRNT program.

## 4.6 References

1. B. C. H. Steele, *Solid state ionics,* **129**, 95-110 (2000)
2. S. P. S. Badwal, F. T. Ciacchi and J. Drenan, *Solid state ionics,* **121**, 253-262 (1999)
3. B. C. H. Steele and A. Heinzel, *Nature*, **414** (2001)
4. H. Zhu, Y. C. Lau, and E. Pfender, *J. of Superconductivity*, **3**(2), 171- 175 (1990)
5. A. L. Mosse, L. I. Krasovska, I. A. Dividenko, and A. V. Gorbunov, *Int. J. of Materials and Product Technology*, **10**(3-6), 566-577 (1995)
6. F. Gitzhofer, M. Boulos, J. Heberlein, R. Henne, T. Ishigaki, *MRS Bulletin,* **25**(7), 38-42 (2000)
7. M. E. Bonneau, *Thése,* Université Sherbrooke, Canada (2001)
8. S. Gutierrez and F. Gitzhofer, *Proceedings 15th ISPC* Orléans, France, **7**, 2749-2756 (2001)
9. G. Schiller, M. Müller, F. Gitzhofer, *J. Therm. Spray Tech.,* **8**(3), 389-392 (1999)
10. G. Lemoine, H. Ménard, J. W. Jurewiczs, *Proceedings 16th ISPC* Taormina, Italy (2003)
11. M. I. Boulos, *J. Therm. Spray Tech.,* **1**, 33-40 (1992)
12. E. Bouyer, M. Muller, M., R. H. Henne, G. Schiller, *J. of Nanoparticle Research,* **3**, 373-378 (2001)

13. Castillo, I. and Munz, R., *Plasma Chemistry and Plasma Processing*, **25**(2), 87-107, (2005)
14. Lu Jia and Gitzhofer, *Proceedings of the ISPC 17*, Toronto, Canada (2005)
15. Goortani, B, et al., International Journal of Chemical Reactor Engineering, **4**, 1330 (2006)
16. Wang, X, Hafiz, J. *et. al.*, Plasma Chemistry and Plasma Processing, **25**(5), 439-453 (2005)
17. Boufendi, L. et al., *Dusty Plasmas: Physics, Chemistry and Technological Impacts in Plasma Processing*, John Wiley & Sons (1999)
18. Forsyth, B. R. and Liu, B. Y. H., *Aerosol Science and Technology,* **36**(5), 515 (2002)
19. Forsyth, B. R. and Liu, B. Y. H., *Aerosol Science and Technology,* **36**(5), 526 (2002)
20. Seol, K. S *et al., Journal of Aerosol Science*, **31**(12), 1389 (2000)
21. Nijhawan, S. *et al., Journal of Aerosol Science*, **34**, 691-711 (2003)
22. Fazilleau, J., *et al. Plasma Chemistry and Plasma Processing*, **26**(4), 371-391 (2006)
23. Delbos, C., et al. *Plasma Chemistry and Plasma Processing*, **26**(4), 393-414 (2006)
24. Castillo, I. and Munz, R., *International. Journal of Heat and Mass Transfer.*, **50**(1-2), 240-256 (2007)
25. Castillo, I. and Munz, R., *Inter. J. Heat Mass Transf.*, (in print)
26. Desroches, M., Castillo, I., and Munz, R. *Particle systems and particle characterization*, **22**(5), 310-319 (2006)
27. SMPS reference,Model 3934 TSI. Instruction manual http://www.tsi.com/Product.aspx?Pid=85
28. Annis, P. *Fine particle pollution. North Central Regional Publication*, 393, 1-8 (1991)
29. FactSage 5.4$^{TM}$. The integrated thermodynamic database system, École Polytechnique de Montréal, (2005) http://www.factsage.com/

# Chapter 5 New in-situ sampling and analysis of the production of $CeO_2$ powders from liquid precursors in a rf thermal plasma reactor. Part 2: Analysis of $CeO_2$ powders, fuel addition and image analysis

In this chapter the second part of the experimental results is presented. Analysis of the synthesis of $CeO_2$ powders at different plasma operating conditions, fuel addition and CCD photographs are described.


## Abstract

A novel reactor design, sampling probe and wet collection system were used to investigate the combined effects of plasma operating parameters and particle collection mechanisms on the synthesis of $CeO_2$ particles from liquid precursors. The sampling of particles in-flight and the collection of particles at several reactor regions were used to provide experimental evidence of particle size at various plasma operating conditions, i.e. power and plasma gas flow rates. This information provided a picture of how $CeO_2$ particles were formed and how these particles were collected in various locations. It was concluded that the explosion of the atomized solution droplets produced intermediate (100 nm to 2 μm) and large (> 2 μm) particles. Also nanoparticles (about 50 nm) were observed as a result of particle nucleation and growth from the cooling of the $CeO_2$-rich plasma gas.

The effect of adding water soluble fuels (alanine and glycine) to the original cerium nitrate solutions was also investigated. Fuel addition decreased the temperature of $CeO_2$ formation by acting as a local heat source as a result of fuel auto-ignition. These additions promoted particle sintering and provided a more homogenous particle size distribution at certain reactor locations.

Photographs of the particles in-flight were taken using a fast speed CCD camera. The results were used to validate particle velocity from numerical simulations and to show evidence of particle explosion by comparing the velocities of different particle sizes.


## Keywords

Radio-frequency inductively coupled plasma, $CeO_2$ particles, sampling probe, solution plasma synthesis of particles, particle size distribution, CCD camera, image analysis


## 5.1 Introduction

In Chapter 4 of this work a novel reactor capable of minimizing gas recirculation and providing a highly symmetrical gas flow to promote equable particle residences times was presented. Also a new near-isokinetic sampling scheme was presented which incorporated the wet collection of sampled particles in real time. Thermodynamic and numerical CFD simulations provided information about the physical state and oxidation state of cerium oxide and information about the temperature and velocity profiles in the reactor. The calculated temperature fields shown reactor temperatures above 2,500 K along the reactor centerline for most of the cases which indicated that $CeO_2$ gas was present in the reactor.

A comprehensive droplet-to-particle formation mechanism was elucidated with information gathered from experimental evidence and former numerical simulations of the effect of a solution droplet submerged in a mixture of argon/oxygen plasma. Three main particles size ranges were indentified, i.e. nanoparticles, intermediate particles of 80 nm to 2 μm and micron particles larger than 2 μm.

Now in Chapter 5 of this work (the present article), the proposed mechanism presented in Chapter 4 is further analyzed and the different reactor particle collection mechanisms are incorporated. The system under study consists of an atomized injection of water soluble cerium nitrate salts into a rf inductively coupled plasma torch. The injected solution produces a fine mist of known droplet size. Particles of $CeO_2$ are formed after calcination of the cerium nitrate droplets in an oxygen rich argon/oxygen plasma. The particles are formed in a water cooled conical reactor operated at a pressure of approximately 1/3 of an atmosphere. A novel sampling probe (described in Chapter 4 of this study) was used to

sample particles in-flight at different reactor locations. The probe is capable of real time analysis and continuous sampling because the particles are collected in a slurry which greatly minimizes particle agglomeration. The effect of varying generator plate power and plasma gas flow rate on particle size was studied at different reactor locations.

In Chapter 4 of this study, it was shown that the droplet-to-solid particle transformation occurs through various mechanisms. Also, from previously published work, it was known that the amount and rate of heat transfer to the initial atomized droplets of dissolved cerium nitrate plays a key role[1,2] in this transformation. When the solution comes into contact with the plasma, a portion of the plasma's energy goes towards evaporating the solution's excess water rather than directly producing oxide particles. The addition of glycine and alanine decreases the amount of water needed to dissolve the cerium nitrate salt by increasing its water solubility. Also, these two compounds act as fuels and thus provide extra local energy to promote the thermal decomposition of the nitrates into the desired oxides at lower temperatures[3]. The effect of adding glycine and alanine on the size of the resulting cerium oxide particles was examined in this work.

## 5.2 Experimental methodology

### *5.2.1 Experimental setup: Plasma unit*

The experimental setup of the plasma reactor is shown schematically in Fig. 5.1 (same as described in Chapter 4 of this work).

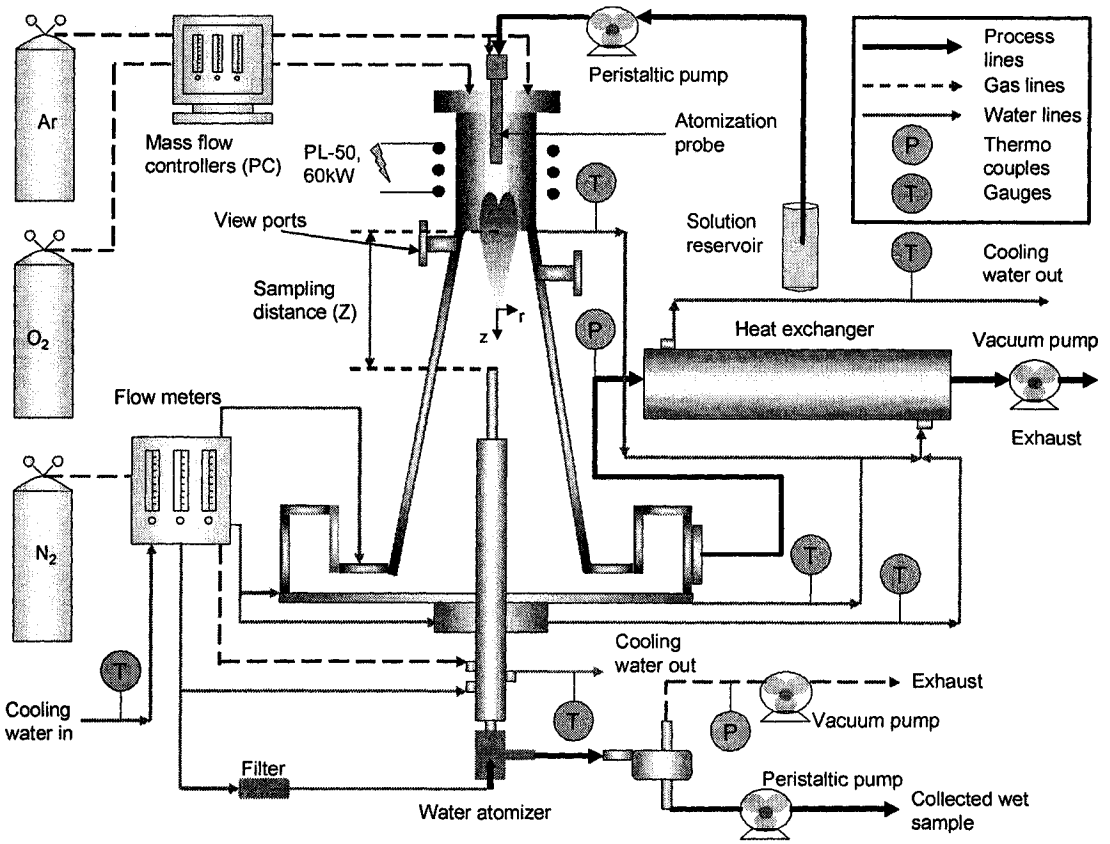


**Fig. 5. 1 Schematic representation of the plasma reactor**

It consists of an induction plasma torch (PL-50 Tekna Inc.), a 60 kW radio frequency power supply (Lepel generator with an oscillator frequency 3-5 MHz) (not shown), a conical stainless steel water-cooled reactor and a cylindrical stainless steel heat exchanger. The reactor was operated under vacuum (roughly 1/3 of an atmosphere). The atomizing probe is a Tekna Plasma Systems Inc. SA-792 x 0.8/1.0 mm. internal diameter x 260 mm long. The tip of the atomizing probe was located just below the first induction coil of the torch. The solutions were injected by means of a peristaltic pump. The sampling probe collected particles at a distance downstream Z which is the distance from

the exit of the torch nozzle to the tip of the sampling probe. The probe was designed to move in the radial and axial directions. Two view ports are located as close as possible to the exit of the torch (4.12 cm and 9.12 cm respectively).

Three different gases were used: the atomizing and central gas was argon, the sheath gas was oxygen and nitrogen was used as quench gas in the sampling probe. Mass flow controllers were used for the torch gases and a calibrated flowmeter was employed for the quench gas ($N_2$). The walls of the conical reactor and bottom plate were water cooled and the water temperature was monitored using T-type thermocouples. The sampling probe shown in Fig. 1 was employed to collect samples at different plasma operating conditions in various reactor locations.

### *5.2.2 Characterization techniques*

Particle size distributions were measured using a Mastersizer 2000 (Malvern Instruments) with the Hydro 2000 S as the liquid injector; the minimum particle diameter detection limit was 20 nm. Each sample was dispersed in distilled water and subjected to 10 minutes of ultrasound to promote particle de-agglomeration. A dispersant agent was used to help stabilize the de-agglomerated suspension and the analysis was done at pH=10. The dispersant agent used was 50% active content 2-phosphonobutane-1,2,4-tricarboxylic acid (PBTCA) supplied by Jiangsu Jianghai (China) and the concentration of the dispersant in the suspension was 0.04% by volume. The pH was adjusted with sodium hydroxide 5N solution (Fisher SS256B). Further details of this technique are explained a previous publication[4]

Finally, the synthesized $CeO_2$ powders were analyzed using a Hitachi 4700 Field Emission Scanning Electron Microscope (FE-SEM) in ultrahigh resolution mode. Each sample was dispersed in ethanol, sonicated for 5 minutes and then mounted on a silicon wafer carbon taped to SEM aluminum stubs.

### *5.2.3 Experimental conditions*

The experimental conditions are shown in Table 5.I. The liquid flow rate of the atomized solution was kept constant at 6.0 ml/min (1.66 g/ml @ 25 °C). The atomization probe was

¾ of a turn open. The reactor pressure was kept constant 0.33 atm. The quench gas flow rate of the sampling probe was kept constant at 14 slpm of $N_2$ except for the results shown in section 5.3.1 where a flow rate of 5 slpm was used.

**Table 5. I Summary of experimental conditions**

| | | Gas flow rates [slpm] | | | Sampling position [cm] | | |
|---|---|---|---|---|---|---|---|
| No | Plate power [kW] | Central (Ar) | Sheath ($O_2$) | Atomizing (Ar) | Z=20 | Z=30 | Z=40 |
| 1 | 45 | 20 | 100 | 5 | | Y | Y |
| **2** | **35** | **20** | **100** | **5** | **Y** | **Y** | **Y** |
| 3 | 35 | 20 | 100 | 5 | | Y (off) | Y (off)* |
| 4 | 35 | 20 | 100 | 5 | | Y (A,G) | Y (A,G)** |
| 5 | 35 | 15 | 80 | 5 | | Y | Y |
| 6 | 25 | 20 | 100 | 5 | | | Y |
| 7 | 25 | 20 | 100 | 5 | | | Y (A,G) |
| 8 | 25 | 15 | 80 | 5 | | | Y |

* Y(off) = the sampling location was 2.5-cm off center
** Y(A,G) = alanine and glycine were added to the atomized solution
Y=Yes, experiment ran at these conditions, base case condition in bold

The different solutions used in this study are shown in Table 5.II.

**Table 5. II Different solution compositions**

| No | Description | Density [g/ml] @ 25 °C | $\frac{n_{cerium\_nitrate}}{n_{fuel}}$ | Precursor Solution Composition | | |
|---|---|---|---|---|---|---|
| | | | | Mass $Ce(NO_3)_3 \cdot 6H_2O$ | Mass Water | Mass fuel |
| 1 | Pure cerium nitrate | 1.66 | | 5.40 g | 3.00 g | |
| 2 | Stoichiometric Glycine | 1.70 | 1 : 1.67 | 5.40 g | 1.40 g | 1.56 g |
| 3 | Stoichiometric Alanine | 1.69 | 1 : 1.00 | 5.40 g | 1.40 g | 1.11 g |

## 5.3 Results and discussion

This section includes a detailed description of the $CeO_2$ droplet-to-particle formation and collection mechanisms and how these two influence particle deposition at different reactor locations. Then the effect of changing plasma plate power and plasma gas flow on particle size is investigated and the work is concluded by analyzing the effect of adding glycine and alanine fuel to the solution mixture. The results shown in section 5.3.1 come

from two sources. First, from samples collected using the sampling probe while the probe was operated at superisokinetic conditions (quench gas of 5 slpm of $N_2$). Second, from particles collected from various reactor locations, i.e. reactor conical walls, reactor bottom plate and all outside walls of the sampling probe (i.e. tip and body walls). All other results shown in this work come from samples collected using the sampling probe while the probe was operated at near-isokinetic conditions (quench gas of 14 slpm of $N_2$) i.e. sections 5.3.2 and 5.3.3.

### *5.3.1 Mechanism of droplet-to-solid particle conversion and how particles are distributed in the reactor for the base case experimental conditions*

The mechanism of droplet-to-particle formation mechanism for $CeO_2$ that was proposed in the first part of this work has been incorporated in the context of the reactor system (Figure 5.2).

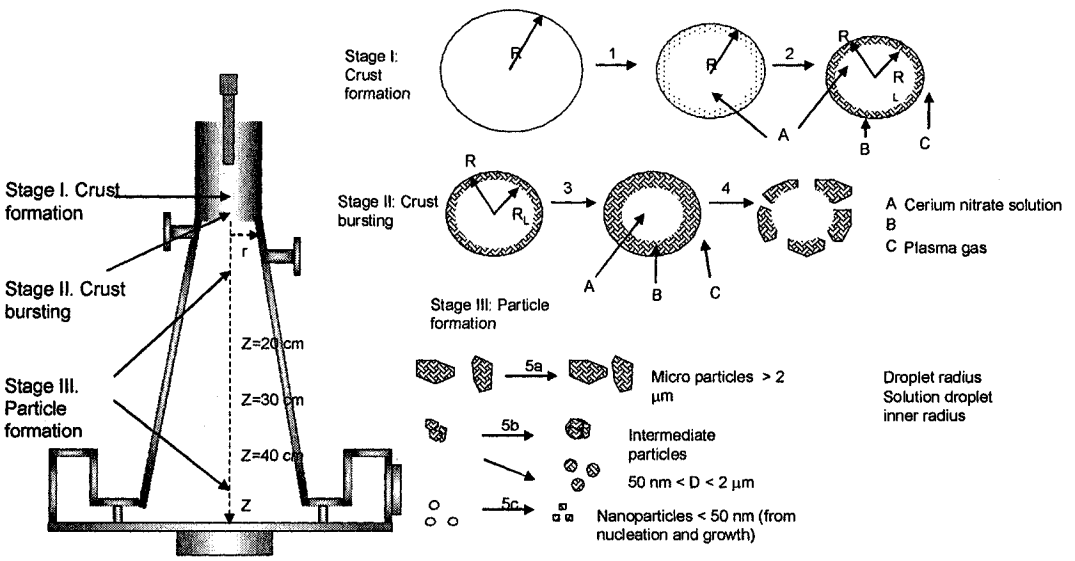


**Fig. 5. 2 Schematic diagram of $CeO_2$ particle formation from atomized droplets**

The conical reactor section shown in Figure 5.2 illustrates several important zones. The first zone comprises the torch and the area in the vicinity of the view ports. This is where Stage I and II take place. The conditions leading to crust formation have been numerically modeled[1,2]. Crust formation and bursting were predicted in all the experimental conditions of the present work. Stage II is considered finished when droplets of cerium nitrate solution explode. After explosion, particle formation takes place in the conical

section of the reactor and this has been labeled as Stage III. A more detailed description of the particle formation is shown in Fig. 5.3. The size of the particles along the centerline of the reactor at different axial locations (Z=20, 30 and 40 cm) as sampled by the probe is shown in Fig. 5.4.

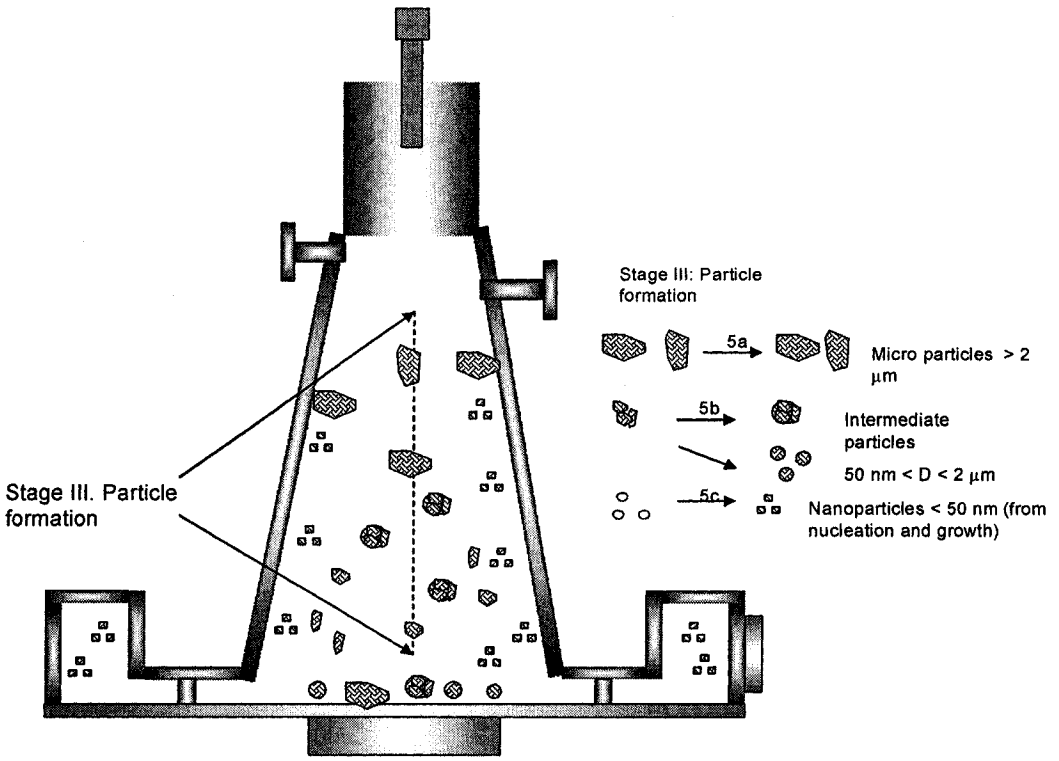


**Fig. 5. 3 Detailed schematic diagram of $CeO_2$ mapping based on both formation and collection mechanisms**

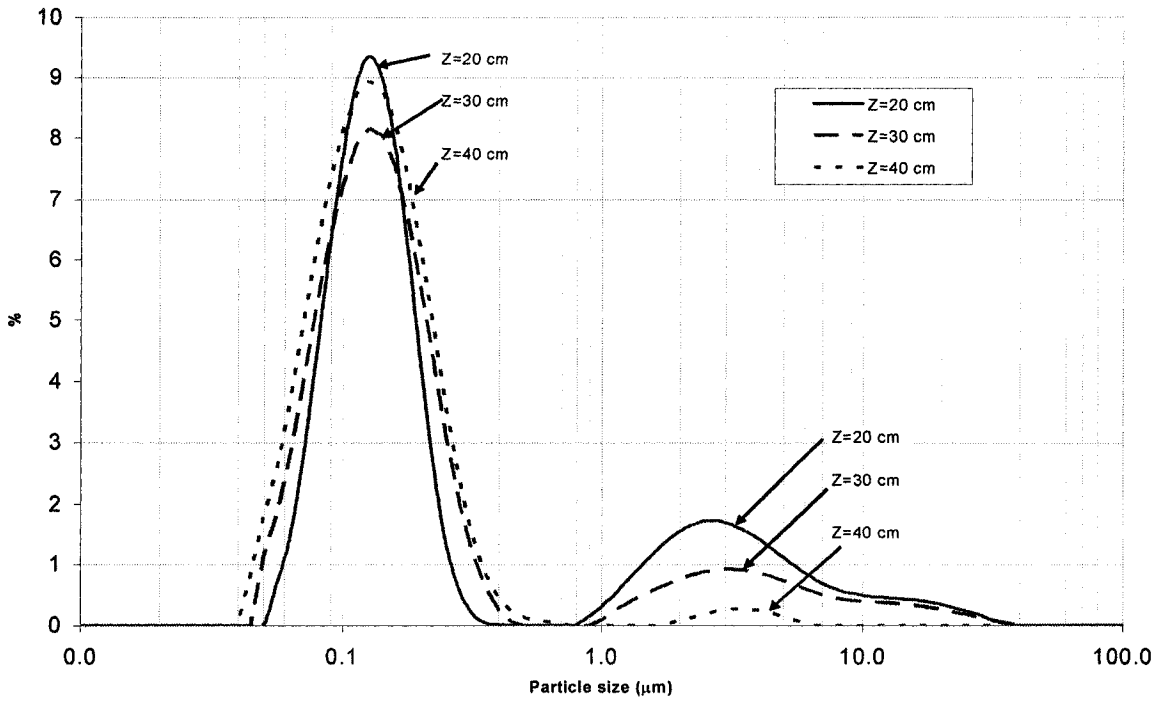


**Fig. 5. 4 Particle size distribution of wet collected samples at different centerline probe locations (Z=20, 30 and 40 cm) @ P=35kW, $C_{(Ar)}/S_{(O2)}/A_{(Ar)}$=20/100/5 slpm, Sampling probe quench gas of 5 slpm of $N_2$**

The sudden droplet explosion forms large crust fragments (micro particles > 2 μm ), intermediate (50 nm < D < 2 μm) fragments and much smaller solution droplets (< 50nm) that are vaporized. The majority of the large crust fragments (> 2 μm) (5a in Fig 5.3) move radially towards the sides of the top conical walls because of radial momentum gained from crust explosion and because particles of this size tend not to follow the gas streamlines closely. The remaining large fragments that are directed in the downstream or upstream directions are entrapped by the gas flow. These fragments remain close to the centerline of the reactor, but as the reactor expands so does the gas flow. Therefore, fewer large fragments remain on the centerline of the reactor with increasing axial distance as shown in Figure 5.4. The size of these large fragments depends on the size of the crust **before** bursting. It is hypothesized that the higher the heat flux to the atomized droplet, the thicker the crust and thus the bigger the fragments will be.

The intermediate particles are formed from smaller crust fragments (50 nm < D < 2 μm) (5b in Fig 5.3) that are calcined and follow the gas streamlines; they also account for the bulk of the $CeO_2$ particles. These intermediate particles show **two distinct ranges**. The first one is from 50 nm to 0.3 μm and the second is from 1.0 μm to 2-3 μm. Particles in the first range are the most common type of particles and are captured by thermophoresis, inertial impaction and turbulent diffusion at various reactor locations depending on their size and gas temperature gradients. Particles in the second range (1.0 μm to 2-3 μm) are formed from aggregation and sintering of particles that originally belonged to the first range or by rapid quenching of crusts of similar sizes. Therefore, particles belonging to either range are termed intermediate size particles. This is schematically shown in 5b in Figure 5.3.

Further, Figure 5.4 shows the particle size distribution for the 2 ranges of intermediate particles of samples collected at the centerline of the reactor. The particle size distribution in the 50 to 0.3 μm range broadens with increasing Z-axial distance, thus suggesting particle growth by sintering or gas deposition on existing particles. The particle size distribution for the intermediate particles in the 1 to 2-3 μm range shows an increase with decreasing Z-axial distance. This favors the hypothesis that particles in the 1 to 2-3 μm range are formed by rapid cooling of the gas flow. Decreasing Z-distance provides additional local cooling at the centerline of the reactor due to the water cooled probe walls. Note that particles in this range represent the left side of the curve shown in the 1 to 2 μm range and must not be confused with the large particles (right side of the curve, i.e. > 2 μm).

Finally, the vaporized droplets enrich the plasma gas with CeO vapor (5c in Fig 5.3) and as the gas cools, particle nucleation and growth of $CeO_2$-fluorite nanocrystals takes place. These nanocrystals are primarily collected by thermophoresis and turbulent diffusion on the lower part of the conical reactor wall and on the bottom plate where temperature gradients are steeper. The gradients were estimated from 450 K/cm to 1,500 K/cm based on the temperature profiles calculated in Chapter 4 of this work depending on the plasma

conditions. Again, Figure 5.4 shows that more nanoparticles are formed as the gas cools with increasing axial Z-distance (left side of the curve in the 30 nm to 1 μm range).

Figure 5.5 shows how the position of the sampling probe affects deposition of particles at different locations, i.e. conical reactor walls, bottom plate and outer walls of the entire sampling probe. The plasma operating conditions were kept constant at P=35kW, $C_{(Ar)}/S_{(O2)}/A_{(Ar)}$=20/100/5 slpm, P=1/3 atm (base case condition). When the probe is closer to the torch exit, more large particles are collected on its walls relative to the amount collected at the other two locations. This could be explained by the fact that the probe is located closer to where crust bursting happens and thus it is more likely that large particles will impact on the probe walls. When the probe is located at distances Z=30 or Z=40 cm, the large particles have an unobstructed path to the side walls of the reactor. Consequently, the fraction of particles in the particle distribution collected on the side walls is higher than the fraction of particles on the outer walls of the probe.

The intermediate particles (bulk of the distribution) (50 nm < D < 2 μm) are formed in the regions that favor particle growth by sintering and/or vapor deposition on existing particles for intermediate particles in the 50 nm to 0.3 μm range and in regions that promote gas quenching for the intermediate particles in the 1 to 2-3 μm range. The growth promoting region is located along the centerline of the reactor from Z=10 cm to the tip of the sampling probe. The gas quenching region is located on the water cooled reactor walls, bottom plate and water cooled sampling probe walls.

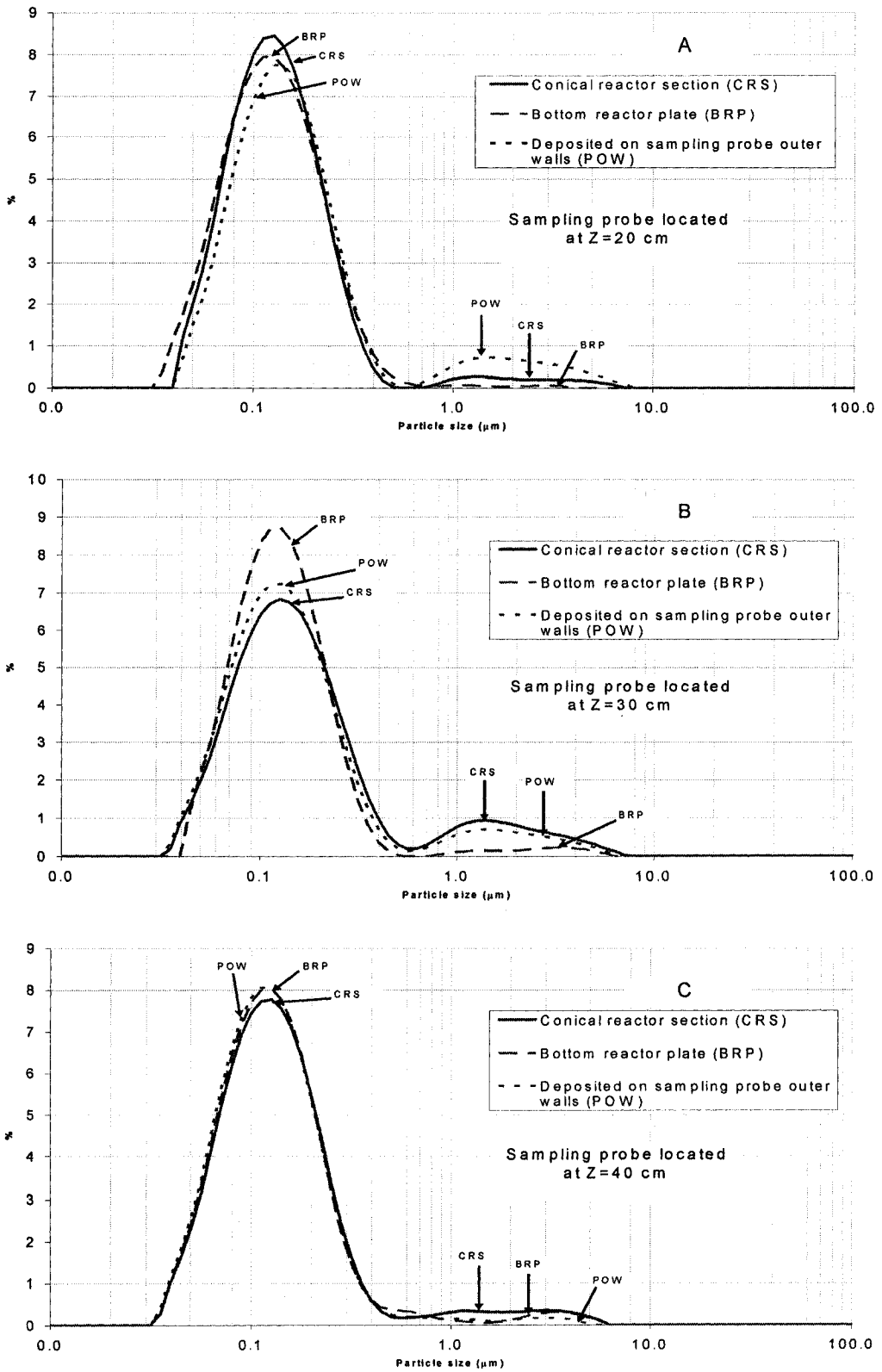


**Fig. 5. 5 Particle size distribution of samples deposited at different reactor locations with varying the location of the sampling probe @ P=35kW, $C_{(Ar)}/S_{(O2)}/A_{(Ar)}$=20/100/5 slpm, 5 slpm of $N_2$ quench gas**

Positioning the probe at Z=20 cm obstructs particle growth on the centerline and favors local cooling. As a result of this cooling effect particles greater than 1.0 μm are deposited on the probe walls where the steepest temperature gradient is found. Also, the fraction of particles smaller than 0.3 μm is larger on the bottom of plate of the reactor (Fig. 5.5a). Conversely, positioning the probe at Z=40 cm minimizes probe local cooling and does not obstruct particle growth, as a result the intermediate particle size distributions at different collection points in the reactor are all very similar (Fig. 5.5b). At Z=30 cm, the effect of probe local cooling promotes again the formation of particles larger than 1.0 μm and these particles are deposited on the probe outer walls and conical reactor section. Particles smaller than 0.3 μm are primarily collected on the bottom plate of the reactor.

Finally, it is difficult to make definitive conclusions about the nanoparticles (< 50nm) apart from the fact that they are present on the conical reactor walls, bottom plate and outer walls of the sampling probe. This is because all these collection points are water cooled which favor step temperature gradients in the neighboring gas and thus nanoparticles are collected by thermophoresis.

### *5.3.2 Analysis of collected powders at different plasma operating conditions and various reactor locations*

All the analyses in section 5.3.2 were **carried out using the sampling probe and the particles collected from the wet collection system**. The numerical simulation of the reactor temperature and velocity profiles presented in Chapter 4 of this work will be used to explain some of the findings in this section.

#### 5.3.2.1 Effect of plate power

The effect of changing plate power on particle size distribution was studied in samples collected 40 cm away from the torch exit. The particle size of the samples collected was analyzed (Figure 5.6) and SEM micrographs were taken (Figure 5.7). Ideally, particles collected at Z-distances less than Z=40 cm at higher plate power (> 35kW) were desired. However, particle deposition on the tip of the probe was observed at Z=30 cm with the maximum power of 45 kW. Particle deposition partially obstructed the probe's tip, greatly

decreasing probe's collection. In order to remove the already deposited particles, the tip of the probe was sand blasted. No attempts were carried out to collect particles at Z=20 cm at the highest plate power to further prevent damage of the probe tip.

Increasing plate power causes more violent droplet bursting and favors the formation of larger crust fragments of approximately 5 to 10 μm size range as shown in Figure 5.6 and in Figure 5.7-A and 5.7- B. Even fragments > 10 μm were detected for the maximum power of 45 kW (Fig. 5.6). However, increasing plate power also provides higher plasma gas temperatures over longer reactor lengths, promoting particle sintering and formation of rounded particles in the 0.5 to 1 μm range. These rounded particles were clearly observed in Figure 5.7-D which is an enlarged image of Figure 5.7-A at maximum plate power of 45 kW. Particles in the range of 0.5 to 1 μm were also observed at lower plate powers (Figure 5.7-B and 5.7-C) but are generally formed at higher gas temperatures. The particle size distribution often detects these particles in the 1 to 2 μm range due to particle agglomeration (Figure 5.6).

For the particle sizes lower than 0.5 μm (intermediate and nanoparticles) a surprising result was obtained. First, no particles in this size range were detected at the highest plate power of 45 kW and second, decreasing power increased the amount of particles lower than 0.5 μm. This was because the temperature of the plasma gas remains largely higher than 2,500 K. At these temperatures, the plasma gas still contains a large amount of CeO(g) and $CeO_2$(g) which has not sufficiently cooled to allow particle formation by nucleation and gas deposition. As the plate power was decreased, lower gas temperatures (< 2,500K) could be expected at Z=40 cm and thus more particles lower than 0.5 μm were observed (Fig 5.6 and Fig 5.7B and 5.7C). It is important to note that particle growth does not happen inside the sampling probe for all the cases analyzed because of gas dilution and quench, and thus the above results are real in-flight particle sizes.

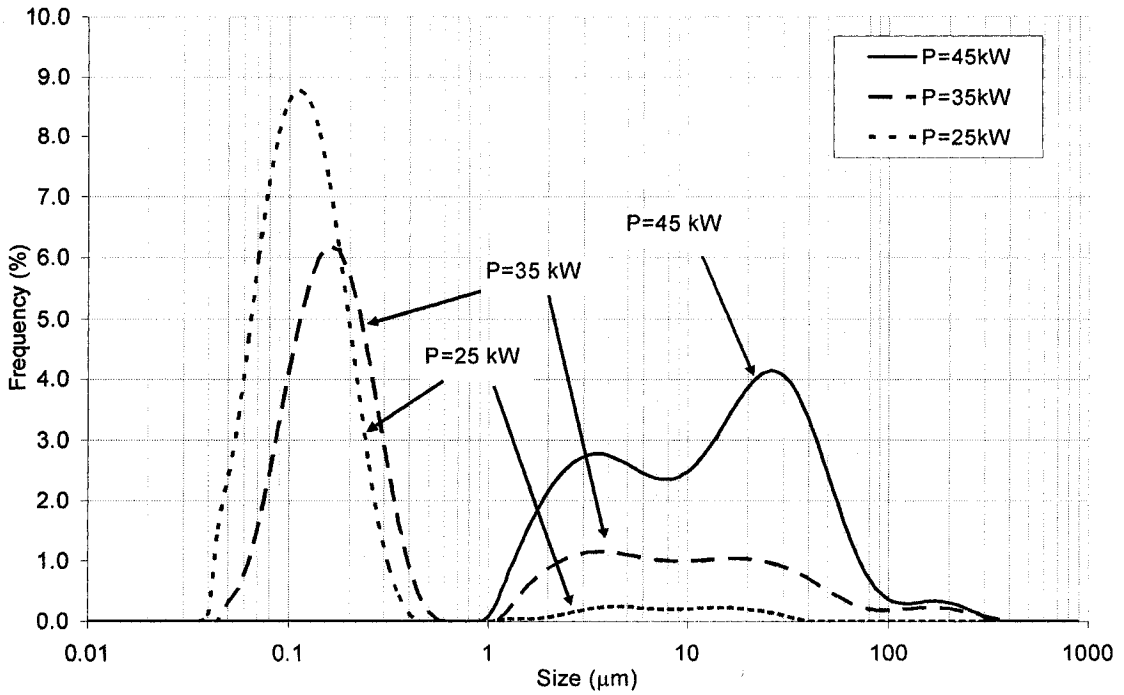


**Fig. 5. 6 Particle size distribution of samples collected at Z=40 cm at different plate powers @ $C_{(Ar)}/S_{(O2)}/A_{(Ar)}$=20/100/5 slpm**

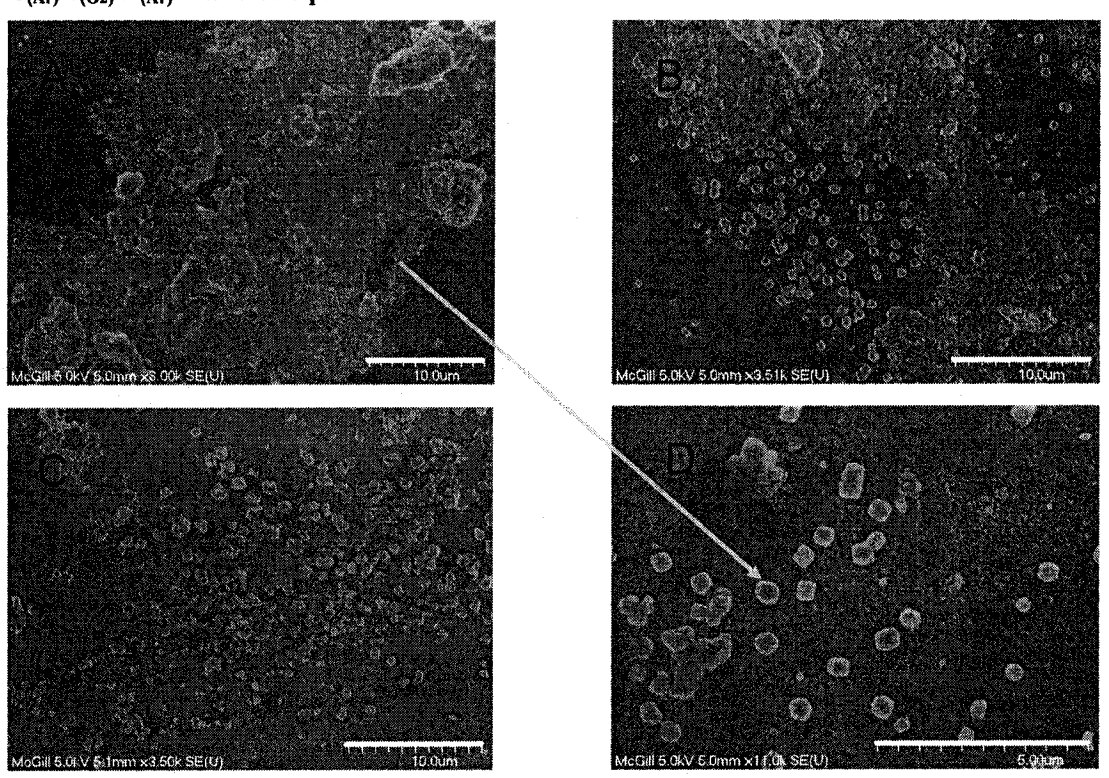


**Fig. 5. 7 SEM micrographs of samples collected at Z=40 cm at different plate powers A) P=45kW, B) 35kW, C) 25 kW, D) 45 kW @ $C_{(Ar)}/S_{(O2)}/A_{(Ar)}$=20/100/5 slpm**

### 5.3.2.2 Effect of reactor location: Radial and axial profiling

Axial: Samples were taken at different centerline reactor locations, i.e. Z=20, 30 and 40 cm at a constant plate power of 35 kW. Their particle sizes were analyzed (Fig. 5.8) and SEM pictures were taken (Fig. 5.9 A-C). At the closer centerline locations (Z=20 cm) the sampled particles are predominantly in the micro range and large fragments (5 to 12 μm) are visible (Fig. 5.9-A). This is because the sampled region is close to the droplet explosion region and mostly large $CeO_2$ fragments are present in the gas. The rest of the cerium nitrate/oxide remains in the vapor form and only a few particles in the 1-5 μm are present at this location. When sampling further away from the torch nozzle, the gas has cooled and more particles lower than 0.5 μm are present in the gas as can be seen in Fig. 5.8B and 5.8C. Some particles in the 1-3 μm range can be observed at Z=30 cm (Fig. 5.9B and Fig. 5.8). Also, particle growth by sintering and vapor deposition can be observed in Fig. 5.9B and 5.9C as more rounded particles were observed with increasing Z-distance. These rounded particles arise from a combination of particle melting and fast freezing and thus their preferred rounded shape.

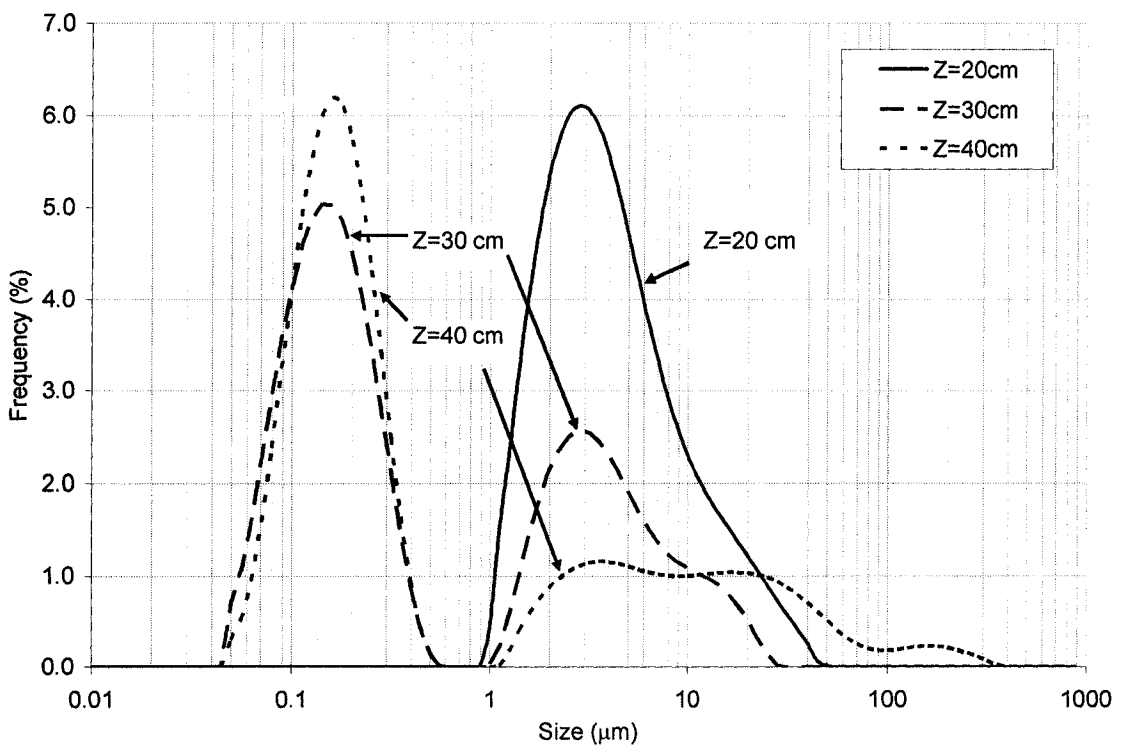


**Fig. 5. 8 Particle size distribution of samples collected at P=35 kW at different Z values (Z=20cm, 30 cm, 40 cm) @ $C_{(Ar)}/S_{(O2)}/A_{(Ar)}$=20/100/5 slpm**

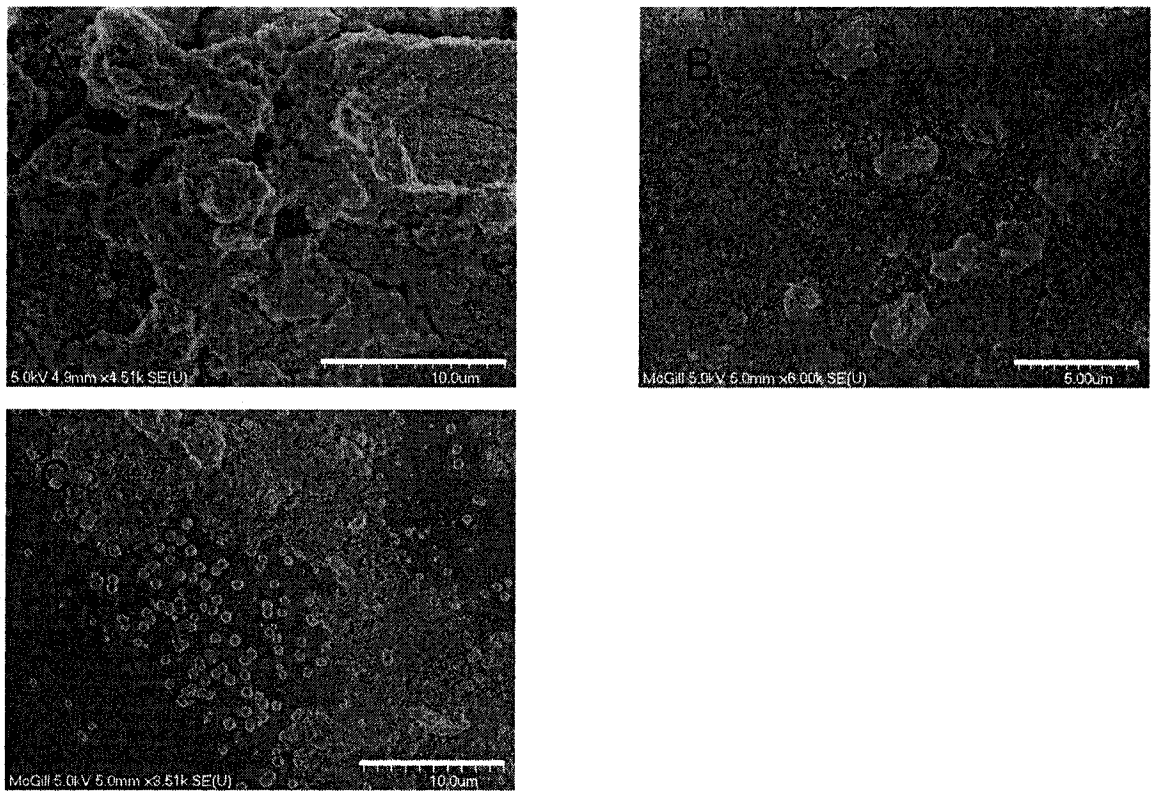


**Fig. 5. 9 SEM micrographs of samples at P=35kW collected at different reactor locationss A) Z=20 cm B) Z=30 cm, C) Z=40 cm @ $C_{(Ar)}/S_{(O2)}/A_{(Ar)}$=20/100/5 slpm**

Radial: Samples were taken at two different 2.5 cm off-center line reactor locations at Z=30 cm and Z=40 cm, their sizes analyzed and SEM micrographs taken. These samples were compared to the center lines samples at the same axial location (Figure 5.10 and Figure 5.11a-d).

The particle size of the 2 pair of samples at Z=30 centerline and Z=30 cm off center (closer to the reactor wall) are similar. However, the off-center sample shows slightly more of the smaller particles (~0.1 μm) and more of the larger crust fragments (Fig 5.11A and 5.11B). Larger crust fragments are expected off-center because they move radially as a result of droplet explosion towards the side walls (large particle in Fig. 5.11B). More particles in the 1-4 μm range were observed in the centerline location because these particles remain in the reactor region where particle growth is favored. A section of Figure 5.11B (indicated by the arrow) has been enlarged to show that fully melted particles in the 0.1 to 1 μm range were collected. These fully melted particles did not take

rounded shapes because they were quickly cooled due to the steep temperature gradients (~1,500 K/cm) closer to the reactor walls.

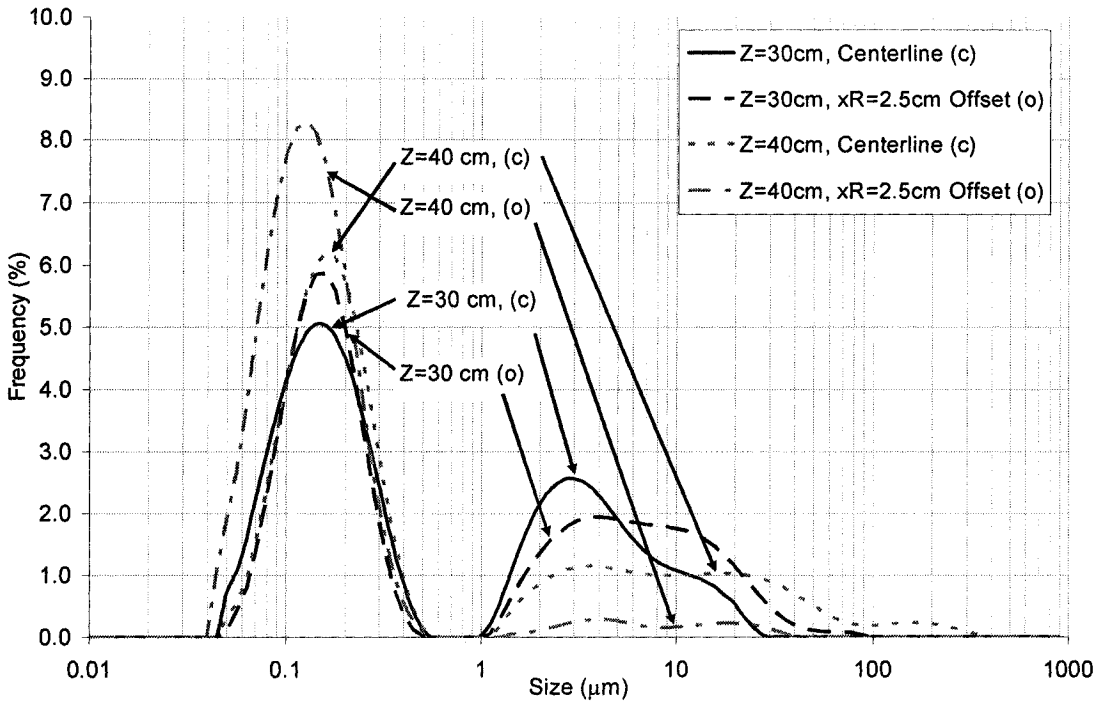


**Fig. 5. 10 Particle size distribution of samples collected at P=35 kW at different reactor locations, i.e. Z=30 cm center, Z=30 cm/2.5 cm off-center, Z=40 cm center and Z=40 cm/2.5 cm off-center @ $C_{(Ar)}/S_{(O2)}/A_{(Ar)}$=20/100/5 slpm**

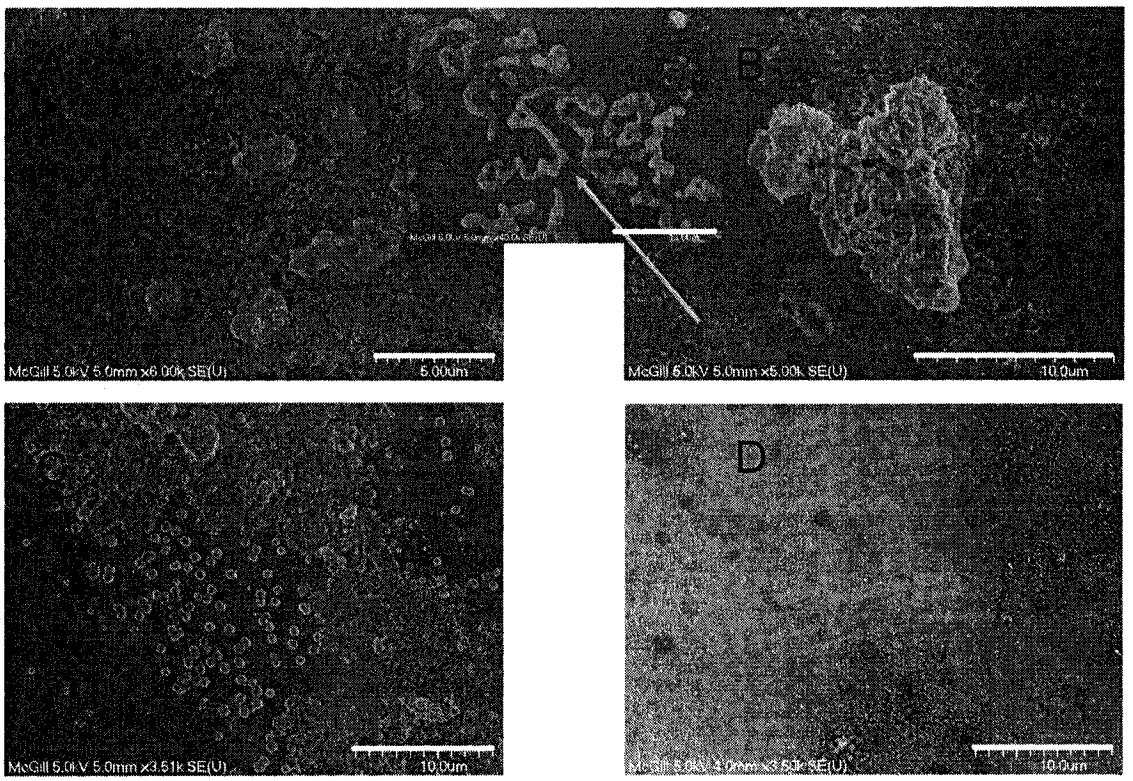


**Fig. 5. 11 SEM micrographs of samples collected at P=35kW at different reactor lengths A) Z=30 cm center, B) Z=30 cm/2.5 cm off-center, C) Z=40 cm center and D) Z=40 cm/2.5 cm off-center @ $C_{(Ar)}/S_{(O2)}/A_{(Ar)}$=20/100/5 slpm**

The samples at Z=40 shown a more distinct particle size change. The off-center sample contains significantly more particles of the intermediate 0.1 μm size and smaller. The SEM micrographs confirmed that more of the smaller particles are present off-center at Z=40 cm (Fig. 5.11C and 5.11D). The majority of the large fragmented crust particles are collected on the top conical section of the reactor and this explained the absence of these particles at off-center locations at Z=40 cm. Further, the cooler off-center gas temperatures promote particle growth by nucleation and vapor deposition favoring the formation of particles in the 0.1 μm range. Hence, the difference in the particle size distributions between Z=40 cm centerline and Z=40 cm off-center shown in Figure 5.10.

#### 5.3.2.3 Effect of plasma gas flow rate

The central and sheath plasma gas flow rates were decreased from 20 slpm to 15 slpm and from 100 slpm to 80 slpm for the central and sheath gas respectively (~25%) while keeping the plate power constant. Two samples were taken at Z=30 on the centerline of

the reactor and their sizes were analyzed (Fig. 5.12). Also, SEM images were taken of these two samples (Fig. 5.13A and B).

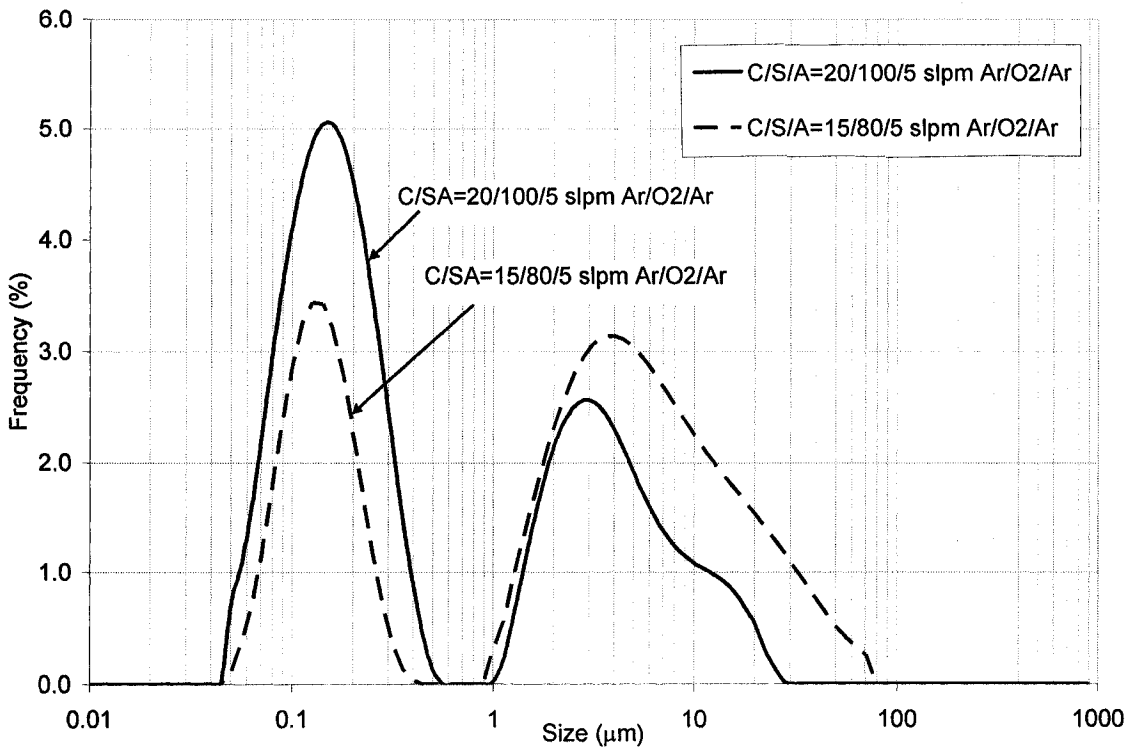


**Fig. 5. 12 Particle size distribution of samples collected at P=35 kW at Z=30 cm for different plasma gas values**

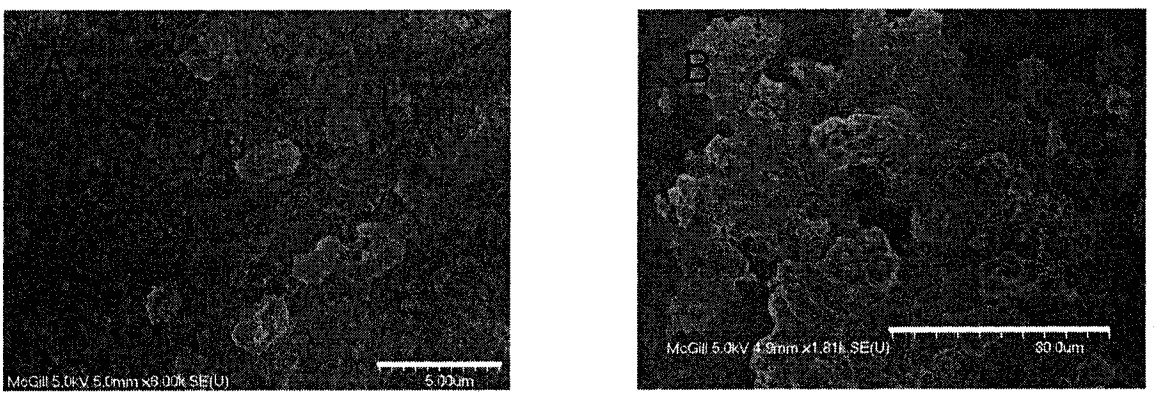

**Fig. 5. 13 SEM micrographs of samples collected at different plasma operating parameters at Z=30 cm A) P=35kW @ $C_{(Ar)}/S_{(O2)}/A_{(Ar)}$=20/100/5 slpm B) P=35kW @ $C_{(Ar)}/S_{(O2)}/A_{(Ar)}$=15/80/5 slpm**

The particle size distribution shown in Fig 5.12 indicates that decreasing the gas flow produces more of the larger particles (> 3 μm) and less of the 100 nm range particles. The results were confirmed by comparing Figure 5.13A and 5.13 B where the samples taken

at a decreased flow rate (B) are compared to the normal base case (A). Figure A shows large crust fragments representative of the particles in the > 1μm range as well as some of the smaller 100 nm range particles in the background. Figure 5.13B shows larger crust fragments than those shown in A of sizes > 15 μm. Also, in Figure 5.13B, the 100 nm range particles appeared much smaller in the background in comparison with those in image A due to the different image magnification. The results can be explained as follows: decreasing the plasma gas flow rate at constant plate power causes an increase of gas temperature because there is the same amount of energy available in less gas. According to the numerical simulations presented in Chapter 4 of this work, the temperature and velocity of the plasma gas at the reactor inlet increased by ~25% and ~30% respectively from the base case. The increased in temperature translates into a higher heat transfer to the atomized droplet. Further, previous numerical modeling conducted by the authors[1,2] in the mechanism of droplet heating had shown that higher plasma temperatures promote two major effects. First, faster crust bursting ranging of up to 4 times faster (i.e. 8 ms to 2 ms) with increasing temperature and second, thicker crusts of up to 5-6 % thicker in diameter (i.e. approximately 75% change in volume) with increasing temperature. Therefore, thicker crusts are expected at higher plasma gas temperatures resulting from decreasing gas flow, despite faster crust bursting at Z=30 cm.

The same experiment was conducted at Z=40 cm, i.e. 25% less central and sheath gas at equal plate power. The results are shown in Figure 5.14 and Figure 5.15 A, B and B1. The particle size distribution does not show a significant change between the base case gas flow and the decreased gas flow experiment at Z=40 cm. This was confirmed by comparing images 5.15A to the set of images labeled 5.15B and 5.15B1 (two images of the same experiment). In both cases, large fragments (5.15A and 5.15B) can be observed as well as intermediate and nano particles (5.15A and 5.15B1). This result suggests that most of the large fragments resulting from the droplet explosion do not remain on the centerline of the reactor from Z=30 cm to Z=40 cm. These fragments tend to move radially towards the reactor walls because of their initial inertia gained from the explosion and because they tend not follow the bulk of the gas flow.

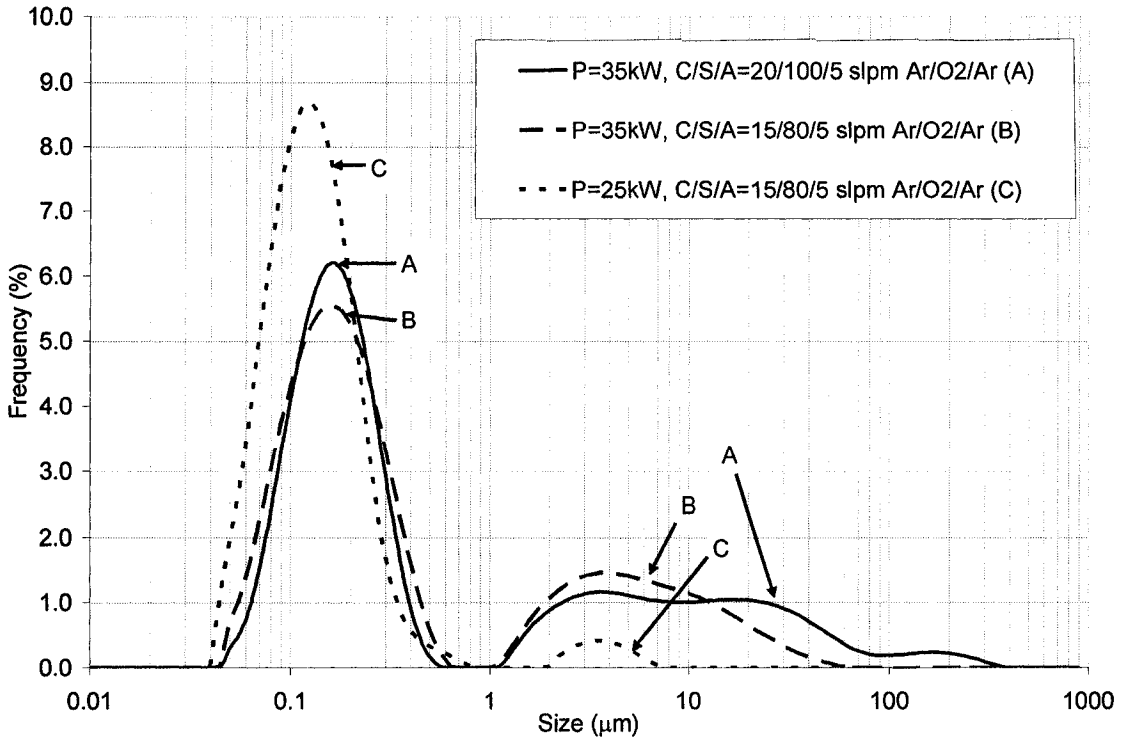


**Fig. 5. 14 Particle size distribution of samples collected at Z=40 cm for different plasma gas values and plasma plate powers**

The other particle size distribution shown in Figure 5.14 represents a sample at Z=40 cm but with both 25% less gas and lower plate power of 25 kW. Two different images of the same sampled are shown in Figure 5.15C and 5.15D. The aim of this experiment was to compare the effect of changing the in-flight residence time of the produced $CeO_2$ particles while keeping the mean plasma temperature history constant.

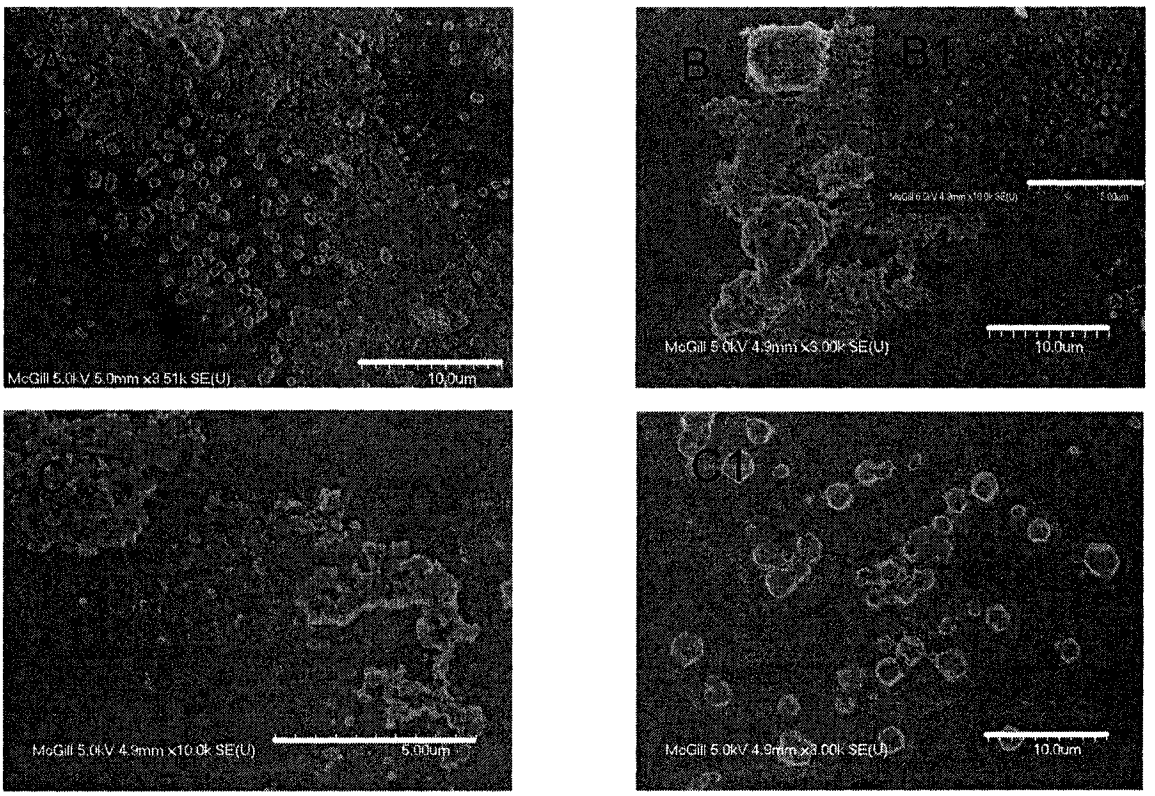


**Fig. 5. 15 SEM micrographs of samples collected at different plasma operating parameters at Z=40 cm A) P=35kW @ $C_{(Ar)}/S_{(O2)}/A_{(Ar)}$=20/100/5 slpm B) and B1) P=35kW @ $C_{(Ar)}/S_{(O2)}/A_{(Ar)}$=15/80/5 slpm C) and C1) P=25kW @ $C_{(Ar)}/S_{(O2)}/A_{(Ar)}$=15/80/5 slpm**

The numerical simulations performed in Chapter 4 of this study indicated that the temperature and velocity values decreased by about 50% at the inlet conditions (3150 K to 2210 K and 34 m/s to 24 m/s, respectively). The same trend (50% decrease) was observed at all other Z-locations (20, 30 and 40 cm) as a result of the combined change of gas flow and plate power. Therefore, comparing different residence times at equal gas temperature histories is not valid because the temperature histories could not be exactly matched between the experiments in Fig 5.14A and 5.14C. Longer residence times (Fig. 5.14C) appeared to decrease the amount of large fragments (> 5 μm) and increased the amount of particles in the 50 to 300 nm range. Most of the sample collected at this Z=40 cm location looked like Fig 5.15C under the microscope. Small particles are shown in the center of the image and on the surface of the larger particles. An interesting feature of this experiment is shown in Figure 5.15D which is another image of the same sample. The particles shown in this image are in the size range of 2-8 μm and appeared in the particle

size distribution as a small "hump" (Fig. 5.14). These particles are larger versions of the smaller fluorite-like structure (angular-cubical shape) particles. The fluorite structure is observed preferentially in intermediate and nanoparticles and not usually in micron size particles. Hence, it is possible that particles with longer reactor residence times grow by vapor deposition on existing fluorite-like particles.

### *5.3.3 Analysis of collected powders with glycine and alanine addition at different plasma operating conditions and various locations*

Alanine and glycine were added to the original solutions for 2 purposes. First, alanine and glycine behave as fuels and thus diminishing the local cooling effect of injecting a solution into the core of the plasma plume. These fuels do not interfere with the chemistry of the calcination of cerium nitrate to cerium oxide because they burn to $CO_2$, $N_2$ and water. By providing extra energy, the combustion of the fuel promotes the thermal decomposition of the nitrates into the desired oxides at lower surrounding gas temperatures. The second purpose was to decrease the amount of water used to dissolve cerium nitrate hexahydrate. The solubility of cerium nitrate increases with the addition of either fuel (see Table 5.II). These two effects combined, i.e. lower water content and lower calcination temperature were believed to affect the $CeO_2$ particle size in the system. A thermogravimetric analysis was conducted in the absence of plasma to determine the optimal amount of fuel.

#### 5.3.3.1 Thermogravimetric analysis of glycine and alanine in the absence of plasma

To obtain the optimal ratio of alanine and glycine the following reactions were considered. Three cases of fuel addition were considered for each fuel, i.e. stoichiometric amounts of fuel and cerium nitrate, and fuel rich and fuel deficient amounts. The different amounts added are shown in Table 5.II and the thermogravimetric analysis graphs are shown in Figure 5.16.

Alanine:

$$Ce(NO_3)_3 \cdot 6H_2O + CH_3CH(NH_2)COOH + \frac{1}{4}O_2 \rightarrow CeO_2 + 2N_2 + 3CO_2 + \frac{19}{2}H_2O$$

Glycine:

$$Ce(NO_3)_3 \cdot 6H_2O + \frac{15}{9}NH_2CH_2COOH + \frac{1}{4}O_2 \rightarrow CeO_2 + \frac{7}{3}N_2 + \frac{10}{3}CO_2 + \frac{61}{6}H_2O$$

Thermogravimetric analyses (Figure 5.16) indicated that alanine and glycine effectively decrease the temperature at which $CeO_2$ is formed (by ~200 °C). In both cases the most favorable fuel addition is the stoichiometric amount since the reaction temperature is the lowest. The combustion of the fuel releases sufficient energy to promote the calcination of cerium nitrate hexahydrate. The complete description of this study can be found elsewhere [5]. Alanine promoted a lower $CeO_2$ formation due to its higher combustion energy (18,000 J/g and 13,000 J/g for alanine and glycine, respectively).

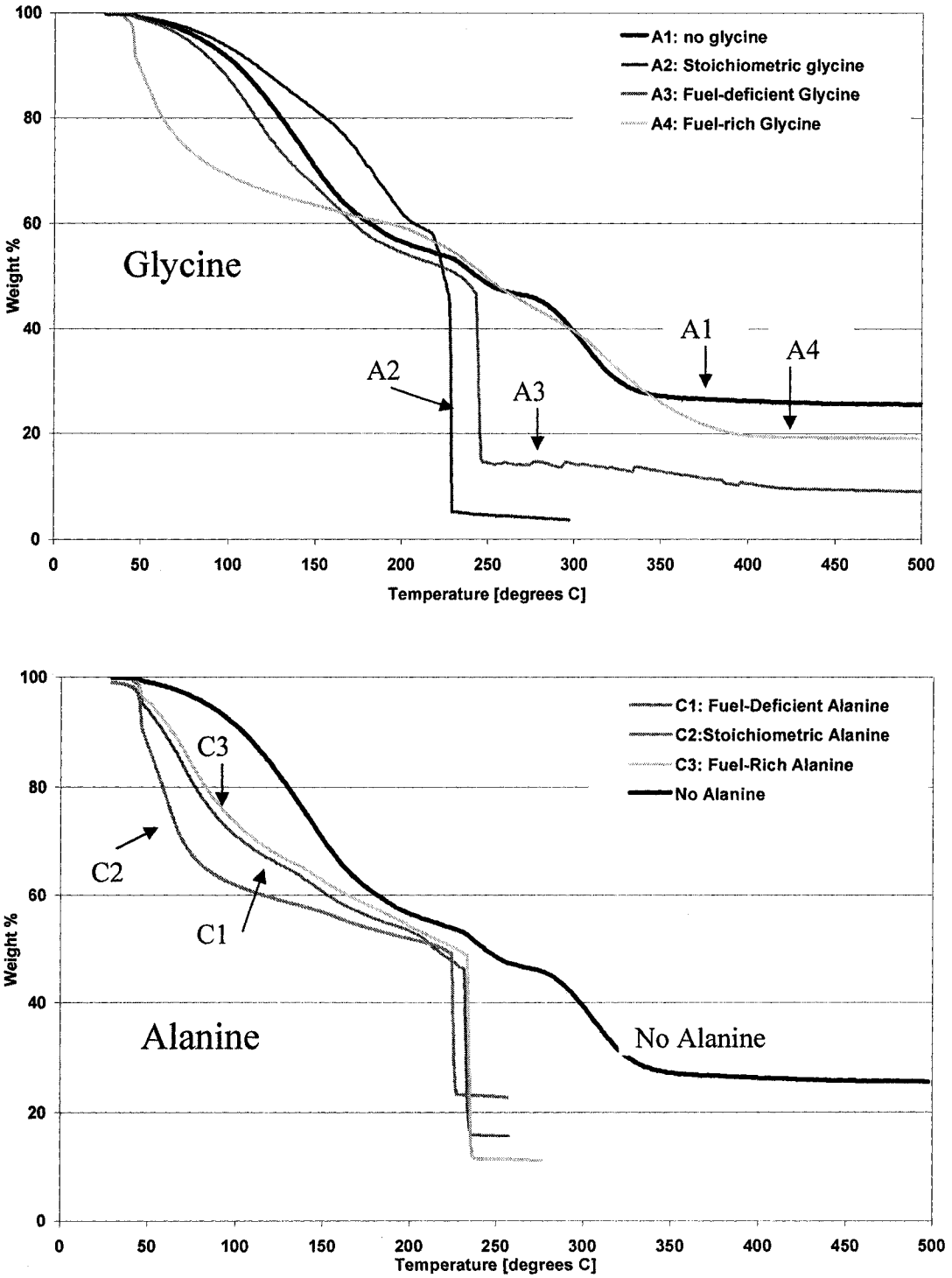


**Fig. 5. 16 TGA results of $Ce(NO_3)_3.6H_2O$ solutions (10°C/min)**

### 5.3.3.2 Effect of glycine and alanine injection in plasma systems

All the analyses in section 5.3.3 were **carried out using the sampling probe and the particles collected from the wet collection system.** Two samples when fuel was added were taken at Z=30 cm (35 kW) and analyzed. The results are shown in Figure 5.17 for the particle size and Figure 5.18 for the SEM images.

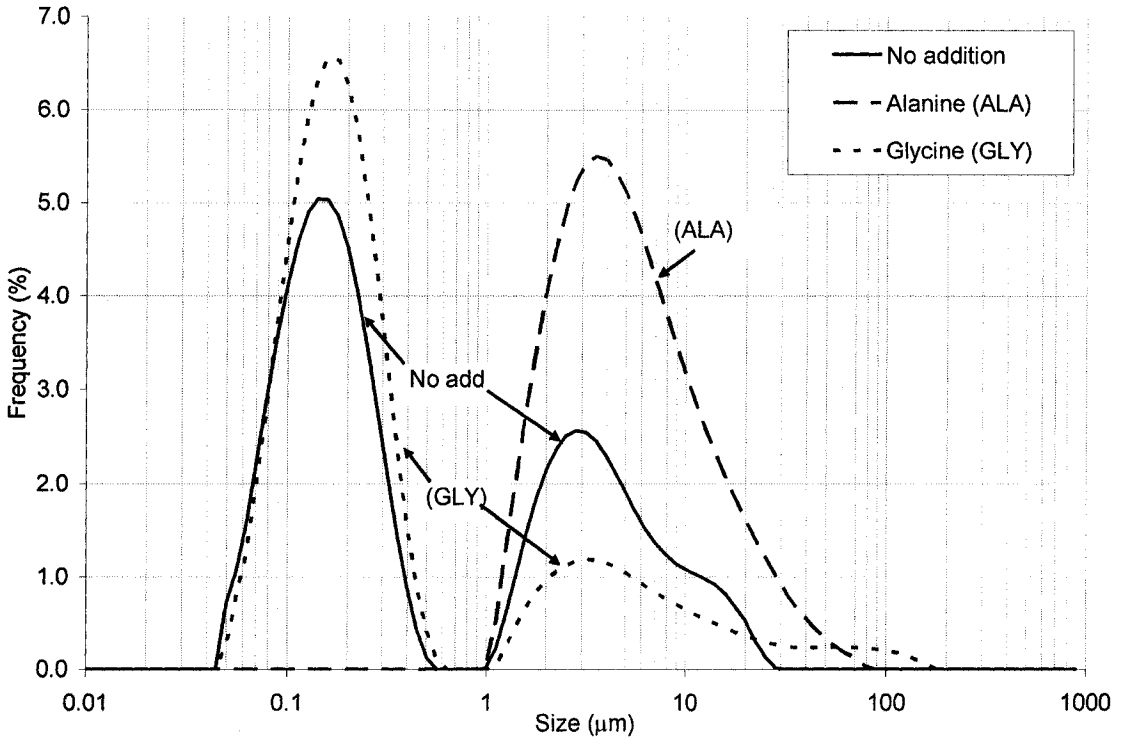


**Fig. 5. 17 Particle size distribution of samples collected at P=35 kW at Z=30 cm values @ $C_{(Ar)}/S_{(O2)}/A_{(Ar)}$=20/100/5 slpm**

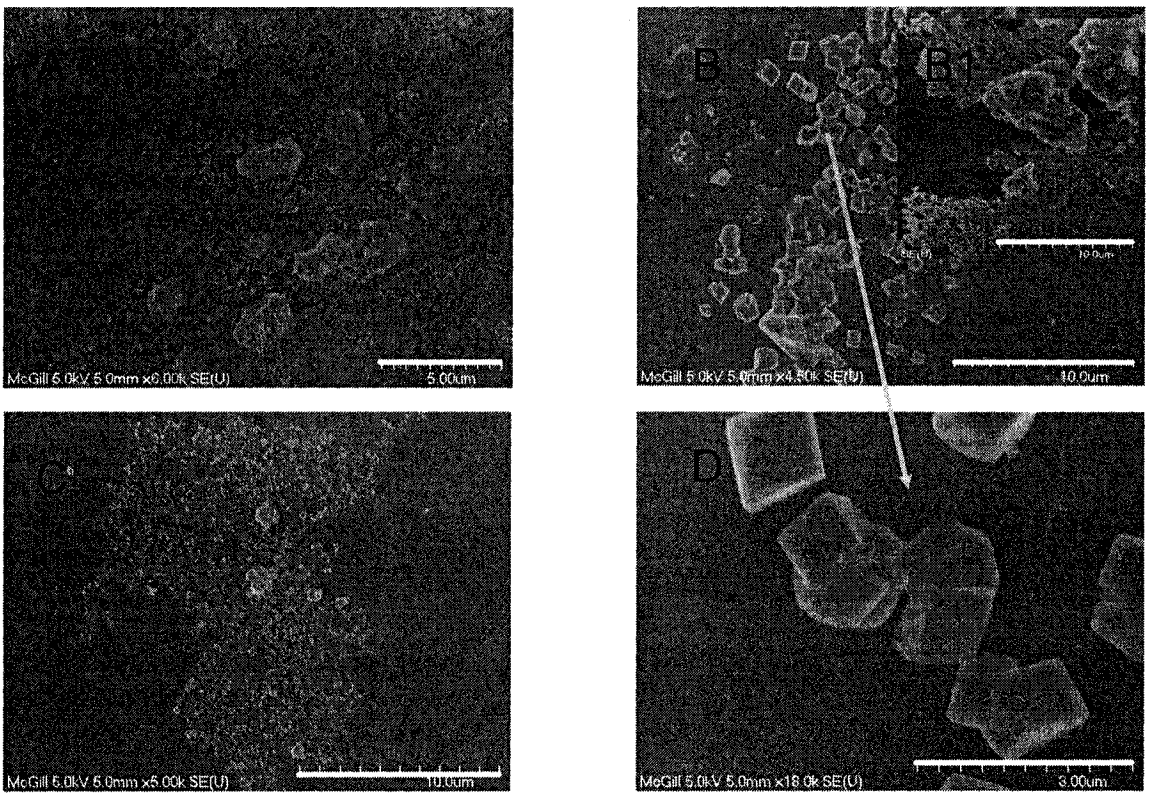


**Fig. 5. 18 SEM micrographs of samples collected at P=35 kW and Z=30 cm A) No fuel addition B) Alanine addition, C) Glycine addition, D) Enlarge image of alanine addition @ $C_{(Ar)}/S_{(O2)}/A_{(Ar)}$=20/100/5 slpm**

Fuel addition significantly increases the amount of larger particles in the 1 to 20 μm range as compared to no fuel. Further, no detectable amount of intermediate (50 to 300 nm) particles was present when alanine was added but particles in this range were present with glycine addition. The SEM images when alanine was added (Fig. 5.18B and 5.18D) show that particle sizes in the 1 to 10 μm were present in the form of large crystal-fluorite like structures, sintered in some cases. Also, some large fragments (11-12 μm) were observed (Fig. 5.18-B1). For the case of glycine (Fig. 5.18C), 2 μm fragments and particles in the 50 to 300 nm range were observed. This image is not very different from what it is observed without fuel addition (Fig. 5.18A), which was confirmed when comparing their particle size distributions (Fig. 5.17).

Two more samples were taken at the same location (Z=40 cm centerline) at the same plate power of 35 kW and their size distributions were compared to the distribution when

no fuel was added (Figure 5.19). Also SEM micrographs were taken of these samples (Figure 5.20).

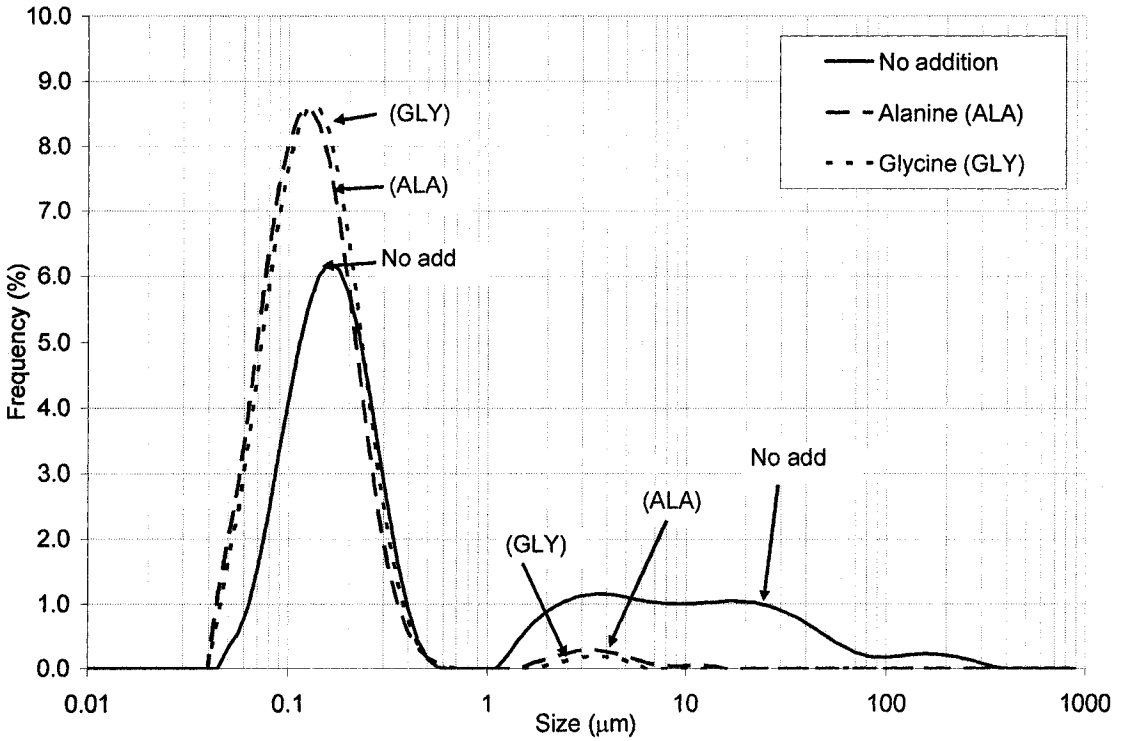


**Fig. 5. 19 Particle size distribution of samples collected at P=35 kW at Z=40 cm values @ $C_{(Ar)}/S_{(O2)}/A_{(Ar)}$=20/100/5 slpm**

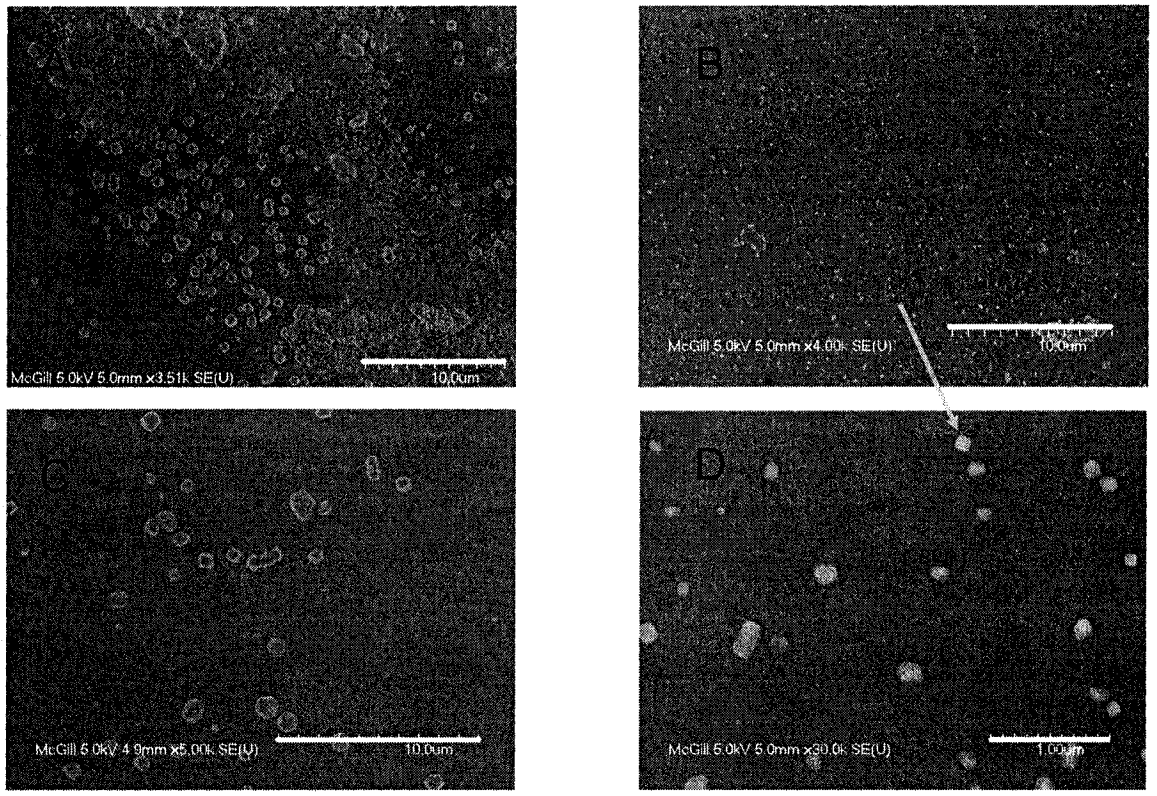


**Fig. 5. 20 SEM micrographs of samples collected at P=35 kW and Z=40 cm A) No fuel addition B) Alanine addition, C) Glycine addition D) Enlarge image of alanine addition @ $C_{(Ar)}/S_{(O2)}/A_{(Ar)}$=20/100/5 slpm**

Figure 5.19 shows that adding alanine or glycine formed a significantly higher amount of intermediate particles (50 to 300 nm) and decreased the amount of large micron particles (>10 μm) at Z=40. These results were confirmed by examining the SEM images of alanine (Fig. 5.20B and 5.20D) and glycine (Fig. 5.20C) and comparing them to Fig. 5.20A where no fuel was added. The particle size present when fuel was added is primarily in the 50 to 300 nm range. Very few particle fragments could be detected in the particle size distribution results and they were not observed in the SEM images (Fig. 5.20B, C and D).

Finally, two samples were taken at P=25 kW and Z=40 cm when alanine and glycine solutions were injected. Their size distributions are shown in Figure 5.21.

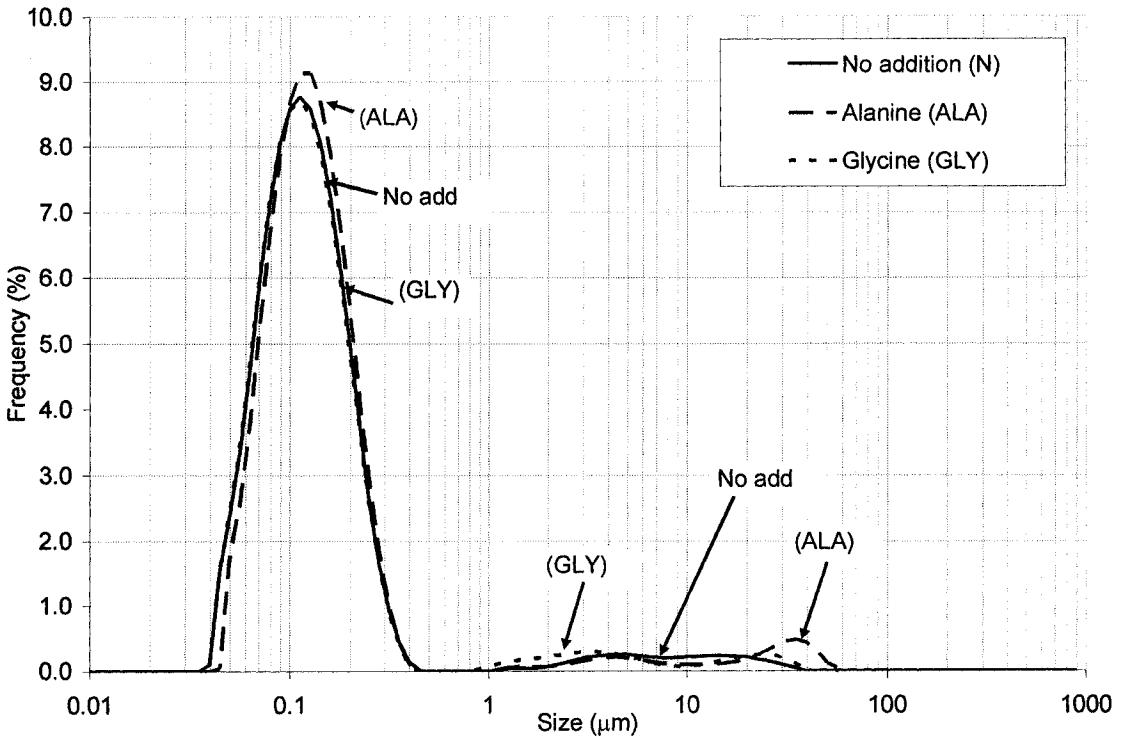


**Fig. 5. 21 Particle size distribution of samples collected at P=25 kW at Z=40 cm values @ $C_{(Ar)}/S_{(O2)}/A_{(Ar)}$=20/100/5 slpm**

There is no apparent effect of adding alanine or glycine to the solutions as their size distributions are quite similar when compared to a sample collected from the same location and the same plasma operating conditions.

It can be concluded that adding fuel significantly increases the local heat available which in turns promotes droplet vaporization and favors more violent crust shattering. Crust shattering is enhanced when fuel is added as $N_2$ and $CO_2$ are released from fuel combustion. These two gases add to the increase of the droplet pressure inside the crust, which is the driving force for crust shattering. The evidence presented in this section also suggests that more large fragments at Z-distances closer to the torch exit (Z=30 cm) were formed when either fuel was added. From previous discussion in this paper, large crusts are formed when gas temperatures are higher. Higher temperatures are expected as a result of fuel combustion, therefore, it is expected that adding alanine produce more of the large fragments because of its higher combustion energy. Glycine also produced more

large crust fragments than when no fuel was added. The most interesting result is that enhanced droplet explosion by fuel addition also causes **"particle size discrimination".** The radial momentum gained by the large particles (> 5μm) forces them to impact the top conical walls of the reactor. As a result, few of these particles are present downstream at Z=40 cm and thus a uniform particle size distribution in the 50 to 300 nm range (Fig. 5.19) is observed when fuels are added at 35 kW.

In summary, fuel addition produces a more uniform particle size distribution as a result of higher plasma gas temperatures which promotes particle sintering and growth of particles by vapor deposition on particle surfaces. Particles larger than 10 μm were rarely found along the centerline of the reactor at locations further than Z=30 cm.

### *5.3.4 Particle velocity based on image analysis*

Photographs of the particles in-flight were taken using a high speed CCD camera. The photographs were taken with the intention of validating the gas velocities calculated in Chapter 4 of this study. Particles in the 30 nm and 0.5 μm (the majority of the particles) are expected to follow closely the gas streamlines, therefore by estimating the particle velocity, the gas velocity can also be known. Also, evidence of droplet explosion can be obtained by comparing the velocities of different particle sizes, as large crust fragments are expected to have different velocities than the bulk of the particles, since they do not follow the gas streamlines. However, the **photographs taken did not provide sufficient evidence to track individual particle velocities but rather particle-cloud speeds,** except in the case of large particles (>10 μm) where velocities can be calculated. The distinction between velocity and speed is necessary because velocity implies direction and magnitude whereas speed has only magnitude.

#### 5.3.4.1 Description

A high speed CCD camera (DI-CAM PRO 2004 from Optikon) with a telescopic zoom (Navitar 1-6265/162922) was used to photograph the particles in the plasma gas at two different reactor locations along the z-axis. The locations were 4.5 cm (upper view port) and 9.5 cm (lower view port) away from the exit of the torch nozzle. The camera was operated in double shutter mode, meaning that each photograph consisted of 2 exposures,

A and B, and a known time delay between exposures. The exposure time was 100 ns per shot with a delay of 10 μs between shots. Typical pictures are shown in Fig 5.22 A and B for the upper view port and Fig 5.22 C and D for the lower view port. Small clouds of particles are shown in all pictures. Also, a large particle is shown Fig. 5.22 C and D; these large particles were rarely seen.

Photographs were taken during the first 2.5 min after beginning solution injection. This was repeated three different times for the upper view port and three more times for the lower view port for a total of 6 independent sets of approximately 60 photographs (120 exposures, 60A + 60B) per set. The plasma operating conditions and injection parameters were kept constant at P=35kW, $C_{(Ar)}/S_{(O2)}/A_{(Ar)}$=20/100/5 slpm (Table 5.I # 2) in all cases. Finally, the best 13 photographs based on clarity, contrast and brightness of each set were selected, i.e. 39 for each of the view ports. The selected images were analyzed as follows to determine particle speed.

#### 5.3.4.2 Methodology

Overview

The methodology consists of three separated steps. First, each photograph was converted into a binary image, i.e. black and white photo. The white regions were particles and black regions were background. A suitable threshold was determined based solely on the information of a given photograph. The threshold was responsible for separating particles from background noise. The second step consisted of segmenting the binary image into smaller regions and calculating the particle density per region, i.e. the number of individual particles in a given region. The regions where particle densities were highest (90%) were then further analyzed. In the final step, the regions of higher particle densities between exposure A and B were compared. Knowing the average locations of these regions and the delay time between exposures, a mean particle cloud speed was calculated. In summary, this technique tracks particle clouds where the number of individual particles per area is the highest between two exposures.

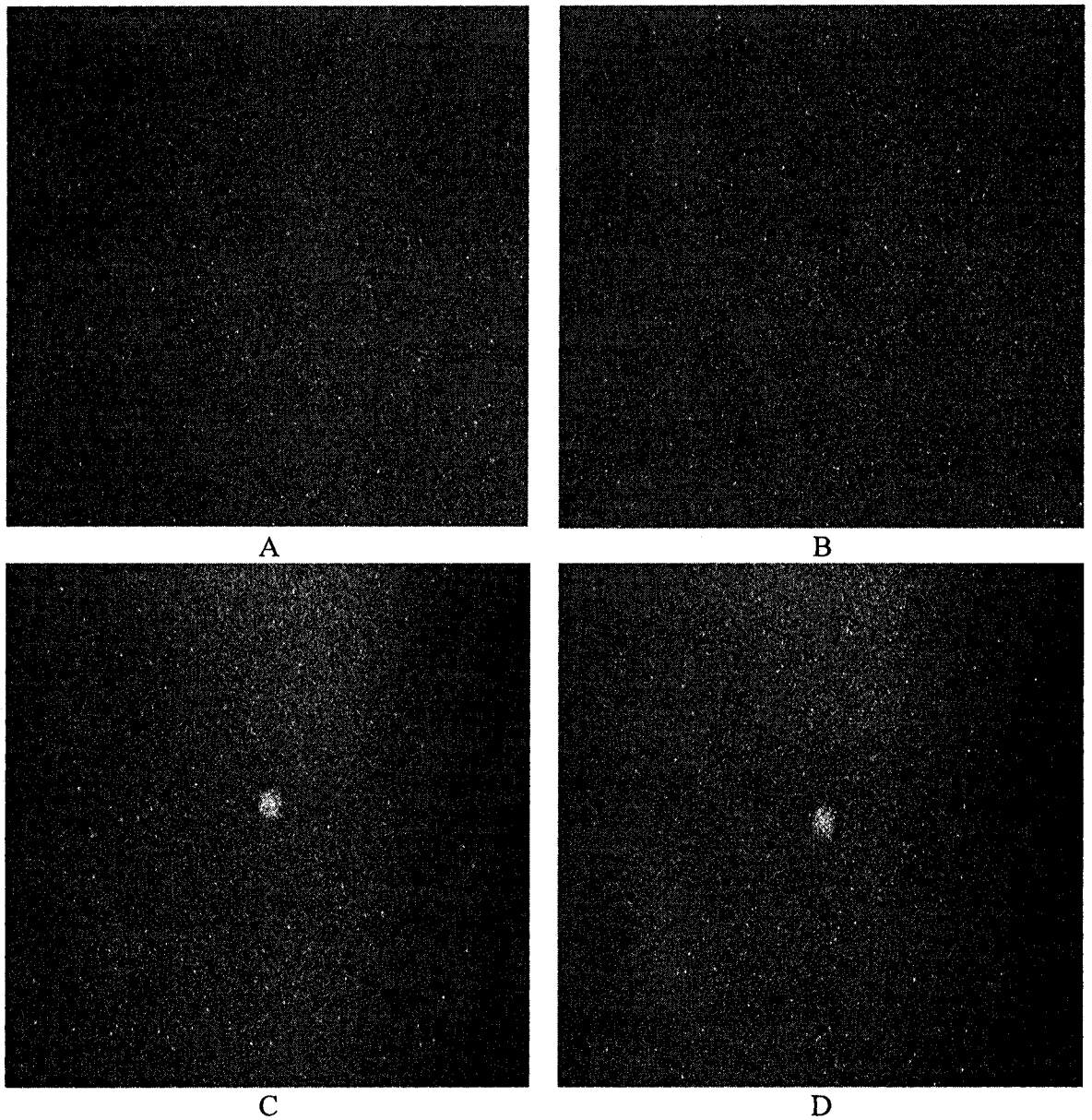


**Fig. 5. 22 Clouds of particles in upper view port A) 100 ns exposure time and B) 100 ns exposure time and in lower view port C) 100 ns exposure time and D) 100 ns exposure time, 10 μs delay Table 1 # 2 @ P=35kW, $C_{(Ar)}/S_{(O2)}/A_{(Ar)}$=20/100/5 slpm**

First step

A suitable threshold was calculated using Otsu's multi-thresholding method[6]. The higher threshold value of the double threshold method was preferred over the threshold value from single thresholding because a single threshold could not adequately discriminate

small particles from the background. After thresholding, a binary image was obtained where particles were observed as white connected regions on a black background. The particles were then labeled and counted by identifying their connected white pixels. Fig 5.23 shows both the original and the final processed image for the 2 exposures A and B.

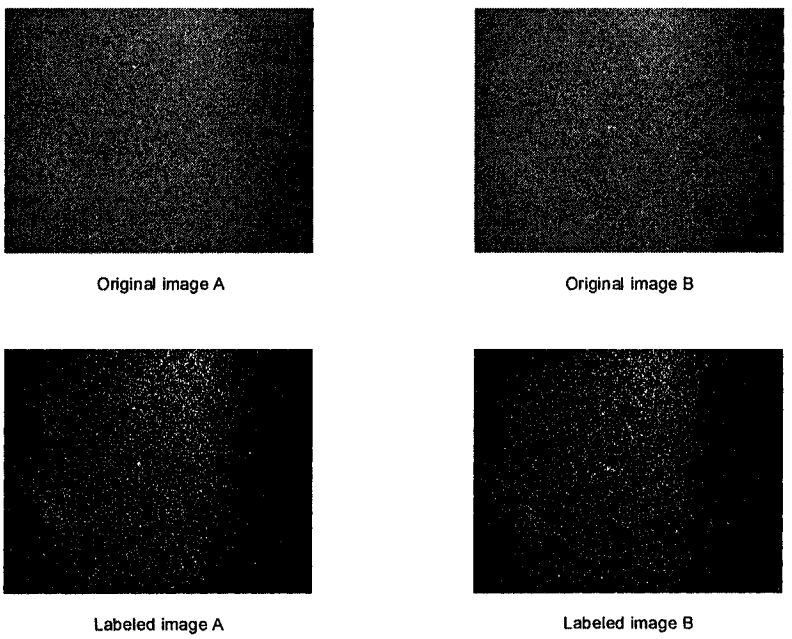


**Fig. 5. 23 Lower view port 100 ns exposure time Original and processed(labeled) images for exposures A and B, 10 μs delay. Table 1 # 2 @ P=35kW, $C_{(Ar)}/S_{(O2)}/A_{(Ar)}$=20/100/5 slpm**

Second step

The processed image was segmented into 40 by 32 pixel segments and the number of particles in each segment was computed. The optimal size of the segments was found to be 40 by 32 pixels. Larger segments would include too many particles per segment which would decrease the spatial resolution of this technique. Smaller segments will increase spatial resolution but would not include a sufficiently representative number of particles to differentiate between neighboring segments. The aim of this technique was to determine the segments where particle concentration was highest and track them from exposure A to B for a given photograph. All segments containing 90% or more of the maximum particle concentration per segment were tracked. A typical result is illustrated

in Figure 5.24 (from the photographs shown in Figure 5.23) where the crosses represent the center position of the segments with high particle concentration in exposure A. Likewise, the circles are the high particle concentration segments in exposure B.

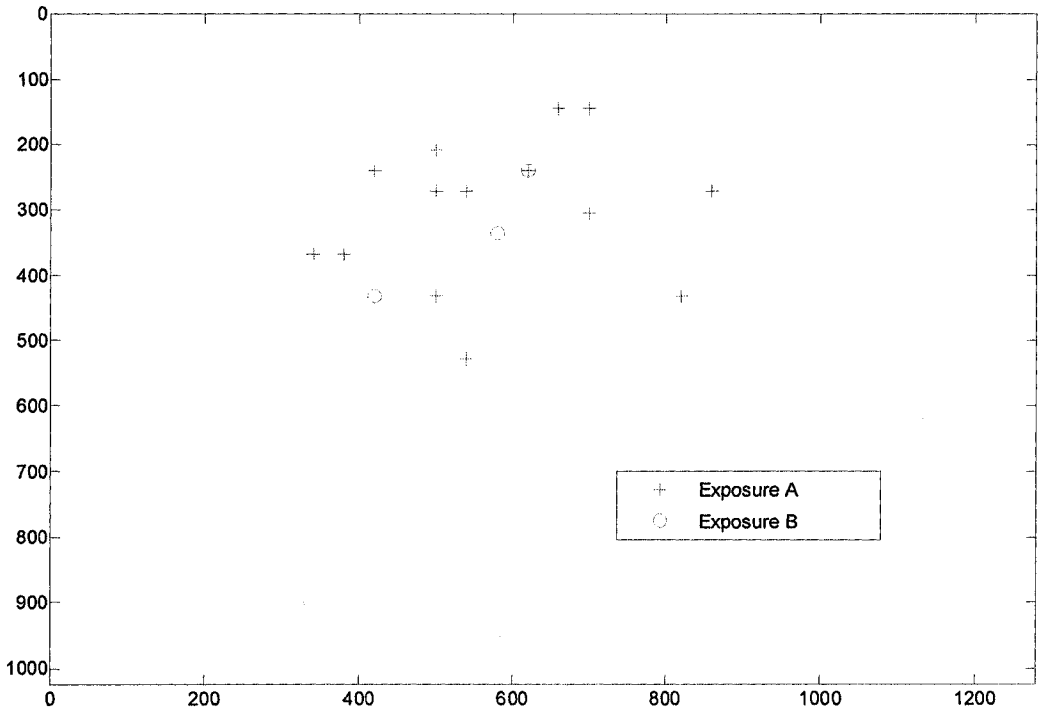


**Fig. 5. 24 Mapping of segments showing >90% of the highest particle concentration per segment for exposure A (crosses) and B (circles) (Data calculated from the photographs shown in Figure 23).**

Third step

Mean speed values can be calculated by comparing the coordinates of neighboring crosses and circles and knowing the delay time between those 2 exposures (10 μs). The particle speed in m/s can be obtained by converting the computed pixel per second. In our study, we estimated that 1 pixel is 11.7 μm by taking photographs of objects of known dimensions using the same camera and optical settings. It is important to note that this technique assumes that cloud of particles "move" only if they appear in adjacent regions from exposure A and B, i.e. out of the 40 by 32 pixel region. This indicates that the minimum detectable speed is ~37 m/s. This detectable speed can be reduced to 18 m/s if the chosen segment size is decreased from 40 by 32 pixels to 20 by 16 pixels, but the amount of particles per segment significantly decreases to unreliable levels. The particles

that are below the detectable limit were grouped in the lowest bracket in Figure 5.25. Apart from this drawback, the technique can be readily automated for large number of photographs which provides a solid statistical support to its results.

### 5.3.4.3 Results

The distribution of particle velocities obtained using this technique is shown in Figure 5.25 for the upper and lower window. Particles analyzed with this technique have an estimated particle diameter of 4-6 μm and are expected to follow very closely the plasma gas velocities previously shown in Chapter 4 of this study (20 to 50 m/s). The velocity of particles larger than 20 μm was simply calculated by comparing the coordinates of the center of the particles from exposure A to B as they could be clearly seen in the CCD photographs without image processing.

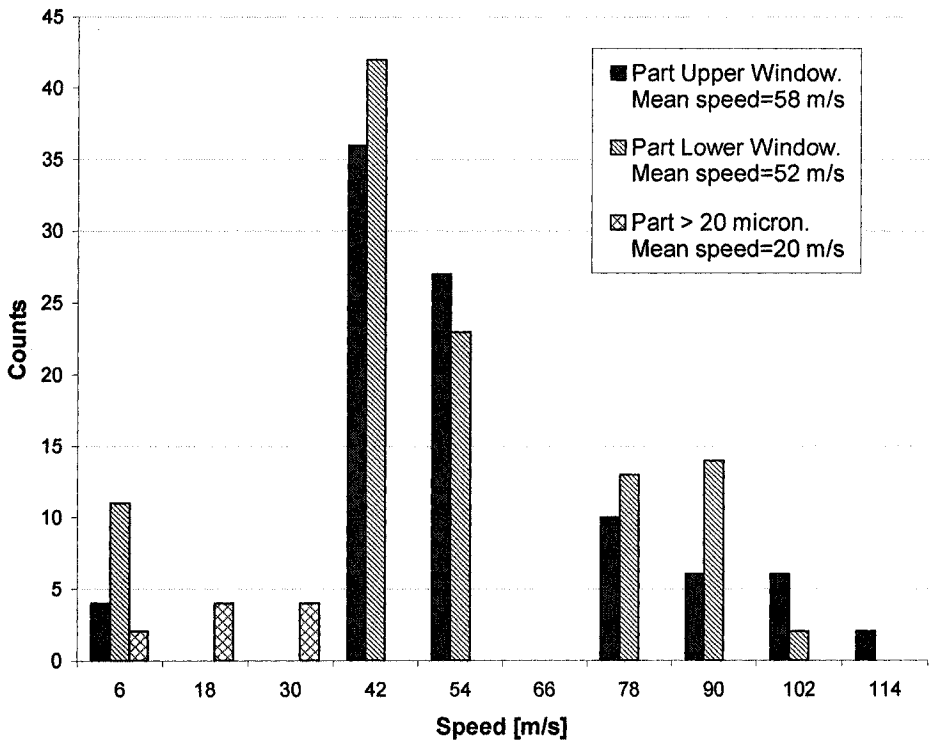


**Fig. 5. 25 Mean speed values of particles at different view ports locations, Table 1 # 2 @ P=35kW, $C_{(Ar)}/S_{(O2)}/A_{(Ar)}$=20/100/5 slpm**

It is observed that particles photographed at the upper window have faster velocities (10 m/s) than those photographed at the lower window. Also, it is observed that particles

larger than 20 μm have much slower velocities (20 m/s) than the bulk of the particles which suggest that they do not follow the gas stream lines. This provides supporting evidence for crust explosion because the resulting crust fragments will tend to move in radial downward with smaller momentum and do not follow the direction of the gas flow. However, the results for particles larger than 20 μm are limited to a few particles. In general the results obtained from analyzing the photographs are 10-15 m/s faster than those estimated from the modeling of the velocity and temperature fields in the reactor (Chapter 4 of this study).

## 5.4 Conclusions

The particle size distribution in the reactor is determined by a combination of several factors that can be grouped into 2 categories: 1) the different droplet-to-particle formation steps involved such as: crust formation, droplet explosion, particle sintering, homogeneous particle nucleation, vapor deposition of particle surface and particle cooling 2) the various particle collection mechanisms such as: particle impaction, turbulent diffusion and thermophoresis. From the first category, crust formation and droplet explosion seemed to have the greater effect and from the second factor, particle impaction and thermophoresis are dominant. Droplet explosion favored the radial movement of large fragments as those particles did not follow the gas streamlines and were mostly deposited on the top conical part of the reactor. Intermediate particles followed 2 main paths: 1) they formed particles in the 50 nm to 0.5 μm 2) the original 50 nm to 0.5 μm grew to 1 to 2 μm by vapor deposition and/or particle sintering depending on their residence time on the reactor. A rapid quenching favored spherical particles whereas a slow quenching favored cubical (fluorite) structures. The nanoparticles (< 50 nm) were formed by nucleation and growth from cerium oxide vapor.

In terms of the effect of plasma operating parameters and sampling location on particle size distribution the following conclusions can be drawn: Increasing the plasma gas temperature favors larger fragmented-crust particles ( > 5 μm). The plasma gas temperature can be increased both by increasing the plate power at a constant gas flow rate and by decreasing the amount of gas while keeping the plate power constant. Particle

size distribution along the axial direction varies depending on reactor location and plasma parameters. Larger crust fragments are formed closer to the reactor inlet. Radial distribution, at locations closer to the torch exit $0 < Z < 30$ cm, shows that centerline and 2.5 cm off centerline locations have similar particle size distributions. This is not true at off centerline locations when Z=40 cm. Increasing the particle residence time promoted particle sintering and more spherical-like particles along the reactor centerline.

Finally, adding glycine and alanine at plate powers lower at 25 kW did not have a significant effect on the size distribution. At higher powers (35 kW) the energy released from the autocombustion reaction of the fuel formed larger particles at Z=30 cm but more homogeneous particle distributions at Z=40 cm (50 nm to 2 μm particles) were observed. This happened because the droplet explosion was more violent at higher powers; as a result, large fragments are forced out radially and impact the top conical section of the reactor. The remaining particles sintered and the cerium oxide gas either deposited on the surface of the sintered particles causing particle growth or nucleated into nanoparticles. Fuel addition effectively removed most of the particles larger than 10 μm forming a narrow particle size distribution between 50 to 2 μm at Z=40 cm along the centerline of the reactor.

An image analysis technique was developed to track particle clouds where the number of individual particles per area is the highest between two photographs. The photographs were taken using a high speed CCD camera. It was concluded that particles photographed closer to the reactor inlet have faster velocities (~10 m/s). Also, particles larger than 20 μm have much slower velocities than the bulk of the particles which suggest that they do not follow the gas stream lines.

## 5.5 Acknowledgments

The authors thank the financial support by the Natural Sciences and Engineering Research Council of Canada and the Ministry of Education of the Province of Quebec through its FQRNT program.

## 5.6 References


1. Castillo, I. and Munz, R., International. Journal of Heat and Mass Transfer., 50(1-2), 240-256 (2007)
2. Castillo, I. and Munz, R., Inter. J. Heat Mass Transf., (in print)
3. Chung, D.Y., Lee, E.H. Journal of Alloys and Compounds. 374(1-2), 69-73 (2004)
4. Desroches, M., Castillo, I., and Munz, R. Particle systems and particle characterization, 22(5), 310-319 (2006)
5. Castillo, I. and Munz, R. Proceedings of the ISPC 17, Toronto, (2005)
6. Otsu, N., A Threshold selection method from gray-level histograms, IEEE Transactions on Systems, Man and Cybernetics, 9(1), 1979

# Chapter 6 Transient heat, mass and momentum transfer of an evaporating stationary droplet containing dissolved cerium nitrate in a rf thermal argon-oxygen plasma under reduced pressure

In this chapter the first part of the modeling results is presented. The first part of the modeling consisted of studying the phenomena affecting droplet evaporation until the point of crust formation. **The results presented in Chapters 6 and 7 correspond to Stages I and II described in Chapter 4 and 5, section 4.3.7 and 5.3.1, respectively.** In this chapter, the following is discussed:

## Abstract

Heat and mass transfer effects in evaporating solution droplets (20-40 μm in diameter) containing dissolved hexahydrated cerium nitrate in a stationary rf Ar-$O_2$ thermal plasma were investigated using a model. The evaporation occurred under reduced pressure. The impact of different plasma operating parameters on temperature and dissolved solid content profiles was studied: surrounding plasma temperature, initial salt content and droplet size, plasma gas composition, and system pressure. Temperature and composition dependant thermophysical properties were used. The model was solved in a moving frame (ALE method) and considered Stefan flow. The results indicate that a salt saturation limit is reached at the droplet surface which leads to salt precipitation and formation of a crust in all cases analyzed. This is favored by higher plasma temperatures, lower pressures, oxygen-rich plasma and higher salt content. Smaller droplets developed a crust faster than larger droplets.

## Nomenclature

C convective velocity (relative velocity between the material V and mesh velocity Ψ), [m/s]

$C_i$ concentration of electrolyte *i*, [mol/L]

$C_s$ concentration of salt at the droplet surface

$C_m$ mean concentration of salt in the droplet

Cp heat capacity, [J/kg.K]

$D_{12}$ diffusion coefficient based on molecular concentration [$m^2/s$]

d droplet diameter [μm]

F Faraday constant

h enthalpy, [J/kg]

K evaporation constant, [$m^2/s$]

$K_p$ partition coefficient

k thermal conductivity, [W/mK]

m molality of the solute, [mol/kg solvent]

$\dot{m}$ mass flow rate at the droplet surface due to vaporization, [$kg/m^2s$]

M molecular weight, [kg/kgmol]

$M_{av}$ average gas molecular weight, [kg/kgmol]

P pressure, [Pa]

Q source/sink term, [$J/m^3s$]

r radial distance, [m]

$R_{(t)}$ radius of the droplet (function of time), [m]

$R_g$ universal gas constant

$\dot{R}$ change of droplet radius with respect to time, [m/s]

T temperature, [K]

$T_d$ dimensionless temperature

t time, [s]

$T_r$ reference temperature, [K]

V radial material velocity, [m/s]

$W_i$ mass fraction of *i* in liquid

$x_i$ mol fraction of *i* in liquid

$Y_i$ mass fraction of *i* in gas

$z_i$ mol fraction of *i* in gas

Greek letters

$\gamma_{\pm}$ mean ionic activity coefficient of the solute

$\lambda^{\circ}_{+},\lambda^{\circ}_{-}$ limiting (zero concentration) ionic conductances, [$(A/cm^2)(V/cm)(mol/cm^3)$]

$\mu$ plasma gas viscosity, [kg/m.s]

$\mu_l$ water viscosity in the droplet, [kg/m.s]

$\rho$ density, [$kg/m^3$]

$\sigma_i$ coefficient characteristic of each ion

$\upsilon_{+},\upsilon_{-}$ valences of cation and anion, respectively

$\Psi$ mesh velocity, [m/s]

Subscripts

1 component 1 (either in the solution or the gas phase)

2 component 2 (either in the solution or the gas phase)

ar argon

d dimensionless

G plasma gas phase

L solution droplet phase

o initial value

ox oxygen

s anhydrous salt

w water

$\chi$ referential domain or moving mesh

$\infty$ conditions at infinity (far away from the droplet)

Superscripts

s saturated condition

## Keywords

Evaporation, solution droplets, ALE, thermal plasma, solid oxide fuel cells

## 6.1 Introduction

The manufacturing of ceramic powders from liquid precursors using radio frequency (rf) thermal plasmas has been developed in the past 10 years [1-5]. This technique consists of the evaporation and calcination of atomized solution or suspension droplets injected axially to the plasma core. In this paper only the case of solution droplets was investigated. Most of these processes are operated under reduced pressure and the droplets usually contain a non-volatile salt (nitrates, acetates, chlorides, etc) dissolved in water or any other suitable solvent. The hot plasma environment provides the driving force for evaporation and calcination of the salt, resulting in the production of high-purity oxide particles. Thus, oxygen-rich plasmas are often employed. The use of liquid precursors encompasses applications such as production of ceramic materials for SOFC (solid oxide fuel cells) (perovskites, $Y_2O_3$, $CeO_2$, NiO, etc) [6] and thermal barrier coatings ($ZrO_2$) [7].

One of the main advantages of rf thermal plasma over other processing techniques is the ability to achieve a uniform chemical composition in the synthesized particles in a clean electrode-free environment. It has been shown that the stoichiometry of these powders can be controlled accurately even when doped oxide particles are synthesized [8]. However, the resulting particles varied greatly in size from few nanometers to micron size, suggesting that more than one droplet-to-particle conversion mechanism was possible. Few attempts have been conducted to understand this large size variation by sampling particles in-flight [9], largely due to the high plasma temperatures and the inaccessibility of sampling in the plasma core. Therefore, studying the droplet-to-particle conversion in rf thermal plasmas through numerical simulation seems to be a logical alternative.

Droplets are injected into the plasma core by means of a liquid blast atomizer that provides a log-normal droplet size distribution centered around 20-30 μm in diameter. This process is similar to the well known spray pyrolysis technique [10], but the operating temperatures are higher, the droplets are often in the low micro size range (< 50 μm) and the reactor chamber is operated under vacuum. As a result, the thermal plasma treatment

is a more "rapid" version of spray pyrolysis, since the conditions for solvent evaporation are enhanced. Previous theoretical and experimental studies in spray pyrolysis of non-volatile solute droplets have suggested the development of a thin crust surrounding the evaporating droplet. The crust is formed because the non-volatile salt precipitates out of solution, primarily at the droplet surface. A fast evaporation rate removes solvent from the droplet surface more quickly than it can be replenished by mass diffusion, resulting in the formation of a crust [11]. Having a crust around an evaporating liquid core retards the rate at which inner solvent escapes from the droplet [12], because the solvent must travel through a solid phase. This effect leads to an increase of the solvent vapor pressure that causes fracturing and/or bursting of the crust. As a consequence, after calcination takes place, solid particles of different sizes are formed. A recent study by Ozturk [13] has shown that solid and hollow particles of $ZrO_2$ can be produced using thermal plasmas from zirconium acetate depending on the plasma operating conditions. Ozturk's findings provide evidence that a comprehensive model explaining droplet-to-particle conversion is needed.

Evaporating droplets were first studied experimentally and theoretically by Charlesworth and Marshall [11]. They suspended droplets containing various dissolved salts in a hot-air stream and pointed out that mass diffusion in the droplet played a key role in determining the onset of salt precipitation. The work of Schlünder [14] and Gardner [15] demonstrated that the product of the drop radius times its rate of change over time remained constant for most of the evaporation process. More recently, Xiong and Kodas [16] investigated the spray pyrolysis of sodium chloride solution drops in air. In this comprehensive study small micron size droplets [1-10 μm] were examined. It was reported that the point of solute nucleation was relatively independent of processing parameters, except solution concentration and initial droplet size. Their findings were based on the evaporation of droplets in air at atmospheric pressure. The change in droplet diameter was not rigorously calculated from the solution of the heat and mass transfer between the drop and the surrounding media. A more formal treatment of the solution of the mass and heat transport equations of these phenomena was conducted by Javanthi *et al* [17]. It was found that droplet shrinkage and solute diffusion were the rate limiting processes, because

their characteristic time constants were larger than those of heat conduction inside and outside the droplet and vapor diffusion outside the droplet. However, bulk flow as a result of solvent evaporation was neglected in this study. A rigorous approach of droplet evaporation was reported by Elperin [12] for the case of slurry droplets, but it was assumed that the evaporation stage resembled that of a pure component droplet. Therefore, there is a need for a rigorous treatment of evaporating solutions droplets when heat-mass-momentum transfers are considered. Also the rate of shrinkage of droplets over time must be taken into account.

In this paper, the effect of temperature, pressure, gas composition, initial solid content and initial droplet size were examined on evaporating solution droplets under thermal plasma conditions. The droplets contained a hexahydrated salt, $Ce(NO_3)_3.6H_2O$, dissolved in water and the mass and thermal history inside the droplet were studied. The hexahydrated cerium nitrate salt was used as a precursor to obtain $CeO_2$, which is used as electrolyte material in SOFCs. The onset of salt precipitation was predicted as a function of different parameters. The droplet was allowed to decrease in size as water was continuously being evaporating. The purpose of this study is to derive understanding of how plasma conditions affect droplet morphology and to predict the onset of crust formation under typical rf thermal plasma operating conditions.

## 6.2 Model development

The physical model studied was the transient evaporation of a solution droplet of approximately 30 μm in diameter immersed in a mixture of stagnant argon-oxygen rf plasma. The solution droplet was a hexahydrated salt, $Ce(NO_3)_3.6H_2O$, dissolved in water. The dissolved salt released all water of hydration and thus the total water content in the droplet was a combination of water of hydration and water already present in the solution. The anhydrous salt was considered to remain largely in molecular form (i.e. as $Ce(NO_3)_3$), since the solution droplet possessed a large salt content, but whenever possible the properties were calculated assuming dissociation of the nitrate and the cerium ions.

Radiation and second order effects, such as Soret and Dufor effects, were assumed to be negligible, but Stefan flow was taken into account. This flow is representative of the diffusional transport of energy. The droplet was considered to be suddenly immersed in a stagnant plasma gas and it reduced in size as water evaporated but remained spherical. Plasma gas absorption on the surface was neglected based on the low system pressures. Spherical symmetry reduced the problem to a transient, two phase process of one dimensional nature. The only fluid motion present was a radial flow field in the gas phase induced by water vaporization. Radial flow inside the droplet was neglected on the basis of the large density difference between the solution droplet and the gas. Viscous dissipation effects were neglected. Water evaporation occurred at the droplet-gas interphase and both gas and liquid phases are treated as ideal phases. The Kelvin effect due to droplet curvature on the equilibrium vapor pressure was negligible since the size of the droplet is larger than 1 μm. Finally, the surrounding gas obeyed the ideal gas law. All the model results were calculated using variable thermophysical properties, except when the comparison between variable and constant properties was made.

Under these conditions the physics of the problem were as follows (Fig. 6.1): solvent (i.e. water) evaporates from the solution droplet which causes droplet shrinkage, the remaining salt diffuses toward the centre of the droplet and a temperature profile is developed in the droplet. The solvent vapors mix with the surrounding gas as a result of bulk flow and diffusion. A temperature profile also develops in the gas phase. This process occurs until the surface of the droplet reaches the saturation limit of the solution and salt precipitates out as small solid "clusters". At this point the most widely accepted theory is that continuing solvent evaporation increases the number of precipitated clusters and favors cluster agglomeration as the droplet reduces in size. This results in the formation of a porous and thin crust at the droplet surface (Fig. 6.1, II to III). The droplet surface tension forces [10] keep the solution droplet spherical. It is then hypothesized that the precipitate undergoes thermolysis and the $Ce(NO_3)_3$ salt is transformed into $CeO_2$, followed by sintering. The present study only considered the problem until the saturation point (Fig. 6.1, III) was reached at the surface of the droplet and the later phenomena are the subject of future investigation.

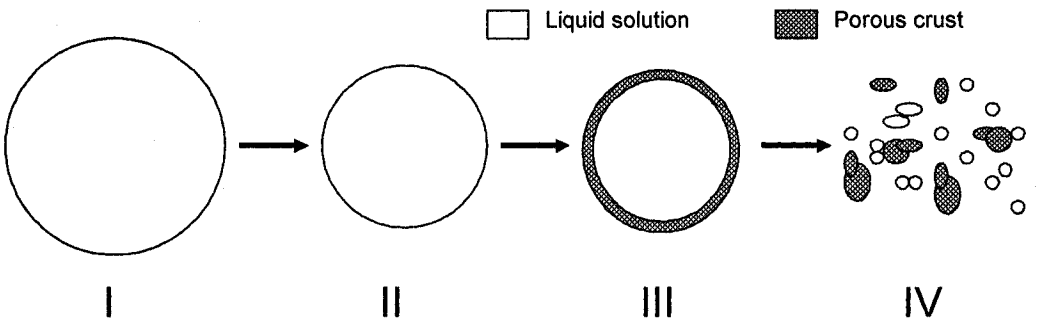


**Fig. 6. 1 Schematic drawing of evaporating droplet history**

This model was solved using the Arbitrary-Lagrangian-Eulerian (ALE) method which has been successfully employed with moving boundary problems [18]. A deformed mesh can be useful when the boundaries of the computational domain are moving in time as a function of a parameter, in this case, the rate of evaporation of the solution droplet. Therefore, a new mesh is not needed to be generated for each configuration of the boundaries; instead the mesh nodes are perturbed so that they conform to the moved boundaries [19]. In doing so, computational time could be saved without losing resolution in the solution.

### *6.2.1 Liquid governing equations*

For the liquid phase, r<R(t), 1) refers to the water and 2) refers to the anhydrous salt (i.e. $Ce(NO_3)_3$). Note that the term containing $h_1$ and $h_2$ in the energy equation for both the liquid and gas phases is representative of the Stefan flow.

species equation

$$\frac{\partial}{\partial t}\left(r^2 \rho_L W_1\right)\Big|_\chi + \frac{\partial}{\partial r}\left(-r^2 \rho_L D_L \frac{\partial W_1}{\partial r}\right) = 0 \qquad (1)$$

energy equation

$$\frac{\partial}{\partial t}\left(r^2 \rho_L C p_L T\right)\Big|_\chi + \frac{\partial}{\partial r}\left(-r^2 k_L \frac{\partial T}{\partial r} - r^2 \rho_L D_L \frac{\partial W_1}{\partial r}(h_1 - h_2)\right) = 0 \qquad (2)$$

### *6.2.2 Gas governing equations*

For the gas phase, r>R(t), 1) refers to the water and 2) refers to the plasma gas argon-oxygen mixture. The convective velocity is defined as $C = V - \psi$

continuity equation

$$r^2 \frac{\partial \rho_G}{\partial t}\bigg|_\chi + \rho_G\left(r^2 \frac{\partial V}{\partial r} + 2rV\right) + r^2 C \frac{\partial \rho_G}{\partial r} = 0 \tag{3}$$

species equation

$$\frac{\partial}{\partial t}\left(r^2 \rho_G Y_1\right)\bigg|_\chi + \frac{\partial}{\partial r}\left(-r^2 \rho_G D_G \frac{\partial Y_1}{\partial r} + r^2 \rho_G Y_1 C\right) = 0 \tag{4}$$

energy equation

$$\frac{\partial}{\partial t}\left(r^2 \rho_G Cp_G T\right)\bigg|_\chi + \frac{\partial}{\partial r}\left(-r^2 k_G \frac{\partial T}{\partial r} - r^2 \rho_G D_G \frac{\partial Y_1}{\partial r}(h_1 - h_2) + r^2 \rho_G Cp_G TC\right) = Q \tag{5}$$

$$Q = -r^2 P\left(\frac{\partial V}{\partial r}\right)$$

momentum equation

$$\frac{\partial}{\partial t}\left(r^2 \rho_G V\right)\bigg|_\chi = \frac{\partial}{\partial r}\left(r^2\left[2\mu \frac{\partial V}{\partial r} - P\right]\right) + r^2\left(F - \rho C \frac{\partial V}{\partial r} - \frac{2(2\mu V/r - P)}{r}\right) \tag{6}$$

$$F = -\frac{\partial}{\partial r}\left(\frac{2}{3}\mu\left(\frac{\partial V}{\partial r}\right)\right)$$

### *6.2.3 Boundary conditions*

At liquid/gas interface

Overall mass

$$\dot{m} = \rho_G\left(V - \dot{R}\right)_G = \rho_L\left(0 - \dot{R}\right)_L \tag{7}$$

Species balance

$$\left(n_{iG} - \dot{R}\rho_G\right)_G = \left(n_{iL} - \dot{R}\rho_L\right)_L ;\ n_{iG} = \rho_G Y_i V - \rho_G D_G \frac{\partial Y_i}{\partial r} ; n_{iL} = -\rho_L D_L \frac{\partial W_i}{\partial r} \tag{8}$$

Energy balance

$$\left(e_G - \dot{R}\sum_{i=1}^{n}\rho_G Y_i h_{iG}\right)_G = \left(e_L - \dot{R}\sum_{i=1}^{n}\rho_L W_i h_{iL}\right)_L ;\ e_G = -k_G\frac{\partial T}{\partial r} + \sum_{i=1}^{n} n_{iG} h_{iG} ;$$

$$e_L = -k_L\frac{\partial T}{\partial r} + \sum_{i=1}^{n} n_{iL} h_{iL} \tag{9}$$

Thermodynamics

$$Pz_i = P_i^s \gamma_i x_i \quad \gamma_i=1 \text{ and } K_p = \frac{P_i^s}{P}; \tag{10}$$

The mol fractions $z_i$ and $x_i$ can be expressed in their corresponding mass fractions $Y_i$ and $W_i$ (considering their respective molecular masses $M_G$, $M_w$,$M_s$). Solving for the mass fraction of water in the gas ($Y_i$) Eq. 10 gives Eq. 11.

$$Y_1 = \left\{\frac{M_G}{M_w K_p}\left(1 + \frac{M_w}{M_s}\left(\frac{1}{W_1} - 1\right) - K_p\right) + 1\right\}^{-1} \tag{11}$$

Temperature

$T_G=T_L$ (12)

Overall mass conservation

$$-\rho_L \dot{R}\Big|_R = \dot{m} + \int_0^{R(t)} \left(\frac{r}{R}\right)^2 \frac{\partial \rho_L}{\partial t} dr \tag{13}$$

At droplet center

$$\frac{\partial W_i}{\partial r} = \frac{\partial T}{\partial r} = 0 \tag{14}$$

At infinity r→ ∞

$$Y_i = 0; \quad T = T_\infty; \quad V = 0; \quad \frac{\partial P}{\partial r} = 0; \tag{15}$$

### *6.2.4 Initial conditions*

In the liquid phase

$$W_i = W_{io} \quad T = T_{Lo} \tag{16}$$

In the gas phase

$$Y_i = 0 \quad T = T_{Go} \quad V = 0 \quad P = Po \tag{17}$$

### *6.2.4 Thermophysical properties*

A more accurate formulation of the problem can be derived taking into account temperature and concentration dependence of the liquid and gas properties (Table 6.I).

**Table 6. I Thermophysical properties**

| Property | Method | Mixing rule |
|---|---|---|
| **Liquid properties** | | |
| Density [kg/m$^3$] | Ideal mixing | $\rho_L=aW_1+bW_2$; a=1,000 b=1,600 [(a)] |
| Specific heat [J/kg.K] | Ideal mixing | $Cp_1=a+bT+cT^2+dT^3$, a=8.958x10$^3$, b=-4.053x10$^1$, c=1.124x10$^{-1}$, d=-1.014x10$^{-4}$ [22] |
| | | $Cp_2$=358.06 [23] |
| | | $Cp_L=Cp_1W_1+Cp_2W_2$ |
| Thermal conductivity [W/m.K] | Riedel for aqueous solutions [24] | $k_{1(Tr)}=a+bT+cT^2$; a=-3.838x10$^{-1}$, b=5.254x10$^{-3}$, c=-6.369x10$^{-6}$ |
| | | $k_{L(Tr)}=k_{1(Tr)}+\Sigma\sigma_iC_i$; $\sigma(NO_3^-)$=-6.978x10$^{-5}$ $\sigma(Ce^{4+})$=-43.61x10$^{-5}$ |
| | | $k_{L(T)}=k_{L(Tr)}*k_{1(T)}/k_{1(Tr)}$ |
| Binary diffusion coefficient [m$^2$/s] | Nerst-Haskell equation and Gordon approach for concentrated solutions [24] | $D^\circ_{12}=R_gT/F^2*(1/\upsilon_+ +1/\upsilon_-)/(1/\lambda^\circ_+ +1/\lambda^\circ_-)/1x10^4$; |
| | | $D_{12(Tr)}=D^\circ_{12}(\eta_s/\eta)(\rho_sV_s)*(1+m\,\partial\ln\gamma_\pm/\partial m)$ [(c)] |
| | | $D_{12(T)}=D_{12(Tr)}(T/T_r)(\mu_{1Tr}/\mu_{1T})$ |
| | | $\partial\ln\gamma_\pm/\partial m$ [25] [(b)] |
| Water viscosity [kg/m.s] | | $M_1=a+bT+cT^2+dT^3$; a=-2.471x10$^1$, b=4.209x10$^3$, c=4.527x10$^{-2}$, d=-3.376x10$^{-5}$ [24] |
| Enthalpy of water [J/kg] | | $h_1=a+bT+cT^2+dT^3$; a=-2.248x10$^6$, b=1.297x10$^4$, c=-2.291x10$^1$, d=1.962x10$^{-2}$ |
| Enthalpy of $Ce(NO_3)_3$ salt [J/kg] | | $H_2=h^\circ_2+Cp_2(T-T_r)$ |

**Gas properties**

| | | |
|---|---|---|
| Density [kg $m^{-3}$] | Ideal gas | $P=PM_{av}/R_gT$ |
| Specific heat [J $kg^{-1}$ $K^{-1}$] | Ideal mixing | $Cp_1=a+bT+cT^2+dT^3+eT^4$, $a=1.652x10^3$, $b=1.295x10^{-1}$, $c=1.850x10^{-3}$, $d=-1.959x10^{-6}$, $e=6.384x10^{-10}$ [26] |
| | | $Cp_{ox}=a+bT+cT^2+dT^3$, $a=8.958x10^3$, $b=-4.053x10^1$, $c=1.124x10^{-1}$, $d=-1.014x10^{-4}$ |
| | | $Cp_{ar}=520.4$ [27] |
| | | $Cp_2=Y_{ar}M_{ar}+Y_{ox}M_{ox}$ |
| | | $Cp_G=Cp_1Y_1+Cp_2M_2$ |
| Thermal conductivity [W $m^{-1}$ $K^{-1}$] | Wassiljewa Eq. with the Mason and Saxena modification [24] | $K_1=a+bT+cT^2+dT^3+eT^4+fT^5$; $a=-1.134x10^{-2}$, $b=2.402x10^{-4}$, $c=-6.519x10^{-7}$, $d=9.231x10^{-10}$, $e=-5.506x10^{-13}$, $f=9.944x10^{-17}$, |
| | | $k_{ar}=a+bT$; $a=1.944x10^{-2}$, $b=2.464x10^{-5}$, |
| | | $k_{ox}=a+bT+cT^2+dT^3$; $a=-1.197x10^{-2}$, $b=1.342x10^{-4}$, $c=-6.456x10^{-8}$, $d=1.782x10^{-11}$, |
| | | $k_G=z_1k_1/(z_1+z_2\Phi_{12})+z_2k_2/(z_2+z_1\Phi_{21})$ (e) |
| Viscosity [kg $m^{-1}$ $s^{-1}$] | Wassiljewa Eq. with the Mason and Saxena modification [24] | $M_1=a+bT+cT^2+dT^3$; $a=-5.424x10^{-6}$, $b=4.855x10^{-8}$, $c=-5.722x10^{-12}$, $d=-2.946x10^{-16}$ |
| | | $\mu_{ar}=a+bT$; $a=2.975x10^{-5}$, $b=2.893x10^{-8}$ |
| | | $\mu_{ox}=a+bT$; $a=2.326x10^{-5}$, $b=2.799x10^{-8}$ |
| | | $\mu_G=z_1\mu_1/(z_1+z_2\Phi_{12})+z_2\mu_2/(z_2+z_1\Phi_{21})$, |
| | | $\Phi_{12}=[1+(\mu_1/\mu_1)^{1/2}(M_2/M_1)^{1/4}]^2/[8(1+(M_1/M_2))]^{1/2}$, |
| | | $\Phi_{21}=\Phi_{12}(\mu_2/\mu_1)(M_1/M_2)$ (d) |
| Binary diffusion coefficient [$m^2$ $s^{-1}$] | Lennard-Jones [28] | $D_{12}=1.8585x10^{-7}*sqrt(T^3(1/M_1+1/M_2))*1/(P\sigma^2{}_{12}\Omega_{12})$ (f) |
| Enthalpy of water [J/kg] | | $h_1=a+bT+cT^2+dT^3+eT^4$; $a=3.443x10^6$, $b=-4.374x10^3$, $c=8.618$, $d=-4.515x10^{-2}$, |

| | |
|---|---|
| | $e=8.496x10^{-7}$, |
| Enthalpy of plasma gas [J/kg] | $h_{ar}=a+bT$; $a=-1.551x10^{-1}$, $b=5.203x10^{-4}$, |
| | $h_{ox}=a+bT+cT^2$; $a=-2.849x10^{-1}$, $b=9.213x10^{-4}$, $c=7.478x10^{-8}$, |
| | $h_2=h_{ar}Y_{ar}+h_{ox}Y_{ox}$, |
| Molecular weights [kg/kgmol] | $M_2=z_{ar}M_{ar}+z_{ox}M_{ox}$; $M_{av}=z_1M_1+z_2M_2$ |
| Enthalpy of vaporization [J/kg] | $h_{1G}-h_{1L}$ |

For the liquid, the subindex 1 refers to water and 2 to the anhydrous salt. For the gas, 1 refers to water vapor and 2 for the mixture of argon and oxygen plasma gas.
(a) Experimental values
(b) The values of $Ce^{4+}$ were approximated from curve fitting values of $Gd^{3+}$ and $Sm^{3+}$
(c) The product of these ratios are $(\eta_s/\eta)(\rho_s V_s)\sim 1$
(d) To obtain $\mu_2$ the same mixing rule was applied but 1 and 2 are argon and oxygen respectively
(e) The same formulae are used to calculate $\Phi_{12}$ and $\Phi_{21}$ for the thermal conductivity as for viscosity
(f) Since argon and oxygen had similar Lennard-Jones potentials, only the values of oxygen are considered which allows the calculation of multicomponent diffusion coefficients. Only, in this case 2 refers to oxygen.

### *6.2.5 Solution procedure*

Comsol Multiphysics ® was used to solve the model. The model consisted of ~12,300 elements distributed in a non-uniform mesh, where a higher number of elements were located at the droplet interface. Mesh independent solutions were obtained. Quadratic Lagrange elements were used for all variables with the exception of pressure in which linear elements were employed. Lagrange multipliers were used to improve solution convergence of the boundary conditions. A Heaviside step function [20] was applied to provide smooth temperature and concentration profiles as initial conditions in the vicinity of the droplet interphase.

## 6.3 Model validation

The model was validated by comparing the ratio of the surface concentration ($C_s$) to the mean concentration ($C_m$) minus one ($C_s/C_m$-1) of a nonvolatile solute in an evaporating drop. These values were estimated by Schlünder [14] and further re-computed by Gardner [15]. Schlünder confirmed experimentally that the ratio approached a constant asymptotic value, which allowed the simplification of equations describing the transient mass transfer inside the droplet. Gardner further formalized that simplification by stating that the product of $R_{(t)}dR_{(t)}/dt$ was constant for the most part during evaporation. In these studies it was assumed that the diffusion coefficient of the salt in the solution droplet was constant. The model presented in this study was in agreement with Gardner's findings with less than 1.5% error and showed that Schlünder's results were off by roughly 20%, but that both had similar trends (Fig. 6.2). It is worth noting that this agreement was confirmed for low values of $K/4D_L$ and a constant value of $D_L$ was used to match their calculations. Further, the work of Xiong and Kodas [16] also based their findings on Gardner's approach to investigate the evolution of the droplet size in spray pyrolysis of sodium chloride aqueous solution droplets; thus, giving credit to this method as a form of model validation.

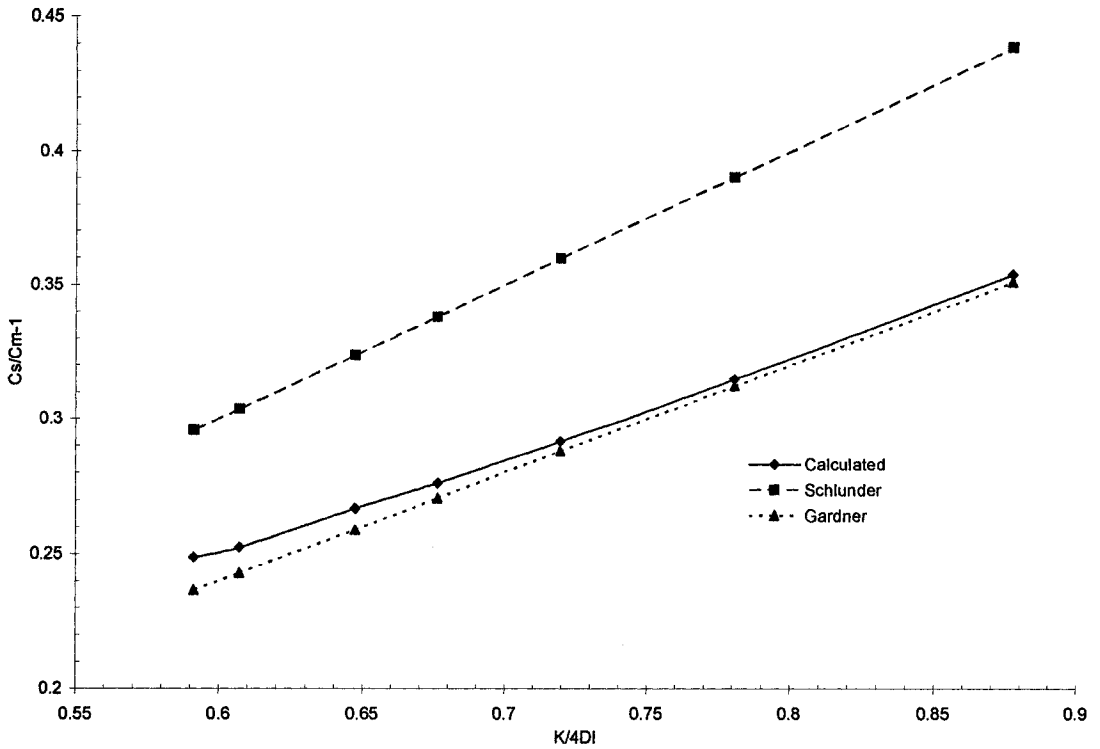


**Fig. 6. 2 Model validation**

## 6.4 Results and discussion

The present simulation considered the effects of plasma temperature, initial salt concentration, system pressure and initial particle size on the temperature and mass profiles in the evaporating droplet. The simulations were stopped when the mass fraction of salt approached the saturation limit, i.e Ws=0.7 (this limit was experimentally determined). In most cases, the saturation limit was reached in approximately $4x10^{-4}$ seconds (almost half of a millisecond). Table 6.II summarizes all the conditions analyzed in this paper; the base case is given in bold. For instance, to analyze the pressure of the system, all the other parameters were $T\infty$=600 K, $W_{so}$=0.5, $z_{Ar}$=0.2, D=30 μm at different pressures, P=0.3, 0.4 and 0.5 atm. The conditions for temperature at infinity are typical of rf plasma systems where the liquid injection into the hot core of the plasma causes a local quenching and thus temperatures below 800 K are expected [21].

**Table 6. II Experimental ranges of studied variables**

| $T_\infty$ [K] | $W_{so}$ | P [atm] | $z_{Ar}/z_{O2}$ | D [μm] |
|---|---|---|---|---|
| 500 | 0.3 | **0.3** | 0.2/0.8 | 20 |
| **600** | 0.4 | 0.4 | **0.3/0.7** | **30** |
| 700 | **0.5** | 0.5 | 0.4/0.6 | 40 |

The salt mass fraction and dimensionless temperature $T_{1d}=(T-T_{Lo}/(T_s-T_{Lo}))$ profiles in the droplet are shown in Fig. 6.3a and 6.3b. The radial position plotted is referred to the moving frame which follows the droplet decrease in size over time. The results indicate that the temperature profile is clearly developed and has reached the centre of the droplet prior to the moment of expected solute precipitation at R (droplet surface). On the contrary, the developing of the salt mass fraction profile is much slower. There is a large mass fraction difference (i.e. from 0.5 to 0.7) in the vicinity of the droplet surface, whereas the remaining of the droplet still remains at its initial value. The differences in profiles are because heat transfer by conduction is much faster than diffusion mass transfer. As a result, a growing crust is expected to form at the droplet surface where the saturation point has been reached.

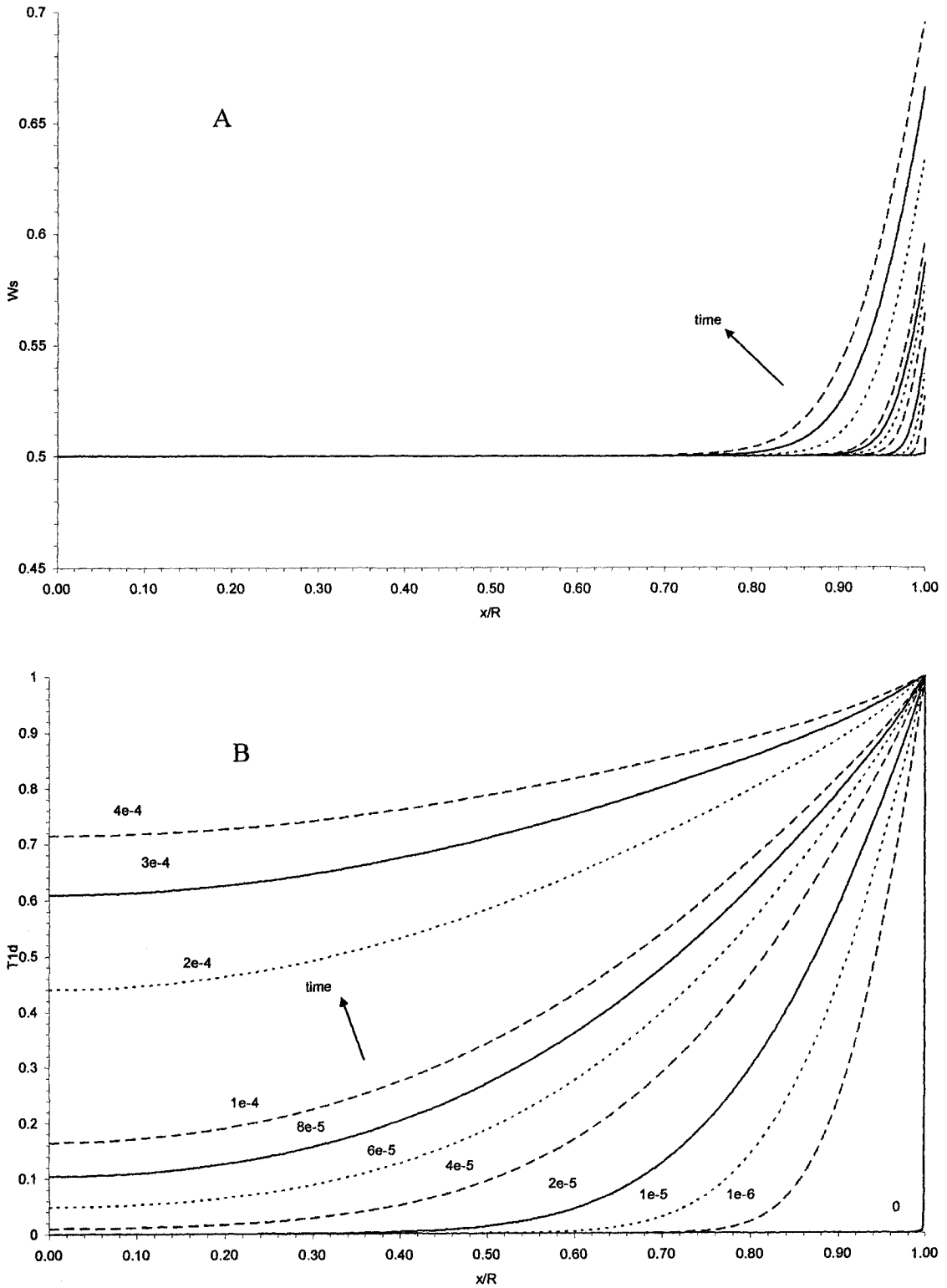


**Fig. 6. 3 A) Mass fraction and B) temperature profiles in the droplet as a function of radial position for different times ($T\infty$=600 K, $W_{s0}$=0.5, P=0.3 atm, $z_{Ar}=0.3/zO_2=0.7$, D= 30 μm, t=0 to $4x10^{-4}$s. Same times in Fig. A and B)**

### *6.4.1 Effect of plasma temperature*

The surrounding plasma temperature ($T_\infty$) was increased from 500K to 700K and the results are presented in Fig. 6.4a and 6.4b at $4x10^{-4}$ seconds (onset of solute nucleation at the surface). It can be seen that the mass fraction of salt is only slightly affected by the increase of plasma gas temperature. It appears that more salt diffuses towards the centre of the droplet as the temperature increases, since mass diffusivity increases with increasing temperature. However, this effect is minor. On the other hand, the temperature profile inside the droplet is affected strongly. Higher plasma temperatures result in more energy transfer to the droplet. Therefore, higher temperatures are expected in the evaporating droplet at the beginning of solute precipitation.

The change of droplet diameter at different plasma temperatures is illustrated in Fig. 6.5, where the ratio of the droplet diameter (d) to the original diameter ($d_o$) is shown as a function of time. As expected, as the temperature of the plasma gas is augmented, more water is vaporized and thus the droplet decreases in size at a faster rate. The graph shows that the droplet has not significantly decreased in size (almost 96% of the original size remains) when its surface has already reached the point of saturation.

### *6.4.2 Effect of initial salt content*

The initial salt content was varied from Ws=0.3 to Ws=0.5. The salt mass fraction at the surface (Fig. 6.6a) and the temperature at the centre and surface of the droplet were plotted (Fig. 6.6b) as a function of time. The mass profile indicates that there are two regions. First, a rapid change of mass content happens before $2x10^{-4}$ seconds, and second, the mass fraction varies almost linearly until the limit of saturation is achieved. There is no apparent change in the way the vaporization occurs or the crust is formed as a function of initial solute content. The differences among the different initial solute concentrations are more related to the time taken to reach the onset of crust formation.

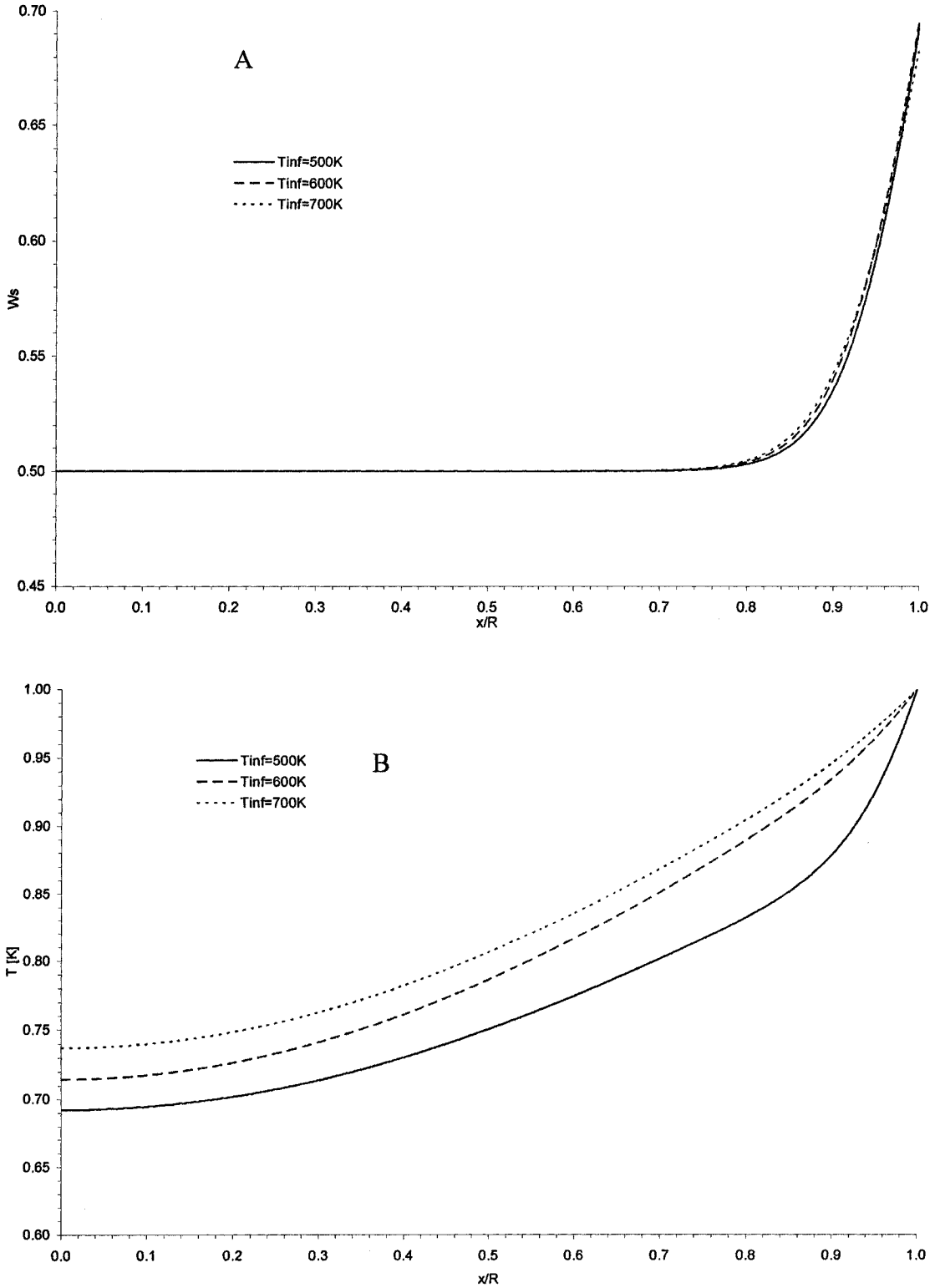


**Fig. 6. 4 A) Mass fraction and B) dimensionless temperature radial profiles in the droplet as a function of plasma temperature at t=4x10-4 seconds ($W_{so}$=0.5, P=0.3 atm, $z_{Ar}$=0.3/$zO_2$=0.7, D= 30 μm)**

The less solute is present (thus more solvent), the longer it takes for the appearance of a crust. Similarly, the temporal temperature profiles in the centre and at the droplet surface do not show a distinct variation as more solvent is present in the droplet. Initially, the temperatures at the centre and surface are the same. Then there is a temperature gradient that increases with time, and towards the end this gradient slowly decreases as heat is conducted throughout the droplet.

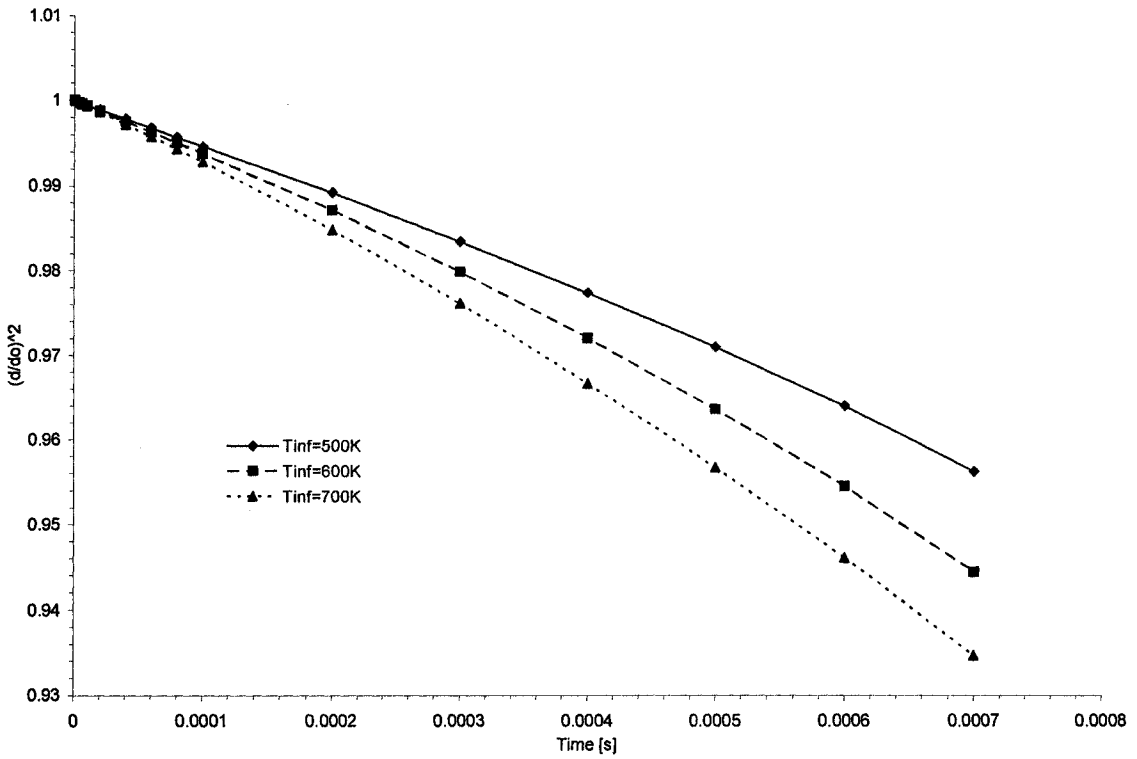


**Fig. 6. 5 Evolution of droplet diameter as a function of time for different plasma temperatures ($W_{s0}$=0.5, P=0.3 atm, $z_{Ar}$=0.3/$zO_2$=0.7, D= 30 μm)**

In summary, the addition of solvent to the droplet has the effect of retarding the formation of a crust as a result of a longer evaporation time. The results showed that mass diffusion and heat conduction are weak functions of concentration for the range studied, even though density, thermal conductivity, heat capacity and mass diffusivity were all functions of solute content.

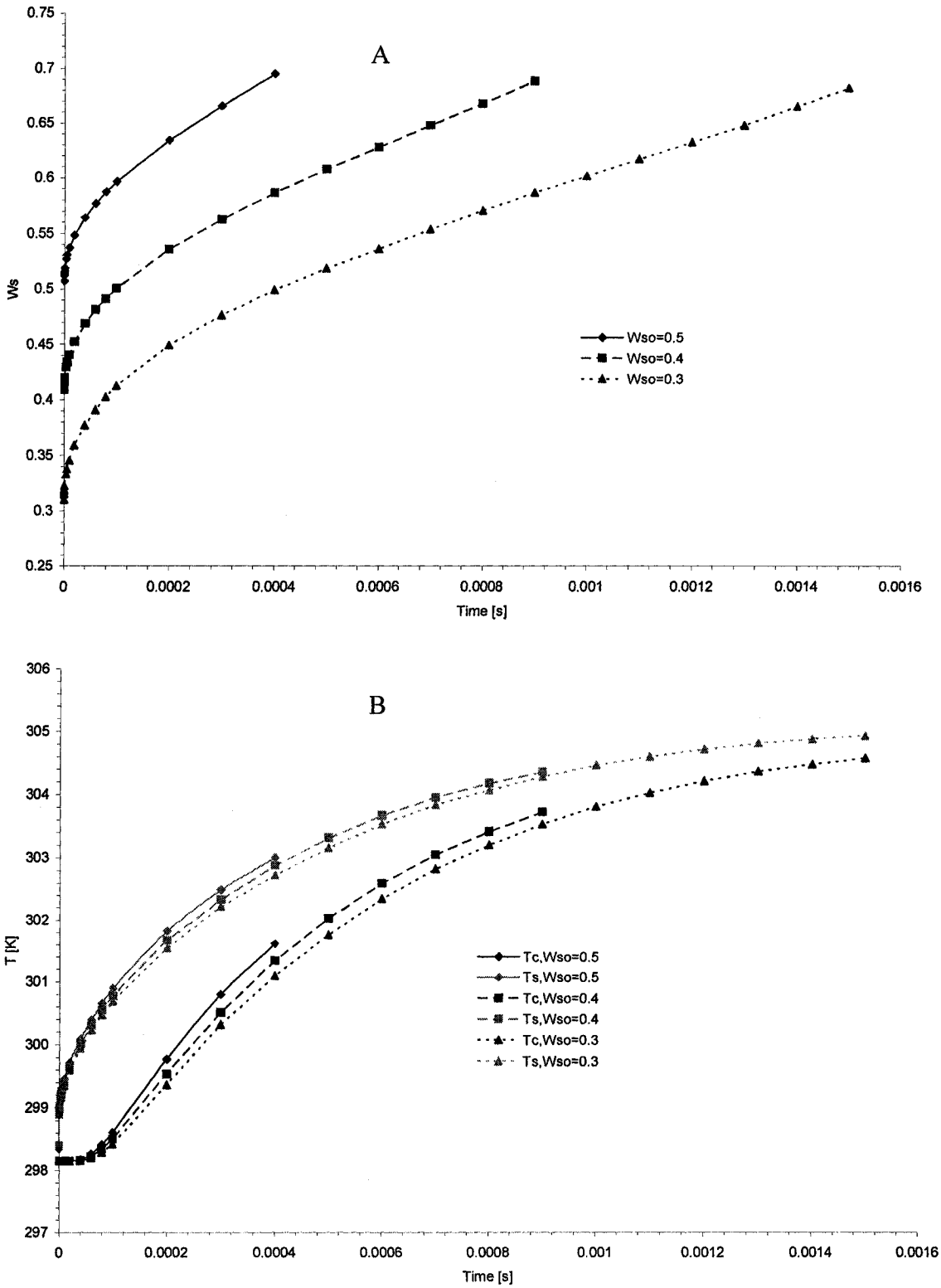


**Fig. 6. 6 Mass fraction profile at the droplet surface as a function of time. Temperature profiles at the droplet centre and surface as a function of time (T∞=600 K, P=0.3 atm, $z_{Ar}$=0.3/$zO_2$=0.7, D= 30 μm)**

### *6.4.3 Effect of system pressure*

The system pressure was varied from 0.3 atm to 0.5 atm since most of the rf thermal plasmas used in this type of application operate under reduced pressure. The surface salt content and the surface temperature and the centre droplet temperature are plotted as a function of time in Fig. 6.7a and 6.7b, respectively. Reducing the pressure, reduces the boiling temperature of the droplet which favors solvent vaporization. Also, because the water is vaporizing into Ar and $O_2$, the boiling point is further lowered. As a result, the droplet surface temperature is only a few degrees above room temperature when the droplet salt content at the droplet-gas interface reaches saturation values. Further, lower pressures cause a faster achievement of the nucleation point at a lower temperature. As expected, the boiling temperature of the droplet surface is higher with increasing pressure and the difference between centre and surface temperatures is larger during the early stages of evaporation.

As a conclusion, the lower the pressure, the faster the onset of crust formation for a given set of operating parameters.

### *6.4.4 Effect of plasma composition*

The plasma gas composition was changed from 0.2/0.8 argon-oxygen (in mol fraction) to a 0.4/0.6 argon-oxygen mixture. These are typical operating ranges in rf thermal plasmas. The salt content temperature profiles at the onset of crust formation were plotted as a function of radial position (Fig. 6.8a and 6.8b). An oxygen-rich plasma has a higher enthalpy at the same temperature. The results suggest that this change of enthalpy has a small effect on the salt diffusion and water evaporation, judging from the similarity of the profiles in all cases. It is also shown that the limit of saturation is achieved slightly faster when an oxygen-rich plasma is employed.

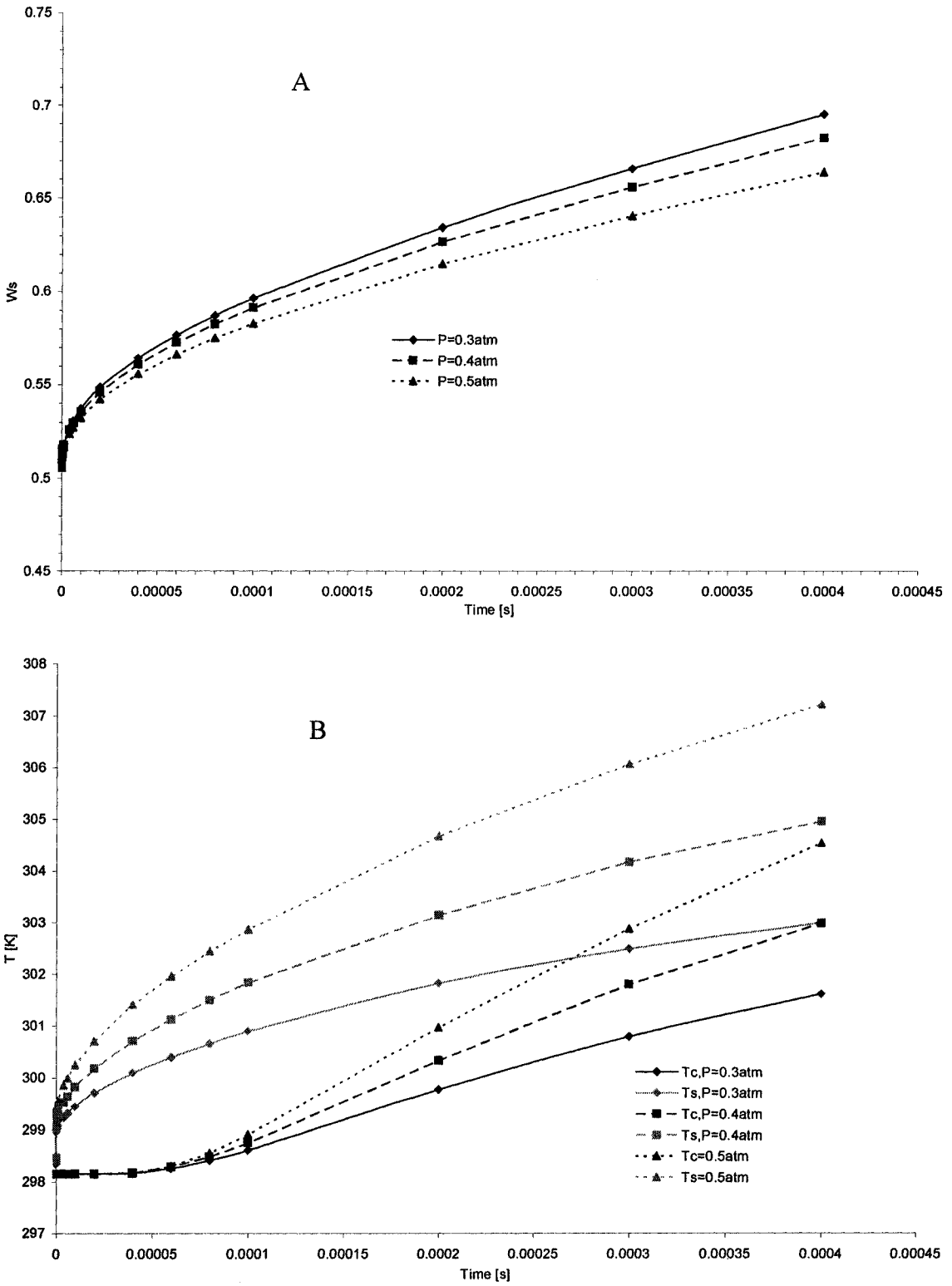


**Fig. 6. 7 A) Mass fraction profile at the droplet surface as a function of time. B) Temperature profiles at the droplet centre and surface as a function of time ($T\infty$=600 K, $W_{so}$=0.5, $z_{Ar}$=0.3/$zO_2$=0.7, D= 30 μm)**

The effect of plasma composition could be more important as the temperature of the surrounding gas increases (>3,000K), especially because, the thermal conductivity of oxygen increases greatly with temperature. However, this range was out of the operating window of the present study.

### *6.4.5 Effect of initial droplet size*

Three different initial droplet sizes were tested, i.e. 20 μm, 30 μm, and 40 μm. Salt content and temperature values were plotted as a function of time (Fig. 6.9a and 6.9b). The results clearly indicate that droplet size has a major effect on the crust-formation and evaporation processes. Smaller droplets reached the point of crust formation faster than larger droplets and the difference between the surface and centre temperature does not seem to depend on droplet size. Despite the small droplet diameter, temperature and salt mass fraction are different from the centre to the surface.

The change of droplet diameter with time is illustrated in Fig. 6.10. The larger droplets show a less pronounced slope and thus take longer to evaporate. Despite the change in size, the phenomena affecting evaporation remain largely unchanged, i.e. faster heat conduction due to smaller droplet sizes and slow development of mass fraction profiles as a result of mass diffusion

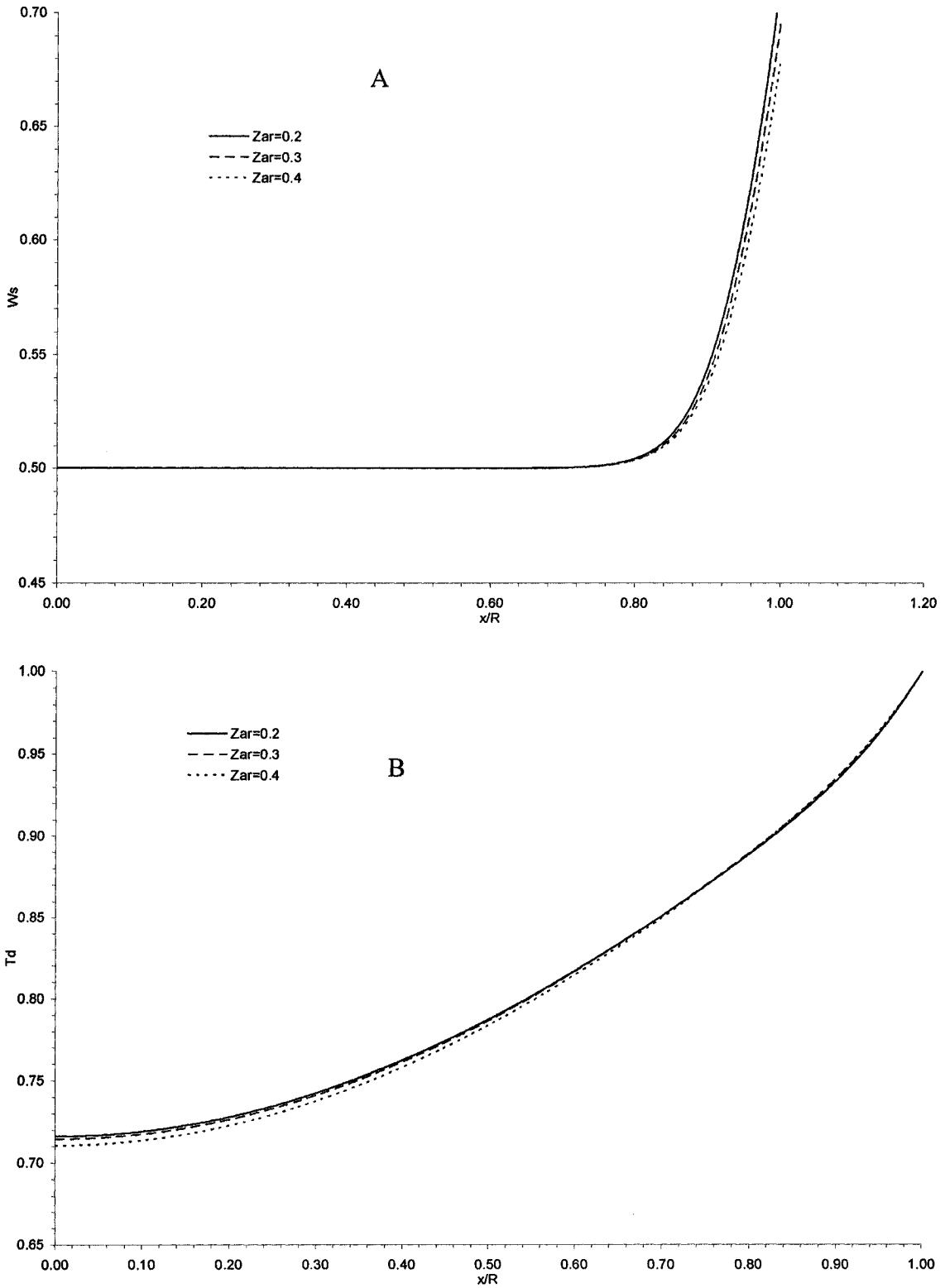


**Fig. 6. 8 A) Mass fraction and B) dimensionless temperature radial profiles in the droplet as a function of plasma gas composition at t=4x10-4 seconds ($T\infty$=600 K, $W_{s0}$=0.5, P=0.3 atm, D= 30 μm)**

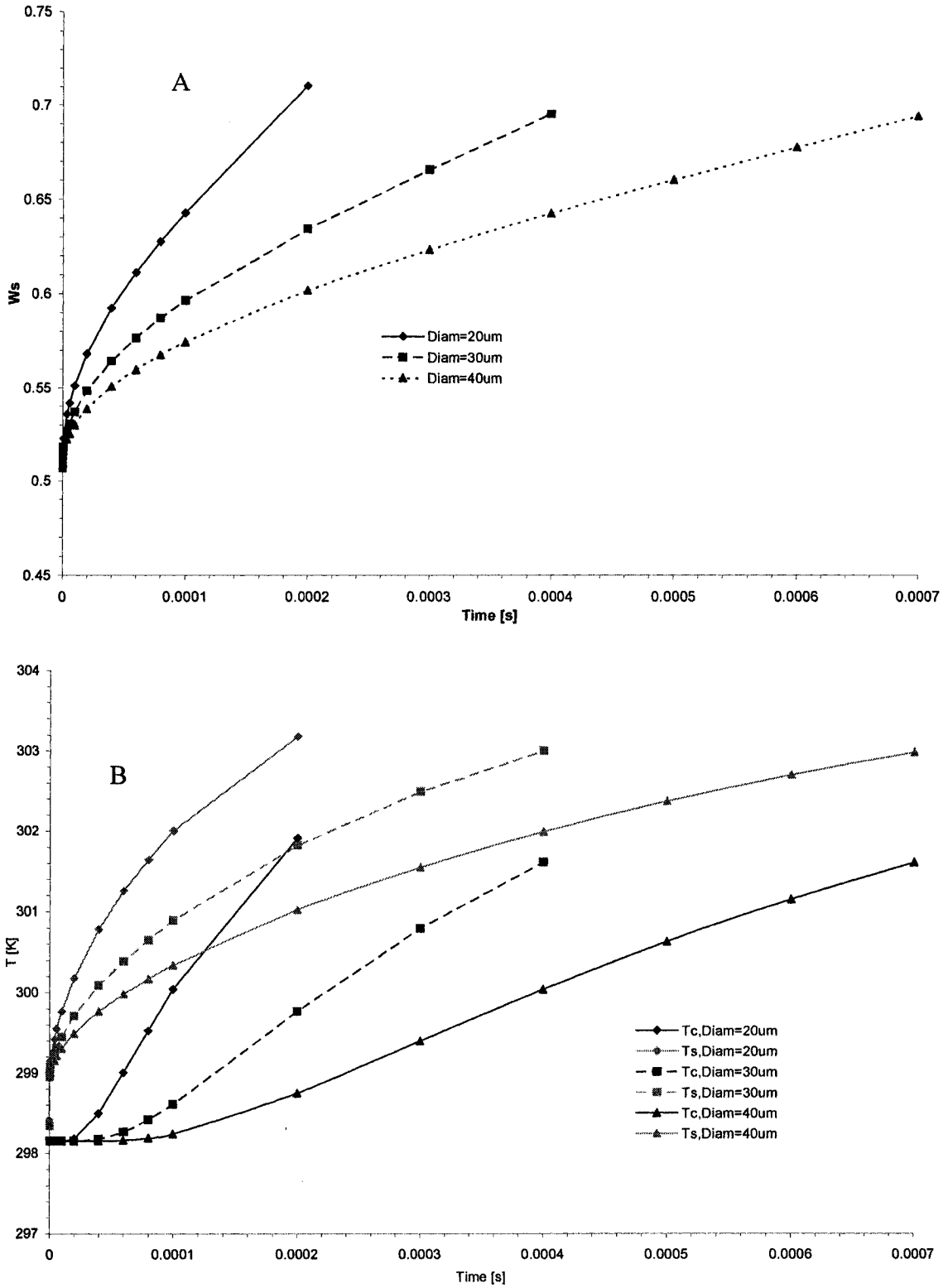


**Fig. 6. 9 A) Mass fraction profile at the droplet surface as a function of time. B) Temperature profiles at the droplet centre and surface as a function of time ($T\infty$=600 K, $W_{s0}$=0.5, P=0.3 atm, $z_{Ar}$=0.3/$zO_2$=0.7)**

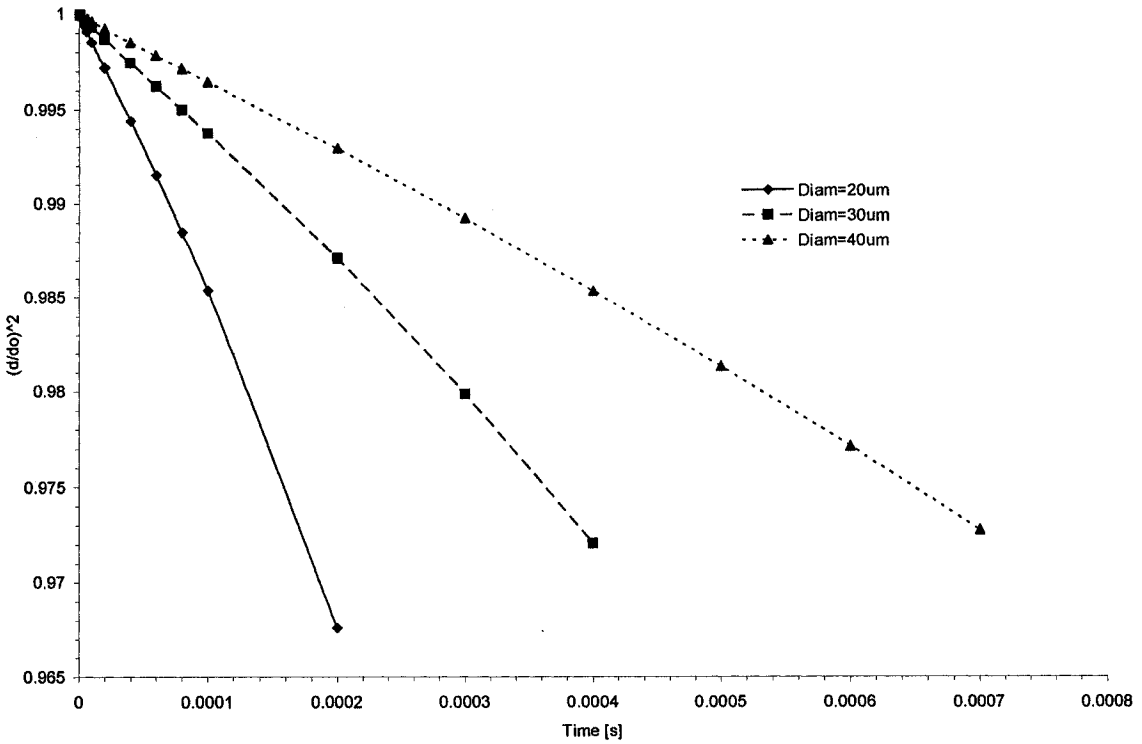


**Fig. 6. 10 Evolution of droplet diameter as a function of time for different initial droplet sizes ($T\infty$=600 K, $W_{so}$=0.5, P=0.3 atm, $z_{Ar}$=0.3/$zO_2$=0.7, D= 30 μm)**

### *6.4.6 Comparison between constant and variable properties*

The model was solved with constant and variable properties to assess the effect on the predicted mass and temperature profiles. The results are presented in Fig. 6.11a and 6.11b and 6.12. The use of constant properties under predicts the development of the mass and temperature profiles inside the droplet and it also under estimates the droplet size change. Therefore, the use of variable properties provides a more realistic and accurate calculation of the onset of crust formation and droplet evaporation.

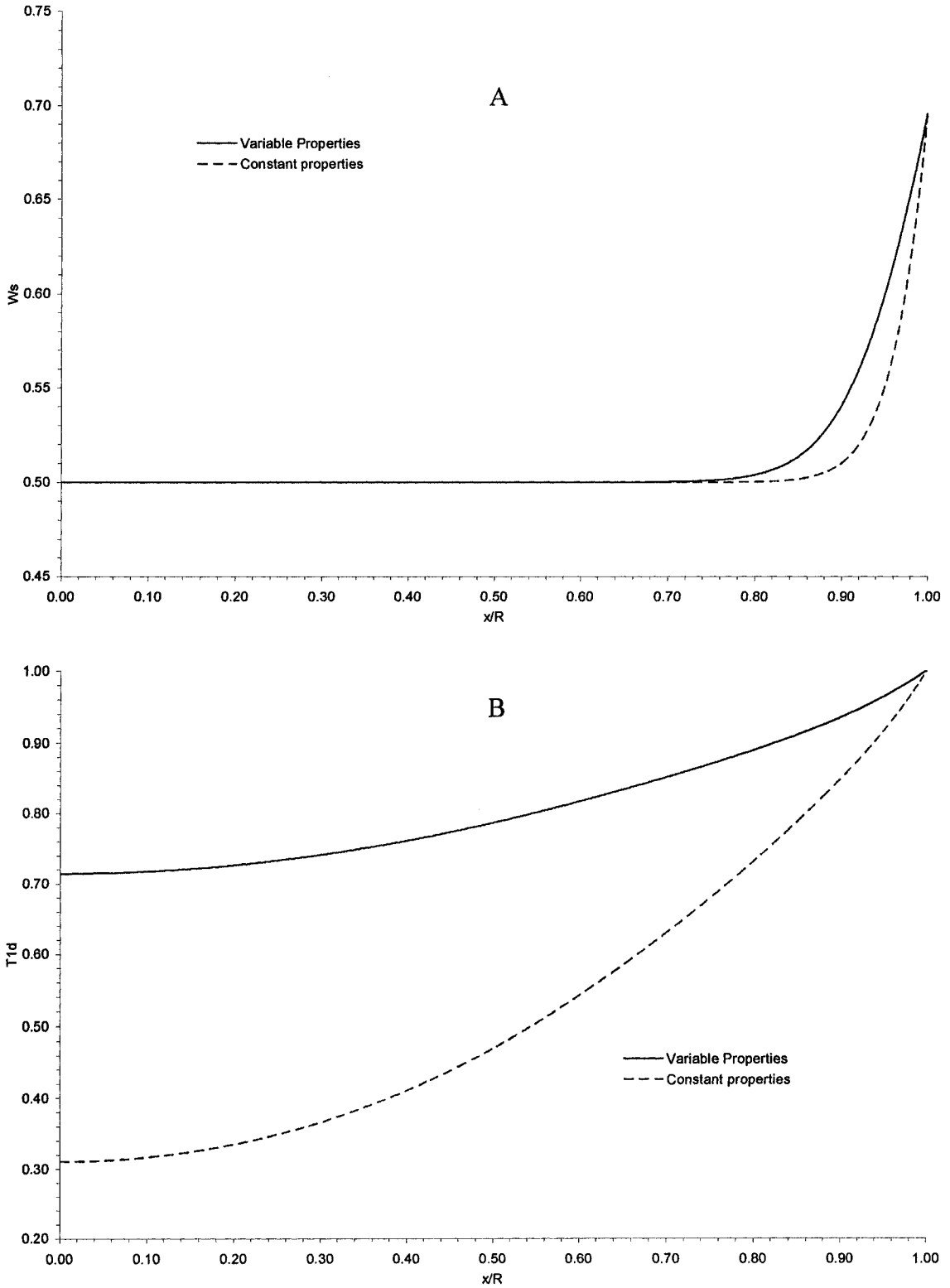


**Fig. 6. 11 A) Mass fraction and B) dimensionless temperature radial profiles in the droplet as a function of plasma temperature at t=4x10-4 seconds ($T\infty$=600 K, $W_{s0}$=0.5, P=0.3 atm, $z_{Ar}$=0.3/$zO_2$=0.7, D= 30 μm)**

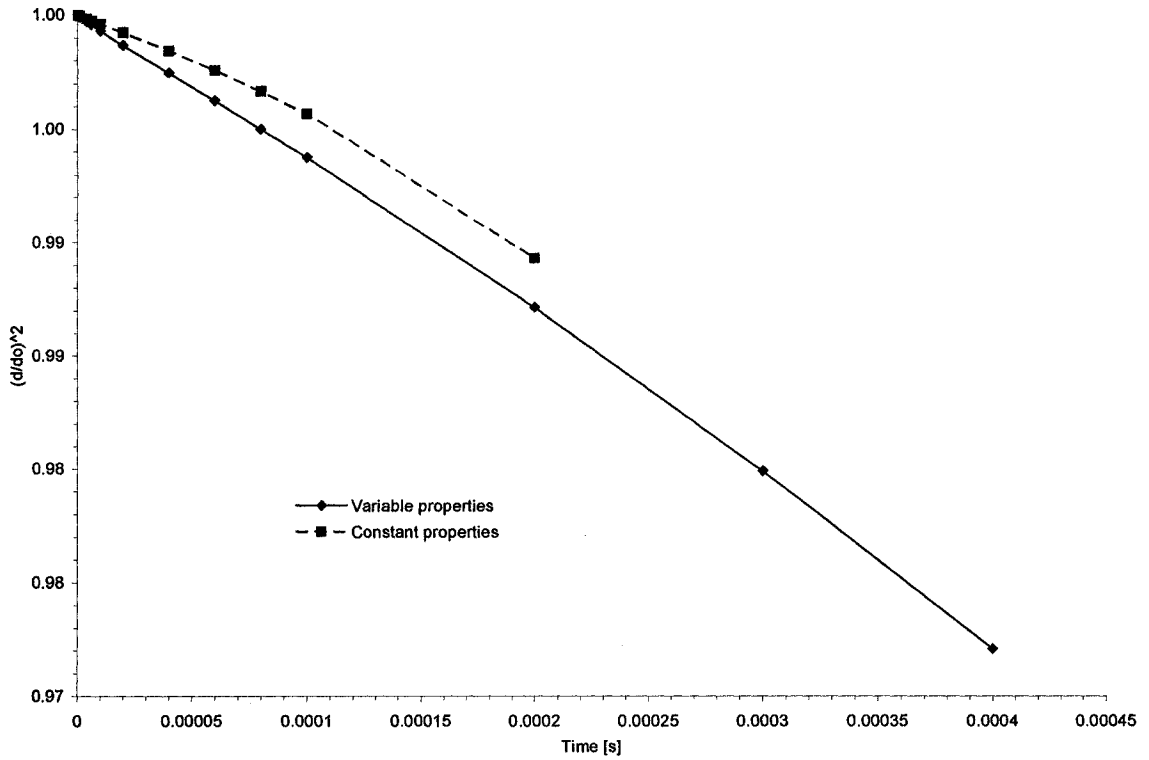


**Fig. 6. 12 Evolution of droplet diameter as a function of time for constant and variable thermophysical properties ($T\infty$=600 K, $W_{s0}$=0.5, P=0.3 atm, $z_{Ar}$=0.3/$zO_2$=0.7, D= 30 μm)**

## 6.5 Conclusions

The present work shows that crust formation in an evaporating solution droplet containing non-volatile compounds is present in all cases. The change of parameters demonstrated that all conditions that favor vaporization will tend to promote crust formation in less time, i.e. higher temperatures, more enthalpic plasma gas, less solvent, lower pressure. Further, the initial droplet size has a marked effect on the time at which crust formation is achieved, and thus rendering droplet size an important parameter to control in rf thermal plasmas.

A crust is formed in all cases as a result of salt precipitation. The slower rate of mass transfer inside the droplet in comparison with the faster heat transfer rate by conduction is responsible for crust formation. Also, the use of temperature and composition variable properties in both the gas and liquid phases results in a more realistic model with increasing predicting scope.

The fact that the supersaturation point is always achieved within the operating range studied at the droplet surface provides encouraging evidence to support droplet explosion. As a result of pressure buildup in the inner core of an evaporating droplet in rf thermal plasma systems.

## 6.6 Acknowledgements

The financial support by the Natural Sciences and Engineering Research Council of Canada and the Ministry of Education of the Province of Quebec through its FQRNT program is gratefully acknowledged.

## 6.7 References

1. Bouyer, E. Gitzhofer, F., Boulos, M. I., Suspension plasma spraying for hydroxyapatite powder preparation by rf plasma, IEEE Transactions on Plasma Science, 25(5), 1066-1072 (1997)

2. Müller, M. et al., Thermal induction plasma processes for the synthesis of SOFC materials, *Materialwissenshchaft und Werkstofftechnik*, **33**(6), 322-330 (2002)

3. Bouyer, E. et al, Thermal plasma chemical vapor deposition of Si-based ceramic coatings from liquid precursors, *Plasma Chemistry and Plasma Processing*, **21**(4), 523-546 (2001)

4. Delbos et al, DC plasma spray elaboration of fine structured coatings by ceramic liquid suspension injection, *Proceedings 16th International Symposium on Plasma Chemistry* (ISPC 16), Italy (2003)

5. Lau, Y. C., Kong, P.C., Pfender, E. Synthesis of zirconia powders in an RF plasma by injection of inorganic liquid precursors, *Ceramic Transactions 1*, 298-303 (1988)

6. Gitzhofer, F. et al. Integrated fabrication processes for solid-oxide fuel cells using thermal plasma spray technology, *MRS Bulletin*, **25**(7), 38-42 (2000)

7. Fauchais, et al, Plasma spraying from thick to thin coatings and micro to nano-structured coatings, , *Proceedings 16th International Symposium on Plasma Chemistry* (ISPC 16), Italy (2003)

8. Castillo, I. and Munz, R. Inductively coupled plasma synthesis of CeO2 –based powders from liquid solutions for SOFC electrolytes, *Plasma Chemistry and Plasma Processing*, 25(2), 87-107 (2005)

9. Jia, L. and Gitzhofer, F. Collection of nano-powders generated by radio frequency (RF) plasma spray synthesis (PSS) processing, using a sampling probe, *Proceedings 17th International Symposium on Plasma Chemistry (ISPC 17)*, Canada (2005)

10. Yu, H. and Liao, W. H. Evaporation of solution droplets in spray pyrolysis. *Int. J. Heat Mass Transfer*. **41**(8-9), 993-1001 (1997)

11. Charlesworth, D. H. and Marshall, W. R. Evaporation from drops containing dissolved solids, *AIChE Journal*, **6**(1), 9-23 (1960)

12. Elperin, T. and Krasovitov, B. Evaporation of liquid droplets containing small solid particles, *Int. J. Heat Mass Transfer*, **38**(12), 2259-2267 (1995)

13. Ozturk, A. and Cetegen, B. M. Modeling of plasma assisted formation of precipitates in zirconium containing liquid precursor droplets, Materials Science and Engineering A, **384**, 331-351 (2004)

14. Schlünder, E. U. Temperatur- und Masseänderung verdunstender Tropfen aus reinen Flüssigkeiten und wässrigen Salzlösungen, *Int. J. Heat Mass Transfer*, **7**, 49-73 (1964)

15. Gardner, G. C., Asymptotic concentration distribution of an involatile solute in an evaporating drop, *Int. J. Heat Mass Transfer*, **8**, 667-668 (1965)

16. Xiong, Y. Kodas, T. T. Droplet evaporation and solute precipitation during spray pyrolysis, *J. Aerosol Sci.*, **24**(7), 893-908 (1993)

17. Jayanthi, G. V., Zhang, S. C., Messing, G. L. Modeling of solid particle formation during solution aerosol thermolysis, *Aerosol Science and Technology*, **19**(4), 478-490 (1993)

18. Donea, J. et al. Arbitraty lagrangian-eulerian methods, Encylcopedia of Computational Mechanics, *John Wiley & Sons*, Chapter 14, Vol. 1. (2004)

19. Comsol, Comsol multiphysics: modeling guide, Version 3.2, (2005)

20. Heaviside functions, http://mathworld.wolfram.com/HeavisideStepFunction.html

21. Colombo, V. Ghedini, E., Mentrelli, A. 3-D Turbulent modeling of an ICPT with detailed gas injection section, *Proceeding of the ISPC 16*, Canada (2005)

22. Touloukian, Y.S. and Makita, T. Thermophysical properties of matter: Specific heat of non-metallic liquids and gases. Vol. **6**, *Plenum* (1970)

23. Dean, J. A. Lange's Handbook of Chemistry, 15th Ed. McGraw Hill (1999)

24. Reid, R. C. et al. The properties of gases and liquids. 4th Ed. McGraw Hill (1987)

25. Rard, J. et al. Isopiestic determination of the activity coefficients of some aqueous rare earth electrolyte solutions at 25C. *Journal of Chemical and Engineering Data*, **22**(3) (1977)

26. Vasic, A., Cheng, A., Groeneveld, D. C., A comparison of predictions of high-temperature steam properties, *Nuclear Engineering and Design,* **132**, 367-379 (1992)

27. Boulos, M. I., Fauchais, P., Pfender, E. Thermal plasmas. Fundamentals and Applications. Vol. 1, Plenum (1994)

28. Bird, R. B., Stewart, W. E., and Lightfoot, E. N. Transport phenomena. John Wiley & Sons, 2nd Ed. (2002)

# Chapter 7 Transient modeling of heat, mass and momentum transfer of an evaporating cerium nitrate solution droplet with a surrounding shell in a rf thermal argon-oxygen plasma under reduced pressure

In this chapter the second part of the modeling results is presented. The second part of the modeling studied the phenomena affecting droplet explosion from the onset of crust formation. In this chapter, an evaporating droplet surrounded by a porous crust immersed in plasma gas is considered.

## Abstract

A model was developed to study the evaporation of a solution droplet surrounded by a porous crust in a stagnant rf Ar-$O_2$ thermal plasma under reduced pressure. This model considered a three phase system: a liquid core of dissolved $Ce(NO_3)_3.6H_2O$ in water, a porous crust of homogeneously precipitated spherical crystals of equal size containingwater vapor, and an Ar-$O_2$ plasma under reduced pressure. The model was solved considering a receding solution/crust interface in an ALE frame using temperature and composition dependant thermophysical properties. Darcy flow with a Knudsen correction to account for the gaseous flow through a porous media composed of nano-sized crystals was employed. The strength of the solid/liquid interface was calculated by computing the strength of liquid bridges formed at this interface. This value was compared to the pressure build-up caused by solvent evaporation and the point of crust breakage was determined at different operating conditions. The effects of plasma gas temperature, pressure and composition, droplet size, size of precipitated crystals and crust porosity on crust bursting were studied. The results showed that crust bursting occurred for all the conditions analyzed and that plasma temperature, droplet size and the size of the precipitated crystals had a significant effect on pressure build-up.

## Nomenclature

C convective velocity (relative velocity between the material V and mesh velocity Ψ), [m/s]

$C_i$ concentration of electrolyte *i*, [mol/L]

Cp heat capacity, [J/kg.K]

$D_{12}$ diffusion coefficient based on molecular concentration [$m^2$/s]

F Faraday constant

$F_{cs}$ capillary and surface force, [N]

h enthalpy, [J/kg]

K crust permeability, [$m^2$]

Kn Knudsen number, $Kn=\lambda/2R_{sp}$

k thermal conductivity, [W/mK]

m molality of the solute, [mol/kg solvent]

$\dot{m}$ mass flow rate at the droplet surface due to vaporization, [kg/$m^2$s]

M molecular weight, [kg/kgmol]

$M_{av}$ average gas molecular weight, [kg/kgmol]

P pressure, [Pa]

$P_{max}$ maximum droplet pressure, [Pa]

$P_{in}$ droplet pressure, [Pa]

$P_{out}$ pressure at the crust/gas interface, [Pa]

$P_i$ partial pressure of i, [Pa]

$P^s$ saturation pressure of water, [Pa]

$P_m$ mean pressure difference across the crust, [Pa]

Q source/sink term, [J/$m^3$s]

r radial distance, [m]

$R_{L(t)}$ radius of the droplet (function of time), [m]

$R_C$ inner crust radius, [m]

$R_g$ universal gas constant, [J/kmol.K]

$R_{sp}$ radius of precipated crystals in porous crust, [m]

$\dot{R}_L$ change of droplet radius with respect to time, [m/s]

$T$ temperature, [K]

$T_d$ dimensionless temperature

$t$ time, [s]

$t_{ch}$ "thickness" of the liquid bridges, [m]

$T_r$ reference temperature, [K]

$U$ radial Darcian velocity, [m/s]

$V$ radial material velocity, [m/s]

$V_m$ molar volume of liquid phase, [$m^3$/mol]

$W_i$ mass fraction of *i* in liquid

$W^s_i$ mass fraction of *i* in liquid at saturation (constant over the range of temperature studied)

$x_i$ mol fraction of *i* in liquid

$Y_i$ mass fraction of *i* in gas

$z_i$ mol fraction of *i* in gas

Greek letters

$\beta$ half filled angle

$\varepsilon$ porosity

$\gamma_{\pm}$ mean ionic activity coefficient of the solute

$\lambda$ mean free path, [m]

$\lambda^{\circ}_{+},\lambda^{\circ}_{-}$ limiting (zero concentration) ionic conductances, [($A/cm^2$)(V/cm)(mol/$cm^3$)]

$\mu_C$ gas viscosity in crust, [kg/m.s]

$\mu_G$ gas viscosity in gas phase, [kg/m.s]

$\mu_l$ water viscosity in the droplet, [kg/m.s]

$\rho_L$ density of liquid solution, [kg/$m^3$]

$\rho_C$ density of gas in crust, [kg/$m^3$]

$\rho_G$ density of gas in gas phase, [kg/$m^3$]

$\sigma_{LG}$ surface tension, [N/m]

$\sigma_i$ coefficient characteristic of each ion

$\sigma_y$ crust yield stress, [$N/m^2$]

$\upsilon_+,\upsilon_-$ valences of cation and anion, respectively

$\theta$ wetting angle

$\Psi$ mesh velocity, [m/s]

Subscripts

1 component 1 (either in the solution or the gas phase)

2 component 2 (either in the solution or the gas phase)

Ar argon

d dimensionless

C crust domain

G plasma gas domain

i i-component

L solution droplet domain

o initial value

$O_2$ oxygen

s anhydrous salt

w water

$\chi$ referential domain or moving mesh

$\infty$ conditions at infinity (far away from the droplet)

Superscripts

s saturated condition

## Keywords

Evaporation, solution droplet, crust formation, cerium nitrate, thermal plasma, ALE model, Darcy flow, Knudsen effect, liquid bridges

## 7.1 Introduction

The manufacturing of ceramic powders from liquid precursors using radio frequency (rf) thermal plasmas has been developed in the past 10 years [1-5]. This technique consists of

the evaporation and calcination of atomized solution droplets injected axially to the plasma core usually under reduced pressure. The solution is atomized by a liquid blast atomizer that provides a log-normal droplet size distribution centered around 20-30 μm in diameter. The droplets usually contain a non-volatile salt (nitrates, acetates, chlorides, etc) dissolved in water or any other suitable solvent. The hot plasma environment provides the driving force for evaporation and calcination of the salt, resulting in the production of high-purity oxide particles. Thus, oxygen-rich plasmas are often employed. The use of liquid precursors encompasses applications such as production of ceramic materials for SOFC (solid oxide fuel cells) (perovskites, $Y_2O_3$, $CeO_2$, NiO, etc) [6,7] and thermal barrier coatings ($ZrO_2$) [8].It has been found in previous studies [7,9] that this technique can produce ceramic particles of known and controlled stochiometry. However these particles varied greatly in size from few nanometers to micron sizes, suggesting that more than one droplet-to-particle conversion mechanism was possible.

The production of ceramic powders in thermal plasmas from liquid precursors is similar to the well known spray pyrolysis technique [10], but the operating temperatures are higher, the droplets are often in the low micro size range (< 50 μm) and the reactor chamber is operated under vacuum. As a result, the thermal plasma treatment is a more "rapid" version of spray pyrolysis, since the conditions for solvent evaporation are enhanced. Previous theoretical and experimental work, including our own studies [11], has shown that solution droplets containing non-volatile solutes tend to form a thin crust surrounding the evaporating droplet.

The crust is formed because the non-volatile salt precipitates out of solution, primarily at the droplet surface. A fast evaporation rate removes solvent from the droplet surface more quickly than it can be replenished by mass diffusion, resulting in the formation of a crust [12]. Having a crust around an evaporating liquid core retards the rate at which inner solvent escapes from the droplet [13], because the solvent must travel through a porous phase. This leads to an increase of the solvent vapor pressure that causes fracturing and/or bursting of the crust. As a consequence, after calcination takes place, solid particles of different sizes are formed (Fig 7.1). A recent study by Ozturk [14] has shown that solid

and hollow particles of $ZrO_2$ can be produced using thermal plasmas from zirconium acetate depending on the plasma operating conditions.

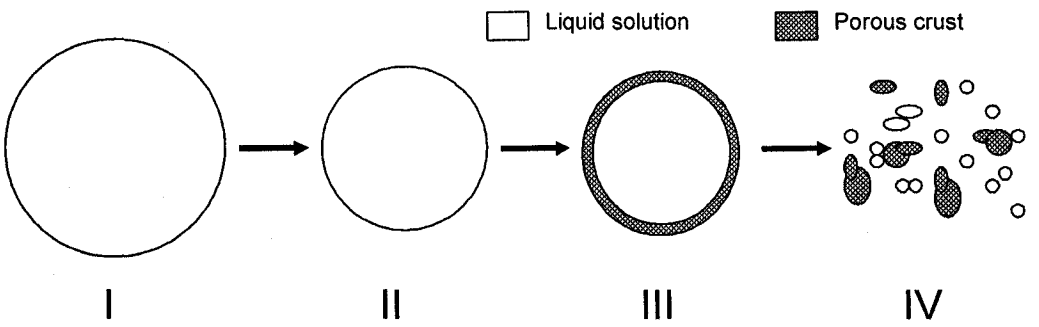


**Fig. 7. 1 Mechanism of droplet to particle conversion considering crust shattering**

Even though pressure build-up inside the crust as a result of solvent evaporation is widely accepted as the main cause of crust bursting, few papers discuss this issue in detail [13, 15]. The shattering of the crust is often related to the degree of superheating of the solution inside the crust and whether the liquid has reached its boiling point. This type of analysis provides little insight of the actual "forces" that prevent the crust from bursting. Therefore, an analysis of these forces acting at the receding crust/droplet interface will give a more realistic picture of when the crust will burst due to pressure build up.

Three different phases co-exist at the droplet/crust interface, i.e. a liquid solution wetting a solid crust and a gaseous evaporating solvent. The solution forms liquid bridges in the form of menisci that connect the newly precipitated solid particles along this interface. The forces present in these bridges are surface tension and a negative capillary pressure as a result of the solid particle curvatures. These two forces are commonly combined and termed capillary forces. The detailed description of meniscus properties and the capillary force for pendular liquid rings has been extensively investigated [16,17,18]. However, the connection of these forces to the problem of evaporating solution droplets with a surrounding crust has not been made to the authors' knowledge. Also, as a result of the small droplet size (20-30 μm in diameter), the precipitated particles forming the crust are likely to be in the nanometer range (i.e. the size of single precipitated crystals). Hence, the flow of evaporating solvent through porous media lies within the transient flow

regime ($0.1 < Kn < 10$), between a continuum flow and a free molecular flow. This effect was considered in this work and it was adapted from the work of Tang [19]

In this paper, the effect of temperature, pressure, gas composition, crust porosity, size of precipitated crystals and initial droplet size (including crust and inner liquid core) were examined under thermal plasma conditions. The droplets contained a hexahydrated salt, $Ce(NO_3)_3.6H_2O$, dissolved in water, surrounded by a porous crust containing water vapor. The mass and thermal histories inside the droplet and throughout the crust were studied. The droplet/crust interface was allowed to recede in time as water was continuously being evaporated. Darcy flow with a Knudsen correction was used for the crust section.

The purpose of this study is to derive understanding of how plasma conditions affect droplet and crust mass and thermal histories and to predict the onset of crust shattering under typical rf thermal plasma operating conditions.

## 7.2 Model development

The physical model studied was the transient evaporation of a solution droplet approximately 30 μm in diameter surrounded by a porous crust (Fig. 7.2). The droplet and its crust are immersed in a mixture of stagnant argon-oxygen rf plasma. The solution droplet was a hexahydrated salt, $Ce(NO_3)_3.6H_2O$, dissolved in water and all water of hydration is assumed to be released and to be part of the total droplet water content. The anhydrous salt was considered to remain largely in molecular form (i.e. as $Ce(NO_3)_3$) as a result of a large salt content in the droplet but whenever possible solution properties were calculated assuming dissociation of the nitrate and the cerium ions. The droplet has reached the point of saturation at the droplet/crust interface.

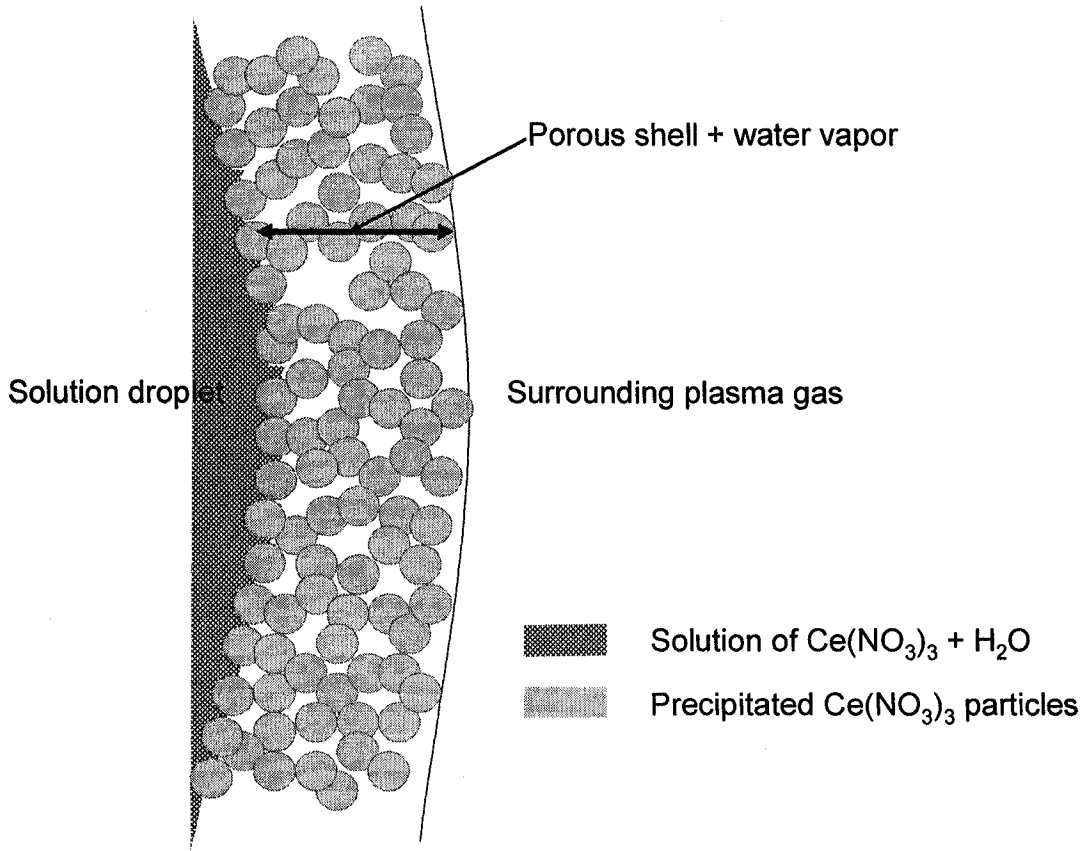


**Fig. 7. 2 Cross section of an evaporating droplet showing the inner liquid core, the homogeneously precipitated spherical crystals particles of a given size comprising the crust and the surrounding plasma gas**

The porous crust is assumed to be rigid and in the shape of a spherical shell with a receding droplet/crust interface. Water vapor is formed at the liquid/crust interface and it then escapes through the porous shell, which is composed of homogeneously nucleated spherical crystals a few nanometers in diameter. These nucleated crystals are assumed to be of uniform size and provide the crust with a characteristic porosity. This porosity is maintained across the whole thickness of the crust. Capillary and surface tension forces prevent crust from bursting through the formation of liquid bridges between the spherical crystals.

Radiation and second order effects, such as Soret and Dufor effects, were assumed to be negligible. Spherical symmetry reduced the problem to a transient, three phase process of one dimensional nature. The only fluid motion present was a radial flow field through the

crust and into the gas phase induced by water vaporization. Darcy flow is assumed in the crust with a non-continuum correction factor as the Knudsen number falls within the transition regime ($0.1 < Kn < 10$). Radial flow inside the droplet was neglected on the basis of the large density difference between the solution droplet and the gas. Viscous dissipation effects were neglected. Finally, the surrounding plasma gas (argon/oxygen) obeyed the ideal gas law.

Under these conditions the physics of the problem are as follows: solvent (i.e. water) evaporates from the solution droplet which causes droplet shrinkage and crust growth. The salt diffuses toward the centre of the droplet and a temperature profile is developed in the droplet. The water vapor escapes through the porous crust and mixes with the surrounding plasma gas. A temperature profile also develops in the crust. The crust opposes solvent flow and allows heat transfer from the surrounding gas into the droplet. This process continues while pressure builds up at the droplet/crust interface as a result of increasing temperature and crust obstruction to flow. This increasing pressure exerts a stress along the droplet/crust interface that is counterbalanced by capillary and surface forces. When this stress exceeds the magnitude of the counterbalancing forces, the crust bursts.

It is then hypothesized that the resulting fragments, i.e. smaller droplets and crust pieces undergo thermolysis and the $Ce(NO_3)_3$ salt is transformed into $CeO_2$ particles. Consequently a multi-modal particle size distribution is expected (Fig. 7.1, IV).

This model was solved using the Arbitrary-Lagrangian-Eulerian (ALE) method which has been successfully employed with moving boundary problems [20]. A deformed mesh can be used when the boundaries of the computational domain deform in time as a result of the physics of the problem, in this case, the evaporation of the solution droplet. Therefore, a new mesh is not needed at each time step; instead the mesh nodes are perturbed so that they conform to the moving boundaries [21]. In this way, computational time can be saved without losing resolution in the solution

### *7.2.1 Liquid governing equations*

For the liquid phase, $r<R_L(t)$, 1) refers to the water and 2) refers to the anhydrous salt (i.e. $Ce(NO_3)_3$)

species equation

$$\frac{\partial}{\partial t}\left(r^2\rho_L W_1\right)\Big|_\chi + \frac{\partial}{\partial r}\left(-r^2\rho_L D_L\frac{\partial W_1}{\partial r}\right)=0 \tag{18}$$

energy equation including Steffan diffusion in the ($h_1$-$h_2$ term)

$$\frac{\partial}{\partial t}\left(r^2\rho_L Cp_L T\right)\Big|_\chi + \frac{\partial}{\partial r}\left(-r^2 k_L\frac{\partial T}{\partial r}-r^2\rho_L D_L\frac{\partial W_1}{\partial r}(h_1-h_2)\right)=0 \tag{19}$$

### *7.2.2 Shell governing equations*

For the porous crust, $R_{L(t)}<r<R_C$, 1) refers to the water and 2) refers to the plasma gas argon-oxygen mixture. The convective velocity is defined as $C = V - \psi$

species equation

$$\frac{\partial}{\partial t}\left(r^2\varepsilon\rho_C Y_1\right)\Big|_\chi + \frac{\partial}{\partial r}\left(-r^2\rho_C D_C\frac{\partial Y_1}{\partial r}+r^2\rho_C Y_1 C\right)=0 \tag{20}$$

energy equation including Steffan diffusion in the ($h_1$-$h_2$ term)

$$\frac{\partial}{\partial t}\left(r^2\rho_C Cp_C T\right)\Big|_\chi + \frac{\partial}{\partial r}\left(-r^2 k_C\frac{\partial T}{\partial r}-r^2\rho_C D_C\frac{\partial Y_1}{\partial r}(h_1-h_2)+r^2\rho_C Cp_C TC\right)=0 \tag{21}$$

Darcy equation

$$U = -\frac{K}{\mu_C}\frac{\partial P}{\partial r} \tag{22}$$

darcian velocity U is related to V by $U = \varepsilon V$

continuity equation

$$\frac{\partial}{\partial t}\left(r^2\varepsilon\rho_C\right)\Big|_\chi + \frac{\partial}{\partial r}\left(r^2\rho_C U\right)=0 \tag{23}$$

which can be also expressed as (combining eq. 5 and eq. 6)

$$\frac{\partial}{\partial t}\left(r^2 \varepsilon \rho_C\right)\Big|_\chi + \frac{\partial}{\partial r}\left(r^2 \rho_C\left(-\frac{K}{\mu_C}\frac{\partial P}{\partial r}\right)\right) = 0 \tag{24}$$

### *7.2.3 Gas governing equations*

For the gas phase, r>$R_C$, 1) refers to the water and 2) refers to the plasma gas argon-oxygen mixture.

continuity equation

$$r^2 \frac{\partial \rho_G}{\partial t} + \rho_G\left(r^2 \frac{\partial V}{\partial r} + 2rV\right) + r^2 V \frac{\partial \rho_G}{\partial r} = 0 \tag{25}$$

species equation

$$\frac{\partial}{\partial t}\left(r^2 \rho_G Y_1\right) + \frac{\partial}{\partial r}\left(-r^2 \rho_G D_G \frac{\partial Y_1}{\partial r} + r^2 \rho_G Y_1 V\right) = 0 \tag{26}$$

energy equation

$$\frac{\partial}{\partial t}\left(r^2 \rho_G Cp_G T\right) + \frac{\partial}{\partial r}\left(-r^2 k_G \frac{\partial T}{\partial r} - r^2 \rho_G D_G \frac{\partial Y_1}{\partial r}\left(h_1 - h_2\right) + r^2 \rho_G Cp_G TV\right) = Q \tag{27}$$

$$Q = -r^2 P\left(\frac{\partial V}{\partial r}\right)$$

momentum equation

$$\frac{\partial}{\partial t}\left(r^2 \rho_G V\right) = \frac{\partial}{\partial r}\left(r^2\left[2\mu \frac{\partial V}{\partial r} - P\right]\right) + r^2\left(F - \rho V \frac{\partial V}{\partial r} - \frac{2\left(2\mu V/r - P\right)}{r}\right) \tag{28}$$

$$F = -\frac{\partial}{\partial r}\left(\frac{2}{3}\mu\left(\frac{\partial V}{\partial r}\right)\right)$$

### *7.2.4 Boundary conditions*

At droplet center

$$\frac{\partial W_i}{\partial r} = \frac{\partial T}{\partial r} = 0 \tag{29}$$

At liquid/crust interface

$W_i = W_{si}$ (30)

Overall mass

$$\dot{m} = \rho_C \left( V - \dot{R}_L \right)_C = \rho_L \left( 0 - \dot{R}_L \right)_L \tag{31}$$

Species balance

$$\left( n_{iC} - \dot{R}_L \rho_C \right)_C = \left( n_{iL} - \dot{R}_L \rho_L \right)_L ;$$

$$n_{iC} = -\rho_C D_C \frac{\partial Y_i}{\partial r} + \rho_C Y_i C ; n_{iL} = -\rho_L D_L \frac{\partial W_i}{\partial r} \tag{32}$$

Energy balance

$$e_L = -k_L \frac{\partial T}{\partial r} - \rho_L D_L \frac{\partial W_1}{\partial r}(h_1 - h_2); \; e_C = -k_C \frac{\partial T}{\partial r} - \rho_C D_C \frac{\partial Y_1}{\partial r}(h_1 - h_2) + \rho_C Cp_C TV$$

$$\left( e_C - \dot{R}_L \sum_{i=1}^{n} \rho_C Y_i h_{iC} \right)_C = \left( e_L - \dot{R}_L \sum_{i=1}^{n} \rho_L W_i h_{iL} \right)_L \tag{33}$$

Kelvin's equation

$$\ln\left( \frac{P_i}{P^s} \right) = -\left( \frac{2\sigma_{LG} \cos\theta}{R_{sp}} \right)\left( \frac{V_m}{R_g T} \right); \qquad P_i = Y_i \rho_C \frac{RT}{M_i} \tag{34}$$

At crust/gas interface

$$Y_i\big|_C = Y_i\big|_L \quad T\big|_C = T\big|_L \quad V\big|_C = V\big|_L \quad P\big|_C = P_i\big|_L \tag{35}$$

At infinity r→ ∞

$$Y_i = 0; \quad T = T_\infty ; \quad V = 0; \quad \frac{\partial P}{\partial r} = 0 ; \tag{36}$$

### *7.2.5 Initial conditions*

Overall mass conservation

$$-\rho_L \dot{R}_L\Big|_{R_L} = \dot{m} + \int_0^{R(t)} \left(\frac{r}{R_L}\right)^2 \frac{\partial \rho_L}{\partial t} dr \tag{37}$$

In the liquid phase

$$W_i = W_{io} \quad T = T_{Lo} \tag{38}$$

In the porous phase

$$Y_i = 0 \quad T = T_{Lo} \quad V = 0 \quad P = Po \tag{39}$$

In the gas phase

$$Y_i = 0 \quad T = T_{Go} \quad V = 0 \quad P = Po \tag{40}$$

### *7.2.6 Thermophysical properties*

A more accurate formulation of the problem can be derived taking into account temperature and concentration dependence of the species in the liquid, crust and gas domains (Table 7.I).

**Table 7. I Thermophysical properties**

| Property | Method | Mixing rule |
|---|---|---|
| **Liquid properties** | | |
| Density [kg/m$^3$] | Ideal mixing | $\rho_L=aW_1+bW_2$; a=1,000 b=1,600 [(a)] |
| Specific heat [J/kg.K] | Ideal mixing | $Cp_1=a+bT+cT^2+dT^3$, a=8.958x10$^3$, b=-4.053x10$^1$, c=1.124x10$^{-1}$, d=-1.014x10$^{-4}$ [26]<br>$Cp_2$=358.06 [27]<br>$Cp_L=Cp_1W_1+Cp_2W_2$ |
| Thermal conductivity [W/m.K] | Riedel for aqueous solutions [27] | $k_{1(Tr)}=a+bT+cT^2$; a=-3.838x10$^{-1}$, b=5.254x10$^{-3}$, c=-6.369x10$^{-6}$<br>$k_{L(Tr)}=k_{1(Tr)}+\Sigma\sigma_iC_i$; $\sigma(NO_3^-)$=-6.978x10$^{-5}$ $\sigma(Ce^{4+})$=-43.61x10$^{-5}$<br>$k_{L(T)}=k_{L(Tr)}*k_{1(T)}/k_{1(Tr)}$ |
| Binary diffusion coefficient [m$^2$/s] | Nerst-Haskell equation and Gordon approach for concentrated solutions [27] | $D^\circ_{12}=R_gT/F^2*(1/\upsilon_+ +1/\upsilon_-)/(1/\lambda^\circ_+ +1/\lambda^\circ_-)/1x10^4$;<br>$D_{12(Tr)}=D^\circ_{12}(\eta_s/\eta)(\rho_sV_s)*(1+m\partial\ln\gamma_\pm/\partial m)$ [(c)]<br>$D_{12(T)}=D_{12(Tr)}(T/T_r)(\mu_{1Tr}/\mu_{1T})$<br>$\partial\ln\gamma_\pm/\partial m$ [29] [(b)] |
| Water viscosity [kg/m.s] | | $M_1=a+bT+cT^2+dT^3$; a=-2.471x10$^1$, b=4.209x10$^3$, c=4.527x10$^{-2}$, d=-3.376x10$^{-5}$ [28] |
| Enthalpy of water [J/kg] | | $h_1=a+bT+cT^2+dT^3$; a=-2.248x10$^6$, b=1.297x10$^4$, c=-2.291x10$^1$, d=1.962x10$^{-2}$ |
| Enthalpy of $Ce(NO_3)_3$ salt [J/kg] | | $H_2=h^\circ_2+Cp_2(T-T_r)$ |
| **Gas properties** | | |
| Density [kg m$^{-3}$] | Ideal gas | $\rho_G=PM_{av}/R_gT$ |
| Specific heat [J kg$^{-1}$ K$^{-1}$] | Ideal mixing | $Cp_1=a+bT+cT^2+dT^3+eT^4$, a=1.652x10$^3$, b=1.295x10$^{-1}$, c=1.850x10$^{-3}$, d=-1.959x10$^{-6}$, e=6.384x10$^{-10}$ [30] |

| | | |
|---|---|---|
| | | $Cp_{ox}=a+bT+cT^2+dT^3$, a=8.958x10$^3$, b=-4.053x10$^1$, c=1.124x10$^{-1}$, d=-1.014x10$^{-4}$<br>$Cp_{ar}$=520.4 [31]<br>$Cp_2=Y_{Ar}M_{Ar}+Y_{O2}M_{O2}$<br>$Cp_G=Cp_1Y_1+Cp_2M_2$ |
| Thermal conductivity [W m$^{-1}$ K$^{-1}$] | Wassiljewa Eq. with the Mason and Saxena modification [27] | $k_l=a+bT+cT^2+dT^3+eT^4+fT^5$; a=-1.134x10$^{-2}$, b=2.402x10$^{-4}$, c=-6.519x10$^{-7}$, d=9.231x10$^{-10}$, e=-5.506x10$^{-13}$, f=9.944x10$^{-17}$,<br>$k_{ar}=a+bT$; a=1.944x10$^{-2}$, b=2.464x10$^{-5}$,<br>$k_{ox}=a+bT+cT^2+dT^3$; a=-1.197x10$^{-2}$, b=1.342x10$^{-4}$, c=-6.456x10$^{-8}$, d=1.782x10$^{-11}$,<br>$k_G=z_1k_1/(z_1+z_2\Phi_{12})+z_2k_2/(z_2+z_1\Phi_{21})$ (e) |
| Viscosity [kg m$^{-1}$ s$^{-1}$] | Wassiljewa Eq. with the Mason and Saxena modification [27] | $M_l=a+bT+cT^2+dT^3$; a=-5.424x10$^{-6}$, b=4.855x10$^{-8}$, c=-5.722x10$^{-12}$, d=-2.946x10$^{-16}$<br>$\mu_{ar}=a+bT$; a=2.975x10$^{-5}$, b=2.893x10$^{-8}$<br>$\mu_{ox}=a+bT$; a=2.326x10$^{-5}$, b=2.799x10$^{-8}$<br>$\mu_G=z_1\mu_1/(z_1+z_2\Phi_{12})+z_2\mu_2/(z_2+z_1\Phi_{21})$,<br>$\Phi_{12}=[1+(\mu_1/\mu_1)^{1/2}(M_2/M_1)^{1/4}]^2/[8(1+(M_1/M_2))]^{1/2}$,<br>$\Phi_{21}=\Phi_{12}(\mu_2/\mu_1)(M_1/M_2)$ (d) |
| Binary diffusion coefficient [m$^2$ s$^{-1}$] | Lennard-Jones [32] | $D_{12}=1.8585x10^{-7}*sqrt(T^3(1/M_1+1/M_2))*1/(P\sigma^2{}_{12}\Omega_{12})$ (f) |
| Enthalpy of water [J/kg] | | $h_l=a+bT+cT^2+dT^3+eT^4$; a=3.443x10$^6$, b=-4.374x10$^3$, c=8.618, d=-4.515x10$^{-2}$, e=8.496x10$^{-7}$, |
| Enthalpy of plasma gas [J/kg] | | $h_{ar}=a+bT$; a=-1.551x10$^{-1}$, b=5.203x10$^{-4}$,<br>$h_{ox}=a+bT+cT^2$; a=-2.849x10$^{-1}$, b=9.213x10$^{-4}$, c=7.478x10$^{-8}$,<br>$h_2=h_{Ar}Y_{Ar}+h_{O2}Y_{O2}$, |
| Molecular weights [kg/kgmol] | | $M_2=z_{Ar}M_{Ar}+z_{O2}M_{O2}$; $M_{av}=z_1M_1+z_2M_2$ |
| **Crust properties** | | |
| Density [kg m$^{-3}$] | Ideal gas | $\rho_C=PM_{av}/R_gT$ |
| Specific heat [J kg$^{-1}$ K$^{-1}$] | Ideal mixing | $Cp_G=Cp_1Y_1+Cp_2M_2$ (calculated as in the gas phase); $Cp_s=a+bT$; a=364.3, b=0.061 (g) [33]<br>$Cp_C=Cp_G*\varepsilon+Cp_s*(1-\varepsilon)$ |
| Thermal conductivity [W m$^{-1}$ K$^{-1}$] | Kaviany [34] | $k_G=z_1k_1/(z_1+z_2\Phi_{12})+z_2k_2/(z_2+z_1\Phi_{21})$ (calculated as in the gas phase); $k_s$=0.5 W/m.K (h)<br>$k_C=k_G*(k_s/k_G)\wedge(0.280-0.757*\log(\varepsilon)-0.057*\log(k_s/k_G))$ |
| Viscosity [kg m$^{-1}$ s$^{-1}$] | | $\mu_G=\mu_C$ (calculated as in the gas phase) |

| | | |
|---|---|---|
| Binary diffusion coefficient [$m^2 s^{-1}$] | Kaviany [34] | $D_{12\,G}= D_{12\,C}$ (calculated as in the gas phase)<br>$D_C=D_{12\,C}*2*\varepsilon*(1-Y_i)/(3-\varepsilon)$ |
| Permeability [$m^2$] | Tang et al. [35] | $\lambda=(\mu_C*\pi*R_g*T/2*P_m*M_{av})^{0.5}$ ; $Kn=\lambda/2*R_{sp}$;<br>$K=R_{sp}^2*(1+8*C_1*Kn+16*C_2*Kn^2)/8$; $C_1=1.1466$, $C_2=0.14$ |
| Enthalpy of water [J/kg] | | $h_{1G}=h_{1C}$ (calculated as in the gas phase) |
| Enthalpy of plasma gas [J/kg] | | $h_{2G}=h_{2C}$ (calculated as in the gas phase) |
| Molecular weights [kg/kgmol] | | $M_2=z_{ar}M_{ar}+z_{ox}M_{ox}$; $M_{av}=z_1M_1+z_2M_2$ |
| Enthalpy of vaporization [J/kg] | | $h_{1C}-h_{1L}$ |

For the liquid, the subindex 1 refers to water and 2 to the anhydrous salt. For the gas and crust, 1 refers to water vapor and 2 for the mixture of argon and oxygen plasma gas.

(a) Experimental values

(b) The values of $Ce^{4+}$ were approximated from curve fitting values of $Gd^{3+}$ and $Sm^{3+}$

(c) The product of these ratios are $(\eta_s/\eta)(\rho_s V_s)\sim 1$

(d) To obtain $\mu_2$ the same mixing rule was applied but 1 and 2 are argon and oxygen respectively

(e) The same formulae are used to calculate $\Phi_{12}$ and $\Phi_{21}$ for the thermal conductivity as for viscosity

(f) Since argon and oxygen had similar Lennard-Jones potentials, only the values of oxygen are considered which allows the calculation of multicomponent diffusion coefficients. Only, in this case 2 refers to oxygen.

(g) The heat capacity of $CeO_2$ is assumed to be the heat capacity of the solid part composing the porous crust

(h) The thermal conductivity of $CeO_2$-$ZrO_2$ plasma sprayed layers (University of Sherbrooke personal communication) was used as the thermal conductivity of the porous layer

### *7.2.7 Maximum pressure at droplet core*

The maximum pressure that the evaporating solvent can exert on the crust before the crust shatters is given by the following equation [22]

$$\Delta P = P_{\max} - P_{out} = \frac{2 * \sigma * t_{ch}}{R_{L(t)}} \tag{41}$$

This equation treats the evaporating droplet as if the core was a pressurized liquid kept within a rigid spherical shell of radius equal to the radius of the droplet; similar to a pressurized spherical vessel of a given "wall thickness" (Fig. 7.3)

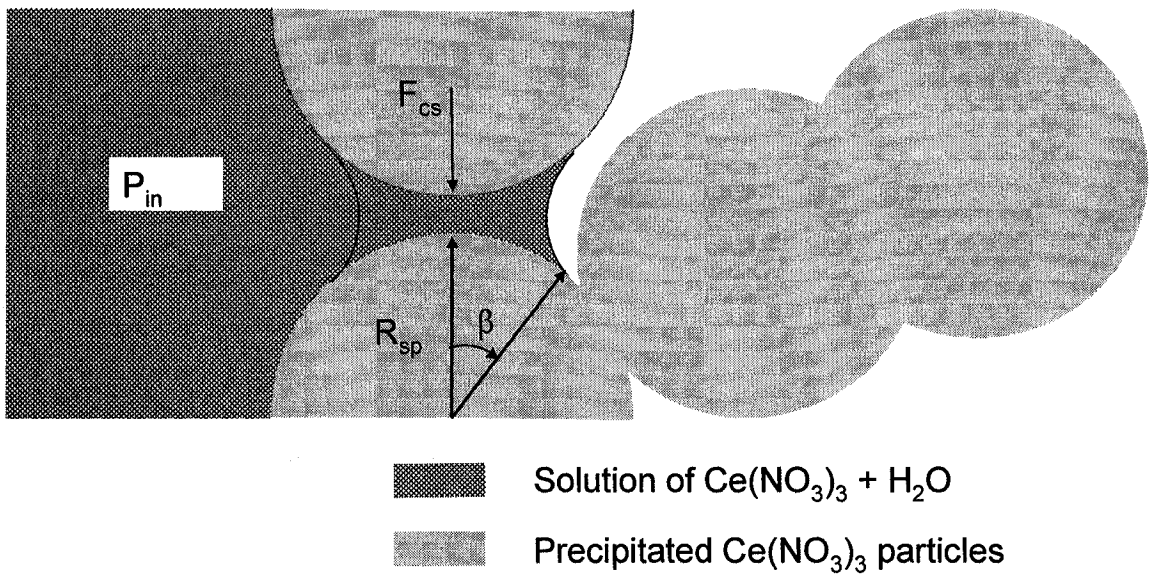


**Fig. 7. 3 Sketch showing the liquid bridges and the forces present. The bridges are formed between precipitated spherical crystals at the liquid crust interface**

The ΔP is the difference between the inner core pressure and the pressure at the crust/gas interface. The liquid bridges formed between the precipitated particles at the droplet/crust interface act as a "wall" of thickness equal to $t_{ch} = 2R_{sp}\sin(\beta)$. This fictitious wall has a maximum yield stress ($\sigma_y$) that is equal to the ratio of the both the capillary and surface forces ($F_{ch}$) to the projected area over which these forces act on, as follows

$$\sigma_y = \frac{F_{ch}}{\pi\left(R_{sp}\sin(\beta)\right)^2} \tag{42}$$

The combined effect of capillary and surface forces was estimated using the method described by Willet [23], who calculated these forces for two spherical bodies connected

by liquid bridges. It was assumed that the crust will burst when the pressure within the droplet exceeded this maximum pressure, i.e. when $P_{in}$ (calculated from the model) = $P_{max}$

### *7.2.7 Solution procedure*

Comsol Multiphysics ® was used to solve the model. The model consisted of approximately 40,000 elements distributed in a non-uniform mesh, a higher number of elements were located at the droplet/crust interface and crust/gas interface. Mesh independent solutions were obtained. Quadratic Lagrange elements were used for all variables, except pressure in which linear elements were employed. Lagrange multipliers were used to improve solution convergence of the boundary conditions. A Heaviside step function [24] was applied to provide smooth temperature and concentration profiles as initial conditions in the vicinity of the droplet/crust interface and crust/gas interface. Heat and mass transfer equations were solved first, assuming a zero velocity flow. This provided a better initial solution estimate for the coupled heat-mass-momentum system at time zero (t=0).

## 7.3 Model validation

This model was qualitatively validated by comparing the results obtained to the spray drying of droplets forming precipitated shells. The models available for spray drying often consider lower gas temperatures and are operated at atmospheric pressure. Few of these models even consider the drying of solution droplets surrounded by a porous crust due to the complexity of solving a three phase problem. To the authors' knowledge, the Knudsen effect has not previously been incorporated so a direct comparison to the available literature models cannot be made. However, a receding interface model of the drying of single drops of slurries of sodium sulfate decahydrate described by Cheong [25] showed remarkably similar features to our present work. These features involved the precipitation of a solute and crust formation and the subsequent simultaneous solution of heat, mass and momentum balance of the evaporating droplet. In Cheong's work, it was indicated that the rate of evaporation of a solution droplet *before* forming a crust increases with time. When the crust is formed, the evaporation rate sharply decreases but then this rate slowly increases again with time as more solvent is vaporized.

Hence to validate the model in this work, the results obtained in previous work [11] were used up to the point of crust formation, and then the present model was used from that point onwards. The results are plotted in Fig. 7.4 for two different plasma gas temperatures

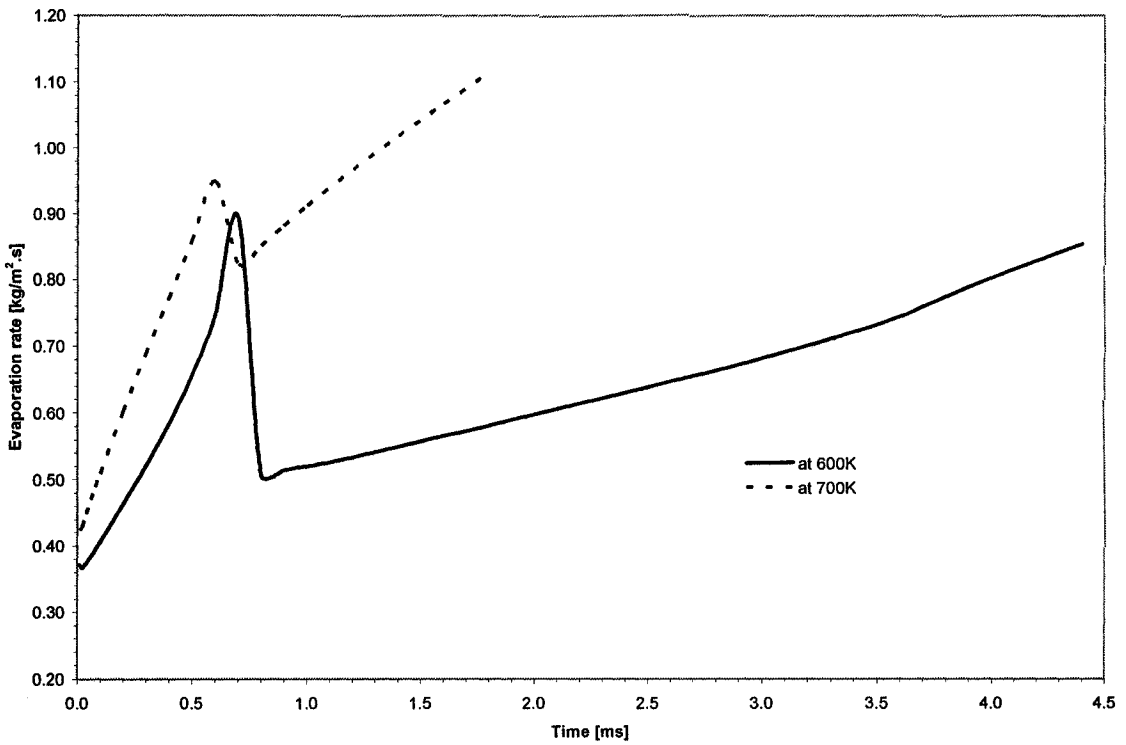


**Fig. 7. 4 Evaporation rate of the solution droplet before and after crust formation at two different plasma gas temperatures (P=0.3 atm for 40 μm diameter droplets, $Z_{Ar}$=0.3/$Z_{O2}$=0.7, ε=0.5, $R_{sp}$=20nm)**

It can be seen that the evaporation rate sharply decreases when the crust is formed since the crust prevents the free flow of evaporating solvent. This rate then increases over time as a result of the higher thermal conductivity of the crust which increases the heat transferred to the inner core of the droplet. The trend showed in Fig. 7.4 is in agreement with what has been reported previously in the work by Cheong, thus providing some re-assurance that the model in this work can adequately portray the physics of solution droplets surrounded by a porous shell.

## 7.4 Results and discussion

The present model considers the effect of plasma temperature, initial droplet size, surrounding pressure, shell porosity, size of precipitated crystals and plasma gas composition. The solution droplet has reached the point of saturation at the droplet/solid interface (i.e. ~$W_s$=0.7). The porous crust was initially considered to be 0.1 μm thick. The crust is formed of homogeneously nucleated spherical crystals a few nanometers in diameter and water vapor. The initial crust thickness was assumed to be 0.1 μm which is approximately between 2 and 3 times the diameter of 3 spherical crystals. This was considered to be the minimum crust thickness based on its minimum number of particles to form liquid bridges. Further solute precipitation was assumed to form similar spherical crystals too. The simulation was stopped when the pressure at this interface exceeded the maximum pressure resisted by the porous shell.

A summary of the different conditions investigated in this work is presented in Table 7.II. The base case conditions are in bold.

**Table 7. II Summary of simulation parameters**

| No | Plasma temperature ($T_\infty$) | Initial droplet size diameter | Gas pressure ($P_\infty$) | Shell porosity (ε) | Radius of precipitated crystals ($R_{sp}$) | Plasma gas composition ($Ar/O_2$) mol fraction ($Z_{Ar}/Z_{O2}$) |
|---|---|---|---|---|---|---|
| | [K] | [μm] | [atm] | | [nm] | |
| 1 | 600 | 30 | **0.3** | 0.4 | 10 | 0.2/0.8 |
| 2 | **700** | **40** | 0.4 | **0.5** | **20** | **0.3/0.7** |
| 3 | 800 | 50 | 0.5 | 0.6 | 30 | 0.4/0.6 |

### *7.4.1 Effect of plasma temperature*

The surrounding plasma temperature was increased from 600 K to 800 K ($T_\infty$). The temperature profiles in the droplet and porous crust are presented in Fig. 7.5a and the salt mass fraction profile in the droplet is shown in Fig. 7.5b at different times, $1x10^{-4}$ and $1x10^{-3}$ seconds. There is a sharp temperature gradient across the porous shell in all cases. Higher droplet and porous temperatures are achieved with increasing plasma temperature. The temperature at the centre of the droplet is close to that of the droplet/crust interface. However, the mass fraction profile of salt in the droplet shows a significant difference between those two locations and most changes happen relatively close to the droplet/crust

interface. This indicates that heat transfer occurs much faster than mass transfer, suggesting that solvent evaporates and the crust grows inwards increasing its thickness.

The crust/droplet interface recedes faster with increasing temperature as can be seen in Fig. 7.6a. This phenomenon is associated with crust growth and continuing solute precipitation. The pressure at the droplet/crust interface is plotted in Fig. 7.6b as a function of time. It can be seen that higher heat transfer resulting from increasing plasma temperature causes the pressure inside the droplet to reach the critical "bursting limit" faster. The maximum pressure that the droplet can withstand is independent of the plasma gas temperature, as this pressure largely depends on the amount of solvent contained in the liquid bridges, geometrical considerations and pore size. Solvent surface tension decreases with increasing temperature, but the temperature increase is relatively small and thus surface tension values remain fairly constant at different plasma temperatures.

The apparent pressure decrease seen at the initial stages of Fig. 7.6b and in some other figures in this work is an artifact of the solution method used to estimate the initial conditions rather than an indication of the physics of the problem. Specifically, this is because the boundary conditions are under-relaxed at the droplet/crust interface, to allow convergence of the solution. This sets the initial pressure slightly higher than originally expected. It must be noted that this erroneous pressure change is very small and is corrected as the solution progresses in time. The important point to notice in this type of figure is the intersection of the pressure lines and the pressure build-up limit lines at the different conditions examined. It may be concluded that the slight initial pressure artifact is only a minor perturbation.

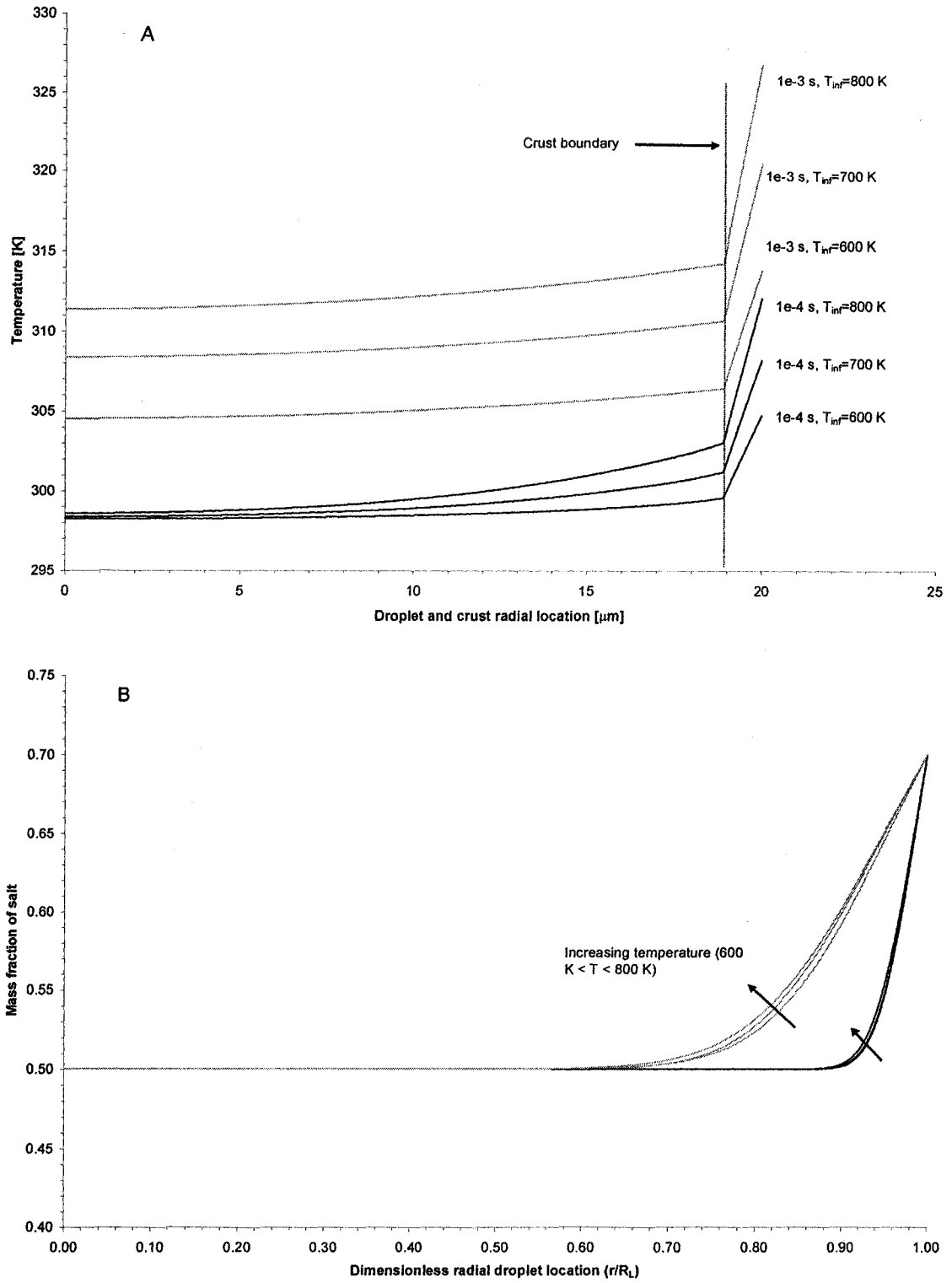


**Fig. 7. 5 Temperature profile in the droplet and crust (A) and mass fraction profile in the droplet (B) as a function of radial distance and temperature at $1x10^{-4}$ and $1x10^{-3}$ s (P=0.3 atm for 40 μm diameter droplets, $Z_{Ar}=0.3/Z_{O2}=0.7$, ε=0.5, $R_{sp}$=20nm)**

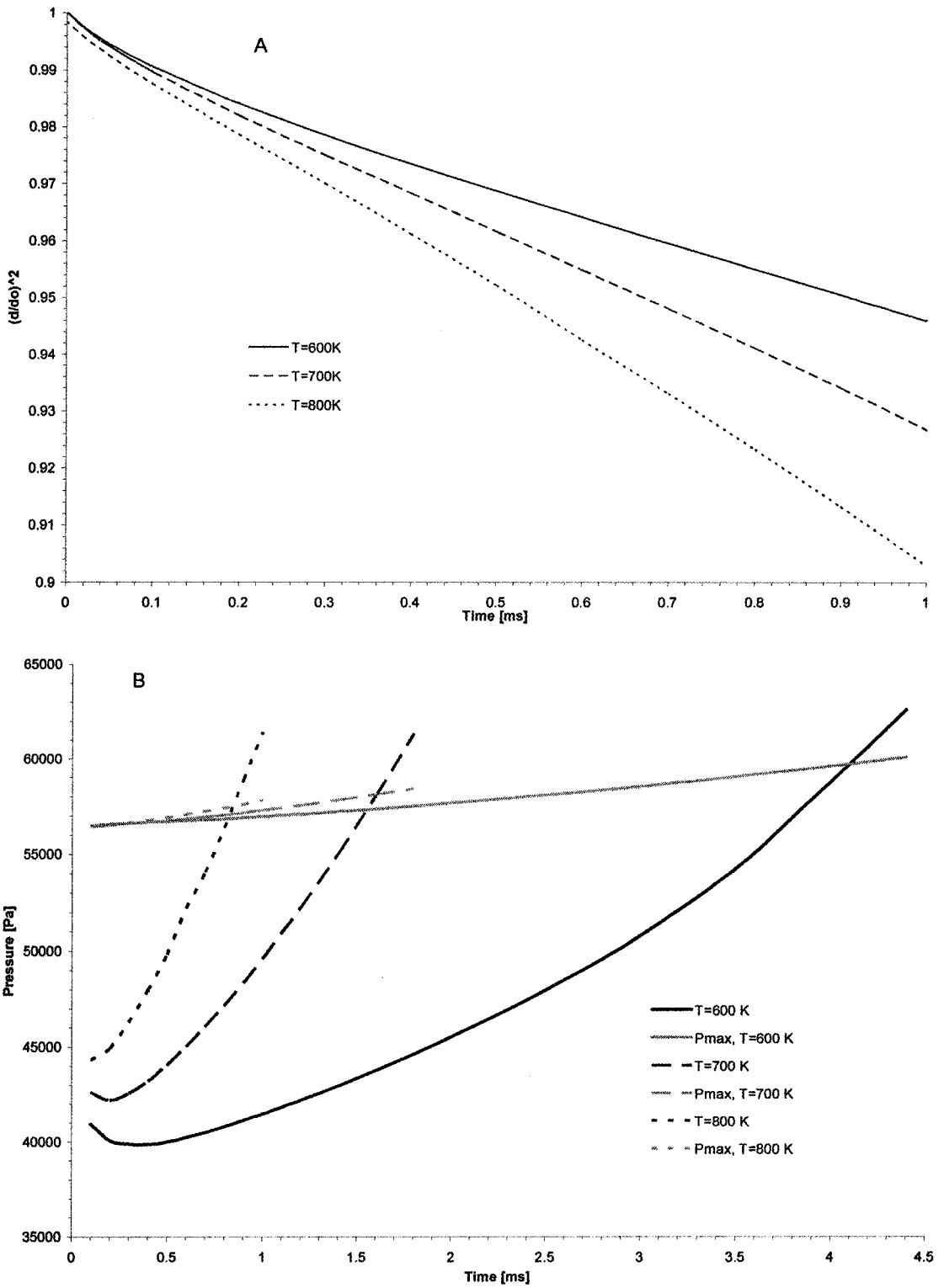


**Fig. 7. 6 Evolution of droplet diameter (A) and pressure build-up (B) as a function of time for different plasma temperatures (P=0.3 atm for 40 μm diameter droplets, $Z_{Ar}$=0.3/$Z_{O2}$=0.7, ε=0.5, $R_{sp}$=20nm)**

### *7.4.2 Effect of initial droplet size*

The temperature and mass fraction profiles are plotted for different initial droplet diameters (Fig. 7.7a and 7.7b, respectively). It can clearly be observed that the temperature inside the droplet and along the porous crust is higher with smaller droplets. The heat transferred from the surrounding gas to the crust and into the droplet increases as droplets decrease in size due to the higher surface to volume ratio of smaller droplets. Therefore, small droplets are heated up faster than larger ones. The rate of mass transfer also increases with decreasing droplet size but once again the mass transfer process is much slower than heat transfer.

As a consequence of the reduced size and higher temperatures, it is expected that smaller droplets will build up pressure at a faster rate. The pressure at the droplet/crust interface is plotted in Fig. 7.8. This figure shows that smaller droplets reach the critical bursting pressure earlier than large ones. However, smaller droplets also have greater shell strength, as predicted by equation 41. The pressure build-up at the droplet core seems to outpace this increasing strength and thus even droplets 30 μm in diameter will burst. The time of droplet bursting is more sensitive to a change in temperature than it is to a change in droplet size (Fig. 7.6b and 7.8, respectively). This was calculated by taking the maximum $\Delta T/T$ and $\Delta R_L/R_L$ ratios using the base case as reference and comparing these ratios at the corresponding $\Delta t$. The results indicate that the droplet bursting time is approximately 6 times more sensitive to temperature than it is to droplet size.

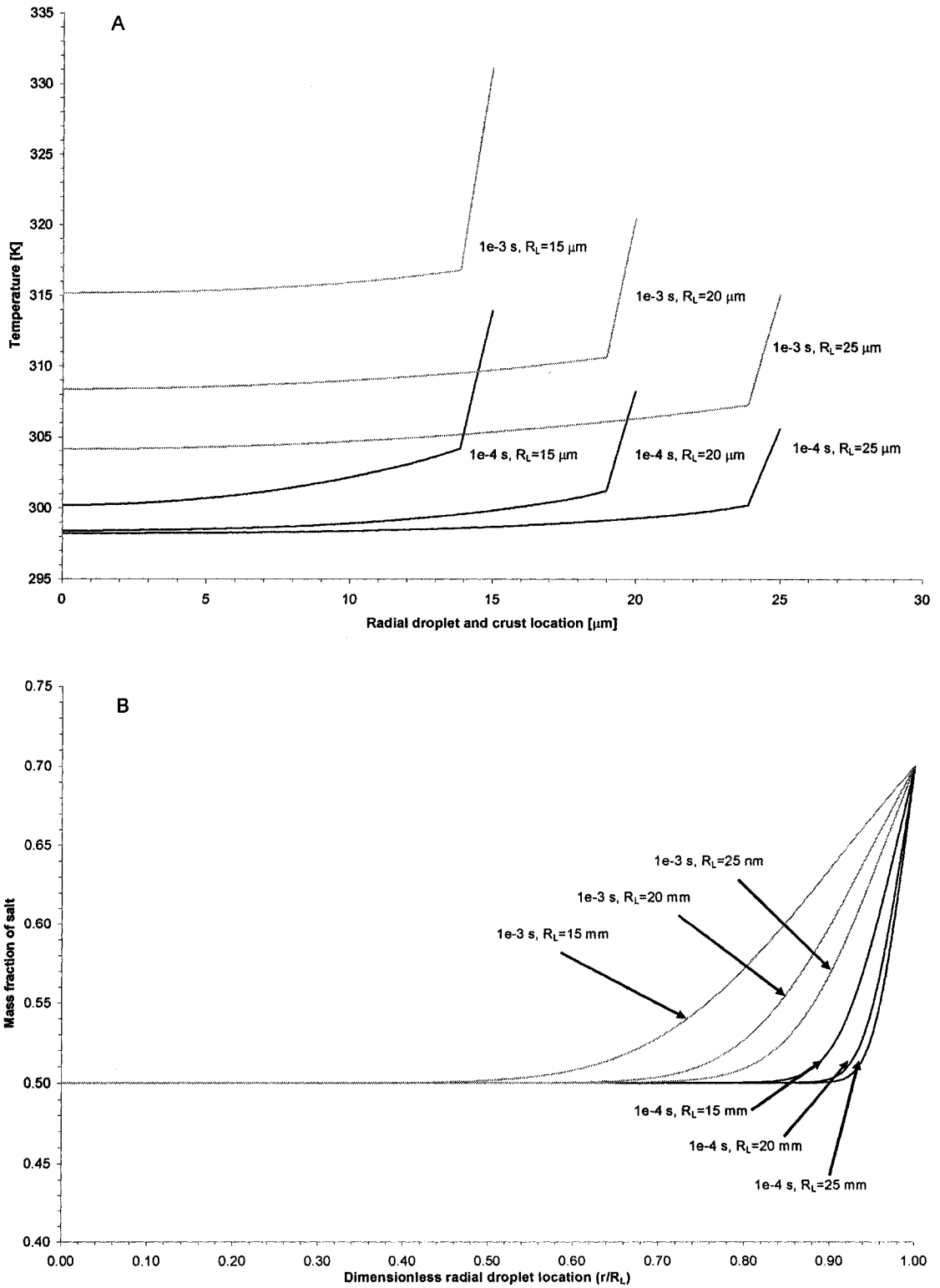


**Fig. 7. 7 Temperature profile in the droplet and crust (A) and mass fraction profile in the droplet (B) as a function of radial distance and initial droplet size at $1x10^{-4}$ and $1x10^{-3}$ s (P=0.3 atm, $T_\infty$=700 K, $Z_{Ar}$=0.3/$Z_{O2}$=0.7, ε=0.5, $R_{sp}$=20nm)**

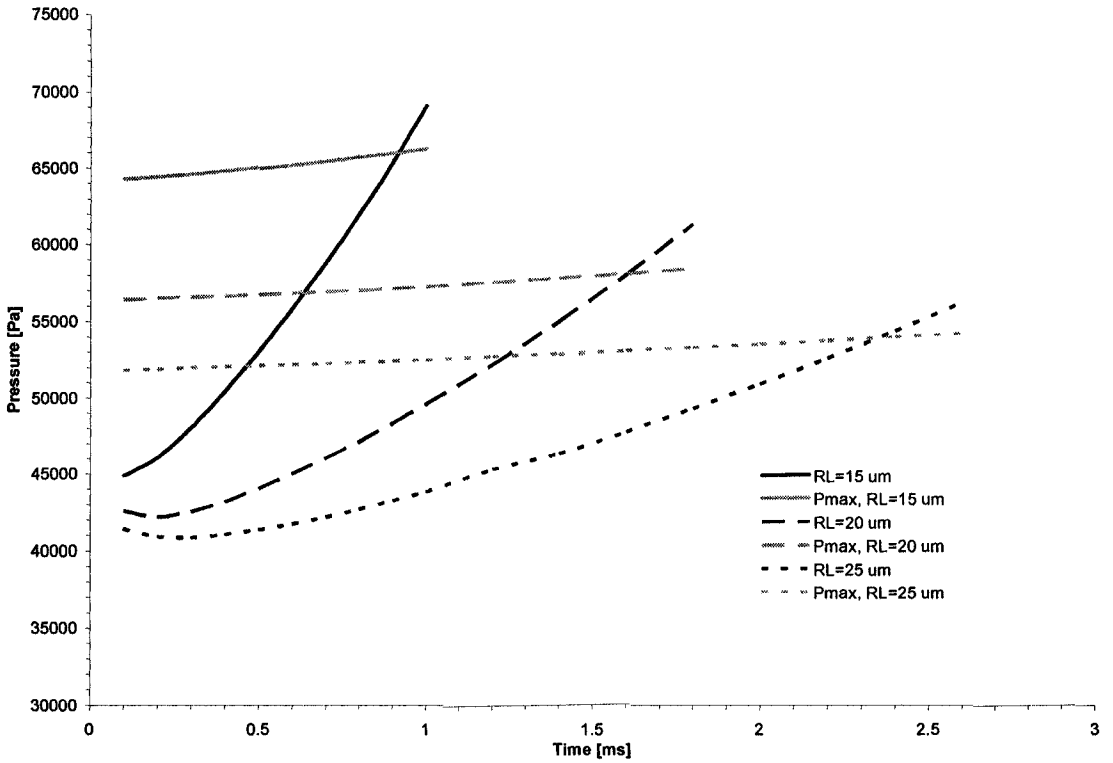


**Fig. 7. 8 Evolution of pressure build-up as a function of time for different initial droplet diameters ($P$=0.3, $T_\infty$=700 K, $Z_{Ar}$=0.3/$Z_{O2}$=0.7, $\varepsilon$=0.5, $R_{sp}$=20nm)**

### *7.4.3 Effect of surrounding pressure*

The pressure of the plasma gas was changed from 0.3 to 0.5 atm. The temperature profile inside the droplet is plotted at two different times in Fig. 7.9a. The pressure at the droplet/crust interface as a function of time is shown in Fig 7.9b. It can be seen that the temperature in the droplet increases with increasing pressure. The solvent needs a higher temperature to evaporate at the higher system pressure. The droplets subjected to higher pressures tend to burst slightly faster than those at lower pressures (Fig. 7.9b). The salt mass fraction and droplet shrinkage remain largely unchanged with pressure variations and thus were not plotted.

The fact that higher pressures favor droplet bursting can be further explained by analyzing both the thermal conductivity and crust permeability at different times (Fig. 7.10a and 7.10b, respectively). The crust thermal conductivity is a combination of the

conductivity of the gas present in the crust and conductivity of the solid crust material. The solid conductivity is unaffected by pressure but the thermal conductivity of the gas increases with pressure. Also, the crust permeability decreases with increasing pressure. This is a consequence of the Knudsen effect. The mean free path is dependent on pressure, temperature and viscosity. As pressure increases, the viscosity of the gas decreases causing a lowering of the permeability of the crust. Consequently, higher pressures provide slightly higher heat transfer and lower permeability. This favors solvent evaporation and also reduces gaseous solvent flow across the porous crust, hence promoting pressure build-up and crust breakage.

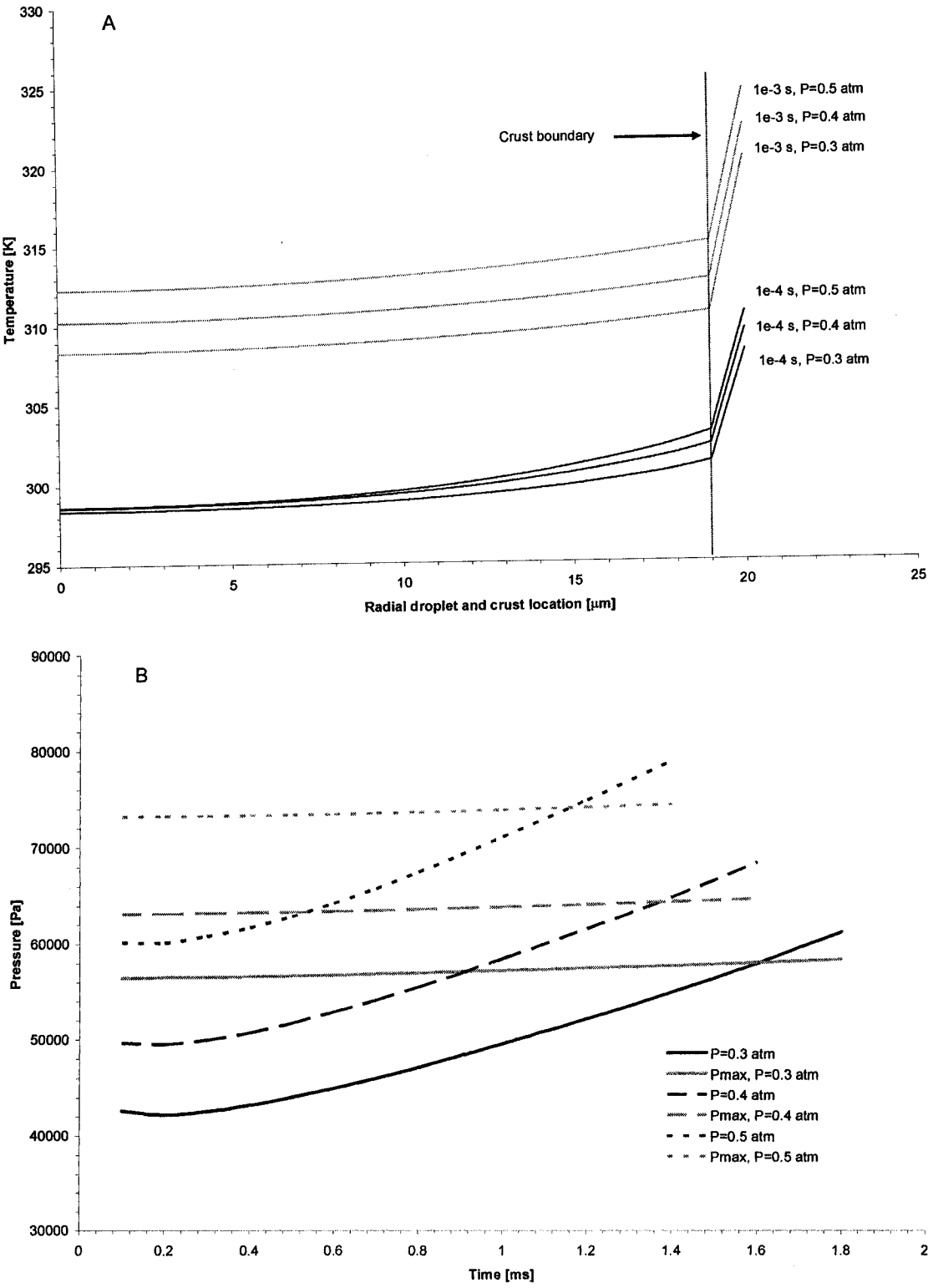


**Fig. 7. 9 Temperature profile in the droplet and crust (A) as a function of radial distance and pressure at $1x10^{-4}$ and $1x10^{-3}$ s and evolution of pressure build-up as a function of time (B) for different pressures ($T_\infty$=700 K for 40 μm diameter droplets, $Z_{Ar}$=0.3/$Z_{O2}$=0.7, ε=0.5, $R_{sp}$=20nm)**

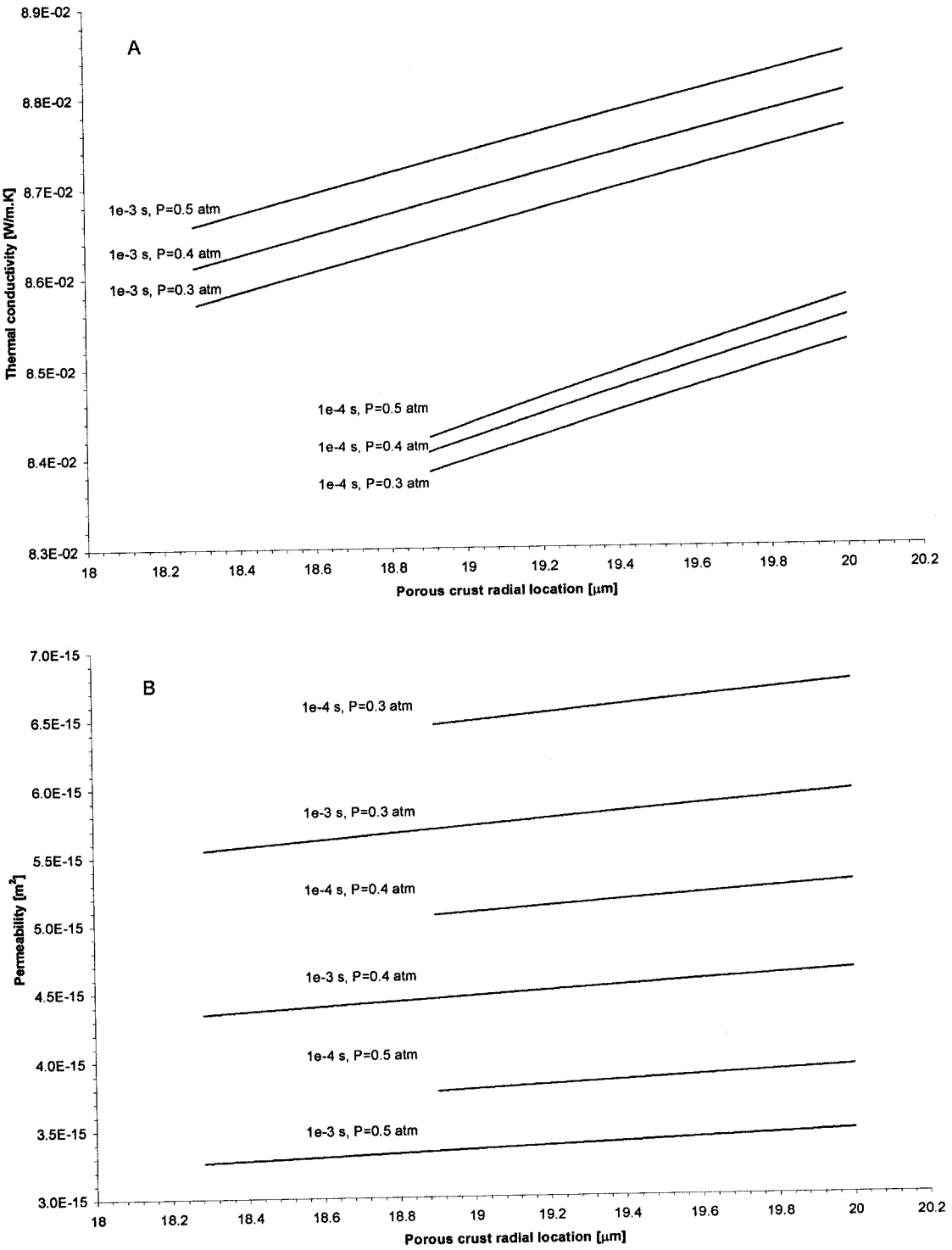


**Fig. 7. 10 Thermal conductivity (A) and crust permeability (B) in the porous crust as a function of radial distance at $1x10^{-4}$ and $1x10^{-3}$ s for different pressures ($T_\infty$=700 K for 40 μm diameter droplets, $Z_{Ar}$=0.3/$Z_{O2}$=0.7, ε=0.5, $R_{sp}$=20nm)**

### *7.4.4 Effect of shell porosity*

The crust porosity was varied from $\epsilon$=0.4 to 0.6 and temperature and droplet pressure are plotted in Fig. 7.11a and 7.11b, respectively. The droplet temperature remains almost unaltered despite the changing porosity although a steeper temperature gradient is observed for larger porosities. The pressure at the interface is significantly affected by larger porosities (Fig. 7.11b), and the time taken to reach bursting decreases as the porosity increases.

To further understand these results the thermal conductivity and permeability of the crust are plotted at different times in Fig. 7.12a and 7.12b. The thermal conductivity is appreciably affected by the change in porosity. Higher thermal conductivities are calculated with lower porosity values, because there is more solid material and the conductivity of the solid is higher than that of the gas. The permeability decreases with increasing porosity. This result is counterintuitive but it can be attributed to the Knudsen effect. In this model, the Knudnsen number lies in the transition regime between continuum and molecular flow. In this regime a change of porosity will not directly affect the permeability of the porous media. The permeability is more dependent on temperature and viscosity rather than on the number of porous channels present in the crust. The smaller porosity directly affects the thermal conductivity which in turn allows more heat to be transferred across the crust. This increases both the temperature and viscosity of the gas. The effect of temperature dominates and thus the permeability increases with decreasing porosity. Finally, as a result of lower permeability crusts, shells of larger porosity tend to break faster as solvent can not escape through the porous media and pressure builds-up.

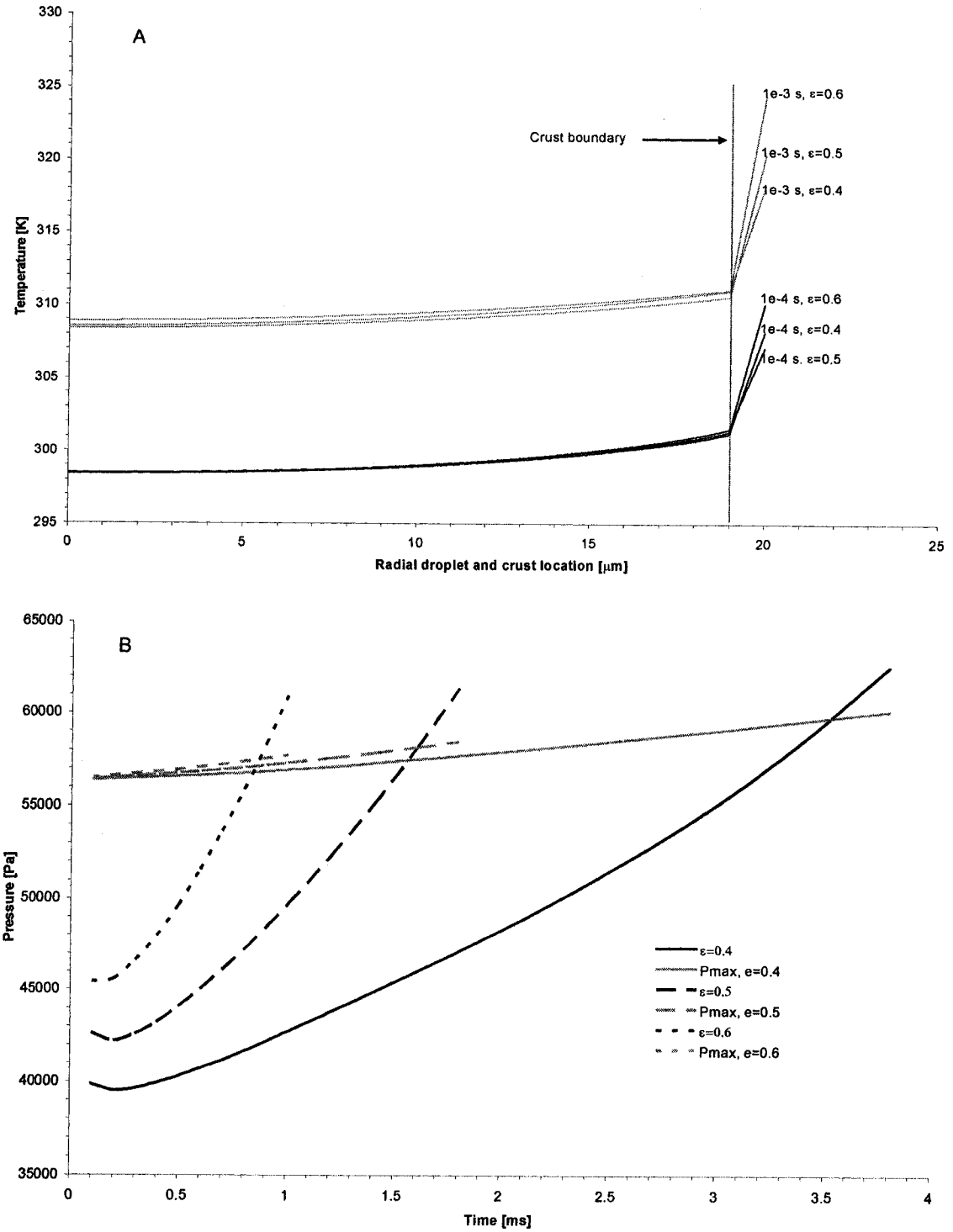


**Fig. 7. 11 Temperature profile in the droplet and crust (A) as a function of radial distance and porosity at $1x10^{-4}$ and $1x10^{-3}$ s and evolution of pressure build-up as a function of time (B) for different crust porosities (P=0.3 atm, $T_\infty$=700 K for 40 μm diameter droplets, $Z_{Ar}$=0.3/$Z_{O2}$=0.7, $R_{sp}$=20nm)**

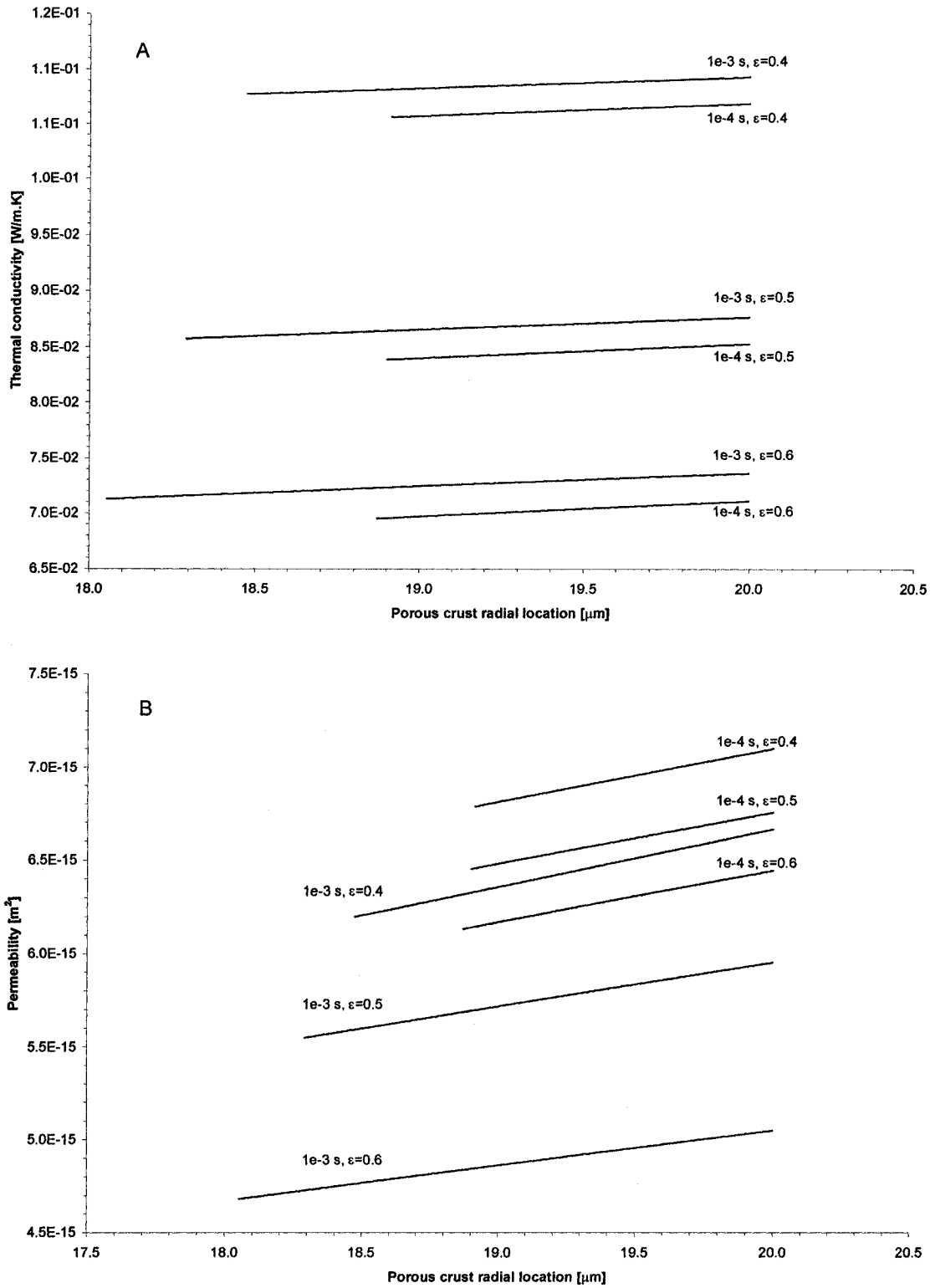


**Fig. 7. 12 Thermal conductivity (A) and crust permeability (B) in the porous crust as a function of radial distance at $1x10^{-4}$ and $1x10^{-3}$ s for different porosities (P=0.3 atm, $T_\infty$=700 K for 40 μm diameter droplets, $Z_{Ar}$=0.3/$Z_{O2}$=0.7, $R_{sp}$=20nm)**

### *7.4.5 Effect of size of precipitated crystals in porous crust*

The size of the precipitated spherical crystals forming the porous crust was varied from 10 to 30 nm in radius (10 nm $<R_{sp}<30$ nm). The temperature profile inside the droplet was plotted at different times in Fig. 7.13a and the droplet shrinkage was plotted in Fig. 7.13b. As the size of the crystals decreases, the temperature inside the droplet increases. This can be explained by higher pressures at the droplet/crust interface which result in a higher solvent evaporation temperature. The pressure increases at the interface because the flow of solvent across the crust meets a larger resistance as a consequence of lower permeability of the crust. In this model the crust pore sizes were assumed to be of the order of the precipitated crystals. The droplet shrinkage seems to remain unchanged despite this slight temperature difference (Fig. 7.13b) and the salt gradient inside the droplet was also unaffected.

The crust strength on the other hand is greatly affected by the crystal size (Fig. 7.14). The smaller crystals decrease the pore diameters and allow much less solvent to be present in the liquid bridges formed between crystals. As a result the crust strength is greatly weakened. A simplistic formula was employed in this model to calculate the crust strength as a function of crystal radius (equation 41). The results presented in this model could be refined if a more detailed and accurate model were to be employed but this is beyond the scope of this investigation.

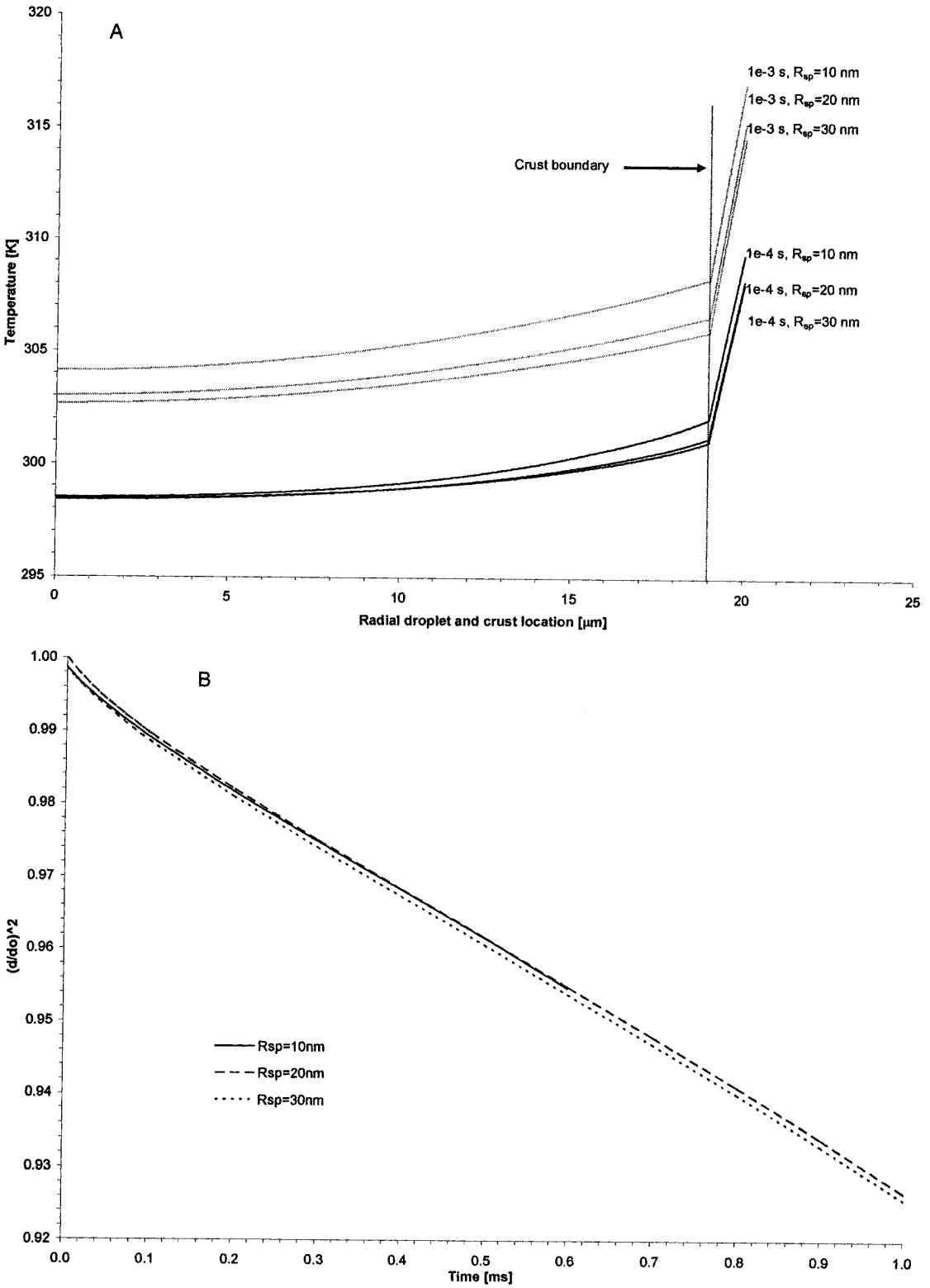


**Fig. 7. 13 Temperature profile in the droplet and crust (A) as function of radial distance and size of precipitated crystals at $1x10^{-4}$ and $1x10^{-3}$ s and evolution of droplet diameter (B) for different size crystals (P=0.3 atm, $T_\infty$=700 K for 40 μm diameter droplets, $Z_{Ar}$=0.3/$Z_{O2}$=0.7, ε=0.5)**

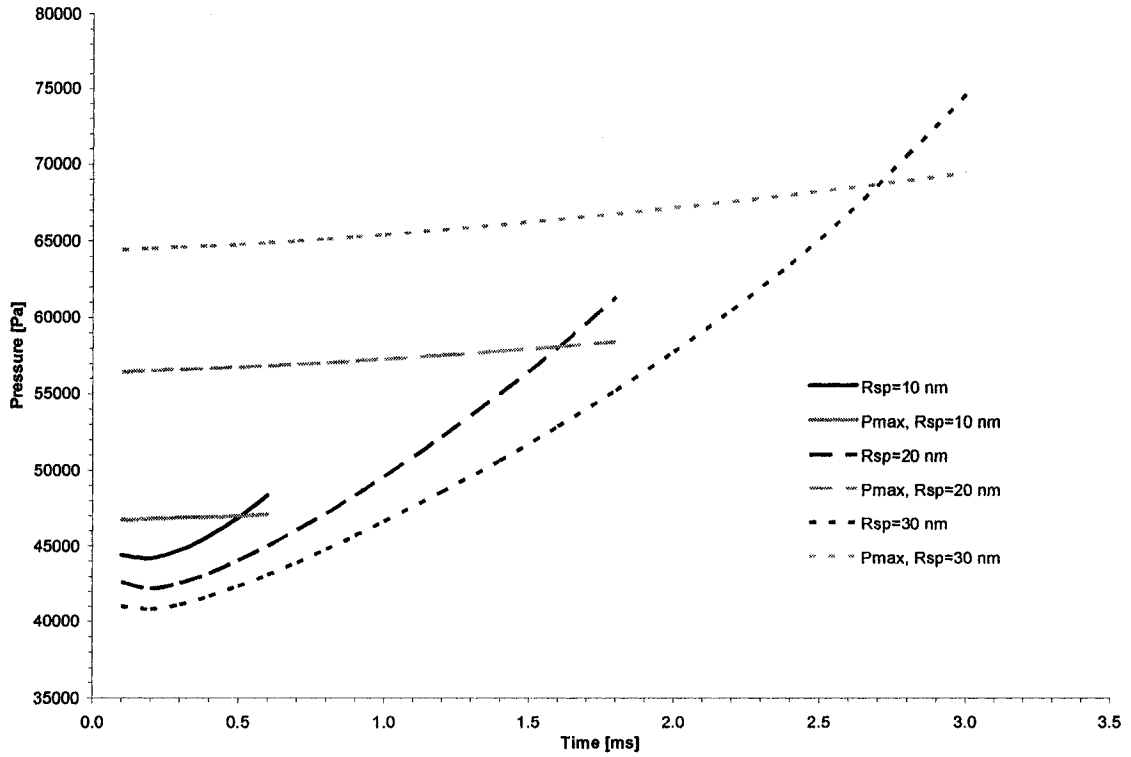


**Fig. 7. 14 Evolution of pressure build-up as a function of time for precipitated crystals size (P=0.3, $T_\infty$=700 K, for 40 μm diameter droplets, $Z_{Ar}$=0.3/$Z_{O2}$=0.7, ε=0.5)**

### *7.4.6 Effect of plasma gas composition*

The plasma gas composition was varied by changing the mole fraction of Ar and $O_2$ in the gas $0.6<Z_{O2}<0.8$. The temperature profile inside the droplet and the pressure at the droplet/crust interface were plotted in Fig. 7.15a and 7.15b, respectively. Oxygen rich plasmas have a higher enthalpy than argon rich plasmas at the same temperature, and thus can transfer more heat to the evaporating droplet. As a result, the temperature inside the droplet is slightly higher than for oxygen rich plasmas. The change of plasma gas composition seems to have a limited effect on the strength of porous crust and for all cases the crust burst at very similar exposure times, as shown in Fig. 7.15b.

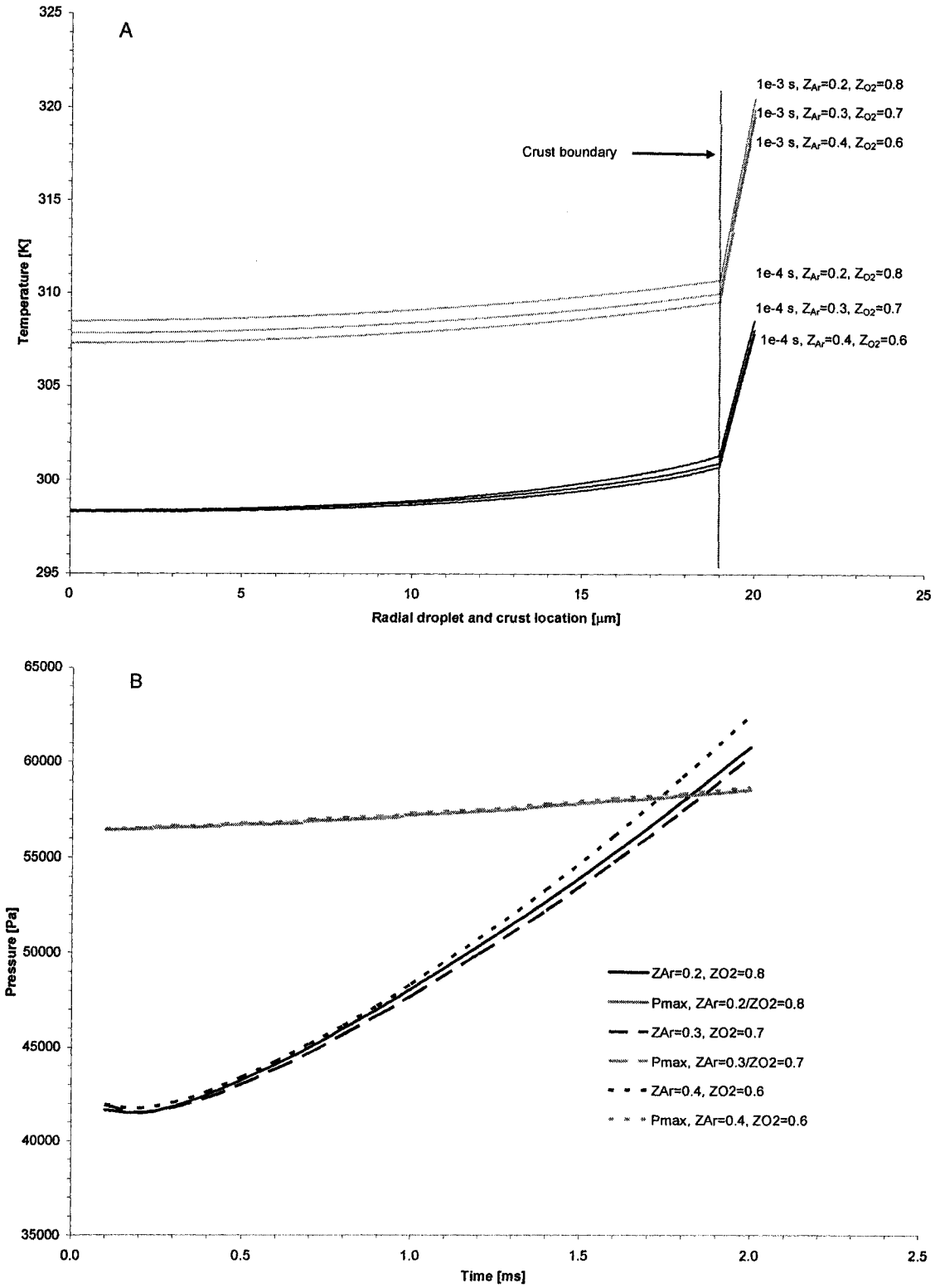


**Fig. 7. 15 Temperature profile in the droplet and crust (A) as a function of radial distance and gas composition at $1x10^{-4}$ and $1x10^{-3}$ s and evolution of pressure build-up as a function of time (B) for different gas compositions (P=0.3 atm, $T_\infty$=700 K for 40 μm diameter droplets, ε=0.5, $R_{sp}$=20nm)**

## 7.5 Conclusions

The heat, mass and momentum transfer of an evaporating droplet surrounded by a crust have been solved. Also, a simple model has been developed to understand crust bursting and it has shown that bursting occurs in all cases within the range analyzed. The plasma temperature, initial size of the solution droplet and size of the precipitated spherical crystals played a major role in this process. The effect of crust porosity on crust strength and crust bursting shows that crust permeability is the most important property. This in turn is closely associated with temperature, viscosity and pressure. The Knudsen correction has a large effect on the results obtained because it directly affects the crust permeability. The time for crust rupture lies in the few milliseconds range for all cases from the start of the exposure of the droplet with crust to the plasma gas.

The solvent evaporation and subsequent gaseous flow through the porous crust are largely driven by heat transfer. The flow across the porous crust is dependent on both heat and momentum transfer, whereas mass transfer is considerably slower than the other two processes.

A simple approximation was used to calculate the strength of liquid bridges formed at the crust/droplet interface. However, this approximation proved sufficient to determine a more realistic time of rupture for solution droplets surrounded by porous crusts than previous models reported in the literature.

## 7.6 Acknowledgements

The financial support by the Natural Sciences and Engineering Research Council of Canada and the Ministry of Education of the Province of Quebec through its FQRNT program is gratefully acknowledged.

## 7.7 References

1. Bouyer, E. Gitzhofer, F., Boulos, M. I., Suspension plasma spraying for hydroxyapatite powder preparation by rf plasma, IEEE Transactions on Plasma Science, **25**(5), 1066-1072 (1997)

2. Müller, M. et al., Thermal induction plasma processes for the synthesis of SOFC materials, *Materialwissenshchaft und werkstofftechnik*, **33**(6), 322-330 (2002)

3. Bouyer, E. et al, Thermal plasma chemical vapor deposition of Si-based ceramic coatings from liquid precursors, *Plasma Chemistry and Plasma Processing*, **21**(4), 523-546 (2001)

4. Delbos et al, DC plasma spray elaboration of fine structured coatings by ceramic liquid suspension injection, *Proceedings 16th International Symposium on Plasma Chemistry* (ISPC 16), Italy (2003)

5. Lau, Y. C., Kong, P.C., Pfender, E. Synthesis of zirconia powders in an RF plasma by injection of inorganic liquid precursors, *Ceramic Transactions 1*, 298-303 (1988)

6. Gitzhofer, F. et al. Integrated fabrication processes for solid-oxide fuel cells using thermal plasma spray technology, *MRS Bulletin*, **25**(7), 38-42 (2000)

7. Castillo, I. and Munz, R. Inductively coupled plasma synthesis of CeO2 –based powders from liquid solutions for SOFC electrolytes, *Plasma Chemistry and Plasma Processing*, **25**(2), 87-107 (2005)

8. Fauchais, et al, Plasma spraying from thick to thin coatings and micro to nano-structured coatings, , *Proceedings 16th International Symposium on Plasma Chemistry* (ISPC 16), Italy (2003)

9. Jia, L. and Gitzhofer, F. Collection of nano-powders generated by radio frequency (RF) plasma spray synthesis (PSS) processing, using a sampling probe, *Proceedings 17th International Symposium on Plasma Chemistry (ISPC 17)*, Canada (2005)

10. Yu, H. and Liao, W. H. Evaporation of solution droplets in spray pyrolysis. *Int. J. Heat Mass Transfer*. **41**(8-9), 993-1001 (1997)

11. Castillo, I and Munz, R. J. Transient heat and mass transfer of an evaporating stationary droplet containing dissolved cerium nitrate in a rf thermal argon-oxygen plasma under reduced pressure, *Inter. J. Heat Mass Transf.*, **50**(1-2), 240-256 (2007)

12. Charlesworth, D. H. and Marshall, W. R. Evaporation from drops containing dissolved solids, *AIChE Journal*, **6**(1), 9-23 (1960)

13. Elperin, T. and Krasovitov, B. Evaporation of liquid droplets containing small solid particles, *Int. J. Heat Mass Transfer*, **38**(12), 2259-2267 (1995)

14. Ozturk, A. and Cetegen, B. M. Modeling of plasma assisted formation of precipitates in zirconium containing liquid precursor droplets, *Materials Science and Engineering A*, **384**, 331-351 (2004)

15. Byun, D. Y. et al. Microexplosion of aluminum slurry droplets, *Int. J. Heat Mass Transfer*, **42**, 4475-4486 (1999)

16. Cho, S. Y., Some theoretical considerations on the combustion and disruption of free slurry droplets, Combust. Sci. and Tech, **67**, 37-57 (1989)

17. Orr, F. M., et al. Pendular rings between solids: Meniscus properties and capillary force, *J. Fluid Mech.*, **67**, 723 (1975)

18. Willett, C., et al. Capillary bridges between two spherical bodies, *Langmuir*, **16**, 9396-9405 (2000)

19. Tang, G. H., et al. Gas slippage effect on microscale porous flow using the lattice Boltzmann method, *Physical Review E.*, **72**, 056301 (2005)

20. Donea, J. et al. Arbitrary lagrangian eulerian methods, Enciclopedia of Computacional Mechanics, John Wiley and Sons, Chapter 14, Vol. **1** (2004)

21. Comsol, Comsol multiphysics: modeling guide, Version 3.2 (2005)

22. Callister W. D., Materials science and engineering: An introduction, *Wiley* 6$^{th}$ Ed. (2003)

23. Willet, C. D. et al. Capillary bridges between two spherical bodies, *Langmuir*, **16**, 9396-9405, (2000)

24. Heaviside functions, http://mathworld.wolfram.com/HeavisdeStepFunction.html

25. Cheong, H. W., A receding interface model for the drying of slurry droplets, *AIChE Journal*, **32**(8), 1334-1346 (1986)

26. Touloukian, Y.S. and Makita, T. Thermophysical properties of matter: Specific heat of non-metallic liquids and gases. Vol. **6**, *Plenum*, (1970)

27. Dean, J. A. Lange's Handbook of Chemistry, 15$^{th}$ Ed. McGraw Hill, (1999)

28. Reid, R. C. et al. The properties of gases and liquids. 4$^{th}$ Ed. McGraw Hill, (1987)

29. Rard, J. et al. Isopiestic determination of the activity coefficients of some aqueous rare earth electrolyte solutions at 25C. *Journal of Chemical and Engineering Data*, **22**(3), (1977)

30. Vasic, A., Cheng, A., Groeneveld, D. C., A comparison of predictions of high-temperature steam properties, *Nuclear Engineering and Design,* **132**, 367-379, (1992)
31. Boulos, M. I., Fauchais, P., Pfender, E. Thermal plasmas. Fundamentals and applications. Vol. 1, Plenum, (1994)
32. Bird, R. B., Stewart, W. E., and Lightfoot, E. N. Transport phenomena. John Wiley & Sons, 2nd Ed., USA, (2002)
33. FactSage™, The integrated thermodynamic databank system, Universite de Montreal, Quebec, Canada, 2001
34. Kaviany, M. Principles of heat transferred in porous media, Springer 2nd Ed, USA, (1995)
35. Tang, G. H. et al. Gas slippage effect on microscale porous flow using the lattice Boltzmann method, Physical Review E, **72**, 056301 (2005)

# Chapter 8 Determination of Particle Size Distribution by Laser Diffraction of Doped-$CeO_2$ Powder Suspensions: Effect of Suspension Stability and Sonication

In this chapter the methodology that was developed to measure the particle size distribution for doped $CeO_2$ and $CeO_2$ particles based on laser diffraction and $\zeta$-potential is described.


## Abstract

The particle size distributions (PSDs) of metal oxide powders are often determined by analyzing suspensions of powders using laser diffraction (e.g. Malvern MasterSizer 2000). Particle agglomeration can effectively bias the resulting distribution towards "unrealistic" particle sizes. Solutions to avoid this problem must be found if a particle distribution based on the elemental or primary particle sizes is desired.

In this work, the particle size distribution of doped-$CeO_2$ powders was studied. These powders show a crystalline single phase structure of controlled stoichiometry as determined by X-ray diffraction and ICP analysis. The apparent size distribution was found to be a strong function of suspension stability. Dispersant agents (PBTCA and phosphonoacetic acid) and suspension pH affected stability as characterized by zeta potential measurements. Sonication of the suspensions further enhanced particle de-agglomeration. Finally, only the combined effect of a dispersant agent, pH adjustment of the suspension and sonication provided a primary particle size distribution. The results presented in this work can be used in the analysis of similar ceramic powders in which strong particle agglomeration is present.



## Keywords

Dispersant agents, laser diffraction, particle size distribution, sonication, suspension stability, zeta potential,

## 8.1 Introduction

The determination of the particle size distribution is one of the most important parameters involved in powder characterization. Laser diffraction measurements are non-intrusive and simple to implement and are frequently employed to assess the size of particles in the *0.1* to *2000 μm* range (ISO 13320). These measurements require many materials, such as clays and metallic oxides, to be measured in liquid suspension where particle agglomeration becomes a major difficulty. The key to quality particle size measurements is then to have a well-dispersed sample.

Recently, cerium oxide ($CeO_2$) powders doped with samarium, yttrium or gadolinium have been identified to replace the conventionally used yttria-stabilized zirconia as alternative material for solid oxide fuel cell electrolyte films [1, 2, 3]. Furthermore, using a radio frequency inductively coupled plasma (RF-ICP) reactor to synthesize different doped $CeO_2$ powders has been proposed as a substitute technology over other conventional ceramic production methods [4, 5, 6]. The produced oxides exhibited a tri-modal particle size distribution (PSD), a feature seldom encountered in other material processing techniques. This suggests that multiple particle formation mechanisms are involved in the plasma synthesis of the $CeO_2$-based powders. The powders are produced from the in-flight calcination of atomized droplets. The following processes are believed to happen: droplet superheating and explosion, droplet evaporation followed by particle nucleation and growth or a combination of both [6], resulting in multimodal distributions. To further understand these phenomena, realistic PSD results of the primary particle sizes are desired. Therefore, the materials' tendency to agglomerate in aqueous medium must be overcome since agglomerated particles falsely suggest the presence of large particles in the samples.

Limited efforts have been devoted to study the relationship between suspension stability and particle size distribution, even though particle agglomeration is frequently encountered in metal oxide suspensions [7, 8, 9]. Frequently, suspension stability is associated with the settling time of the suspended solids or with the solid content of the suspension after centrifugation [10]. The different action of either the gravitational or

centrifugal forces acting on particles of different mass (i.e. large and small) could hinder the true stability of the suspension. For instance, Moughal [9] has found that calcium caseinate samples with the largest particles had the lowest suspension stability.

The objective of this project was to investigate the stability of different plasma synthesized doped cerium oxide suspensions, as determined by zeta potential measurements. This work discusses the relationship between suspension stability and the corresponding PSD. The effects of two different anionic dispersants, sonication and suspension pH on suspension stability were investigated.

## 8.2 Theory

A suspension consists of insoluble or slightly soluble solid particles dispersed within a continuous liquid phase and are considered stable if the number of particles remains relatively constant for an extended period of time [10]. Another parameter for characterizing the degree of repulsive forces, and hence the stability of a suspension, is the zeta ($\zeta$) potential. In colloid science, a suspension having an absolute value of $\zeta$-potential above $30\ mV$ is considered to have sufficient repulsive force between the particles to help inhibit agglomeration [12]. Experimental $\zeta$-potential measurements of suspensions are most commonly obtained using the electrophoretic light scattering (ELS) technique [13], which was used in this project to obtain $\zeta$-potential measurements (ZetaPlus Zeta Potential Analyzer from Brookhaven Instruments Corporation).

Laser diffraction techniques are common and reliable methods used in both industrial and university environments to obtain the PSD of materials. The Mastersizer performs light scattering experiments to produce different patterns of scattered light. These patterns can then be analyzed and, by applying the Mie light scattering theory along with other numerical algorithms proprietary to the manufacturer, the resulting diffraction patterns can be related to a certain particle size distribution [14].

## 8.3 Experimental Methodology

### *8.3.1 Materials Employed*

The following three doped $CeO_2$ powders were investigated: $Ce_{0.887}Y_{0.114}O_{1.944}$, $Ce_{0.85}Gd_{0.15}O_{1.925}$, and $Ce_{0.9}Sm_{0.1}O_{1.95}$. These materials were previously synthesized using a RF-ICP reactor [6]. The two different anionic dispersants investigated in this project were phosphonoacetic acid (in powder form from Alfa Aesar) and 50% active content 2-phosphonobutane-1,2,4-tricarboxylic acid (PBTCA) supplied by Jiangsu Jianghai Chemical Factory in China. Figure 8.1 shows the molecular structure of the two dispersants used.

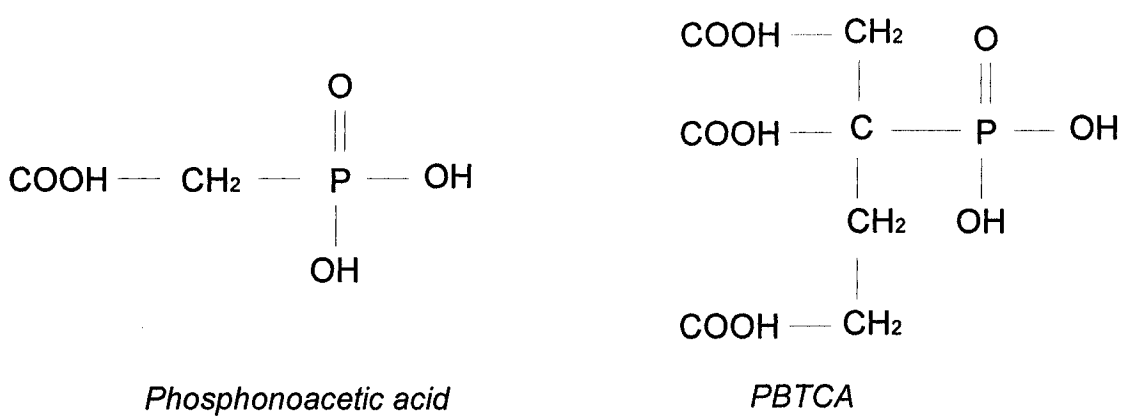


**Fig. 8. 1 Molecular structure of the 2 investigated dispersants**

### *8.3.2 Zeta-Potential Experiments*

For each doped $CeO_2$ powder, *2 mg* of each powder were weighed using a Sartorious S4 Ultramicro balance and placed inside a Fisher *50 mL* centrifuge vial. Using a pipette, *10 mL* of de-ionized water was added to each vial to create a suspension. De-ionized water was used to prepare all the suspensions. Based on previous findings, *2 wt%* of phosphonoacetic acid was added [15]. A *0.04 mL* PBTCA drop was added to the *10 mL* samples, which led to an active PBTCA concentration of *0.04 vol%*. The pH was adjusted using either hydrochloric acid (Fisher A144) or sodium hydroxide 5N solution (Fisher SS256B) from *pH=3* to *pH=10*. The pH values of the adjusted samples were noted to vary with time, mainly due to an equilibrium reaction between $H^+/OH^-$ ions and the metal

oxides' hydroxyl group. The samples were therefore allowed to sit undisturbed for *48* hours, at which time the pH was measured again and the necessary adjustments were made prior to running the experiments.

### *8.3.3 Instrumentation*

The zeta potential measurements of the suspensions were performed using the ZetaPlus Zeta Potential Analyzer from Brookhaven Instruments. Samples of *2 mL* were injected. All trapped bubbles were removed and the electrodes were thoroughly rinsed with de-ionized water. Four runs were performed for all the samples analyzed. The X-Ray diffraction analysis was done using a PHILIPS PW1710 powder X-ray diffraction system equipped with a copper X-ray source operated at *800* W. The Philips PC APD and Philips PC Identify software were used. Prior to analysis, all samples were air dried. The ICP optical emission analyses were done using a Thermo Jarrel Ash Trace Scan ICP spectrometer. The wavelengths used for elemental identification were *335.0* nm for Gd, *442.4* nm for Sm, *418.6* nm for Ce and *488.3* nm for Y.

### *8.3.4 PSD Experiments*

Based on the results obtained from the ZetaPlus experiments, a few samples were selected to be analyzed using the Mastersizer 2000. Larger volumes of these selected samples were made in *120 mL* graduate flasks: *20 mg* of the appropriate doped $CeO_2$ powders were dispersed in *100 mL* of de-ionized water. The corresponding amount of dispersant was also added, depending on the sample being prepared. The pH of the larger samples was then adjusted so that its value was within 0.1 of the original sample. Like the smaller samples prepared for the ZetaPlus, the larger samples were left undisturbed for *48* hours to allow the pH to stabilize. Any necessary pH adjustments were made prior to running the experiments with the Mastersizer.

In order to keep the particle concentration and the sample pH constant, the Hydro-S vessel (wet dispersion unit of the Mastersizer) was emptied after the background measurement had been obtained. Then, approximately *60 mL* of the pre-made sample was added directly. The stirrer/pump speed was set constant at *1500 rpm* for all experiments. Four to six PSD measurements were made per sample. The refractive index

of $CeO_2$ was 2.2 [16] and the absorption index was 0.1 with a weighted residual error of less than 1.5 % for all the measurements.

## 8.4 Results and Discussion

### *8.4.1 Morphology, Composition and Structure of $CeO_2$-based Powders*

The synthesized doped $CeO_2$ powders were examined using the Hitachi 4700 Field Emission Scanning Electron Microscope (SEM). The resulting SEM micrographs obtained provided information as to what types and sizes of particles were present. Three different types of particle sizes were observed for each powder. The largest of these, which could be described as hard agglomerates of the material, ranged in size between *5* to *20 μm*. Figure 8.2, a micrograph of a Gd-doped $CeO_2$ powder, illustrates these large agglomerates present in every sample.

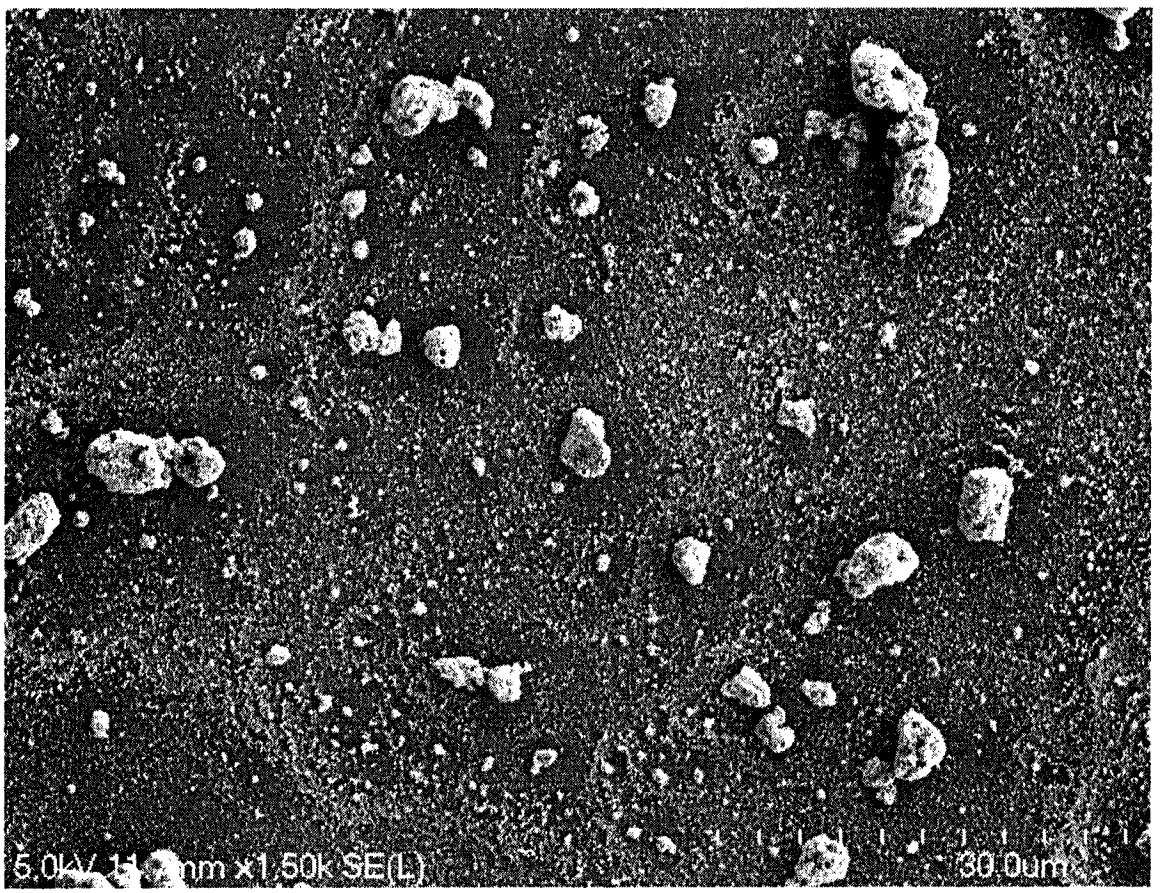


**Fig. 8. 2 SEM micrograph of a Gd-doped $CeO_2$ powder depicting agglomerates whose sizes range from approximately 5 to 20 μm.**

The next type of particles observed in the samples was dense spherical particles and loose agglomerates of porous material ranging in size from *~0.1* to *1 μm*. These are illustrated in Figure 8.3a and 8.3b, which correspond to Sm-doped and Y-doped $CeO_2$ powders, respectively.

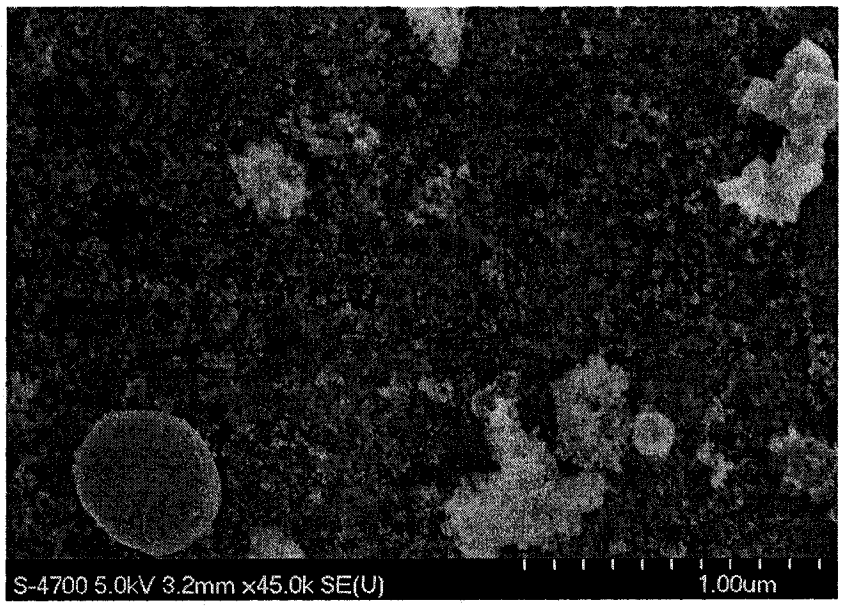


**(a)**

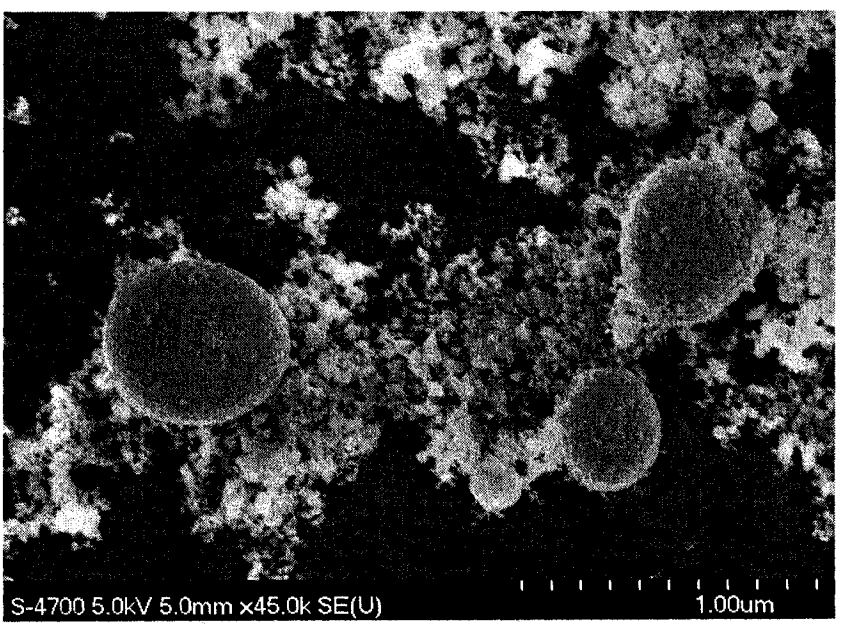


**(b)**

**Fig. 8. 3 SEM micrographs illustrating the presence of dense spherical particles and agglomerates ranging in size from 0.1 to 1 μm: *(a)* Sm-doped $CeO_2$ powder, *(b)* Y-doped $CeO_2$ powder**

Lastly, large amounts of nanoparticles were present in all the analyzed samples. These angular particles were less than *0.1 μm* (or *100 nm*, equivalently) in size. Figure 8.4 illustrates the nanoparticles present in a Sm-doped $CeO_2$ sample.

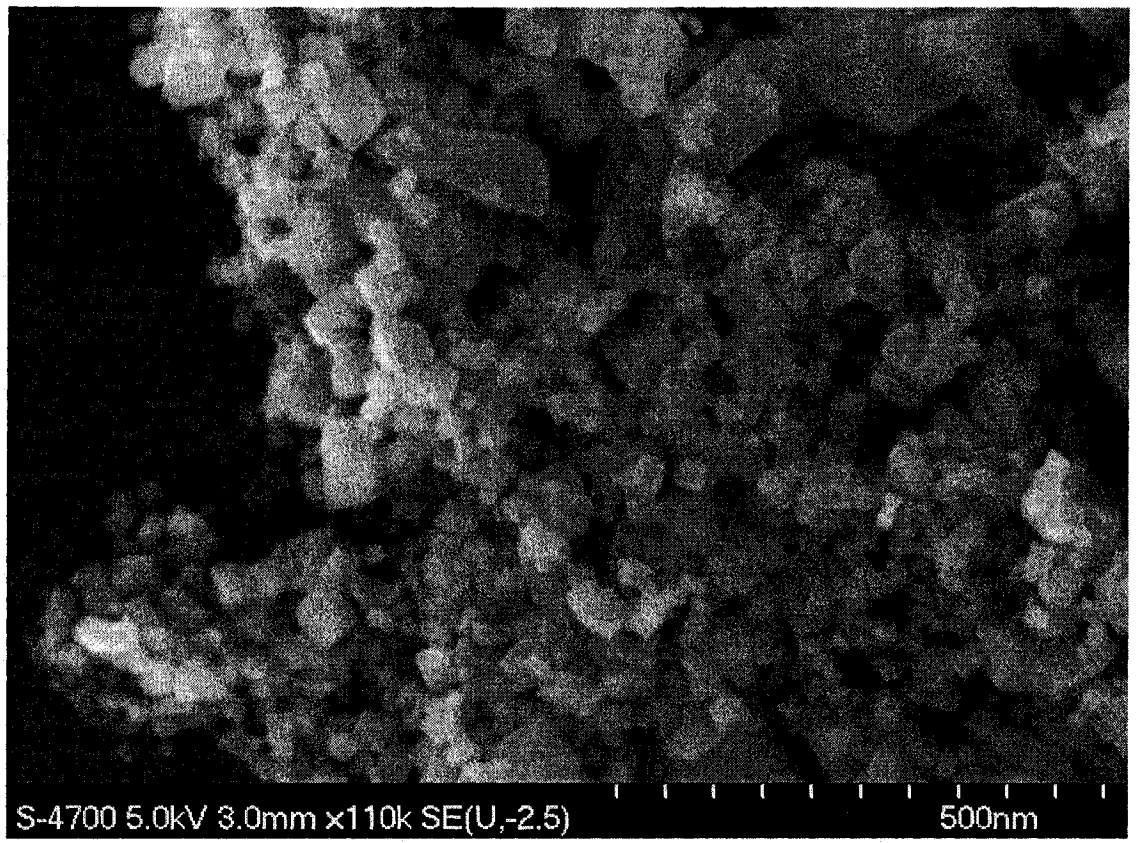


**Fig. 8. 4 SEM micrograph of a Sm-doped CeO2 powder showing angular nanoparticles sized less than 0.1 μm.**

Based on this information, PSD results showing multiple peaks for the different types of particles present in the samples could be expected. The stoichiometry of the particles was confirmed using ICP (inductively coupled plasma). The target powder composition was achieved within a 95% confidence interval (Table 8.I)

**Table 8.I As-synthesized particle stoichiometry**

| Target powder composition | Cerium content (Mole fraction) | | | Dopant content (Mole fraction) | | |
|---|---|---|---|---|---|---|
| | Ce $\mu$ | Std | 95% Confidence Interval | $\mu$ | Std | 95% Confidence Interval |
| $Ce_{0.85}Gd_{0.15}O_{1.925}$ | 0.834 | 0.019 | $0.804 < \mu < 0.864$ | 0.166 | 0.006 | $0.156 < \mu < 0.176$ |
| $Ce_{0.9}Sm_{0.1}O_{1.95}$ | 0.888 | 0.031 | $0.839 < \mu < 0.937$ | 0.112 | 0.002 | $0.109 < \mu < 0.115$ |
| $Ce_{0.88}Y_{0.12}O_{1.94}$ | 0.884 | 0.019 | $0.854 < \mu < 0.914$ | 0.116 | 0.002 | $0.113 < \mu < 0.119$ |

The synthesized particles showed a high degree of crystallinity as indicated by the sharp and narrow peaks obtained from the X-ray diffraction patterns (Figure 8.5). The typical fluorite structure is observed in all doped samples as compared to the reference fluorite structure of pure $CeO_2$ suggesting little disruption of the $CeO_2$ matrix.

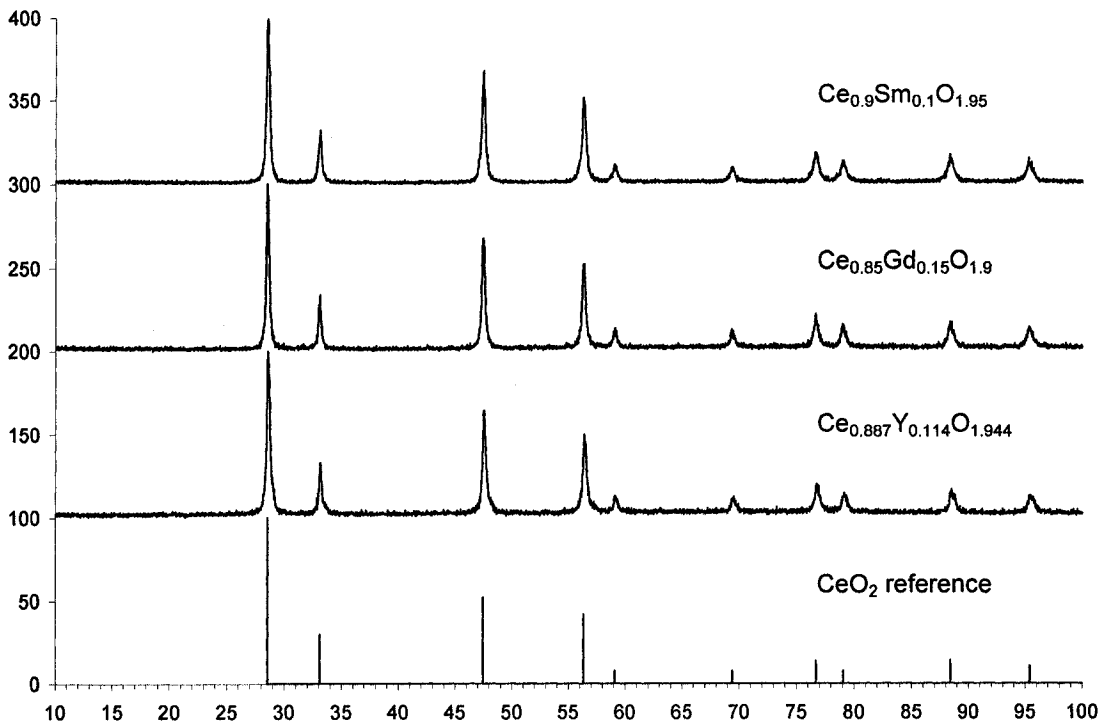


**Fig. 8. 5 X-ray diffraction patterns of plasma synthesized powders**

### *8.4.2 Visual Characterization of Suspension Stability*

The stability of a suspension is traditionally characterized by the settling time of the suspended particles. Figure 8.6 shows two different pH suspensions of Y-doped $CeO_2$, clear and cloudy. In the clear suspension, almost all particles settled after 48 hours. In contrast, the cloudy suspension shows how surface forces have kept particles apart and thus preventing particle settling.

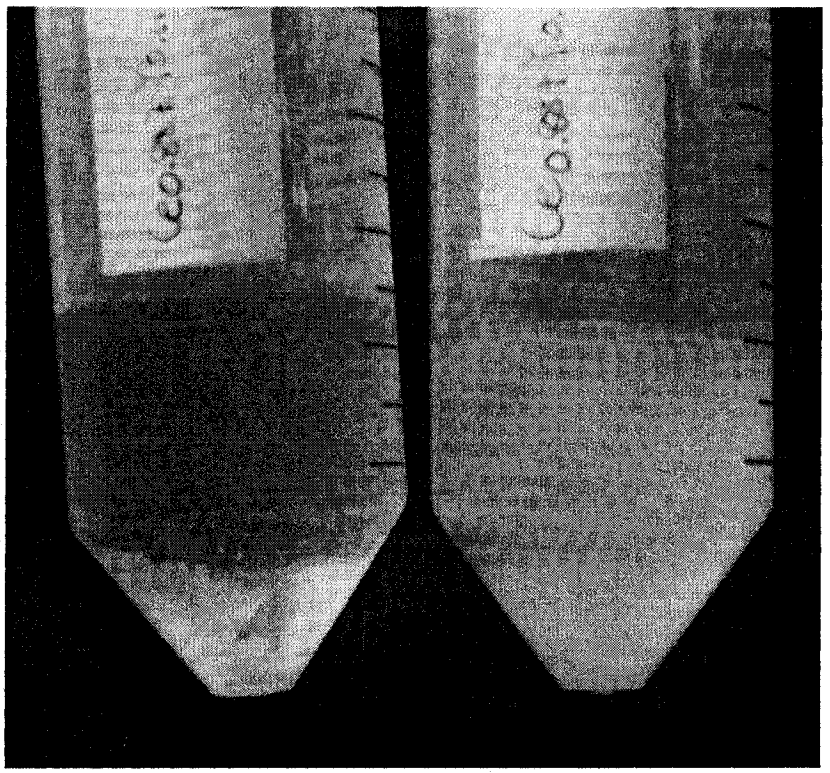

**Fig. 8. 6: (a) an unstable $Ce_{0.887}Y_{0.114}O_{1.944}$ suspension with $\zeta$-potential ~ 10 mV and a pH 8 showing a deposit of agglomerated oxide particles (b) a stable sample with pH ~ 5 and $\zeta$-potential ~ 40 mV characterized by a cloudy aqueous phase.**

The clear suspension had a pH close to the isoelectric point (IEP) (the point at zero $\zeta$-potential) whereas the stable suspension had a pH that was in the stable range. In this article, all samples referred to as "stable" showed an appearance similar to the stable Y-doped $CeO_2$ picture. The concept of stability will be later formalized with the $\zeta$-potential measurements.

### *8.4.3 Effect of pH on Suspension Stability and Corresponding PSD*

The $\zeta$-potential measurements of eight doped $CeO_2$ powder aqueous suspensions with no added dispersant are presented as a function of pH in Figure 8.7.

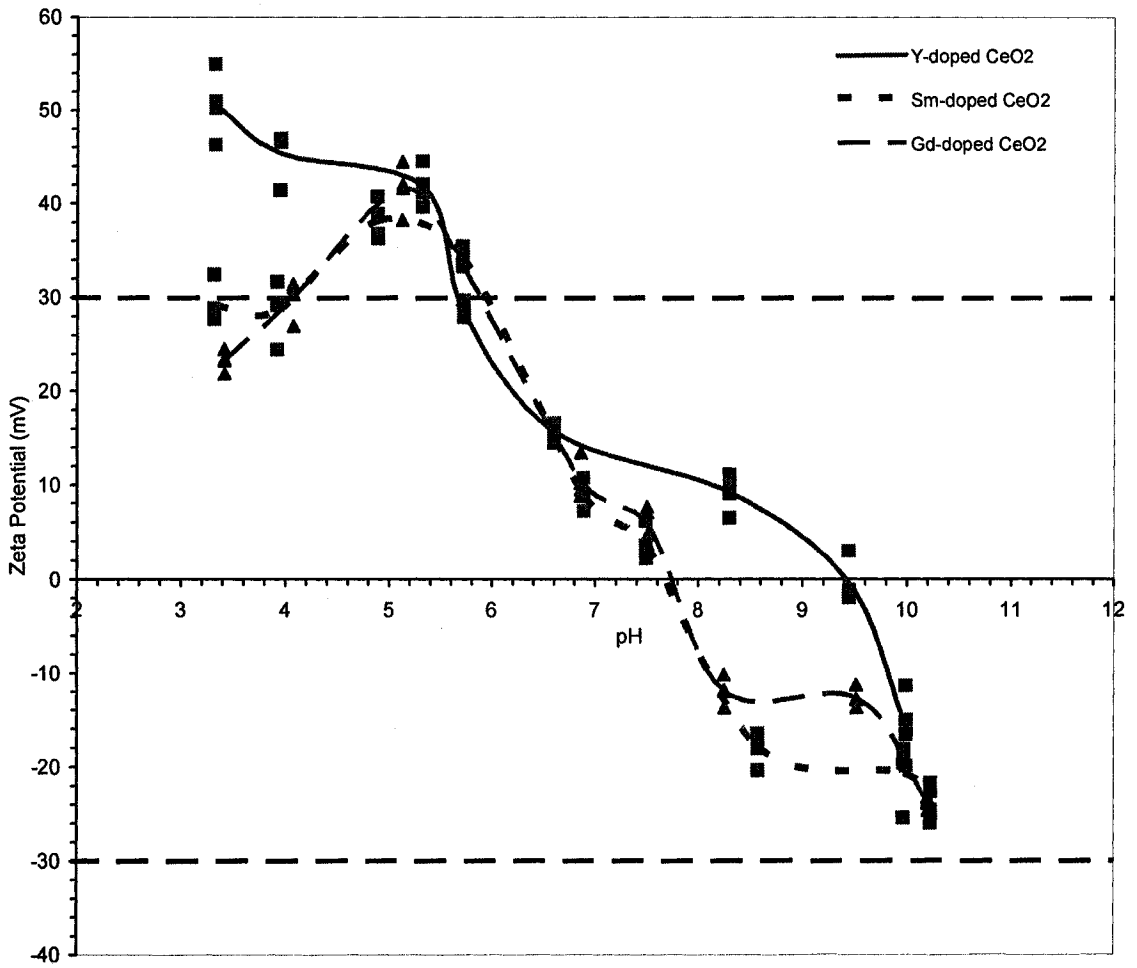


**Fig. 8. 7 Experimental results of $\zeta$-potential variation as a function of pH for aqueous doped $CeO_2$ suspensions having no added dispersants.**

The two $\zeta$-potential curves for both the $Ce_{0.85}Gd_{0.15}O_{1.925}$ and the $Ce_{0.9}Sm_{0.1}O_{1.95}$ materials follow the same trend. These curves indicate that the samples with a pH ranging from roughly 3 to 5 have the greatest degree of suspension stability since the $\zeta$-potential measurements were greater than or equal to $30\ mV$ in magnitude. The similarity between the Gd and Sm-doped $CeO_2$ curves could be attributed to the closeness of these two

transition elements in terms of chemical properties. Further, the IEP for the aqueous suspensions of both suspensions lies close to *pH=8*. All samples whose pH value resided close to this point of zero $\zeta$-potential showed the greatest degree of instability.

The curve of $\zeta$-potential variation as a function of pH of $Ce_{0.887}Y_{0.114}O_{1.944}$ oxide showed a slightly different trend than that of the other two oxides. This is because yttria is a second-row transition metal and therefore does not posses identical chemical properties as those in the Lanthanides series. Furthermore, the $\zeta$-potential curve showed a slight increase at a *pH=3*, which may result from the partial dissolution of yttria that has been reported to occur in acidic environments [15]. Like the other two oxides, the $Ce_{0.887}Y_{0.114}O_{1.944}$ samples that were visually observed to be the most stable had $\zeta$-potentials greater than 30 mV (in absolute magnitude) and a pH ranging from *3* to *6*.

The results presented thus far confirmed that the pH played an important role in affecting the stability of the aqueous oxide suspensions. Therefore, 2 samples of each dopant were chosen to determine the corresponding PSD (Table 8.II).

**Table 8.II Selected samples for PSD determination based on their stability**

| Sample | pH | $\zeta$-potential (*mV*) | Description |
|---|---|---|---|
| $Ce_{0.887}Y_{0.114}O_{1.944}$ | 3.5 | 50 | Stable |
| $Ce_{0.887}Y_{0.114}O_{1.944}$ | 6.7 | 16 | Unstable |
| $Ce_{0.85}Gd_{0.15}O_{1.925}$ | 5.2 | 40 | Stable |
| $Ce_{0.85}Gd_{0.15}O_{1.925}$ | 7.5 | 10 | Unstable |
| $Ce_{0.9}Sm_{0.1}O_{1.95}$ | 4.8 | 40 | Stable |
| $Ce_{0.9}Sm_{0.1}O_{1.95}$ | 7.6 | 4 | Unstable |

The PSD results obtained for all three stable samples and for the three unstable samples are presented in Figure 8.8(a) and 8.8(b), respectively.

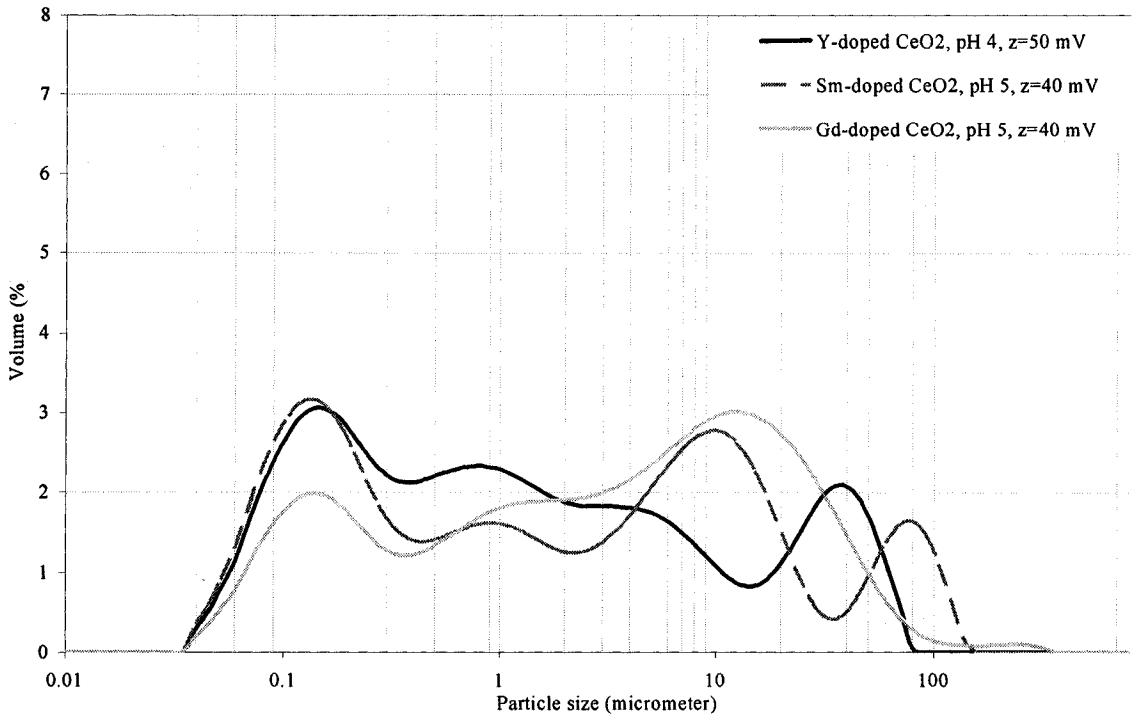


*(a)*

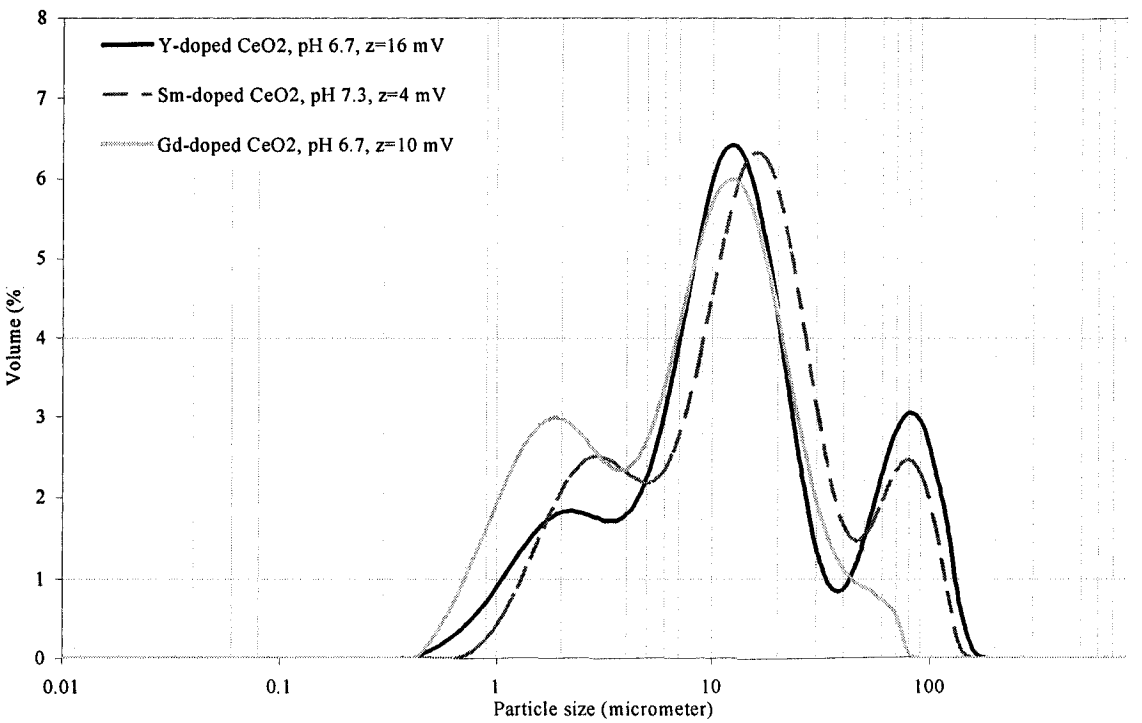


*(b)*

**Fig. 8. 8 PSD results for each of the doped $CeO_2$ oxides *(a)* stable samples *(b)* unstable samples**

The difference in stability, which arises only from a pH adjustment of the suspensions, leads to PSD peaks that differ by several orders of magnitudes. Based on a visual analysis of the SEM micrographs, it was determined that particles smaller than *1 μm* were dominant in the oxides. For the unstable samples shown in Figure 8.8(b), however, these small particles were not detected. Rather, the results obtained indicated that a great portion of the particles resided in the *5* to *20 μm* size range. A significant peak was also detected in the size range from *40* to *100 μm*. Since no such particles were observed with the SEM, the peak could therefore be the result of a large amount of particle agglomeration. Particle agglomeration would also explain why no significant amount of particles below *1 μm* was detected with the unstable samples. The repulsive forces between the nanoparticles were not strong enough to prevent their agglomeration, and thus they were not be detected by the instrument. The stable samples depicted in Figure 8.8(a) did show a more realistic PSD of the materials. In this case, the PSD results for the three materials show a peak in the *0.1 μm* size range that represents the nanoparticles. A slight peak was also observed in the 1 μm location, representing the spherical particles observed in the SEM micrographs. There was still evidence of some particle agglomeration illustrated by the peak ranging from *20* to *60 μm*, even though agglomerates exceeding *20 μm* in size were not observed in the SEM micrographs.

### *8.4.4 Effect of Dispersant Addition on Suspension Stability and Corresponding PSD*

Dispersant was added to the suspensions along with the subsequent pH adjustment in an attempt to further reduce the particle agglomeration and thus obtain superior PSD results for the oxides. In order to preserve material, the addition of both phosphonoacetic acid and PBTCA was investigated only on the Y-doped oxide, whereas only PBTCA was added to Gd and Sm-doped oxides. The $\zeta$-potential measurements shown in Figure 8.9 demonstrate the effect of adding the two different dispersants to the $Ce_{0.887}Y_{0.114}O_{1.944}$ suspensions.

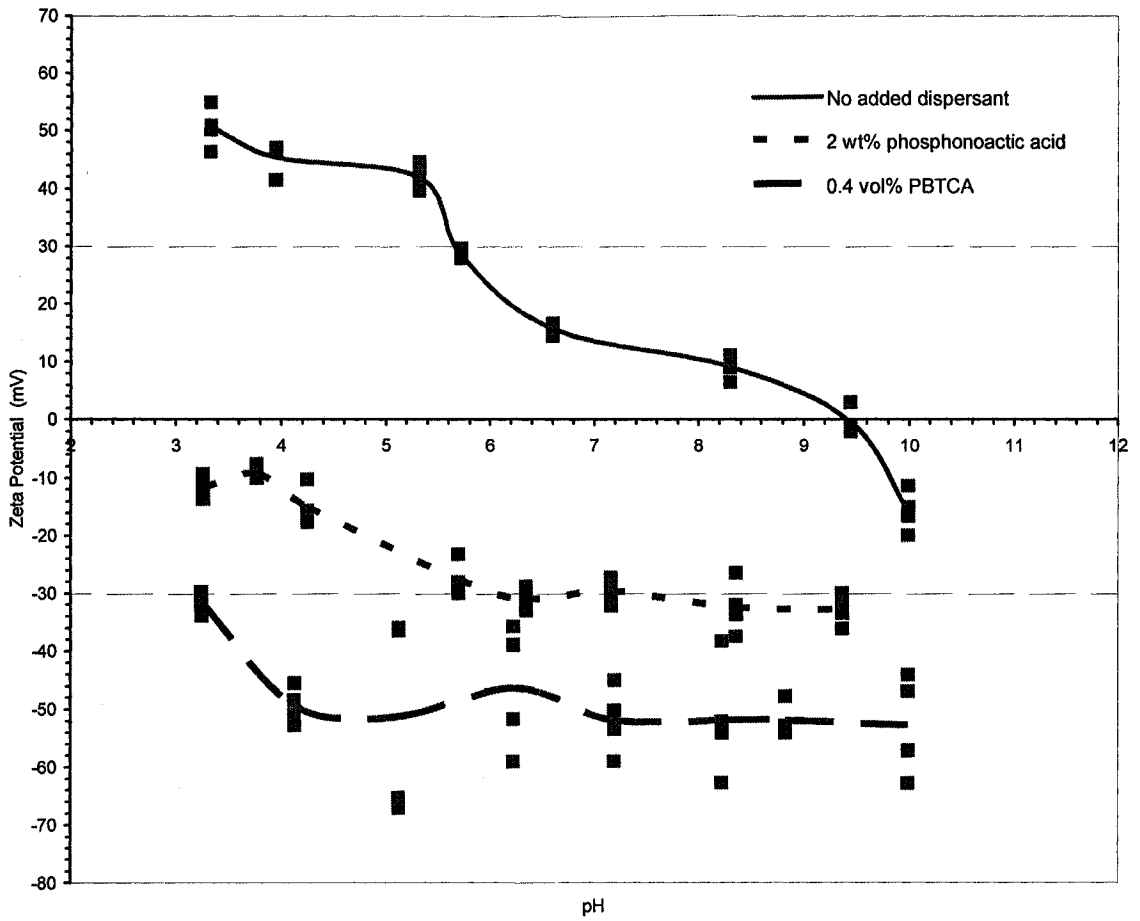


**Fig. 8. 9 Effect of adding two different dispersants to the $Ce_{0.887}Y_{0.114}O_{1.944}$ suspensions.**

The dispersed particles acquired a negative surface charge, as reflected by the increasingly negative values of the $\zeta$-potential. This indicated that both anionic dispersants had adsorbed onto the oxide particles, leading to an increased electrostatic repulsion between the particles as their surface charge was modified. The $Ce_{0.887}Y_{0.114}O_{1.944}$ samples that had once been unstable in the alkaline region were rendered stable by both dispersants, since the $\zeta$-potential dropped at or below the *-30 mV* line. The $\zeta$-potential measurements also revealed that PBTCA was a more effective dispersant than phosphonoacetic acid. PBTCA was able to increase the $\zeta$-potential to higher values over the pH range investigated, reaching a maximum magnitude of approximately *50 mV*. Phosphonoacetic acid, on the other hand, only allowed the

particles to attain a maximum $\zeta$-potential of $30\ mV$ in magnitude. The increased stabilization efficiency of PBTCA over phosphonoacetic acid can be explained by examining the dispersants' molecular structure. A PBTCA molecule has three carboxylic groups (-COOH) and one $-PO(OH)_2$ group. A phosphonoacetic acid molecule also includes the $-PO(OH)_2$ group, but only has one carboxylic acid group. When these dispersants dissociate in the suspension medium, the PBTCA molecule can carry up to five negative charges, as opposed to phosphonoacetic acid which can carry three. The adsorption behavior of dispersants on metal oxide surfaces can be described by the ligand-exchange model where the metal oxide in suspension can basically "exchange" its surface hydroxyl (-OH) group for other anions through a series of protonation reactions [17]. It has also been reported that phosphonyl groups have a high affinity for adsorbing onto metal oxide surfaces [17]. It can therefore be hypothesized that when a PBTCA molecule adsorbs onto the doped $CeO_2$ particle through its $-PO(OH)_2$ functional group, the three negative charges arising from the dissociated carboxylic acid groups are left free to modify the surface charge of the particle. Assuming the same adsorption mechanism occurs with phosphonoacetic acid, only one negative charge is left free to modify the surface charge. Figure 8.10 illustrates the corresponding PSD of the $Ce_{0.887}Y_{0.114}O_{1.944}$ samples having phosphonoacetic acid and PBTCA.

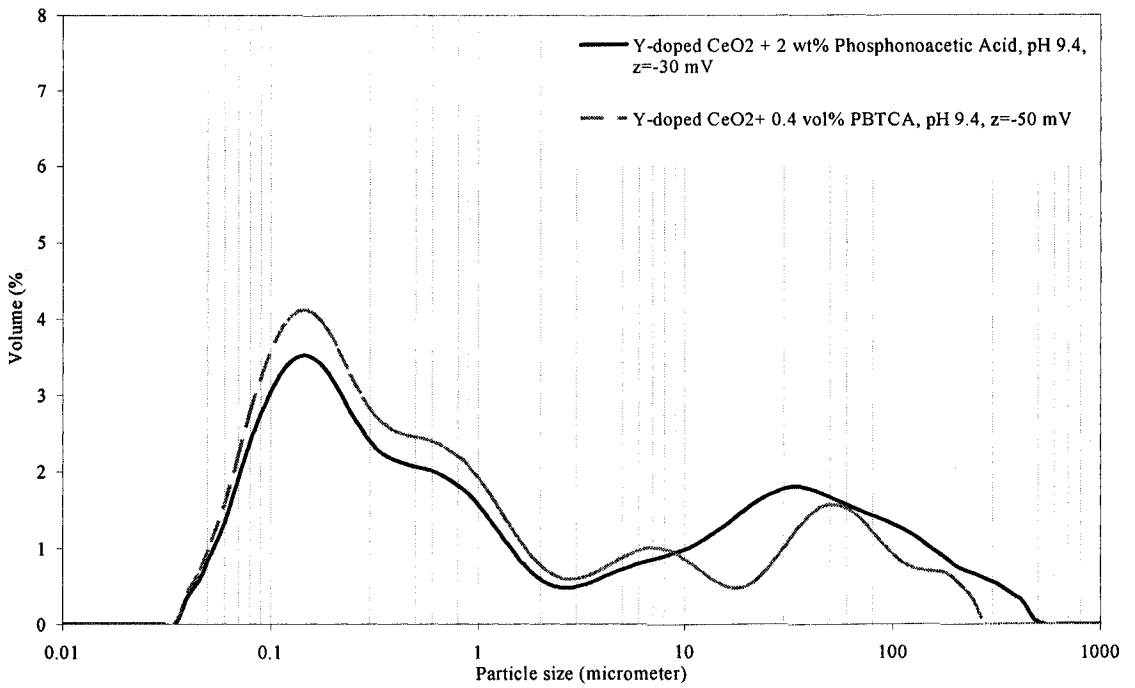


**Fig. 8. 10 PSD for $Ce_{0.887}Y_{0.114}O_{1.944}$ samples having phosphonoacetic acid and PBTCA as dispersants.**

The main particle size modes are located at similar particle diameters for both cases, despite the difference in $\zeta$-potential of about *20 mV* between the sample containing phosphonoacetic acid and the sample with PBTCA. The addition of PBTCA seemed to slightly improve the PSD judging from the lower volume fraction of particles in the *10-400 μm* size range. In general, the addition of dispersant resulted in a higher volume fraction of nanoparticles (in the 0.1 μm size), but particle agglomeration was not completely eliminated since the large particles exceeding *30 μm* in size were still present.

Upon determining the greater stabilizing effect PBTCA had over phosphonoacetic acid, PBTCA was added to the $Ce_{0.85}Gd_{0.15}O_{1.925}$ and $Ce_{0.9}Sm_{0.1}O_{1.95}$ oxide samples. Much like the results obtained with the $Ce_{0.887}Y_{0.114}O_{1.944}$ samples, the addition of PBTCA to the suspensions caused the $\zeta$-potential measurements to again increase up to *50 mV* in magnitude (Figure 8.11). Due to the consequent increase in electrostatic repulsion between the particles, almost all of the previously unstable samples became stable.

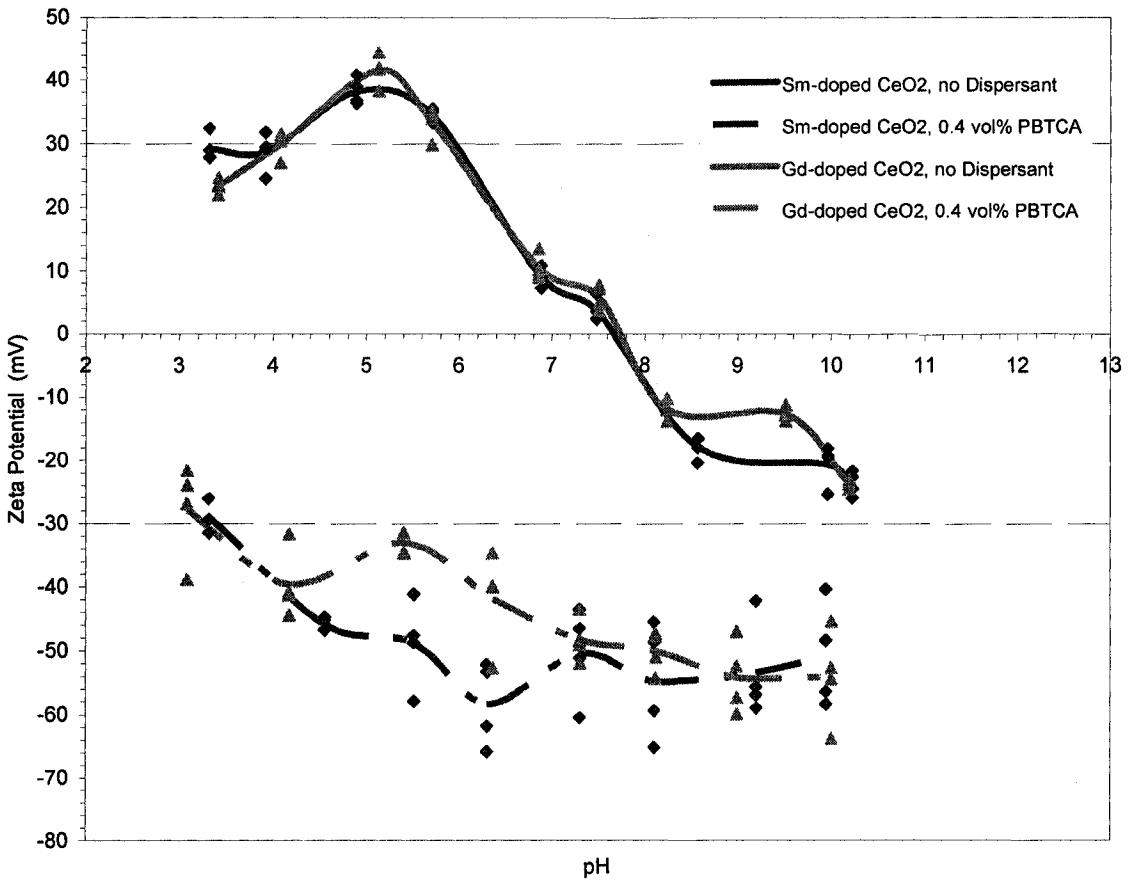


**Fig. 8. 11 Effect of adding PBTCA to the $Ce_{0.85}Gd_{0.15}O_{1.925}$ and $Ce_{0.9}Sm_{0.1}O_{1.95}$ oxide samples.**

Further comparisons of the Sm and Gd-doped samples are shown in Figure 8.12. The PSDs of stable pH-only-adjusted samples are compared to the ones containing PBTCA. Figure 8.12(a) depicts the PSD for a $Ce_{0.9}Sm_{0.1}O_{1.95}$ whereas Figure 8.12(b) shows the PSD for a $Ce_{0.85}Gd_{0.15}O_{1.925}$ for samples having similar pH. The two PBTCA samples had a $\zeta$-potential of *-50 mV*, whereas the ones having only pH adjustment had $\zeta$-potential of *-40 mV*. In both cases, the samples having PBTCA showed a higher volume fraction of nanoparticles, and hence a more realistic PSD. Nevertheless, the extensive peaks present for the larger particle sizes still indicated that particle agglomeration was occurring.

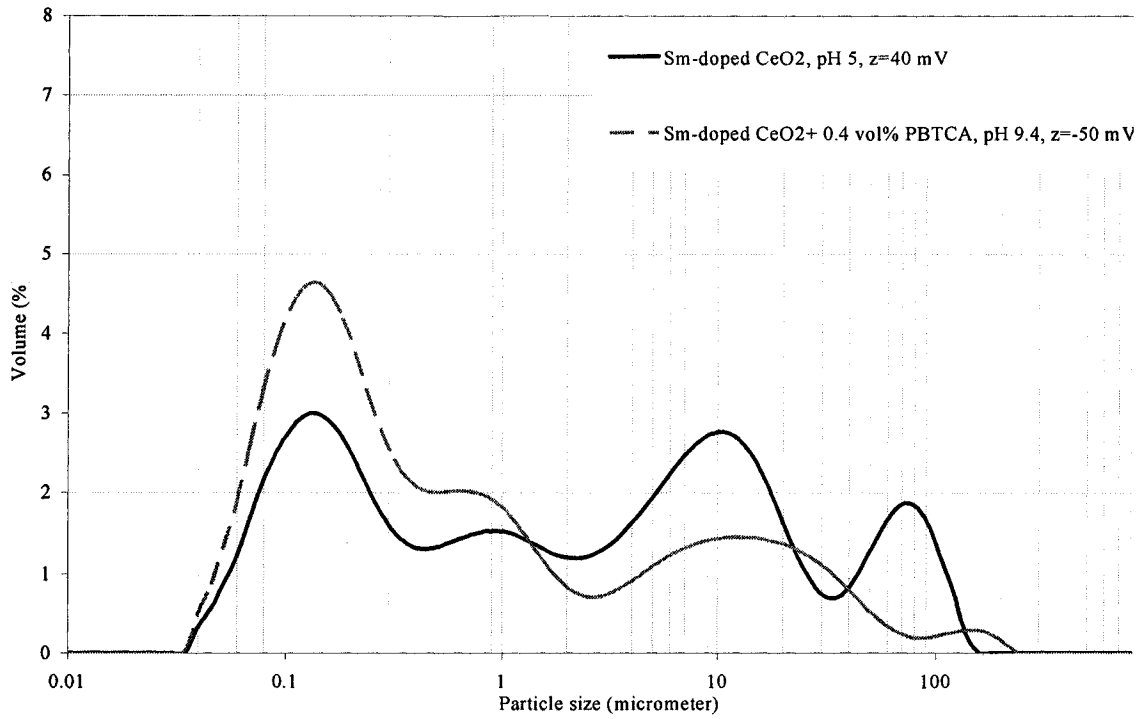


*(a)*

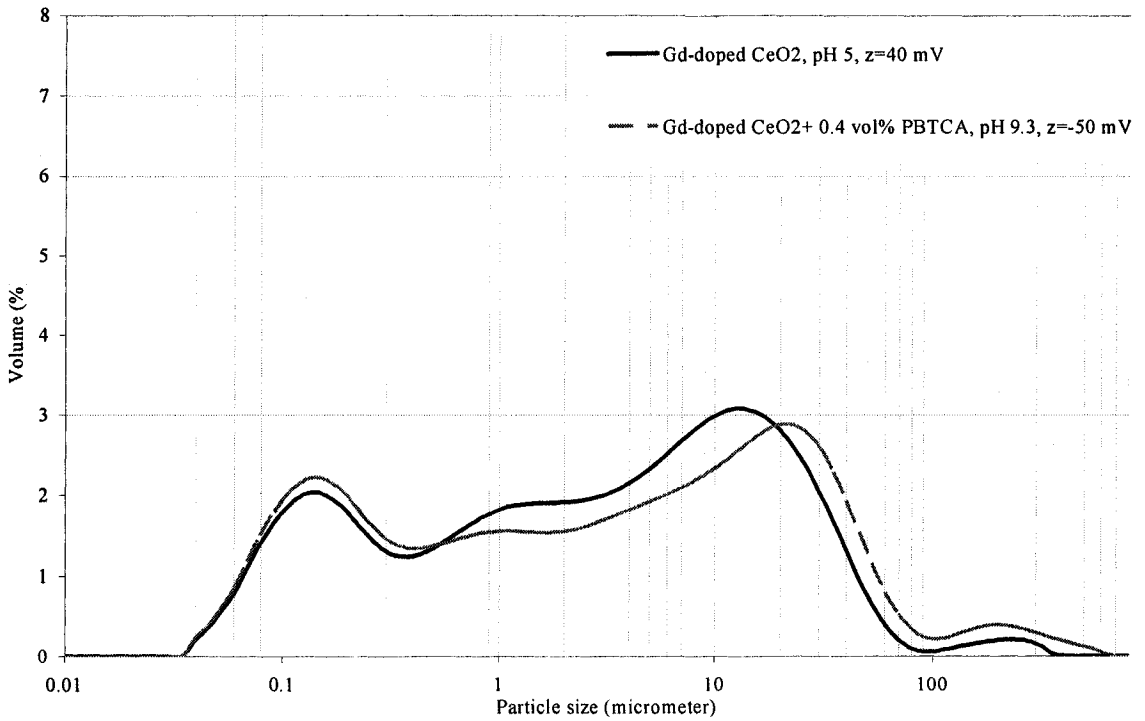


*(b)*

**Fig. 8. 12 Comparison of PSD for samples with PBTCA and samples having only a pH adjustment: *(a)* $Ce_{0.9}Sm_{0.1}O_{1.95}$ *(b)* $Ce_{0.85}Gd_{0.15}O_{1.925}$.**

### *8.4.5 Effect of Sonication on Suspensions having pH Adjustment and Dispersant Addition and Corresponding PSD*

Adding PBTCA as a dispersant definitely improved the stability of the doped $CeO_2$ suspensions, as noted from the increased magnitudes of the $\zeta$-potentials, but their PSD showed only a minor improvement over the PSDs of the suspensions having only a pH adjustment. Particle agglomeration was not completely eliminated. It was possible that the enhanced electrostatic repulsive forces created by PBTCA alone were not enough to overcome the physical interactions the particles experienced while re-circulating through the cell of the Mastersizer. Therefore, to further reduce particle agglomeration, the Mastersizer's ultrasonic probe was applied to the samples containing PBTCA. Figure 8.13 represents the progression of a $Ce_{0.887}Y_{0.114}O_{1.944}$ sample's PSD. The solid dark curve represents the stable samples having only a pH adjustment, the dotted curve represents a stable sample having a pH adjustment and added PBTCA, and the light solid curve represents a sample having a pH adjustment, PBTCA and sonication.

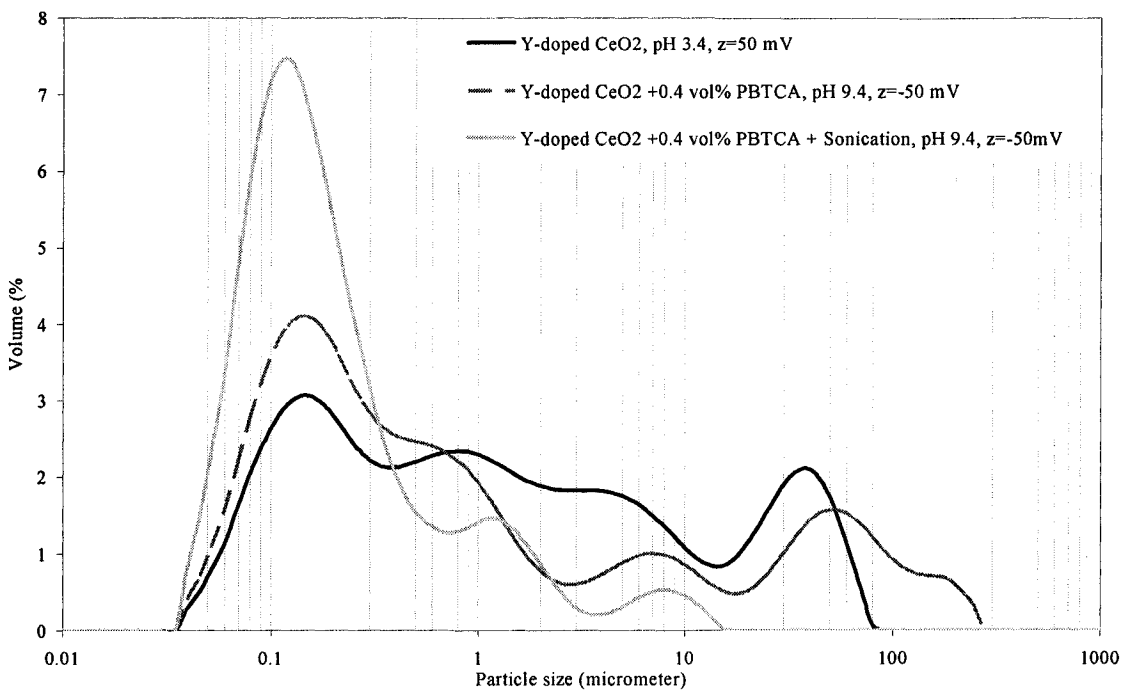


**Fig. 8. 13 Progression of the observed PSD for a $Ce_{0.887}Y_{0.114}O_{1.944}$ sample.**

It is possible to see a general shift of the PSD curves to the left, indicating that the larger agglomerates are being broken down into the individual particles. Adding ultrasound resulted in the expected tri-modal PSD, where each peak represents the three different types of particle sizes that were observed in the SEM micrographs. The largest of these peaks, located at the *0.1 μm* particle size, was indicative of the large volume fraction of nanoparticles. A smaller peak located at the *1 μm* particle size represented the spherical particles, and the last peak ranging from *~5* to *20 μm* belonged to the larger hard agglomerates. The same progression in the PSD was observed for both the $Ce_{0.9}Sm_{0.1}O_{1.95}$ (Fig. 8.14 a) and the $Ce_{0.85}Gd_{0.15}O_{1.925}$ samples (Fig. 8.14 b).

It was therefore necessary to incorporate both chemical and mechanical treatments to the suspensions in order to obtain the most realistic PSD that accurately described the oxides based on the visual information gathered from the SEM micrographs. The chemical treatments involved the addition of PBTCA as a dispersant and a succeeding pH adjustment. Applying ultrasound to the suspension once in the Mastersizer was the final mechanical treatment. The three final realistic particle size distributions for $Ce_{0.887}Y_{0.114}O_{1.944}$, $Ce_{0.9}Sm_{0.1}O_{1.95}$, and $Ce_{0.85}Gd_{0.15}O_{1.925}$, respectively, are presented in Figure 8.14 (a,b,)

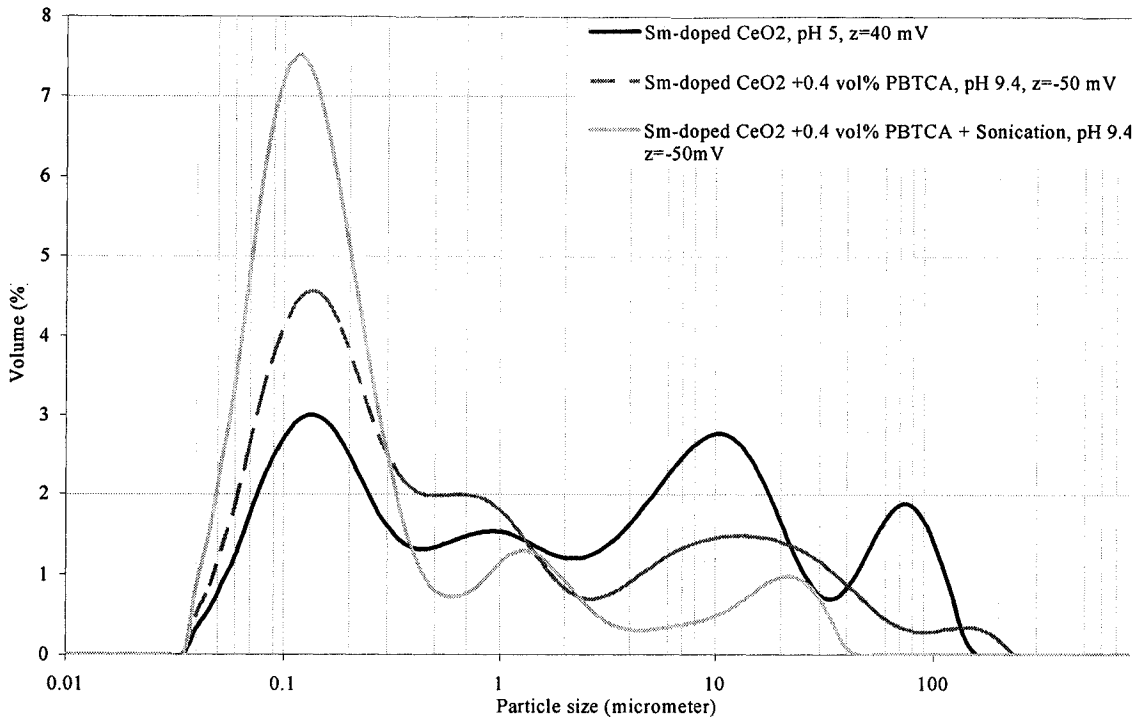


*(a)*

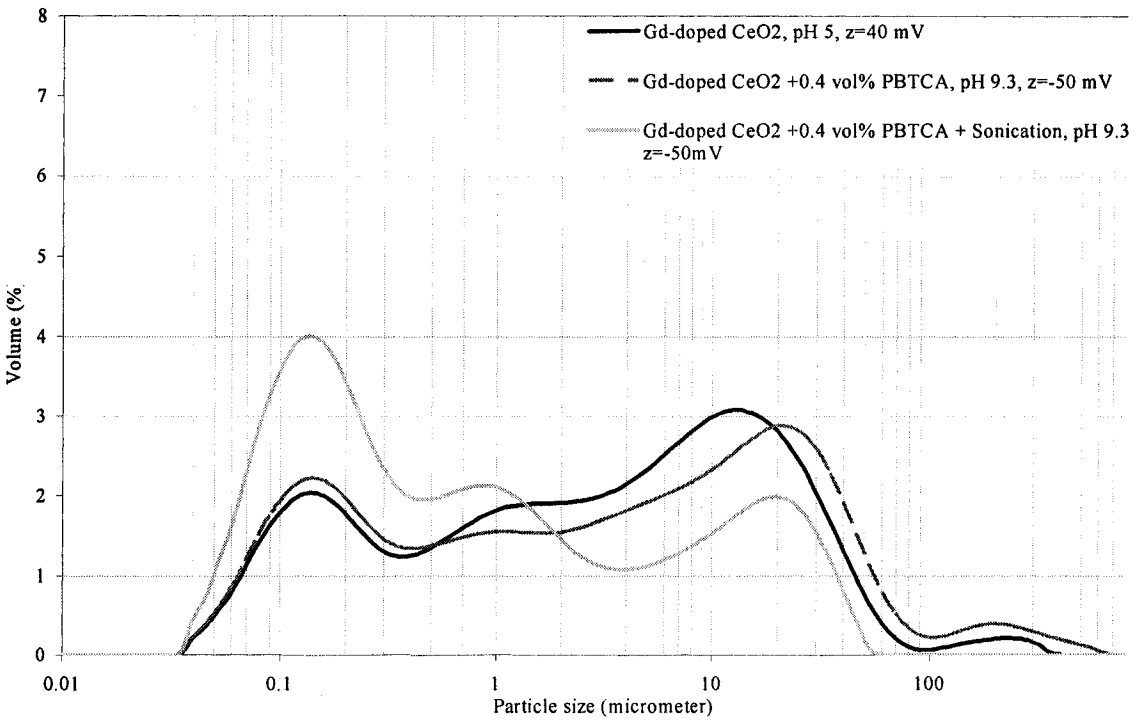


*(b)*

**Fig. 8. 14 Progression of the observed PSD for *(a)* $Ce_{0.9}Sm_{0.1}O_{1.95}$ *(b)* $Ce_{0.85}Gd_{0.15}O_{1.925}$.**

### *8.4.6 Sole Effect of Sonication on PSD*

The strong impact of sonication on PSD was discussed earlier. However, it is important to note that the sole effect of sonication was insufficient to provide a realistic PSD. The PSD obtained with a Y-doped $CeO_2$ sample in which neither was the pH adjusted nor was the dispersant added is shown in Figure 8.15.

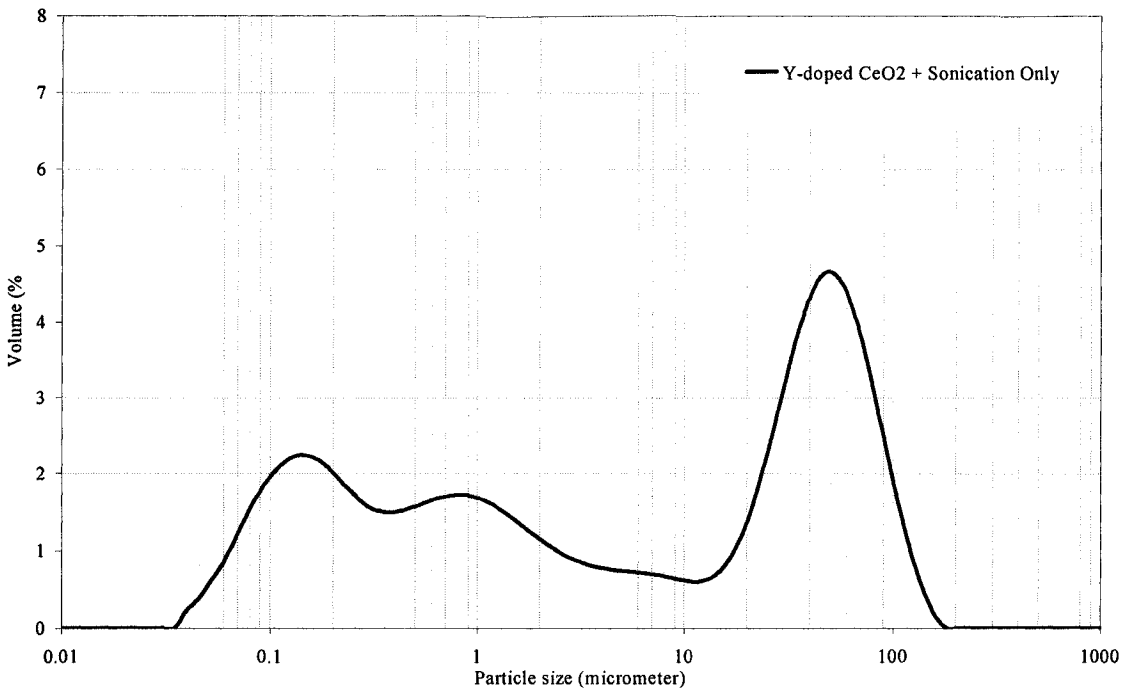


**Fig. 8. 15 Effect of solely sonication for a $Ce_{0.887}Y_{0.114}O_{1.944}$ sample**

This sample was subjected to sonication and the agglomerates were left unbroken as depicted by the large peak in the *20* to *100 μm* range. Similar, behaviors were seen for the Gd and Sm-doped samples. Therefore, it was evident that only the *combined* effect of pH adjustement, dispersant addition and sonication provided the most meaningful particle size distribution.

## 8.5 Conclusions

The final realistic particle size distribution of three doped $CeO_2$ powders were obtained after submitting the aqueous oxide suspensions to chemical and sonication treatments. As a first treatment, pH adjustment of the samples proved to be an important variable that affected the stability of the suspensions. In addition, the stabilizing effect of two different dispersants was investigated. PBTCA was found to be more efficient than phosphonoacetic acid in increasing the magnitude of the suspensions' $\zeta$-potentials. Both of these stabilizing chemical treatments therefore helped to inhibit particle agglomeration, and hence provided more realistic PSD results. As a last step, sonication was applied to the suspensions to favor de-agglomeration. The *combination* of these three treatments resulted in realistic particle size distributions that accurately described the oxide samples based on the information obtained from the SEM micrographs.

## 8.6 Acknowledgements

The financial support of the Department of Chemical Engineering at McGill University and the National Research Council of Canada (NSERC) is gratefully acknowledged.

## 8.7 References

[1] N.Q. Minh, Ceramic Fuel Cells. *J. Am. Ceram. Soc.* **1993**, *76*, 563-588.

[2] B.C.H. Steele, Appraisal of $Ce_{1-y}Gd_yO_{2-y/2}$ electrolytes for the IT-SOFC operation at 500°C. *Solid State Ionics* **2000**, *129*, 95-110.

[3] H. Inaba, Ceria-based solid electrolytes. *Solid State Ionics* **1996**, *83*, 1-16.

[4] F. Gitzhofer, M. Boulos, J. Heberlein, R. Henne, T. Ishigaki, T. Yoshida, Integrated fabrication processes for solid-oxide fuel cells using thermal plasma spray technology. *MRS Bulletin* **2000**, *25*, 38-42.

[5] C. Li, C. Li, X. Ning, Performance of YSZ electrolyte layer deposited by atmospheric plasma spraying for cermet-supported tubular SOFC. *Vacuum* **2004**, *73*, 699-703.

[6] I. Castillo, *Solution plasma synthesis of CeO2-based powders for solid oxide fuel cell electrolytes from liquid precursors*, M. Eng. Thesis, McGill University, Canada, **2003**.

[7] A. Abbas, D. Nobbs, Jose A. Romagnoli, Investigation of on-line optical particle characterization in reaction and cooling of crystallization systems: Current state of the art. *Meas. Sci. Technol.* **2002**, *13*, 343-356.

[8] E. Jorge, T. Chartier, Ultrasonic dispersion of ceramic powders. *J. Am. Ceram. Soc.* **1990**, *73(8)*, 2552-2554.

[9] K.I. Moughal, P.A. Munro, H. Singh, Suspension stability and size distribution of particles in reconstituted, commercial calcium caseinates. *Int. Diary J.* **2000**, *10*, 683-690.

[10] E. Kissa, *Dispersions: Characterization, Testing and Measurement*. New York, **1999**, pp. 14-19.

[11] R. O'Brien, Measuring Zeta Potential. *Ceramic Industry Online*. http://www.ceramicindustry.com/CDA/ArticleInformation/features/BNP__Features__Item/0,2710,73678,00.html

[12] R.J. Hunter, *Introduction to Modern Colloid Science*. New York, **1993**, pp.230-233.

[13] V.A. Hackley, R.S. Premachandran, S.G. Malghan, S.B. Schiller, A standard reference material for the measurement of particle mobility by electrophoretic light scattering. *Colloids Surf.* **1995**, *98*, 209-224.

[14] M.W. Wedd, Determination of particle size distributions using laser diffraction. *Educ. Resour. Part. Technol.* **2003**, *32*, 1-4.

[15] Y. Liu, L. Gao, J. Guo, Comparative study on the stabilizing effect of 2-phosphonobutane-1,2,4-tricarboxulic acid and citric acid for alumina suspensions. *Colloids Surf.* **2001**, *193*, 187-195.

[16] E. E. Khawaja, S. M. A. Durrani, M. F. Al-Kuhaili, Determination of average refractive index of thin $CeO_2$ films with large homogeneities. *J. Phys. D: Appl. Phys.* **2003**, *36*, 545-551

[17] P.C. Hidber, T.J. Graule, L.J. Gauckler, Influence of the dispersant structure on properties of electrostatically stabilized aqueous alumina. *J. Eur. Ceram. Soc.* **1997**, *17*, 239-249.

# Chapter 9 Conclusions

This chapter summarizes the conclusions obtained from both experimental work and the numerical simulations. All the thesis objectives were achieved except measuring the in-flight temperature of synthesized $CeO_2$ particles which was part of objective 3. However, an alternative technique is suggested in Chapter 10 (future work).

The most relevant conclusions in this study are the following:

## 9.1 Experimental conclusions

1 A novel reactor was designed to minimize plasma gas recirculation and provide a highly uniform gas flow suitable for in-flight particle sampling.

2 A novel sampling probe was designed to allow continuous particle sampling at different plasma operating conditions and reactor locations without the need of stopping the plasma flow and without sample cross contamination.

3 A wet collection method was devised and implemented to prevent particle agglomeration and to provide a near real-time particle size distribution analysis.

4 A calorimetric study of the reactor was conducted in the 25 to 45 kW range. The study allowed the calculation of the mean reactor inlet temperature which was used as a boundary condition for the numerical simulation of the velocity and temperature profiles of the reactor system at different plate powers and gas flows.

5 A thermodynamic study was conducted to identify the most favorable cerium oxide species using free Gibbs energy minimization over the 1,000 to 4,000 K range. Cerium oxide gas, liquid and solid phases were identified at different temperature ranges.

6 The temperature and velocity profiles of the plasma gas present in the reactor were computed at different plasma operating conditions using Fluent. The effect of plasma gas power and gas flow rate was investigated. The calculated temperature fields showed reactor temperatures higher than 2,500 K along the reactor centerline for most of the cases analyzed which suggests that some form of $CeO_2$ gas was present in the reactor. The velocity profiles along the centerline suggested that the maximum gas velocity is approximately 50 m/s and the velocity decreases downstream of the reactor inlet. The gas temperature and velocity increased with increasing plate power along the reactor centerline.

7 Multimodal particle size distributions were obtained for $CeO_2$ particles synthesized from dissolved cerium nitrate salts in water. The different particles sizes include: 1) Angular nanoparticles < 50 nm; two type of intermediate particles in the 50 to 2 μm range, i.e. 50 to 0.5 μm fluorite-like structure $CeO_2$ particles and 0.5 to 2 μm spherical-like $CeO_2$ particles, and finally large particle fragments in the 2 to 15 μm range. The most abundant particle size is the intermediate particles in the 50 to 2 μm range.

8 X-ray diffraction patterns of the collected product indicated $CeO_2$ with a fluorite structure. No $Ce_2O_3$ was detected.

9 The particle size distribution in the reactor is determined by a combination of several factors that can be grouped into 2 categories: 1) the different droplet-to-particle formation steps involved such as: crust formation, droplet explosion, particle sintering, homogeneous particle nucleation, vapor deposition on particle surface and particle cooling 2) the various particle collection mechanisms such as: particle impaction, turbulent diffusion and thermophoresis. From the first category, crust formation and droplet explosion seemed to have the greater effect and from the second factor, particle impaction and thermophoresis are dominant.

10 Droplet explosion favored the radial movement of large fragments as those particles did not follow the gas streamlines and were mostly deposited on the top conical part of the reactor. Intermediate particles followed 2 main paths: 1) they formed particles in the 50 nm to 0.5 μm, 2) the original 50 nm to 0.5 μm grew to 1 to 2 μm by vapor deposition and/or particle sintering depending on their residence time on the reactor. A rapid quenching favored spherical particles whereas a slow quenching favored cubical (fluorite) structures. The nanoparticles (< 50 nm) were formed by nucleation and growth from cerium oxide vapor.

11 Increasing the plasma gas temperature favors larger fragmented-crust particles ( > 5 μm). The plasma gas temperature can be increased both by increasing the plate power and by decreasing the amount of gas. The particle size distribution along the axial direction varies depending on reactor location and plasma parameters. Larger crust fragments are formed closer to the reactor inlet. Radial distribution, at locations closer to the torch exit $0 < Z < 30$ cm, show that centerline and 2.5 cm off centerline locations have similar particle size distributions. This is not true at off centerline locations at Z=40 cm. Increasing the particle residence time promoted particle sintering and more spherical-like particles along the reactor centerline.

12 Droplet explosion was more violent at higher powers; as a result, large fragments are forced out radially and impact the top conical section of the reactor. The remaining particles sintered and the cerium oxide gas either deposited on the surface of the sintered particles causing particle growth or nucleated into nanoparticles.

13 Adding glycine and alanine at lower plate powers (25 kW) did not have a significant effect on the size distribution. At higher powers (35 kW) the energy released from the combustion reaction of the fuel formed larger particles at Z=30 cm but more homogeneous particle distributions downstream of the reactor. This "particle size discrimination effect" allows a near single modal distribution at Z=40 cm between 50 nm to 140 nm.

14 A digital image analysis was implemented that allowed the estimation of the speed of particle clouds (i.e. clusters of individual particles) at two reactor locations (i.e. Z=4.5 and 9.5 cm). It was demonstrated that these clusters, particles of 1-5 μm size, have a significantly higher speeds than particles larger than 10 μm. This finding strengthens the evidence of droplet explosion.

## 9.2 Numerical modeling conclusions

The numerical modeling conclusions are separated into two categories, i.e. before and after the crust is formed. The conclusions are as follows:

**Before the crust is formed**

1 A 2-phase (droplet and plasma gas) numerical model was developed the calculate the heat, mass and momentum transfer of an evaporating solution droplet containing dissolved cerium nitrate in a stationary rf Ar-$O_2$ thermal plasma. The model was solved in a moving frame, i.e. a receding droplet interface, in spherical coordinates. It takes into account temperature and composition dependent thermophysical properties.

2 The temperature and mass fraction profiles in both the evaporating droplet and surrounding gas were calculated. The radial gas velocity profile in the surrounding gas was also computed.

3 The model was validated against existing numerical models and experimental values.

4 The model predicted that a salt saturation limit is reached at the droplet surface which leads to salt precipitation and formation of a crust in all cases analyzed.

5 The slower rate of mass transfer inside the droplet in comparison with that of heat transfer is responsible for crust formation.

6 Faster crust formation is favored by higher plasma temperatures, lower gas pressures, oxygen-richer plasmas and higher initial salt content. Also, smaller droplets developed a crust faster than larger ones.

7 The use of temperature and composition dependent thermophysical properties provides a more realistic computation. The results indicated that the use of variable properties is justified.

**After the crust is formed**

8 A 3-phase (droplet, crust and plasma gas) numerical model was developed the calculate the heat, mass and momentum transfer of an evaporating solution droplet containing dissolved cerium nitrate surrounded by a porous crust in a stationary rf Ar-$O_2$ thermal plasma. The model was solved in a moving frame, i.e. a receding droplet interface, in spherical coordinates. It takes into account temperature and composition dependent thermophysical properties. Darcy flow with a Knudsen correction to account for the gaseous flow through a porous crust composed of nano-sized crystals was employed.

9 The 3-phase model was compared to similar existing models and model predictions matched the previously reported trends.

10 A new model was developed to calculate the strength of the solid/liquid interface by computing the strength of liquid bridges formed at this interface. Pressure build-up caused by solvent evaporation and the point of crust breakage (i.e. time) were determined at different operating conditions.

11 The plasma temperature, initial size of the solution droplet and the size of the precipitated spherical crystals played a major role in crust bursting.

12 The effect of crust porosity on crust strength and crust bursting shows that crust permeability is the most important property. This in turn is closely associated with

temperature, viscosity and pressure. The Knudsen correction has a large effect on the results obtained because it directly affects the crust permeability.

13 The solvent evaporation and subsequent gaseous flow through the porous crust are largely driven by heat transfer. The flow across the porous crust is dependent on both heat and momentum transfer, whereas mass transfer is considerably slower than the other two processes.

14 The time of crust rupture lies in the few milliseconds range for all cases analyzed

## 9.3 Original contributions

The most relevant original contributions in this study are listed below:

- The development of a reactor system capable of studying in-flight spatial evolution of synthesized particles from liquid precursors minimizing particle recirculation and providing a uniform gas flow

- The development of a new sampling probe for in-flight continuous particle sampling.

- The development of a wet collection technique that allows near-real time particle size measurements based on particle postreatment, i.e. sonication and dispersant addition.

- The development of a comprehensive model of droplet-to-particle transformation that takes into account plasma parameters, transformation phenomena and particle collection mechanisms based on experimental and numerical work.

- The development of a transient numerical model showing temperature, velocity and mass fraction profiles of the droplet, crust and surrounding gas regions.

- The transient numerical model incorporated for the first time moving boundaries, Knudsen effects, crust porosity and allowed the prediction of time of crust formation and crust bursting at different plasma conditions by incorporating a way to quantify crust strength.

- The development of a reliable technique to measure primary particle size for doped cerium oxide particles based on laser diffraction and $\zeta$-potential was achieved

# Chapter 10 Future work and recommendations

The following future work and recommendations are proposed for experimental and modeling work.

## 10.1 Experimental recommendations

Three different experimental future projects are proposed.

### *10.1.1 Sampling of $CeO_2$ powders at different pressures*

The sampling of $CeO_2$ powders in-flight presented in this thesis was conducted at a reduced pressure of 0.33 atmospheres, because that is the most typical operating pressure used to spray $CeO_2$ powders to form SOFCs electrolytes. However, the modeling results suggested that gas pressure is an important parameter that affects crust formation and crust rupture. It was hypothesized that lower reactor pressures would promote crust formation and rupture faster than near atmospheric reactor pressures. Therefore, reactor pressure is a parameter that should be investigated.

Two experiments were conducted at reactor pressures of 0.5 and 0.7 atmospheres (7.3 and 10.3 psig respectively) but their results were not reliable due to two factors. First, the sampling probe was operated at near-isokinetic conditions by adjusting the quench gas flow rate and by setting the reduced pressure of the vacuum pump that is connected to the sampling probe by throttling a valve. The vacuum pump was typically operated at a reduced pressure of 19-22 in of Hg. It was noticed during experimentation that should the pressure of the reactor increase, the amount of gas that can be withdrawn would also increase. In order to maintain near-isokinetic conditions, the quench gas flow rate must be re-adjusted to the new conditions.

Due to time constrains, it was not possible to recheck all these conditions at different pressures. Second, the control loop installed in the Tekna system is not adequate to sustain a set reactor pressure in the 0.6-0.8 atmosphere (8.8-11.7 psig) range. A minimal

flow disturbance forces the control valve to either open or close which in turn changes the reactor pressure significantly (1 to 1.5 psig). This problem could not be fixed by tuning the PID-controller parameters to a less aggressive response. It is proposed that a valve (manual or automated) be installed between the exit of the reactor and the control valve so that the gas flow can be throttled and thus reactor pressure would be less sensitive to the opening/closing of the control valve.

### *10.1.2 Analysis of gas composition in-flight*

The formation of cerium oxide gas ($CeO_2$) is an important part of the discussion of the transformation of cerium nitrate salts to cerium oxide particles. The thermodynamic simulations predicted the formation of this gas in all cases analyzed and the experimental results strongly suggest that some form of cerium (Ce) or cerium oxide ($CeO_2$/CeO) vapor is present in the reactor. Therefore, the study of the gas composition is relevant to these findings.

The implementation of an optical emission spectrometer is proposed to elucidate the species present in the gas. Some key points must be addressed in order to obtain a successful reading. First, the reactor quartz windows must be kept "particle-free" and as clean as possible during the experiment. This can be achieved if a small gas bleed can be injected (perpendicular or at an angle) to prevent particles depositing on the windows. Second, the centres of the two reactor windows are located at 4.5 and 9.5 cm, respectively, away from the reactor inlet along the centerline. An emission signal as close as Z=10 cm can be obtained for CN and $C_2$ in an argon rf thermal plasma used in the production of fullerenes as demonstrated by Markovic [*Markovic, 2005*]. Third, emission signals of the oxygen-argon plasma in this study must not interfere with the potential cerium oxide gas emissions. The glow region of an argon-oxygen mixture in rf asymmetrically capacitively coupled plasma was studied by Aflori [*Aflori, 2004*]. The emission spectra showed the strongest intensity lines in the 750 to 850 nm and only trace lines for wavelengths shorter than 700 nm. The scanned range was from 200 to 900 nm. According to the National Institute of Standards and Technology Atomic Spectra Database [*NIST, 2007*], the two strongest emission lines for ArI are at 811.7 and 912.2

nm and for OI the strongest emission line is at 844.6 nm. Those results are in accordance with the information presented by Aflori. Also based on NIST database, CeIII shows its strongest emission lines at 566, 596, 603 and 606 nm. In addition, the optical emission spectra lines of $CeO_2$ have been reported in the work by Linares [Linares, 1966] and their strongest lines are located at 591.0 and 632.5 nm. This proves that the emission lines of the argon-oxygen plasma do not interfere with the emission lines of CeIII or $CeO_2$ (and presumably any other form of cerium oxide) since their highest wavelength is approximately 650 nm and the plasma region is located in wavelengths larger than 750 nm.

### *10.1.3 Measuring $CeO_2$ powders temperature in-flight*

The temperature of solid $CeO_2$ powders is an important parameter that we could not measure in this work. A DPV-2000 was used to attempt to measure the temperature of the particles based on two-color pyrometry and grey body approximation. However, particle deposition on the windows, insufficiently hot particles smaller than 15 μm and a relative low particle concentration prevented emission acquisition. The problem of measuring particle temperature is not trivial and a possible method that could work in plasma environments has been described by Vaulina [*Vaulina, 1998*]. This method involves considerable accessory equipment, lamps and the reactor needs to be modified to accommodate another view port opposite to either of the existing ones. This technique has been shown to measure the temperature of $CeO_2$ powder flowing in a propane-air flame in the temperature range of 1,900 to 2,100 K. This technique calculates emission-absorption parameters in a wide wavelength region beyond the gas emission lines. The mathematical algorithm is described in detail by Nefedov [*Nefedov, 2005*] and is based on solving a system of radiative transfer equations for light intensity measurements of different signals: i.e. the signal of a reference lamp plus the gas (flame in their case) ($S_{pl}$), the gas only signal ($S_p$), and the reference lamp signal in the absence of gas ($S_l$) at several wavelengths $\lambda_i$ ($i=1$-$N$). A more detailed description of the technique is beyond the scope of this section but the results shown for the case of $CeO_2$ powders in a propane-air flame are encouraging enough to justify a closer look at this technique.

## 10.2 Modeling recommendations

Two different modeling ideas are proposed to complement the modeling carried out in this thesis.

### *10.2.1. Aggregative crystal growth model*

The modeling work in this thesis does not include a model that takes into account crystal growth to form the crust from the first precipitated cerium oxide crystals. The assumption has been that the crystals precipitate when the evaporating solution droplet reaches the point of saturation. The crystals will precipitate as spherical particles. As more solvent is evaporated, more particles precipitate and form a thicker crust of a given porosity. A more realistic way to describe crust growth from precipitated crystals could be achieved by including an aggregative crystal growth model. One of the most promising and newest models for oxide systems has been described by Drews [*Drews, 2005*]. He developed a mathematical model to describe aggregative crystal growth, including oriented aggregation, from evolving pre-existing primary nanoparticles with composition and structure that are different from that of the final crystalline aggregate. The model is based on the results described by Buyanov [*Buyanov, 1976*] which investigated the growth of iron oxides. The model is simple and can be implemented as a series of reactions between different stages of crystal species, i.e. fresh, mature and nucleated primary particles. The model is capable of describing the crystal size evolution which is a key parameter in determining the crust porosity and strength.

### *10.2.2 Shape of nucleated $CeO_2$ particles*

The experimental evidence shown in this work suggested that the fluorite structure (cubical-like structure) is the preferred configuration for particles smaller than 0.5 μm. Also, particles in the range of 1 to 2 μm are often spherical-like. The hypothesis is that most of the smaller particles including the nanoparticles (less than 50 nm) nucleate into the most stable configuration, i.e. fluorite structure. However, there is experimental evidence that shows that particles could be partially/fully melted in flight and thus spherical particles could be expected due to favorable surface tension energies which was not the case in our results. Therefore, the introduction of a numerical model that can

provide supporting evidence for a preferred particle shape based on particle size, temperature and surface tension is desired.

The most promising route seems to be the model proposed by Barnard [Barnard, 2004]. He developed a thermodynamic model describing relative stability of different shapes for nanoparticles as a function of their size for arbitrary crystalline solids and applied it to group IV semiconductors. This model could be applied to cerium oxide because it takes into account surface tension (a temperature dependent property) and free energy minimization of the edges, corners, etc of different geometrical configurations. Barnard also compared his results to spherical particles for the case of C, Ge and Si and he clearly showed that in certain regions depending on the number of atoms present, a cubical configuration is preferred over a spherical one. The addition of a model that could predict particle shape can significantly increase the predictive capabilities of the model developed in this thesis should other materials were to be investigated.

## References (not included in the individual papers)


- Aflori, M. et al., *31st EPS Conference on Plasma Physics*, **28G**, P4.057 (2004)
- Barnard, et al. *Journal of Chemical Physics*, 121(9), 4276-4283 (2004)
- Baron, S. Intermediate temperature (500-850 °C) solid oxide fuel cells explained, *Fuel Cell Today*, 2004
- Bonneau, M. E., *Thése,* Université Sherbrooke, Canada (2001)
- Boufendi, L. et al., *Dusty Plasmas: Physics, Chemistry and Technological Impacts in Plasma Processing*, John Wiley & Sons (1999)
- Boulos, M. I. RF induction plasma spraying: State-of-the-art review. *Journal of Thermal Spray Technology*. **1**, 33-40, (1992)
- Boulos, M. I. Thermal plasma processing. *IEEE Transactions on Plasma Science*. **19**(6), 1078, (1991)
- Boulos, M. I., *J. Therm. Spray Tech.*, **1**, 33-40 (1992)
- Bouyer, E. et al, Thermal plasma chemical vapor deposition of Si-based ceramic coatings from liquid precursors, *Plasma Chemistry and Plasma Processing*, **21**(4), 523-546 (2001)
- Bouyer, E. Gitzhofer, F., Boulos, M. I., Suspension plasma spraying for hydroxyapatite powder preparation by rf plasma, IEEE Transactions on Plasma Science, 25(5), 1066-1072 (1997)
- Bouyer, E. Muller, M., Henne, R.H., Schiller, G. *J. of Nanoparticle Research,* **3**, 373-378 (2001)
- Bouyer, E., Schiller, G., Muller, M., Henne, R. H. Thermal plasma chemical vapor deposition of Si-based ceramic coatings from liquid precursors. *Plasma Chemistry and Plasma Processing*. **21**(4), 523-546, (2001)
- Byun, D. Y. et al. Microexplosion of aluminum slurry droplets, *Int. J. Heat Mass Transfer*, **42**, 4475-4486 (1999)
- Castillo, I and Munz, R. J. Transient heat and mass transfer of an evaporating stationary droplet containing dissolved cerium nitrate in a rf thermal argon-oxygen

plasma under reduced pressure, *Inter. J. Heat Mass Transf.*, **50**(1-2), 240-256 (2007)

- Castillo, I. and Munz, Inductively coupled plasma synthesis of $CeO_2$ –based powders from liquid solutions for SOFC electrolytes. *Plasma Chemistry and Plasma Processing*, **25**(2), 87-107, (2005)
- Charlesworth, D. H. and Marshall, W. R. Evaporation from drops containing dissolved solids, *AIChE Journal*, **6**(1), 9-23 (1960)
- Cho, S. Y., Some theoretical considerations on the combustion and disruption of free slurry droplets, Combust. Sci. and Tech, **67**, 37-57 (1989)
- Delbos et al, DC plasma spray elaboration of fine structured coatings by ceramic liquid suspension injection, *Proceedings 16th International Symposium on Plasma Chemistry* (ISPC 16), Italy (2003)
- Delbos et al, DC plasma spray elaboration of fine structured coatings by ceramic liquid suspension injection, *Proceedings 16th International Symposium on Plasma Chemistry* (ISPC 16), Italy (2003)
- Delbos, C., et al. *Plasma Chemistry and Plasma Processing*, **26**(4), 393-414 (2006)
- Drews, T., et al. *Journal of Physical Chemistry B.*, **109**, 23879-23887 (2005)
- Elperin, T. and Krasovitov, B. Evaporation of liquid droplets containing small solid particles, *Int. J. Heat Mass Transfer*, **38**(12), 2259-2267 (1995)
- Fauchais, et al, Plasma spraying from thick to thin coatings and micro to nano-structured coatings, , *Proceedings 16th International Symposium on Plasma Chemistry* (ISPC 16), Italy (2003)
- Fazilleau, J., *et al. Plasma Chemistry and Plasma Processing*, **26**(4), 371-391 (2006)
- Forsyth, B. R. and Liu, B. Y. H., *Aerosol Science and Technology,* **36**(5), 515 (2002)
- Gardner, G. C., Asymptotic concentration distribution of an involatile solute in an evaporating drop, *Int. J. Heat Mass Transfer*, **8**, 667-668 (1965)
- Gitzhofer, F. et al. Integrated fabrication processes for solid-oxide fuel cells using thermal plasma spray technology, *MRS Bulletin*, **25**(7), 38-42 (2000)

- Gitzhofer, F., Boulos, M., Heberlein, J., Henne, R., Ishigaki, T., Integrated fabrication processes for solid-oxide fuel cells using thermal plasma spray technology, *MRS Bulletin,* **25**(7), 38-42 (2000)
- Goortani, B, et al., International Journal of Chemical Reactor Engineering, **4**, 1330 (2006)
- Gutierrez, S., and Gitzhofer, F., *Proceedings 15th ISPC* Orléans, France, **7**, 2749-2756 (2001)
- Javanthi, G. V., Zhang, S. C., Messing, G. L. Modeling of solid particle formation during solution aerosol thermolysis, *Aerosol Science and Technology*, **19**(4), 478-490 (1993)
- Jia, L. and Gitzhofer, F. Collection of nano-powders generated by radio frequency (RF) plasma spray synthesis (PSS) processing, using a sampling probe, *Proceedings 17$^{th}$ International Symposium on Plasma Chemistry (ISPC 17)*, Canada (2005)
- Lau, Y. C., Kong, P.C., Pfender, E. Synthesis of zirconia powders in an RF plasma by injection of inorganic liquid precursors, *Ceramic Transactions 1*, 298-303 (1988)
- Lemoine, G., Ménard, H., Jurewiczs, J. W., *Proceedings 16th ISPC* Taormina, Italy (2003)
- Linares, R., *Journal of the Optical Society of America,* 56(12), 1700-1703 (1966)
- Lu Jia and Gitzhofer, Collection of nano-powders generated by radio frequency (RF) plasma spray synthesis (PSS) processing, using a sampling probe, *Proceedings of the ISPC 17*, Toronto, Canada (2005)
- Markovic, Z., et al. *Fullerenes, Nanotubes and Carbon Nanostructures*, **13**, 215-226 (2005)
- Merkouf, A., Boulos, M. I. Distributed energy analysis for an integrated radio frequency induction plasma system. *J. Phys. D: Appl. Phys.* **33**, 1581-1587, (2000)
- Müller, M. et al., Thermal induction plasma processes for the synthesis of SOFC materials, *Materialwissenshchaft und Werkstofftechnik*, **33**(6), 322-330 (2002)

- Nefedov, A., et al. *Journal of Quantitative Spectroscopy Radiative Transfer*, **54**(3), 453-470 (1995)
- Nijhawan, S. *et al.*, *Journal of Aerosol Science*, **34**, 691-711 (2003)
- NIST Atomic Spectra database, http://physics.nist.gov/PhysRefData/ASD/index.html
- Ormerod, R. M. Solid oxide fuel cells. *Chemical Society Reviews*. **32**, 17-28, (2003)
- Orr, F. M., et al. Pendular rings between solids: Meniscus properties and capillary force, *J. Fluid Mech.*, **67**, 723 (1975)
- Ozturk, A. and Cetegen, B. M. Modeling of plasma assisted formation of precipitates in zirconium containing liquid precursor droplets, Materials Science and Engineering A, **384**, 331-351 (2004)
- Rambabu, et al., Novel wet-chemical synthesis and characterization of nanocrystalline $CeO_2$ and $Ce_{0.8}Gd_{0.2}O_{1.9}$ as solid electrolyte for intermediate temperature solid oxide fuel cell (IT-SOFC) applications. *Journal of Materials Science*, **41**, 7530-7536 (2006)
- Schiller, G., Müller, M., Gitzhofer, F., *J. Therm. Spray Tech.*, **8**(3), 389-392 (1999)
- Schlünder, E. U. Temperatur- und Masseänderung verdunstender Tropfen aus reinen Flüssigkeiten und wässrigen Salzlösungen, *Int. J. Heat Mass Transfer*, **7**, 49-73 (1964)
- Seol, K. S *et al.*, *Journal of Aerosol Science*, **31**(12), 1389 (2000)
- Song, H. Z., et al. Aerosol-assisted MOCVD growth of $Gd_2O_3$-doped $CeO_2$ thin SOFC electrolyte film on anode substrate. *Solid State Ionics*. **156**, 249-254, (2003)
- Stambouli, A. B., Traversa, E. Solid oxide fuel cells (SOFCs): a review of an environmentally clean and efficient source of energy. *Renewable and Sustainable Energy Reviews*, **6**, 433-455, (2002)
- Steele, B.C.H. and Heinzel, A. Materials for fuel-cell technologies. *Nature*. **414**, 345-352, (2001)
- Tang, G. H., et al. Gas slippage effect on microscale porous flow using the lattice Boltzmann method, *Physical Review E.*, **72**, 056301 (2005)

- Vaulina et al, *Combustion and flame,* **155**(3), 364-371 (1998)
- Wang, X, Hafiz, J. *et. al.*, Plasma Chemistry and Plasma Processing, **25**(5), 439-453 (2005)
- Willett, C., et al. Capillary bridges between two spherical bodies, *Langmuir,* **16**, 9396-9405 (2000)
- Xiong, Y. Kodas, T. T. Droplet evaporation and solute precipitation during spray pyrolysis, *J. Aerosol Sci.,* **24**(7), 893-908 (1993)
- Yano, M, et al., Recent advance in single chamber solid oxide fuel cells: A review. *Solid State Ionics*, **177**, 3351-3359 (2007)
- Yu, H. and Liao, W. H. Evaporation of solution droplets in spray pyrolysis. *Int. J. Heat Mass Transfer*. **41**(8-9), 993-1001 (1997)

## *Appendix A. Operation manual for the experimental setup*

This manual describes how to start the utilities for the Tekna system with argon and oxygen as central and sheath (auxiliary) gases, respectively. Also, the key to open the control console door is in one of the shelves of the blue cabinet next to inter-labs door. PLEASE, if you use it, put it back in place.

### The steps are as follows:

1. Turn on the generator switch breaker which is in the service corridor (red switch), and the control console switch breaker that is behind the generator (next to the electrode erosion system). Then, rotate 90 deg clockwise the yellow knob located on the control console (next to the rotameters). The computer should be on after a few seconds.
2. Allow argon and auxiliary gas to the control console by opening all the necessary valves; for argon, valves 16, 17, and 19 and for oxygen valves 15, 18 and 20. The ideal operating conditions will require 100-120 psig of both gases as the inlet operating pressure. There is no need to adjust the regulators, they have already been adjusted! The sequence to follow is:

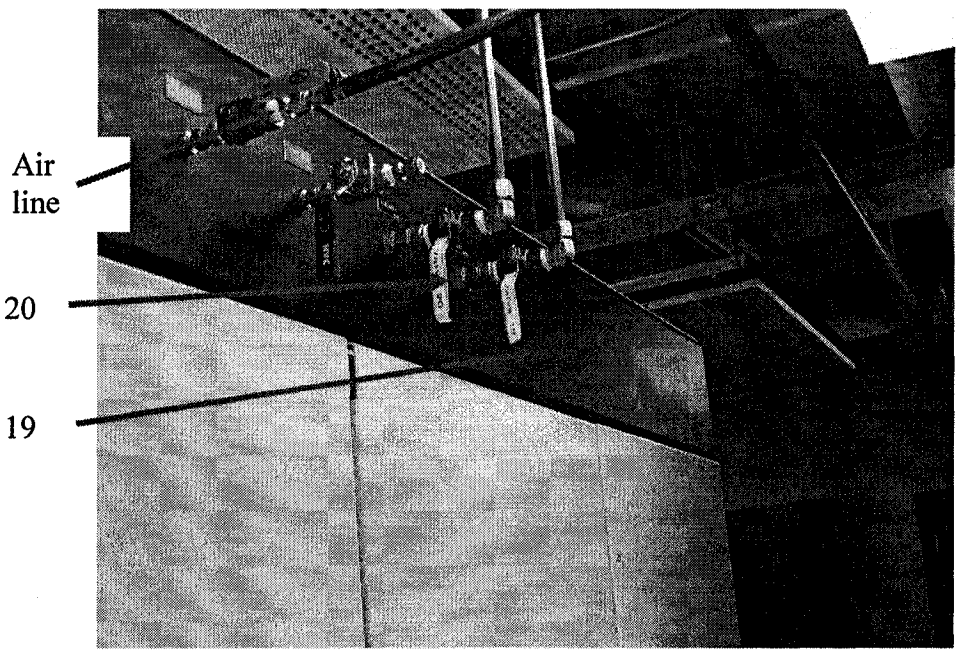


**Fig. 1**

Valves 19 and 20 (Fig 1) are to be closed. Open valves 15 and 16 (Fig. 2) and check that the pressure in the regulators exceeds 120 psig (these pressure readings will decrease when the vacuum is on; hence the excess pressure is needed to achieve the operating conditions of 100 psig). Finally, open valves 17 and 18 FIRST (Fig 3) and then valves 19 and 20. You should now have gas going to the control console. **NOTE: All the valves in the compressed air line, green line, must always be open. There is no need to adjust them.**

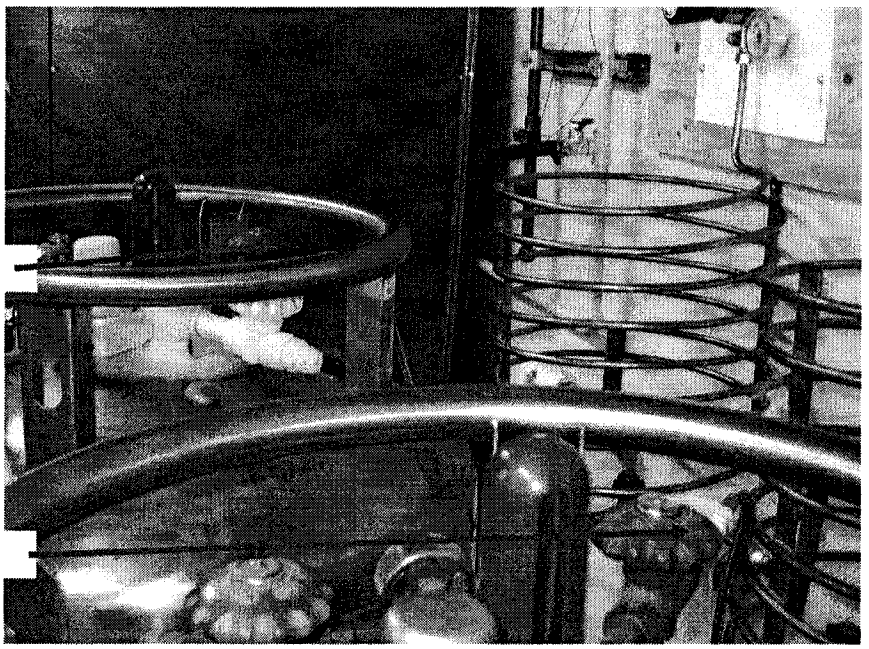


**Fig. 2**

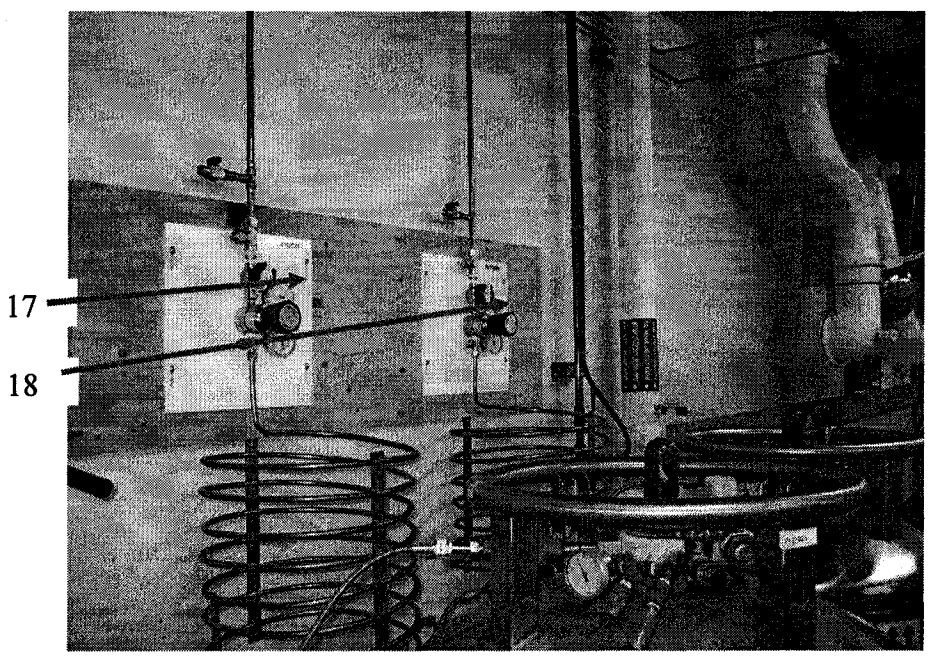


**Fig. 3**

3. Before starting the cooling water in the lab, check that valves 2, 25 and 26 are closed. Also make sure that valve 9 is closed (Fig. 4). Valves 28 and 29 must also be closed. Start the lab cooling water by opening the main on/off valve (1). This valve is red and is the first valve following the white tube water line (Fig.4 shows the water line but not the

valve). This valve is located next to the side B of the Tekna generator. Check that there is cooling water running by opening the drain valve (3) (Fig 4 and 5). Once the water is running, open the on/off valve that supplies cooling water to the generator (2)**SLOWLY** (Fig. 5). This valve has a safety switch! Don't force it. Pull the switch before turning.

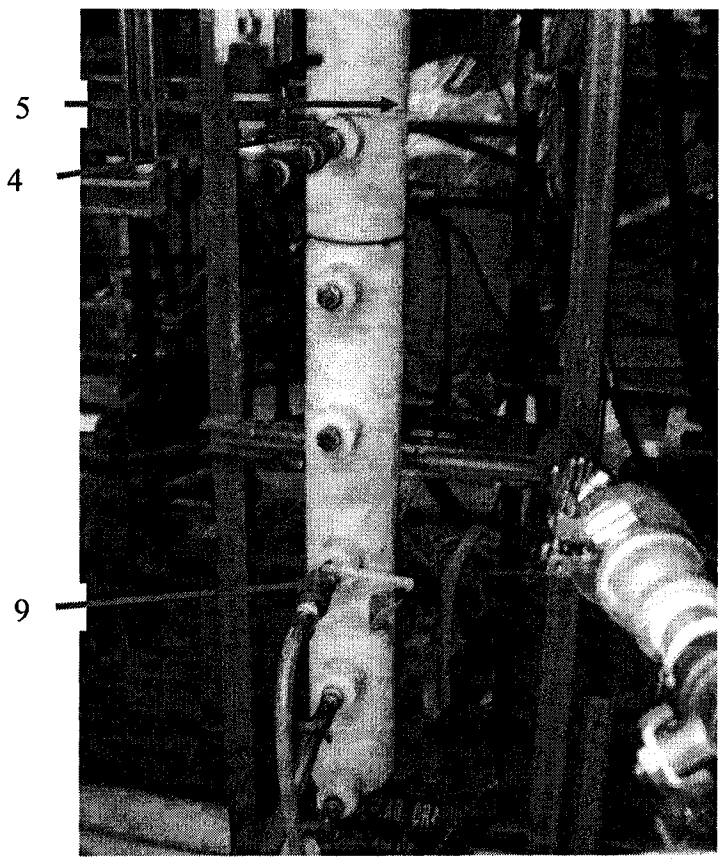


**Fig. 4**

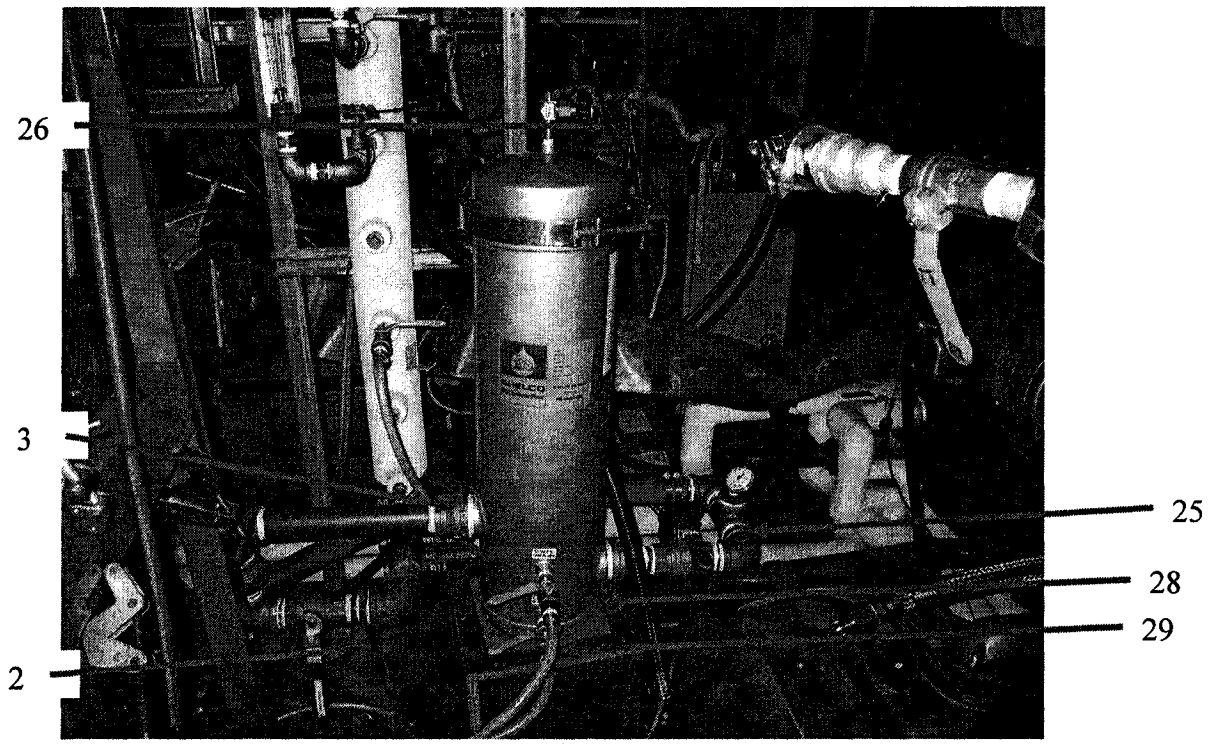


**Fig. 5**

As water fills up the filter, slowly open valve 26 and wait until the first drop of water comes out of valve 26 and then close it. The filter should be full by now. Slowly, open valve 25 to let water into the Tekna system

4. The lab is equipped with a booster pump that you need to turn on after the cooling water has been started. Turn the switch breaker label booster pump and then rotate the knob located in the adjacent controller to AUTO (remember that the breaker must always be turned on *first* before you can switch on the controller). You would find the controller and breaker on the corner wall of the lab next to the DC plasma system.

5. The vacuum pump also needs water to operate. Close the valve label DC torch (11) and open the valve label RF torch (12) (Fig. 6). Also, close the drain valve of the vacuum pump water reservoir (14) (This valve is located under the blue tank in Fig. 6) and open valve 27 which is the drain of the pump itself. All these steps are necessary to allow the vacuum pump tank to accumulate water and therefore run. Valve 13, located on the top of the vacuum pump and should always be open. You need to go to side of the lab that has the DC plasma system to open these valves.

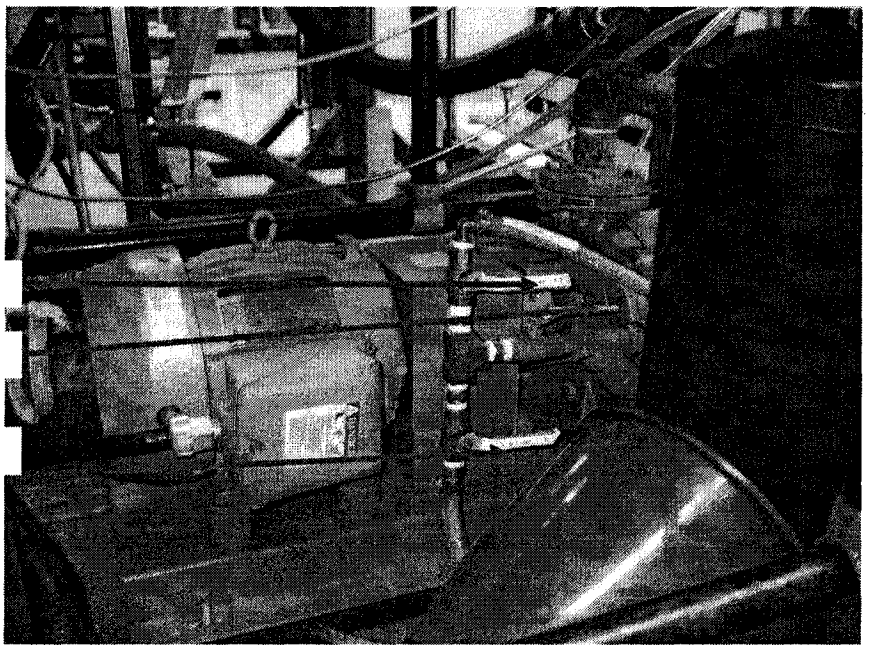


**Fig. 6**

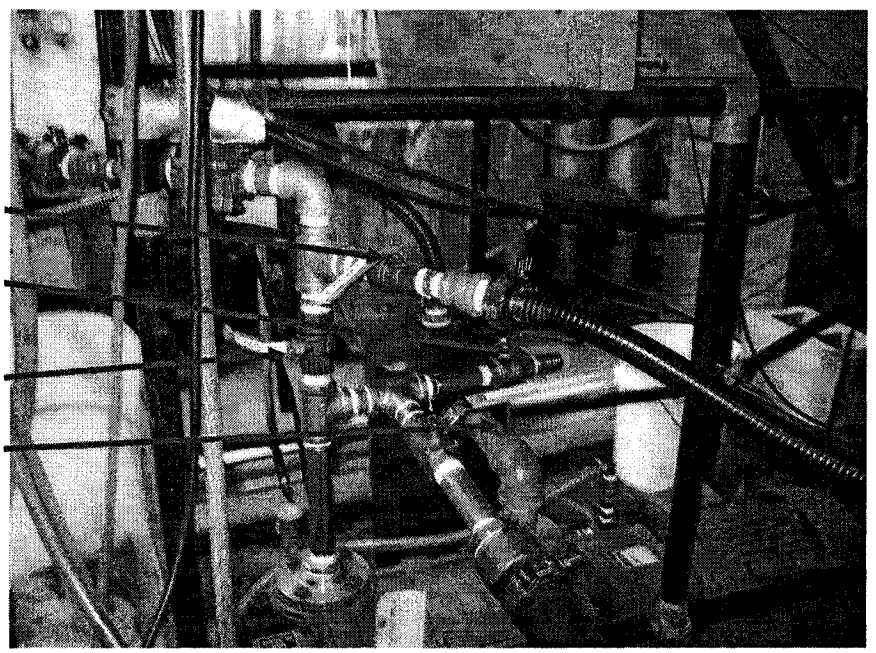


**Fig. 7**

6. Close the valves that allow the exhaust of gas from the DC torch reactor, i.e. valves 8 and 10. This is VERY important to prevent contamination of DC torch system to the Tekna plasma system. (Fig. 7) Then, open vale 6. This valve opens the vacuum line from the Tekna system to the vacuum pump. All these valves are better accessed from the Tekna generator side of the lab. Also PARTIALLY open the vent valve (7) that is located right on top of the vacuum pump (Fig. 7). This valve should be opened more if the pump starts shaking and vibrating during operation, failure to do so, will break the pump.

Essentially, the vent valve controls the strength of the vacuum. It has been adjusted and it should only be re-adjusted if you need a vacuum lower than 2 psig.

7. Open the water line for the vacuum pump by opening valve 4 (Fig. 4) You should see water going through the rotameter. A reading of 8 is sufficient to run the pump, if 8 is not achieved, gently adjust valve 5 (Fig. 4) (Tekna side of the lab). Further, check that valve 21 is open. This valve should always be open to allow the exhaust of gases from the reactors.

8. The vacuum pump can now be turned on by switching on the breaker label vacuum pump and then pressing the green Start buttom on the controller underneath the breaker. **However, it is recommended that you turn on the vacuum pump ONLY when you are ready to start the vacuum on the Tekna touch pad screen.**

9. The sampling probe collection system is composed of different components: sampling probe cooling water, cooling water for the cyclonic chamber and a peristaltic pump. The utilities are shown in Figure 8 and 9. Make sure that the water in the main line is clean by first closing valves 32 and 34 and opening valve 31 (drain valve) while you slightly open valve 30. Do this for 10 sec or until the water going to the drain is clean. Close valve 31 and slowly open valve 32 to fill up the filter. You should see water going through the flow meter that measures the water exiting the sampling probe. Wait until there are no more air bubbles in the flow meter. **Make sure that valve 33 is partially open before turning on the booster pump for the sampling probe**. Otherwise, the pump is going to burn a fuse. When there are no more bubbles in the flow meter you can start the booster pump and the discharge pressure must be at least 100 psig, preferably 120 psig. You can now open valve 34 and turn on the peristaltic pump that collects the liquid from the cyclonic chamber and the quench gas for the sampling probe can also be started

10. At this point you can follow the Tekna operating manual to get the plasma started.

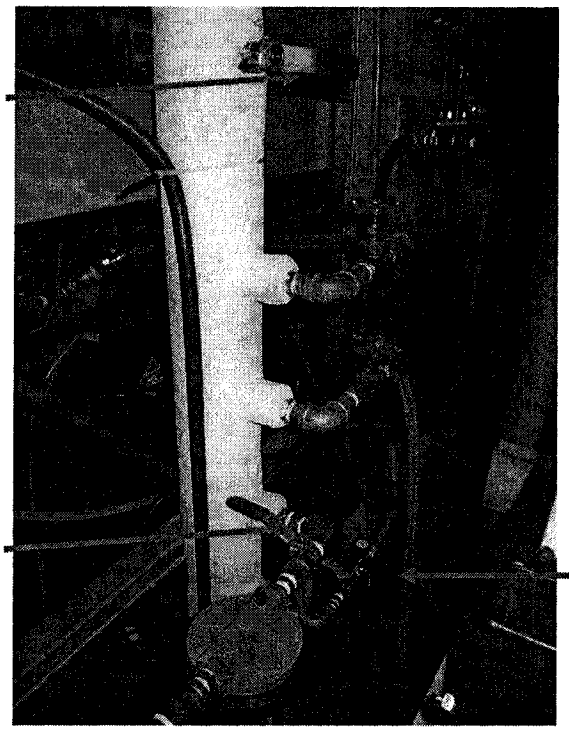


Fig. 8

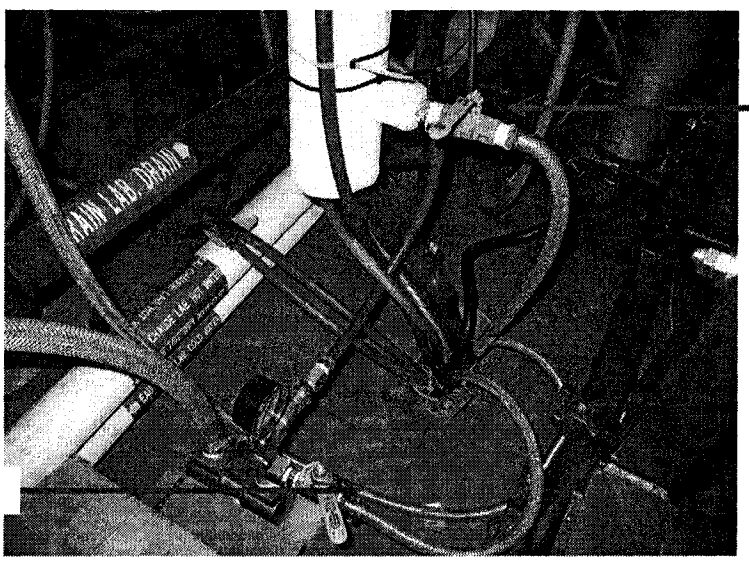


Fig. 9

## To shutdown the utilities follow these steps:

1. The vacuum must be stopped by switching off the vacuum pump controller and then the switch breaker. **Make sure that you stop the flow of gas to the reactor immediately after you stop the vacuum pump. You may have to run across the lab to do this otherwise the pressure in the reactor will build up quite fast**

2. Similarly, the lab booster pump must be switched off. Turn the controller to the middle position, i.e. between auto and manual and then switch off the breaker.

3. The vacuum valve must be closed thus isolating the Tekna system from the DC torch setup (valve 6).

4. Stop the flow of water to the water rotameter feeding the vacuum pump (4) and open the drain valve (14). This will drain the tank and will prevent the tank to rust. You need to disconnect the quick disconnect and use a bucket for an effecting draining (Fig. 6 shows how you should do it). Close valve 27 to prevent backflow from the main lab drain line

5. The gas flow rates can be stopped by closing the gas tanks valves first (15 and 16) and then venting off the lines using the vent valves (valves that open to atmosphere). You will need to close the valves preventing the gas going into the control console for a faster vent (19 and 20). Valves 17 and 18 must be GENTLY closed, hand tight is sufficient.

6. Close the main lab cooling water supply (1). You may need to drain off the line by opening the lab drain (3) and opening valve 26 to vent out the filter. Valves 28 and 29 should also be open

7. Switch off the booster pump that supplies water to the sampling probe. Close valves 30 and 34. Drain the water from the filter by opening valve 31 and 32 and venting out the filter by pressing the red button. After the water is drained, valves 31 and 32 must be closed

7. Shutdown the power to the generator by switching off the generator switch (outside in the corridor)
8. After you finish analyzing and saving your results you can switch off the computer and the yellow knob on the control console. Finally, switch off the console breaker that is located behind the generator.

NOTE: This set of instructions is not error free, if you hear an unusual noise or an alarm goes off, check that all utilities are running properly. Make sure that the vacuum pump has enough water to run and if you need a lower vacuum you need to close valve 7 more, **BUT DO NOT ever completely close it unless you need a very strong vacuum for few seconds. The vacuum pump could break.**